Nonlinear stabilization of magnetohydrodynamic equations and applications to multiphase flows

Loïc Cappanera

NNT : 2015SACLS149

Thèse de doctorat

de l'université Paris-Saclay

préparée à l'université Paris-Sud

Ecole Doctorale N° 579 :
Sciences mécaniques et énergétiques, matériaux et géosciences
Laboratoire d'Informatique pour la Mécanique et les Sciences de l'Ingénieur (LIMSI)

Discipline : Mécanique des fluides

Soutenue le 3 décembre 2015 au LIMSI (Orsay) par

Loïc Cappanera

Stabilisation non linéaire des équations de la magnétohydrodynamique et applications aux écoulements multiphasiques

Directeur de thèse :	Mme. Caroline Nore	Professeur (Université Paris Sud, LIMSI-CNRS, Orsay)
Encadrant de thèse :	M. Jean-Luc Guermond	Professeur (Texas A&M University, College Station, Texas)

Composition du jury :

Président du jury :	M. François Daviaud	Directeur de Recherche (CEA Saclay)
Rapporteurs :	M. Richard Pasquetti	Directeur de Recherche (Université de Nice Sophia-Antipolis)
	M. Kai Schneider	Professeur (Université Aix-Marseille)
Examinateurs :	Mme. Astrid Decoene	Maître de Conférences (Université Paris Sud)
	Mme. Caroline Nore	Professeur (Université Paris Sud)
Invités :	M. Jacques Léorat	Directeur de Recherche (Observatoire de Paris-Meudon)

Abstract

The investigations presented in this manuscript focus on the numerical approximation of the magnetohydrodynamics (MHD) equations and on their stabilization for problems involving either large kinetic Reynolds numbers or multiphase flows. We validate numerically a new Large Eddy Simulation (LES) model, called entropy viscosity, on flows driven by precessing cylindrical containers or counter-rotating impellers (Von Kármán flow). These studies are performed with SFEMaNS MHD-code developed by J.-L. Guermond and C. Nore since 2002 for axisymmetric geometries. This code is based on a spectral decomposition in the azimuthal direction and a Lagrange finite element approximation in a meridian plane. We adapt a pseudo-penalization method to report the action of rotating impellers that extends the range of SFEMaNS's applications to any geometry. We also present an original approximation method of the Navier-Stokes equations with variable density. This method uses the momentum as variable and stabilizes both mass and momentum equations with the same entropy viscosity.

Key words: Multiphase flows, entropy viscosity, pseudo-penalization method, level set method, magnetohydrodynamics

Résumé

Les travaux présentés dans ce manuscrit se concentrent sur l'approximation numérique des équations de la magnétohydrodynamique (MHD) et sur leur stabilisation pour des problèmes caractérisés par des nombres de Reynolds cinétique élevés ou par des écoulements multiphasiques. Nous validons numériquement un nouveau modèle de Simulation des Grandes Échelles (ou Large Eddy Simulations, LES), dit de viscosité entropique, sur des écoulements de cylindre en précession ou créés par des turbines contra-rotatives (écoulement de Von Kármán). Ces études sont réalisées avec le code MHD SFEMaNS développé par J.-L. Guermond et C. Nore depuis 2002 pour des géométries axisymétriques. Ce code est basé sur une décomposition spectrale dans la direction azimutale et des éléments finis de Lagrange dans un plan méridien. Nous adaptons une méthode de pseudo-pénalisation pour prendre en compte des turbines en mouvement, ce qui étend le code SFEMaNS à des géométries quelconques. Nous présentons aussi une méthode originale d'approximation des équations de Navier-Stokes à densité variable qui utilise la quantité de mouvement comme variable et la viscosité entropique pour stabiliser les équations de la masse et du mouvement.

Mots clés: Écoulements multiphasiques, viscosité entropique, méthode de pseudo-pénalisation, méthode de level set, magnétohydrodynamique

Acknowledgments

All the work presented in this PhD thesis would not have been possible without the help of many people that I would like to thank here. Firstly I want to thank my advisors, Caroline Nore and Jean-Luc Guermond, who allowed me to enter the world of scientific research. Their combined experiences in fluids mechanics and mathematics let me adapt and develop numerical model for a large range of physical problems. Moreover their collaboration led me to spend one year in Texas A&M University which was a wonderful experience (personally and professionally). Thank you again for the trust and advice you gave me during all my PhD period.

I would like to thank Richard Pasquetti and Kai Schneider who had the kindness and the courage to review my manuscript. I thank too François Daviaud and Astrid Decoene who accepted to be examiners for my PhD defence. I am also thankful to Jacques Léorat for accepting to be a member of my jury and whose experience on physics has been a great help for my PhD research.

As this thesis took place in LIMSI and TAMU, I had the luck to work and discuss with many people that I thank here. More particularly, I thank Wietze Herreman that shared his experience of research with me and also help me understanding many concepts while we were working together. I am also thankful to Nicolas Grenier who gave me the opportunity, with talk and discussion, to learn more about multiphase flow. Thanks also to Yann Fraigneau, Christian Tenaud and Laurent Martin Witkowski for their help and discussion. I do not forget the help of LIMSI's computer support group and thank particularly Jalel Chergui and Olivier Lassale for their help.

A special thanks to Ludomir, Can, Shreyas, Marko, Andres, Daniel, Matthew, who allow me to work in places with a very good ambiance. I also thank Francky Luddens who gave me many information and advice so I could start my PhD in the best condition.

Eventually I would like to thank all my family, and also my friends, who support me during my PhD thesis period. Moreover I give a special thanks to Katrina who has been by my side in all moments, good and bad, which allows me to go through many difficulties.

Contents

Introduction

1.1 Context and motivations

The magnetohydrodynamic (MHD) equations describe the interactions between a fluid conductor of electricity and the ambient magnetic field. The evolution of the magnetic field is governed by the Maxwell equations in the quasi-static limit while the Navier-Stokes equations describe the evolution of the fluid's velocity field. The coupling is handled by the action of the Lorentz force and the Ohm law. The non dimensionalization of these equations involves two dimensionless parameters: the kinetic Reynolds number R_e and the magnetic Reynolds number R_m that characterize the ratio of the convective time with the kinetic and ohmic diffusion times. MHD phenomena take place in a large range of problems such as industrial processes (aluminium production in Hall-Héroult cells or Liquid Metal Battery), natural phenomena (generation of magnetic field in astrophysics) or laboratory experiments. The numerical approximation of such problems may give relevant information to improve the efficiency of experimental or industrial set ups and presents one asset: they are easier to put in place. However, most of these applications involve either large kinetic Reynolds numbers that makes the dynamics of the flow too rich to be fully approximated with present computational resources, or immiscible multiphase flows which require to report of the evolution of the density, solution of a conservation law presenting singularities due to the discontinuity of densities between two adjacent fluids. To overcome these difficulties the scientific community develops stabilization methods that aim either at approximating the large scales of flows with too rich dynamics to be fully approximated (called LES for Large Eddy Simulation) or at reducing the spurious oscillations generated when approximating discontinuous solutions.

In that frame this PhD thesis proposes to face these difficulties by using a nonlinear stabilization method called entropy viscosity. This method was developed by Guermond et al [36, 37, 38] and consists of adding an artificial viscosity made proportional to the residual of an energy equation. It allows to dissipate the energy accumulated by the approximations due to the presence of large gradients that are not represented correctly by the mesh. It can also be seen as a way to select the unique entropy solution of Kružkov [61] for conservation laws or to approximate a suitable solution of the Navier-Stokes equations in the sense of Scheffer [101]. In both cases it allows to approximate a physical solution, meaning a solution that does not produce energy. On one hand we propose to enhance the benefit of the entropy viscosity as a LES method for approximating solutions of problems with large kinetic Reynolds numbers. In echoes of previous studies of the team where

this PhD took place, this study is performed on two physical problems where the fluid is either driven by a precessing cylindrical container or by counter rotating impellers. These problems are subjects of current experiments in CEA Saclay and future experiments in Dresden (Germany) which, unlike natural phenomena with many unknown parameters, would allow future comparisons with our numerical results. The numerical simulations of these problems are done with SFEMaNS code (Spectral/Finite Element for Maxwell and Navier-Stokes), developed for the past decade by Guermond and Nore in cylindrical coordinates. As this code uses a Fourier expansion in the azimuthal direction and Lagrange finite elements in a meridian plane, the representation of rotating impellers becomes a challenge which is overcome by adapting a pseudo-penalization technique of Pasquetti et al [89]. On the other hand we also extend the range of SFEMaNS code to multiphase flows. Such problems present two main difficulties: tracking the evolution of interfaces between immiscible fluids and dealing with time independent algebra for computational efficiency. While we propose to track the evolution of interfaces with a level set method, we present a new approximation method, inspired from Guermond et al [41]. This methods uses the momentum, equal to the density times the velocity field, as variable for the Navier-Stokes equations. Its main novelty relies on reducing spurious oscillations, that may emerge when considering large ratios of density and viscosity, by stabilizing both the mass and the momentum equations with the same entropy viscosity. The correct behavior of this method is investigated using numerous tests cases. Eventually all the developments of this thesis expand the range of SFEMaNS code action to many geophysical or MHD applications. The use of the entropy viscosity enables to increase the range of parameters in numerical simulations in the quest to the still out-reach experimental ones.

1.2 Thesis outline

This dissertation is composed of six chapters and one french substantial summary in appendix. After a chapter of introduction, chapters 2 and 3 describe the SFEMaNS code and the entropy viscosity method, that we use to numerically approximate the solutions of hydrodynamic or magnetohydrodynamic problems. Chapter 4 aims to validate the entropy viscosity as a stabilization method for high Reynolds number simulations in the frame of Large Eddy Simulations (LES). In chapter 5 we introduce a new method to approximate multiphase flow problems. A conclusion of the present studies and their prospects are given in the final chapter.

Chapter 1 - Introduction. We describe the magnetohydrodynamic equations and their nondimensionalization that leads to the use of the kinetic Reynolds number R_e and the magnetic Reynolds number R_m. In reference to chapter 5, the Navier-Stokes equations are described for constant and variable density problems.

Chapter 2 - Magnetohydrodynamics and SFEMaNS MHD-code. In this chapter we present the numerical code used to approximate MHD problems. Details on the numerical method used, a mixing of Fourier and Finite elements, are given. We also describe the code operation and restrictions before we present the past and recent developments to enhance all its possibilities.

Chapter 3 - Nonlinear stabilization method: entropy viscosity. We give an overview of present Large Eddy Simulation (LES) models and introduce the entropy viscosity as a new LES model. We draw attention to consistency and diffusive properties

of entropy viscosity and explain its connection to suitable weak solutions in the sense of Scheffer [101]. Eventually details on its implementation in the SFEMaNS code are given and its consistency property is checked with analytical tests.

Chapter 4 - Large Eddy Simulation with entropy viscosity. This chapter is devoted to validate the entropy viscosity as a LES method. The chapter is split in to two, first the entropy viscosity is used to approximate the solution of a Von Kármán Sodium (VKS) set-up. It proves to be efficient as it is in agreement with Direct Numerical Simulations (DNS) performed on a finer mesh and recovers previous experimental or numerical results of similar set-ups. Next two configurations of precessing cylinders are presented in the form of an article in preparation. The entropy viscosity is used to extend the range of kinetic Reynolds numbers studied for one configuration after being validated with DNS comparisons at $R_e = 4000$. Then a MHD study of both configurations is performed with DNS to determine the most favorable one to the generation of magnetic field.

Chapter 5 - Applications to multiphase flows with momentum based approximation. We present, in the form of an article in preparation, a new approximation method for multiphase flow problems that involves a momentum based approximation for the Navier-Stokes equations and the entropy viscosity as a stabilization method for both mass and momentum equations. The method is validated for a set of tests involving gravity, rotating containers, surface tension and MHD effects. We note that the method has been used to study Liquid Metal Batteries (LMB) instabilities in [46].

Chapter 6 - Conclusion and prospects. Finally we sum up the main results obtained during this PhD thesis and introduce possible developments connected to large Reynolds number computations and studies of Liquid Metal Battery instabilities.

1.3 Magnetohydrodynamic equations

The magnetohydrodynamic equations describe the reciprocal actions between the magnetic field and the velocity field inside an electrical conducting fluid. As we plan to study hydrodynamic instabilities due to the presence of a magnetic field or dynamo effect, i.e., conversion of kinetic energy into magnetic energy, we give details about the MHD equation formulations we use. We refer to [79, 98] for a full description of the MHD equations and note that all equations described in this section are considered on a domain $\Omega \subset \mathcal{R}^3$ and for time $t \geq 0$. They also involve boundaries and initial conditions that are not specified.

1.3.1 Navier-Stokes Equations

We start to describe the evolution of an incompressible Newtonian fluid governed by the Navier-Stokes equations that we write:

$$\partial_t \mathbf{u} + (\nabla \times \mathbf{u}) \times \mathbf{u} - \nu \Delta \mathbf{u} = -\frac{1}{\rho} \nabla p + \frac{1}{\rho} \mathbf{f}, \tag{1.3.1}$$

$$\nabla \cdot \mathbf{u} = 0, \tag{1.3.2}$$

where $\mathbf{u}$ is the velocity field, ρ the density, ν the kinematic viscosity, $\mathbf{f}$ a body force and p the hydrodynamic pressure equal to $\rho \frac{\mathbf{u}^2}{2} + P$ with P the fluid pressure. One can note that the vector fields are in bold so we can differentiate them from a scalar field, this notation is kept all along this dissertation. We write these equations with the hydrodynamic pressure

because the SFEMaNS code uses this formulation. Since we consider only one fluid, we can notice that the density and the kinematic viscosity are constant (in time and space). To get dimensionless equations, we introduce a reference length scale L_{ref}, a reference velocity U_{ref}, a reference time scale T_{ref}, a reference pressure P_{ref} and a reference body force f_{ref}. Equation (1.3.1) can now be rewritten in the following dimensionless form:

$$\frac{U_{\text{ref}}}{T_{\text{ref}}}\partial_t \mathbf{u} + \frac{U_{\text{ref}}^2}{L_{\text{ref}}}(\nabla\times\mathbf{u})\times\mathbf{u} - \frac{\nu U_{\text{ref}}}{L_{\text{ref}}}\Delta\mathbf{u} = -\frac{P_{\text{ref}}}{\rho L_{\text{ref}}}\nabla p + \frac{f_{\text{ref}}}{\rho}\mathbf{f}. \tag{1.3.3}$$

We set $T_{\text{ref}} := L_{\text{ref}}/U_{\text{ref}}$, $P_{\text{ref}} = \rho U_{\text{ref}}^2$, $f_{\text{ref}} = \frac{\rho U_{\text{ref}}^2}{L_{\text{ref}}}$ and introduce the kinetic Reynolds number:

$$R_e = \frac{U_{\text{ref}} L_{\text{ref}}}{\nu}, \tag{1.3.4}$$

so the Navier-Stokes equations become:

$$\partial_t \mathbf{u} + (\nabla\times\mathbf{u})\times\mathbf{u} - \frac{1}{R_e}\Delta\mathbf{u} = -\nabla p + \mathbf{f}, \tag{1.3.5}$$

$$\nabla\cdot\mathbf{u} = 0. \tag{1.3.6}$$

Remark 1.3.1. We note that the variables, such as the velocity field $\mathbf{u}$, or the operators, such as the time derivative ∂_t, are written the same way independently from being dimensionless or with dimension.

Extension to multiphase flow problems

In the frame of chapter 5, we introduce the momentum $\mathbf{m} = \rho\mathbf{u}$ with ρ the density and $\mathbf{u}$ the velocity field. The Navier-Stokes system is then composed of the mass and momentum equations which can be written in the following dimensionless form:

$$\partial_t \rho + \nabla\cdot(\mathbf{m}) = 0, \tag{1.3.7}$$

$$\partial_t(\mathbf{m}) + \nabla\cdot(\mathbf{m}\otimes\mathbf{u}) - \frac{2}{R_e}\nabla\cdot(\eta\varepsilon(\mathbf{u})) = -\nabla p + \mathbf{f}, \tag{1.3.8}$$

$$\nabla\cdot\mathbf{u} = 0, \tag{1.3.9}$$

where $\varepsilon(\mathbf{u}) = \nabla^s\mathbf{u} = \frac{1}{2}(\nabla\mathbf{u} + (\nabla\mathbf{u})^{\mathsf{T}})$ is the strain rate tensor. The scalar field $\eta = \rho\nu$ is the distribution of dynamic viscosity. To write these equations in a non-dimensionalized form, we introduce the reference length scale L_{ref}, the reference velocity U_{ref} so the reference time scale is $L_{\text{ref}}/U_{\text{ref}}$. The reference density and dynamic viscosity are denoted ρ_{ref} and η_{ref} respectively, so we can define the Reynolds number by:

$$R_e = \frac{\rho_{\text{ref}} U_{\text{ref}} L_{\text{ref}}}{\eta_{\text{ref}}}. \tag{1.3.10}$$

1.3.2 Maxwell Equations

The Maxwell equations govern the evolution of the magnetic field $\mathbf{H}$. Before writing these equations in a conducting domain, we introduce the induction field $\mathbf{B}$, the electrical field $\mathbf{E}$ and the electric displacement field $\mathbf{D}$, so we have:

$$\partial_t \mathbf{B} = -\nabla\times\mathbf{E}, \tag{1.3.11}$$

$$\nabla\times\mathbf{H} = \mathbf{j} + \partial_t\mathbf{D} + \chi\mathbf{u}, \tag{1.3.12}$$

$$\nabla\cdot\mathbf{D} = \chi, \tag{1.3.13}$$

$$\nabla\cdot\mathbf{B} = 0, \tag{1.3.14}$$

where $\mathbf{j}$ is the current density, χ the charge density and $\mathbf{u}$ the velocity field of the body considered. In the following we only consider these equations in the quasi-static approximation, meaning the velocity $\mathbf{u}$ is way smaller than the speed of light. It allows to disregard the terms connected to χ and $\partial_t\mathbf{D}$ (see [79, 98] for more details). As a consequence, equations (1.3.12) and (1.3.13) can be rewritten:

$$\nabla\times\mathbf{H} = \mathbf{j}, \tag{1.3.15}$$

$$\nabla\cdot\mathbf{D} = 0. \tag{1.3.16}$$

Before writing the equations in a dimensionless form we consider Ohm's law:

$$\mathbf{j} = \sigma(\mathbf{E} + \mathbf{u}\times\mu\mathbf{H}), \tag{1.3.17}$$

and the two constitutive relations:

$$\mathbf{D} = \epsilon\mathbf{E}, \tag{1.3.18}$$

$$\mathbf{B} = \mu\mathbf{H}, \tag{1.3.19}$$

where σ is the electrical conductivity, ϵ the electrical permittivity and μ the magnetic permeability. The last three equations allow us to remove the variable $\mathbf{E}$ from the equations, so we only need to consider the following equations:

$$\partial_t(\mu\mathbf{H}) = -\nabla\times(\frac{1}{\sigma}\nabla\times\mathbf{H}) + \nabla\times(\mathbf{u}\times(\mu\mathbf{H})), \tag{1.3.20}$$

$$\nabla\cdot(\mu\mathbf{H}) = 0. \tag{1.3.21}$$

To get dimensionless equations, we introduce a reference length scale L_{ref}, a reference time scale T_{ref} so we can define a reference velocity $U_{\text{ref}} = \frac{L_{\text{ref}}}{T_{\text{ref}}}$. We also use the vacuum permittivity ϵ_0 as reference permittivity and the vacuum permeability μ_0 as reference permeability. This allows us to rewrite the Maxwell equations in the following dimensionless form:

$$\partial_t(\mu\mathbf{H}) = -\frac{1}{R_m}\nabla\times(\frac{1}{\sigma}\nabla\times\mathbf{H}) + \nabla\times(\mathbf{u}\times(\mu\mathbf{H})), \tag{1.3.22}$$

$$\nabla\cdot(\mu\mathbf{H}) = 0. \tag{1.3.23}$$

where we define the magnetic Reynolds number:

$$R_m = \mu_0\sigma_0 L_{\text{ref}} U_{\text{ref}}. \tag{1.3.24}$$

1.3.3 Magnetohydrodynamic Equations

The magnetohydrodynamic equations describe the coupling between a magnetic field and a velocity field in an electrically conducting fluid. While the action of the fluid velocity on the magnetic field is already visible in the Maxwell equations (1.3.22), the feedback of the magnetic field on the fluid's velocity is represented by the Lorentz force, defined by $\mathbf{f}_L := \mathbf{j}\times\mathbf{B}$. Using Ohm's law (1.3.17) and (1.3.19), this force can be written as follows:

$$\mathbf{f}_L = (\nabla\times\mathbf{H})\times(\mu\mathbf{H}). \tag{1.3.25}$$

After switching the term $\mathbf{f}$ with $\mathbf{f}_L$ in equation (1.3.5), the dimensionless MHD equations are:

$$\begin{cases} \partial_t \mathbf{u} + (\nabla\times\mathbf{u}) \times \mathbf{u} - \frac{1}{R_e}\Delta\mathbf{u} = -\nabla p + A(\nabla\times\mathbf{H}) \times (\mu\mathbf{H}), \\ \partial_t(\mu\mathbf{H}) = -\frac{1}{R_m}\nabla\times(\frac{1}{\sigma}\nabla\times\mathbf{H}) + \nabla\times(\mathbf{u} \times (\mu\mathbf{H})), \\ \nabla\cdot\mathbf{u} = 0, \\ \nabla\cdot(\mu\mathbf{H}) = 0, \end{cases} \tag{1.3.26}$$

with $A = \dfrac{\mu_0 H_{\text{ref}}^2}{\rho U_{\text{ref}}^2}$ where we denote H_{ref} the reference magnetic scale. To remain consistent with the formulation of these equations in the SFEMaNS code, we use the Alfvén velocity: $U_{\text{ref}} = \sqrt{\frac{\mu_0}{\rho}} H_{\text{ref}}$. As a consequence, we set $A = 1$.

SFEMaNS MHD-code

This chapter is dedicated to describe the SFEMaNS MHD-code developed in Fortran90 since 2002 by J.-L. Guermond et al. [31, 33, 35]. Firstly, we give details about the restrictions on the domain of computation and the three main problem set-ups. We also present the numerical approximation method implemented in SFEMaNS. Eventually we show the code's possibilities and the developments implemented during this PhD period.

Contents

2.1 Framework

The SFEMaNS code is born with the idea to develop a code that can study dynamo effect with a hybrid spectral/Lagrange finite element formulation using the velocity field **u** and the magnetic field **H** as variables for the MHD equations. Before describing the main set-up that the code offers, we show the domain restrictions we are subjected to.

Domain geometry: axisymmetric hypothesis

The code uses cylindrical coordinates (r, θ, z) so a spectral/finite element method can be applied. This method, detailed in section 2.2, consists in using a Fourier decomposition in the azimuthal direction and solves the problem in a meridian plane with Lagrange finite elements. While this choice allows to reduce the computational cost of simulations, it also implies that the computation domain, denoted by Ω, must be axisymmetric (due to the θ-periodicity).

The choice of an axisymmetric geometry may seem restrictive as we cannot study backward step problems for hydrodynamics study, the dynamo effect of a Von Kármán set-up as in the Cadarache experiment (presence of blades fitted on a rotating disk) or other problems with non axisymmetric geometry. However, we consider that this hypothesis allows us to approximate most of physical situations with dynamo effect (geodynamo, stellar dynamo) and some laboratory experiments (with cylinder, sphere and torus). This restriction is however circumvented by implementing a pseudo-penalization method in SFEMaNS so non axisymmetric domains for the Navier-Stokes equations can be taken into account, we refer to section 2.4 for more details.

Domain decomposition: simply connected insulating sub-domain hypothesis

In order to take into account a large range of problems, we divide the domain Ω of computation into the three following parts:

- a conducting fluid domain, denoted by $\Omega_{c,f}$, where the conductivity, permeability, viscosity and density of the fluid are assumed constant and positive.
- a conducting solid domain, denoted by $\Omega_{c,s}$, where the velocity of the solid is imposed. This sub-domain is assumed to be a finite union of disjoint solid domains $\Omega^i_{c,s}$ with positive constant conductivity σ_i and permeability μ_i.
- an insulating domain, called vacuum and denoted by Ω_v, where the electrical conductivity σ is zero and the relative magnetic permeability μ is 1.

We note that, unlike the Maxwell equations that need to be approximated in all of the sub-domains, the Navier-Stokes equations are only solved in $\Omega_{c,f}$. All of these sub-domains are assumed to be axisymmetric so we can approximate the problem sub-domain per sub-domain. Due to the zero conductivity of the insulating domain, the Maxwell equations cannot be written as equation (1.3.22) in Ω_v. As a consequence, we only consider a simply connected domain Ω_v. This extra hypothesis, combined to the condition $\nabla\times\mathbf{H} = 0$ in Ω_v, allows us to look for a magnetic field of the form $\mathbf{H} = \nabla\phi$ with ϕ a scalar field defined on Ω_v. We can show, by taking the divergence of (1.3.11), that ϕ is solution of:

$$\mu\partial_t\Delta\phi = 0. \tag{2.1.1}$$

We call ϕ the vacuum potential and refer to [31] for more details on the Maxwell equations numerical approach. This decomposition allows to study the mutual retro-action between the fluid's velocity field and the magnetic field in $\Omega_{c,f}$ while realistic boundary or interface conditions can be represented by the presence of an insulating domain or containers walls.

Hydrodynamic, Magnetic or MHD set-up

SFEMaNS allows to solve the Maxwell and the Navier-Stokes equations either independently or by coupling them. As a result we can study three main kind of problems:

- hydrodynamic set-up, where only the Navier-Stokes equations (1.3.5) are approximated after setting an adequate forcing **f**.
- magnetic set-up, where the Maxwell equations (1.3.22) are solved with a velocity field defined by the user.
- magnetohydrodynamics, where we solve the equations (1.3.26).

We note that hydrodynamics study may lead to find stationary or statistically stationary velocity fields that can later be injected in the Maxwell equations to analyse the conversion of kinetic energy into magnetic energy. The influence of a stationary magnetic field on a fluid can also be investigated while studying the Navier-Stokes equations alone with the corresponding Lorentz force. These strategies may avoid to compute the full MHD equations but require a good knowledge of the problem that can only come from experiments or full MHD numerical studies.

2.2 Numerical approximation

The SFEMaNS code approximates the MHD equations using a hybrid Fourier/Finite element formulation. The Fourier decomposition allows to approximate the problem's solutions for each Fourier mode independently, modulo nonlinear terms. These nonlinear terms are always made explicit, with second order extrapolation in time, so the algebra of the problem is time independent. It induces a computational gain as the stiffness matrices only need to be assembled and preconditioned at initialization.

2.2.1 Fourier discretization

To present the Fourier discretization, we choose a number M such that all variables are approximated over $M+1$ complex Fourier modes. Thus all numerical approximations of a function f are written in the generic form:

$$f(r,\theta,z,t) = \sum_{m=-M}^{M} f_h^m(r,z,t)e^{im\theta}, \tag{2.2.1}$$

where (r,θ,z) are the cylindrical coordinates and t is the time. The function f_h^m takes values in finite element spaces defined later. We note that SFEMaNS does not directly approximate the f_h^m but some functions $f_h^{m,\cos}$ and $f_h^{m,\sin}$ defined below. As we only considerer real valued functions, for all m in $[|-M,M|]$ we have:

$$f_h^m = \overline{f_h^{-m}}. \tag{2.2.2}$$

So we can now rewrite (2.2.1) as follows:

$$f(r,\theta,z,t) = f_h^{0,\cos}(r,z,t) + \sum_{m=1}^{M} f_h^{m,\cos}\cos(m\theta) + f_h^{m,\sin}\sin(m\theta), \tag{2.2.3}$$

where $f_h^{0,\cos} = f_h^0$, and for $1 \leq m \leq M$, we have $f_h^{m,\cos} = 2\Re(f_h^m)$ and $f_h^{m,\sin} = -2\Im(f_h^m)$ with $\Re(f_h^m)$ and $\Im(f_h^m)$ the real and imaginary parts of the complex f_h^m. Introducing the functions $\cos_m = \cos(m\theta)$, $\sin_m = \sin(m\theta)$ and a basis functions $(\phi_j)_{j\in J}$ of the finite element space of the meridian plane results in $(\phi_j \cos_m)_{j\in J, m\in[|0,M|]} \cup (\phi_j \sin_m)_{j\in J, m\in[|1,M|]}$

being a basis of the functions approximation spaces. The formulation (2.2.3) allows to approximate each Fourier component (cosine and sine) independently modulo the computation of the nonlinear terms. Moreover only real valued functions are approximated which allows to avoid dealing with complex spaces.

2.2.2 Finite Element representation

We give details on the numerical approximation of a MHD problem in the meridian plane. Firstly we describe the spaces of approximation where the functions live, then we explain the time marching of the algorithm for a MHD set-up. We end up by giving details of the scheme used to approximate the Navier-Stokes equations. We only describe the Navier-Stokes formulation so it facilitates us to show the modifications we did to take into account non axisymmetric configurations, see section 2.4.1, or variable density problems, see chapter 5.

Spaces of Approximation

To introduce the space of approximations where the variables $\mathbf{u}$, p , $\mathbf{H}$ and ϕ live, we define $\Omega_{c,f}^{2D}$, $\Omega_{c,s}^{2D}$, Ω_{v}^{2D} meridian sections of $\Omega_{c,f}$, $\Omega_{c,s}$, Ω_v. We also consider $\{\mathcal{T}_h\}_{h>0}$ a family of meshes of the meridian plane Ω^{2D} composed of disjoint triangular cells K of diameters at most h. For given $h > 0$, we assume we can divide the mesh $\mathcal{T}_h$ in a conducting (fluid and solid) and an insulating meshes, so we can write $\mathcal{T} = \mathcal{T}_h^c \cup \mathcal{T}_h^v$ with $\mathcal{T}_h^c = \mathcal{T}_h^{c,f} \cup \mathcal{T}_h^{c,s}$. The approximation of the solutions of the Navier-Stokes equations in a meridian plane involves Taylor-Hood, $\mathbb{P}_2/\mathbb{P}_1$, finite elements. So we introduce the following two real spaces of finite dimension:

$$\mathbf{V}_h^{2D} := \left\{ \mathbf{v}_h \in C^0(\overline{\Omega_{c,f}^{2D}}); \mathbf{v}_h|_K \in \mathbb{P}_2^6 \ \forall K \in \mathcal{T}_h^{c,f} \right\},$$
$$M_h^{2D} := \left\{ q_h \in C^0(\overline{\Omega_{c,f}^{2D}}); q_h|_K \in \mathbb{P}_1^2 \ \forall K \in \mathcal{T}_h^{c,f} \right\}.$$

At a given time, the velocity field $\mathbf{u}$ and the pressure p are approximated in the respective spaces:

$$\mathbf{V}_h := \left\{ \mathbf{v} = \sum_{k=-M}^{M} \mathbf{v}_h^k(r,z)e^{ik\theta}; \mathbf{v}_h^k \in \mathbf{V}_h^{2D}, \ \overline{\mathbf{v}_h^k} = \mathbf{v}_h^{-k}, \ -M \leq k \leq M \right\},$$
$$M_h := \left\{ q_h = \sum_{k=-M}^{M} q_h^k(r,z)e^{ik\theta}; q_h^k \in M_h^{2D}, \ \overline{q_h^k} = q_h^{-k}, \ -M \leq k \leq M \right\}.$$

For detailed purpose about Navier-Stokes approximation, we also define the sub-space $\mathbf{V}_{h,0}$ of $\mathbf{V}_h$ whose elements are zero in $\Omega_{c,f}$ boundaries, denoted $\partial\Omega_{c,f}$. In the same way, we introduce the two real spaces of finite dimension:

$$\mathbf{X}_h^{\mathbf{H},2D} := \left\{ \mathbf{b}_h \in C^0(\overline{\Omega_c^{2D}}); \mathbf{b}_h|_K \in \mathbb{P}_{l_\mathbf{H}}^6 \ \forall K \in \mathcal{T}_h^c \right\},$$
$$X_h^{\phi,2D} := \left\{ \varphi_h \in C^0(\overline{\Omega_v^{2D}}); \varphi_h|_K \in \mathbb{P}_2^2 \ \forall K \in \mathcal{T}_h^v \right\}.$$

with $l_\mathbf{H} \in \{1,2\}$ to approximate the Maxwell equations. So for a given time, the magnetic

field $\mathbf{H}$ and the scalar potential ϕ are respectively approximated in:

$$\mathbf{X}_h^{\mathbf{H}} := \left\{ \mathbf{b} = \sum_{k=-M}^{M} \mathbf{b}_h^k(r,z)e^{ik\theta}; \mathbf{b}_h^k \in \mathbf{X}_h^{\mathbf{H},2D},\ -M \leq k \leq M \right\},$$
$$X_h^{\phi} := \left\{ \varphi = \sum_{k=-M}^{M} \varphi_h^k(r,z)e^{ik\theta}; \varphi_h^k \in X_h^{\phi,2D},\ -M \leq k \leq M \right\}.$$

Time marching

To present the time marching of the code for a MHD problem, we introduce a time step τ and denote by f^n the approximation of a function f at the time $t_n = n\tau$. We note that the Maxwell and the Navier-Stokes equations are not solved simultaneously, meaning we first approximate the solution of the Navier-Stokes equations. Then the updated velocity field is used to approximate the Maxwell equations. So the time marching of a MHD approximation can be summarized by the three following steps:

- initialization of the velocity fields $\mathbf{u}^0, \mathbf{u}^1$, the dynamical pressure p^0, p^1, the magnetic field $\mathbf{H}^0, \mathbf{H}^1$ and the vacuum potential ϕ^0, ϕ^1.
- computation of $\mathbf{u}^{n+1}$ and p^{n+1} after we compute the nonlinear terms with extrapolation involving $\mathbf{u}^n, \mathbf{u}^{n-1}, \mathbf{H}^n$ and $\mathbf{H}^{n-1}$.
- computation of $\mathbf{H}^{n+1}$ and ϕ^{n+1} after nonlinear terms are computed with extrapolation involving $\mathbf{u}^{n+1}, \mathbf{H}^n$ and $\mathbf{H}^{n-1}$.

As this manuscript focuses on the Navier-Stokes equations approximation and their stabilization for high Reynolds numbers flows and variable density problems, we propose to describe the Navier-Stokes equations approximation in the following. Details on the approximations of the Maxwell equations in the SFEMaNS code can be found in [31] and [33]. We just note that the approximations of the variables $\mathbf{H}$ and ϕ of the Maxwell equation are second order in time and second and a half order in space in L^2-norm.

Navier-Stokes equations weak formulation

The approximation of the Navier-Stokes equations is based on a rotational form of the prediction-correction projection method detailled in [43]. The main idea of this algorithm is to determine a prediction $\tilde{\mathbf{u}}$ of the velocity field $\mathbf{u}$ by solving:

$$\frac{3\tilde{\mathbf{u}}^{n+1} - 4\mathbf{u}^n + \mathbf{u}^{n-1}}{2\tau} - \frac{1}{R_e}\Delta\tilde{\mathbf{u}}^{n+1} + \nabla p^n = \mathbf{f}(t_{n+1}), \tag{2.2.4}$$

where we do not report nonlinear effects. As this first step does not take into account the incompressibility hypothesis, a correction of the predicted velocity field $\tilde{\mathbf{u}}$ is applied by solving:

$$\begin{cases} \dfrac{3\mathbf{u}^{n+1} - 3\tilde{\mathbf{u}}^{n+1}}{2\tau} + \nabla(p^{n+1} - p^n + \frac{1}{R_e}\nabla\cdot\tilde{\mathbf{u}}^{n+1}) = 0, \\ \nabla\cdot\mathbf{u}^{n+1} = 0. \end{cases} \tag{2.2.5}$$

Apart from accounting for incompressibility, this correction step allows to get consistent boundary conditions on the pressure due to the presence of the quantity $\nabla\cdot\tilde{\mathbf{u}}^{n+1}$. We refer to [43] for more details on this algorithm. The implementation of this algorithm in SFEMaNS involves a scalar field ψ^{n+1}, solution of:

$$-\Delta\psi^{n+1} = -\frac{3}{2\tau}\nabla\cdot\tilde{\mathbf{u}}^{n+1}. \tag{2.2.6}$$

It allows us to remove the variable $\mathbf{u}$ from the equation (2.2.4) by noticing that:

$$\mathbf{u}^{n+1} = \tilde{\mathbf{u}}^{n+1} - \frac{2\tau}{3}\nabla\psi^{n+1}. \tag{2.2.7}$$

As a consequence the SFEMaNS code focuses on approximating the predicted velocity $\tilde{\mathbf{u}}$ that we abusively denote $\mathbf{u}$. The Navier-Stokes approximation then consists in approximating a velocity field $\mathbf{u}^{n+1}$, that matches the Dirichlet boundary conditions of the problem, solutions of the following formulation for all $\mathbf{v}$ in $\mathbf{V}_{h,0}$:

$$\int_\Omega \frac{3}{2\tau}\mathbf{u}^{n+1}\cdot\mathbf{v} + \frac{1}{R_e}\nabla\mathbf{u}^{n+1} : \nabla\mathbf{v} = -\int_\Omega \left(\frac{-4\mathbf{u}^n + \mathbf{u}^{n-1}}{2\tau} + \nabla\left(p^n + \frac{4\psi^n - \psi^{n-1}}{3}\right)\right)\cdot\mathbf{v} + \int_\Omega (\mathbf{f}^{n+1} - (\nabla\times\mathbf{u}^{*,n+1})\times\mathbf{u}^{*,n+1})\cdot\mathbf{v}, \tag{2.2.8}$$

where $\mathbf{u}^{*,n+1} = 2\mathbf{u}^n - \mathbf{u}^{n-1}$ and $\nabla\mathbf{u} : \nabla\mathbf{v} = \sum_{i,j}\partial_i u_j \partial_i v_j$. The pressure is then updated by solving ψ^{n+1} and δ^{n+1} in M_h solutions of:

$$\int_\Omega \nabla\psi^{n+1}\cdot\nabla q = \frac{3}{2\tau}\int_\Omega \mathbf{u}^{n+1}\cdot\nabla q, \tag{2.2.9}$$

$$\int_\Omega q\delta^{n+1} = \int_\Omega q\nabla\cdot\mathbf{u}^{n+1}, \tag{2.2.10}$$

for all q in M_h. Eventually the pressure is computed as follows:

$$p^{n+1} = p^n + \psi^{n+1} - \frac{1}{R_e}\delta^{n+1}. \tag{2.2.11}$$

We note that the precision of this scheme, measured in L^2-norm, is second order in time for pressure and velocity while it is third order in space for the velocity and second order in space for the pressure.

Remark 2.2.1. The good behavior of the code has been checked over more than twenty analytical tests involving hydrodynamic, magnetic and magnetohydrodynamic problems. We refer to [74] for a description of the first seven analytical tests implemented in SFEMaNS.

Remark 2.2.2. As we do not correct the predicted velocity $\tilde{\mathbf{u}}$ (now denoted $\mathbf{u}$) via equation (2.2.7), we recently implement a penalty method on the divergence of the velocity. This method consists in adding the term $-C\nabla(\nabla\cdot\mathbf{u})$ in the left hand side of the Navier-Stokes equations with C a constant bigger than 1 (set to 1 by default). The choice of penalizing the divergence is done so we can work with reasonable velocity's divergence while avoiding computing (2.2.7). We note that computing equation (2.2.7) would drive us to inverse an extra matrix to obtain the value of $\nabla\psi^{n+1}$, defined on Gauss points of the finite element mesh, on the nodes of the finite element mesh where the velocity is defined. As a consequence this penalty method allows us to deal with reasonable divergence velocity field without increasing the computational cost of numerical simulations.

2.3 SFEMaNS possibilities

As this code has been developed throughout the years, the range of problems approximated has been extended and the computational cost was reduced. Enumerating all SFEMaNS possibilities, like taking into account periodic boundary conditions for infinite geometry along the symmetry axis, is not relevant here. However, we still decide to enhance the last three most important developments implemented before this PhD period.

2.3.1 Parallelization

The code presents two layers of parallelization: one involving the Fourier decomposition and one involving a decomposition of the meridian domain where the finite element approximation is done. The Fourier decomposition allows to solve the problem independently, modulo nonlinear terms, for each Fourier mode so we can apply a parallelization in Fourier space using MPI (Message Passing Interface). The nonlinear terms, made explicit in time, are computed using a pseudo-spectral method and the fast Fourier transform subroutines from the FFTW3 package [25]. We note that the zero-padding technique (2/3-rule) is applied to prevent aliasing. On the other hand, the code is also parallelized in the meridian sections by using METIS [55] for the domain decomposition and PETSC (Portable, Extensible Toolkit for Scientific Computation) [6, 7, 8] for the parallel linear algebra. Eventually each computation is done by splitting the meridian domain in N_S subdomains and regrouping the M Fourier modes in N_F groups of same size. So the total number of processors N used by the simulation satisfies the relation:

$$N = N_F N_S \tag{2.3.1}$$

where each processor solves the problem for one of the N_S sub domains over one of the N_F groups of Fourier modes. More details on the Fourier parallelization can be found in [33] while the parallelization in meridian sections has been implemented during F. Luddens thesis [74].

Parallel Scaling Performance

To emphasize the satisfying parallelization of SFEMaNS we propose to study the weak and the strong scalability of the code. The weak scalability consists in studying the evolution of the computational time with the number of processors when fixing the problem size allocated to each processor. The strong scalability considers a problem of fixed complexity and studies the evolution of the computational time with the number of processors. While the weak scalability allows to foresee the computational time of an increasing complexity problem, we note it is not of practical use. Indeed such scaling does not allow to compare the communication time with the time spent to solve the problem, so the choice of the fixed problem size can induce undesired high communication times. It makes the strong scalability more informative as it allows to determine the maximum number of processors that can be allocated to approximate a fixed problem without wasting computational resources.

The study of SFEMaNS weak scalability has been done by Hiroaki Matsui from UC Davis in the frame of the CIG benchmark [51] with Stampede supercomputer from Texas Advanced Computing Center (TACC) of University of Austin Texas. The scaling is done on a MHD problem with pseudo vacuum boundary conditions over a hundred time steps and consists in studying the evolution of the quantity:

$$S_{WS}(N) = \frac{T_{N_{\text{ref}}}}{T_N}, \tag{2.3.2}$$

where N is the number of processors, T_N is the average computational time of an iteration time per processor and N_{ref} the minimum number of processors used to start the scaling. Table 2.1 shows the results of the weak scaling where we define N_{med} the number of degrees of freedom in the meridian plane and N_θ the number of degrees of freedom in the azimuthal direction. We note that N_θ is equal to $2M$ with M the number of Fourier modes used for the computations. The results are very conclusive as going from 32 to 8192 processors

induces a 15% difference of a processor time computation. We note that the parallelization in Fourier modes is more efficient than the one in meridian space as the computational time mainly rises when increasing the number N_S of meridian sub domains.

N	N_S	N_F	$\sqrt{N_{\text{med}}}$	N_θ	T_N	$S_{WS}(N)$
32	2	16	87.29	64	0.893	1
64	2	32	87.29	128	0.768	1.16
128	2	64	87.29	256	0.726	1.23
256	8	32	175.12	128	0.943	0.95
512	8	64	175.12	256	0.865	1.03
1024	8	128	175.12	512	0.904	0.99
2048	32	64	345.82	256	1.066	0.84
4096	32	128	345.82	512	1.072	0.83
8192	32	256	345.82	1024	1.047	0.85

Table 2.1: Weak scaling of SFEMaNS code with the reference number of processors $N_{\text{ref}} = 32$ and a fixed space number of degrees of freedom per processor equal to 15240.

On the other hand we performed the strong scalability analysis of SFEMaNS on the same physical problem with cluster Ada from Institut du Développement et des Ressources en Informatique Scientifique (IDRIS) in Orsay. Now the number of degrees of freedom in the meridian domain and in the azimuthal direction are fixed so the problem complexity C is constant. Then we study the variation of $S_{SS}(N)$ defined by:

$$S_{SS}(N) = \frac{T_{N_{\text{ref}}} N_{\text{ref}}}{T_N N}. \tag{2.3.3}$$

with the same notations of the weak scaling case. When $S_{SS}(N) = 1$ it means the time of communication is negligible compared to the time of computation so the code can be used with N processors for a problem of complexity C without wasting computational resources. The results of the strong scaling are displayed in table 2.2. As previously

N	N_S	N_F	T_N	$S_{SS}(N)$
16	1	16	3.65	1
32	1	32	1.91	0.96
64	2	32	1.07	0.85
128	4	32	0.59	0.77
256	8	32	0.36	0.63

Table 2.2: Strong scaling of SFEMaNS code with $N_{\text{ref}} = 16$ done with $\sqrt{N_{\text{med}}} = 230.82$ and $N_\theta = 64$.

noted when studying the weak scalability of SFEMaNS code, the parallelization in Fourier mode is more efficient than the one in meridian space as allocating 1 or 2 Fourier modes to one processor, see the first two lines of table 2.2, is nearly as efficient. On the other

hand the parallelization efficiency seems to decrease when the domain is subdivided into 8 subdomains. As the meridian section contains 53280 $\mathbb{P}_2$ grid points, we can conclude that the parallelization remains efficient as each processor treated around 10000 grid points of the meridian section.

2.3.2 Heat Equation

The range of problems approximated by SFEMaNS is extended to thermodynamic problems under the Boussinesq approximation. In this situation the temperature is written in a dimensionless form by setting $T = \frac{T-\overline{T}}{\Delta T}$ with $\overline{T}$ the mean value of the temperature and ΔT the maximum difference of temperature. The equations to solve can be written in the following dimensionless form:

$$\begin{cases} \partial_t T + \nabla\cdot(T\mathbf{u}) - \kappa\Delta T = f_T, \\ \partial_t \mathbf{u} + (\nabla\times\mathbf{u})\times\mathbf{u} - \frac{1}{R_e}\Delta\mathbf{u} = -\nabla p + \gamma T\mathbf{e}_z + \mathbf{f}, \\ \nabla\cdot\mathbf{u} = 0, \end{cases} \tag{2.3.4}$$

where κ is the thermal diffusivity and γ the thermal gravity. This development allows to compute some stellar or geodynamo problems and is validated with an analytical test described below. We also note that this development was used to participate in a benchmark of a convection driven magnetohydrodynamic dynamo [51, 77]. This benchmark purpose is to get qualitatively asymptotic results on a MHD problem with thermal convection while studying the parallelization of each participant's code. SFEMaNS, as a local code, proves as efficient as spectral code and may participate to future benchmarks which, as proposed in [51], could focus on efficiency of each participants codes in comparison of their results and time computational cost.

Analytical test with manufactured solutions

To check the well behavior of the code for the Boussinesq set-up, we propose to describe an analytical test implemented in SFEMaNS. This test consists in approximating in a cylindrical domain $\Omega = \{(r,\theta,z) \mid 0 \le r \le 1; 0 \le \theta \le 2\pi; 0 \le z \le 1\}$ the functions:

$$\begin{cases} T(r,\theta,z,t) &= \big(r^2 z + r^2 z^2(\cos(\theta) + 2\sin(2\theta))\big)\cos(t), \\ u_r(r,\theta,z,t) &= r^3\cos(2\pi z)\sin(t), \\ u_\theta(r,\theta,z,t) &= r^2 z\sin(t), \\ u_z(r,\theta,z,t) &= -\frac{4r^2}{2\pi}\sin(2\pi z)\sin(t), \\ p(r,\theta,z,t) &= 0, \end{cases} \tag{2.3.5}$$

solutions of the equations (2.3.4) satisfying Dirichlet boundary conditions. Figure 2.1 displays the profile of the temperature and the velocity magnitude at final time $t_{\text{end}} = 1$. We also set $\kappa = 0.1$, $\gamma = 10$ and $R_e = 1$. The source terms f_T and $\mathbf{f}$ are respectively equal to $\partial_t T + \nabla\cdot(T\mathbf{u}) - \kappa\Delta T$ and $\partial_t\mathbf{u} + (\nabla\times\mathbf{u})\times\mathbf{u} - \frac{1}{R_e}\Delta\mathbf{u} + \nabla p - \gamma T\mathbf{e}_z$, meaning we set:

$$\begin{aligned} f_T := &-r^2 z\sin(t) + (2u_r rz + u_z r^2 - 4\kappa z)\cos(t) - r^2 z^2\sin(t)\cos(\theta) + 2(u_r rz^2 + u_z r^2 z)\cos(t)\cos(\theta) \\ &- \kappa(3z^2 + 2r^2)\cos(\theta) - u_\theta rz^2\cos(t)\sin(\theta) + u_\theta 4rz^2\cos(t)\cos(2\theta) - 2r^2 z^2\sin(t)\sin(2\theta) \\ &+ (u_r 4rz^2 + u_z 4r^2 z)\cos(t)\sin(2\theta) - 4\kappa r^2\cos(t)\sin(2\theta), \end{aligned} \tag{2.3.6}$$

$$f_r := r^3\cos(2\pi z)\cos(t) + (2\pi r^3 - 4r/\pi)2r^2/\pi \sin(2\pi z)^2\sin(t)^2 - 3r^3z^2\sin(t)^2 - \frac{1}{Re}(8r - (2\pi)^2 r^3)\cos(2\pi z)\sin(t), \quad (2.3.7)$$

$$f_\theta := r^2 z\cos(t) + 3r^4 z\cos(2\pi z)\sin(t)^2 - 2r^4/\pi \sin(2\pi z)\sin(t)^2 - \frac{1}{Re}(3z)\sin(t), \quad (2.3.8)$$

$$f_z := -(2r^2/\pi)\sin(2\pi z)\cos(t) - r^4 z\sin(t)^2 + (2\pi r^3 - 4r/\pi)r^3\cos(2\pi z)\sin(2\pi z)\sin(t)^2 - \frac{1}{Re}(-(8/\pi) + 2\pi 4r^2)\sin(2\pi z)\sin(t) - \gamma T. \quad (2.3.9)$$

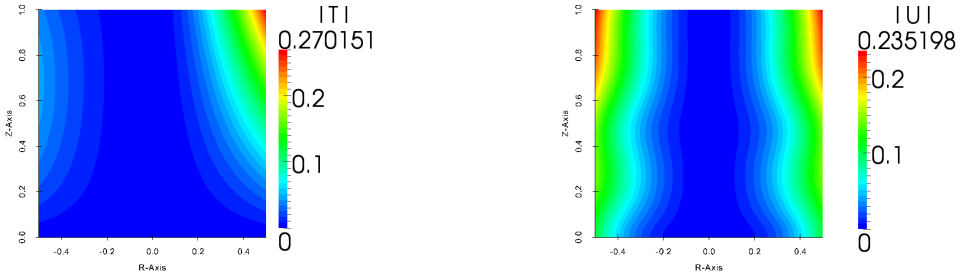

(a) Final temperature (b) Final velocity

Figure 2.1: Final profile of temperature and velocity magnitude in the meridian plane $\theta = 0$ and $\theta = \pi$ at $t = 1$..

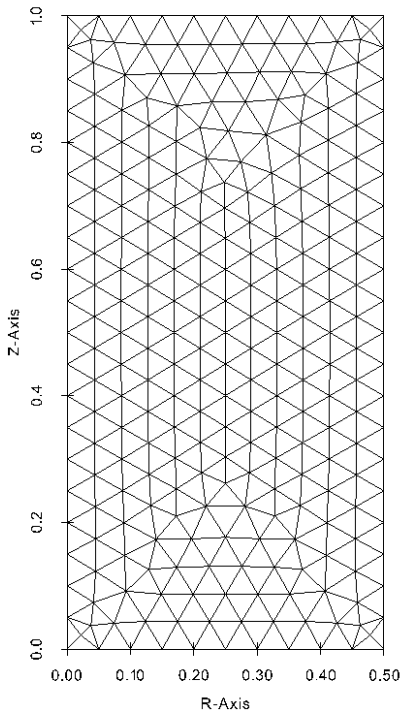

Figure 2.2: Finite element mesh of the meridian plane ($h = 1/20$ in $\mathbb{P}_1$).

The problem is approximated on four different meshes of typical mesh-size : $h = 0.1$, $h = 0.05$, $h = 0.025$, and $h = 0.0125$, we refer to figure 2.2 for a representation of the discrete domain Ω. The time steps tested are $\tau = 0.01$, $\tau = 0.005$, $\tau = 0.0025$ and

$\tau = 0.00125$. The errors on the velocity and the temperature fields in $\mathbf{L}^2$-norm at the final time $t_{\text{end}} = 1$ are reported in tables 2.3 and 2.4. One can notice that fixing a mesh size and diminishing the time step does not change the error on the velocity field, it means the error is dominated by a space-error. This phenomenon is enhanced when we look at the space convergence with the biggest time-step $\tau = 0.01$. Indeed, the velocity error decreases with the mesh-size with an order of convergence a little above the theoretical's one: three.

time step τ / mesh size h	0.01	0.005	0.0025	0.00125
0.1	3.1096E-005	3.1227E-005	3.1278E-005	3.1298E-005
0.05	2.3612E-006	2.3710E-006	2.3749E-006	2.3766E-006
0.025	1.8240E-007	1.8194E-007	1.8217E-007	1.8229E-007
0.0125	2.6963E-008	1.5682E-008	1.4732E-008	1.4683E-008

Table 2.3: $\mathbf{L}^2$-norm of the error on the velocity at time $t = 1$.

time step τ / mesh size h	0.01	0.005	0.0025	0.00125
0.1	2.2499E-006	2.2631E-006	2.2708E-006	2.2730E-006
0.05	3.5666E-007	1.8746E-007	1.7643E-007	1.7697E-007
0.025	3.2809E-007	8.2602E-008	2.4672E-008	1.5658E-008
0.0125	3.2877E-007	8.2241E-008	2.0558E-008	5.2333E-009

Table 2.4: $\mathbf{L}^2$-norm of the error on the temperature at time $t = 1$.

2.3.3 Magnetic permeability jumps in r and z

We end our description of SFEMaNS possibilities with the last development implemented before this PhD period: the implementation of magnetic permeability jumps in r and z directions. This new method, implemented during the thesis period of F. Luddens [74], allows jumps in the electrical conductivity and magnetic permeability between the fluid domain $\Omega_{c,f}$ and the different conducting solid domains $\Omega^i_{c,s}$ introduced in section 2.1. The main difficulties of such problems are to satisfy continuity conditions across interfaces between $\Omega_{c,f}$, $\Omega^i_{c,s}$, Ω_v and to impose a zero divergence on the induction field $\mathbf{B} = \mu\mathbf{H}$. Indeed by denoting Σ_μ the interface between conducting domains and Σ the interface between insulating domain Ω_v with conducting domains, approximations need to satisfy:

$$\begin{cases} [|\mathbf{H} \times \mathbf{n}^c|] = 0 & \text{on } \Sigma_\mu, \\ [|\mu^c \mathbf{H}^c \cdot \mathbf{n}^c|] = 0 & \text{on } \Sigma_\mu, \\ \mathbf{H}^c \times \mathbf{n}^c + \nabla\phi \times \mathbf{n}^v = 0 & \text{on } \Sigma, \\ \mu^c \mathbf{H}^c \cdot \mathbf{n}^c + \mu^v \nabla\phi \cdot \mathbf{n}^v = 0 & \text{on } \Sigma, \end{cases} \tag{2.3.10}$$

where $\mathbf{H} = \mathbf{H}^c$ in $\Omega_c = \Omega_{c,f} \cup \{\Omega^i_{c,s}\}_i$, $\mathbf{H} = \nabla\phi$ in Ω_v and $\mathbf{n}^c$, $\mathbf{n}^v$ are the outward normal on the interfaces. While conditions on tangential components of $\mathbf{H}^c$ and $\nabla\phi$ are enforced via a standard penalty technique, conditions on their normal components are naturally enforced by the weak formulation implemented in SFEMaNS [35]. On the other hand the zero divergence condition on the induction field becomes a constraint for steady state problem and cannot be enforced by standard penalization technique for non-smooth or non-convex domains when using $\mathbf{H}^1$ conforming Lagrange finite element as SFEMaNS code does [20]. As a consequence a new technique was developed and consists in replacing the induction equation in the conducting domain Ω_c by:

$$\partial_t(\mu^c\mathbf{H}) = -\nabla\times\mathbf{E}^c - \mu^c\nabla p^c_m, \tag{2.3.11}$$

with p^c_m solution in Ω_c of:

$$\begin{cases} -\nabla\cdot(h_{\text{loc}}^{2(1-\alpha)}\nabla p^c_m) = -\nabla\cdot(\mu^c\nabla\mathbf{H}^c), \\ p^c_m|_{\partial\Omega_c} = 0, \end{cases} \tag{2.3.12}$$

where h_{loc} is the local mesh size and α a constant parameter in $[0.6, 0.8]$. The induction in the insulating domain Ω_v is also replaced by:

$$\partial_t(\mu^v\nabla\phi) = -\nabla\times\mathbf{E}^v - \mu^v\nabla p^v_m, \tag{2.3.13}$$

where p^v_m is solution of:

$$\begin{cases} \Delta p^v_m = \Delta\phi, \\ \nabla p^v_m\cdot\mathbf{n}|_{\partial\Omega_v} = 0. \end{cases} \tag{2.3.14}$$

The quantity p_m is called magnetic pressure as an analogy to the dynamical pressure that allows to enforce the zero divergence condition on the velocity field for the Navier-Stokes equations. As we remark that p^v_m can be eliminated from the formulation (2.3.13) after applying the divergence operator, we refer to [12] for details on the theoretical convergence of this method and note that various numerical tests are performed in [35, 74].

This technique is the first step to study the dynamo of the von Kárṁan Sodium (VKS) experiments [81]. The set-up consists of driving liquid sodium in a cylindrical container with counter-rotating impellers and was shown to generate dynamo effect depending of the magnetic permeability of the impellers. Although the SFEMaNS code could only take into account axisymmetric geometries, a first set of study [28, 29, 35] has been done by modelling the impellers with a rotating disk and by using an axisymmetric velocity field resulting from time averaged measurements or analytical analysis [76]. Due to Cowling's theorem [23], the resulting magnetic field cannot be axisymmeric as observed in experiments and is indeed dominated by the Fourier mode $m = 1$. In order to be able to study the hydrodynamic and magnetohydrodynamic regimes of this problem with the proper geometry, or more generally to allow SFEMaNS to approximate problems with non axisymmetric geometry, we implement a pseudo-penalization method of Pasquetti et al. [89] that is presented in the following section.

2.4 Extension to non axisymmetric geometry

In this section we present a method, called pseudo-penalization and introduced by Pasquetti et al. [89], which we implemented in SFEMaNS to consider non axisymmetric geometry. Firstly we describe the method and give details on its use with prediction-correction

scheme for the Navier-Stokes equations. Then we present various numerical tests involving manufactured solutions or physical problems so we can attest of the correct behavior of the method and enhance some of its properties.

2.4.1 Pseudo-penalization method and prediction-correction scheme for the Navier-Stokes equations

The goal of the following is to describe a technique which allows us to take into account a non axisymmetric domain Ω that we split into a fluid domain, denoted by Ω_{fluid} , and a solid domain, denoted by Ω_{obs}. While we would like to approximate the solutions of the Navier-Stokes equations (1.3.5) in Ω_{fluid}, we also want to enforce the velocity field to be zero in the solid domain Ω_{obs} that represents an obstacle. To do so we plan to use a pseudo-penalization method that is described in the following for prediction-correction scheme. Eventually we give details on its implementation in the SFEMaNS code, while extending the method to solid obstacles with non zero velocity $\mathbf{u}_{\text{obs}}$. In the following the time step is denoted by τ, a function at time $t^n = n\tau$ is denoted f^n.

Pseudo-penalization method

The pseudo-penalization method, introduced by Pasquetti et al [89] and used in [47] and [90] to model particle or obstacle, relies on the idea of modifying the Navier-Stokes equations so the velocity is cancelled inside the solid obstacle Ω_{obs}. To do so a penalty function χ equal to 1 in the fluid domain Ω_{fluid} and 0 in the obstacle domain Ω_{obs} is introduced so the time discretization of the Navier-Stokes equations becomes:

$$\begin{aligned} \frac{\mathbf{u}^{n+1} - \chi \mathbf{u}^n}{\tau} - R_e^{-1} \Delta \mathbf{u}^{n+1} + \nabla p^{n+1} &= \chi \mathbf{f}^{n+1}, \\ \nabla \cdot \mathbf{u}^{n+1} &= 0, \end{aligned} \tag{2.4.1}$$

where the term $\mathbf{f}$ takes into account the forcing term and the nonlinear terms. One can note that inside the fluid domain, where $\chi = 1$, the equations approximated are exactly the Navier-Stokes equations. On the other hand inside the solid domain, where $\chi = 0$, the approximations are solutions of the following equations:

$$\begin{aligned} \frac{\mathbf{u}^{n+1}}{\tau} - R_e^{-1} \Delta \mathbf{u}^{n+1} + \nabla p^{n+1} &= 0, \\ \nabla \cdot \mathbf{u}^{n+1} &= 0. \end{aligned} \tag{2.4.2}$$

As a consequence the velocity is a $O(\tau)$ inside the solid obstacle, so this method is at most of order 1 in time. The order of consistency of this method also depends of the Reynolds number, as a factor R_e^{-1} is present, so this method is more efficient as the Reynolds number is large. Furthermore one can note that this penalization of the velocity inside the obstacle in τR_e^{-1} involves a time dependency of the approximated solutions even for stationary problem so such a behavior should not surprise any user of this pseudo-penalization method. Before describing this method in the frame of SFEMaNS code, we point out that the pressure is not relevant in the obstacle which represents a solid. Indeed inside the fluid the pressure allows to get a velocity with zero divergence while in the solid the pressure has no physical meaning and one can check that it is only the solution of a Poisson equation by taking the divergence of equation (2.4.2).

Description of the method for prediction-correction scheme

Since SFEMaNS code uses a prediction-correction scheme to approximate solutions of the Navier-Stokes equations, we describe how to implement the pseudo-penalization method for this kind of numerical scheme. In that purpose, we keep the notation of section 2.2.2 so the first step of the algorithm consists in solving a predicted velocity $\tilde{\mathbf{u}}$ solution of the equation:

$$\frac{\tilde{\mathbf{u}}^{n+1} - \chi \mathbf{u}^n}{\tau} - \frac{1}{R_e}\Delta\tilde{\mathbf{u}}^{n+1} + \nabla p^n = \chi \mathbf{f}^{n+1}, \tag{2.4.3}$$

where $\mathbf{f}$ takes into account the forcing term and nonlinear term as in (2.4.1) and χ is the penalty function defined by:

$$\chi = \begin{cases} 1 \text{ in } \Omega_{\text{fluid}}, \\ 0 \text{ in } \Omega_{\text{obs}}. \end{cases} \tag{2.4.4}$$

This first step does not take into account the incompressibility hypothesis, so a correction of the predicted velocity field $\tilde{\mathbf{u}}$ is applied as follows:

$$\begin{cases} \dfrac{\mathbf{u}^{n+1} - \tilde{\mathbf{u}}^{n+1}}{\tau} + \nabla(\psi^{n+1}) = 0, \\ \nabla\cdot\mathbf{u}^{n+1} = 0. \end{cases} \tag{2.4.5}$$

The pressure is then updated by solving the following equations:

$$-\Delta\psi^{n+1} = \frac{-1}{\tau}\nabla\cdot\tilde{\mathbf{u}}^{n+1}, \tag{2.4.6}$$

$$q^{n+1} = -\frac{1}{R_e}\nabla\cdot\tilde{\mathbf{u}}^{n+1}, \tag{2.4.7}$$

so we can set:

$$p^{n+1} = p^n + \psi^{n+1} + q^{n+1}. \tag{2.4.8}$$

We induce from equation (2.4.5) that $\nabla\times\nabla\times\mathbf{u} = \nabla\times\nabla\times\tilde{\mathbf{u}}$. One can notice by summing equations (2.4.3) and (2.4.5) and using relation $-\Delta\mathbf{v} = \nabla\times\nabla\times\mathbf{v} - \nabla\nabla\cdot\mathbf{v}$ applied to $\mathbf{u}$ and $\tilde{\mathbf{u}}$, that the couple ($\mathbf{u}$,p) solution of equations (2.4.3) and (2.4.5) is also the solution of equations (2.4.1). On the other hand it is interesting to note that the predicted velocity $\tilde{\mathbf{u}}$ is solution of the equation:

$$\frac{\tilde{\mathbf{u}}^{n+1} - \chi \tilde{\mathbf{u}}^n}{\tau} - \frac{1}{R_e}\Delta\tilde{\mathbf{u}}^{n+1} + \nabla p^n + \chi\nabla\psi^n = \chi \mathbf{f}^{n+1}. \tag{2.4.9}$$

We draw the attention of the reader on the increment of pressure ψ that, unlike the gradient of pressure, needs to be penalized. As mentioned earlier we note that inside the solid obstacle the pressure is not relevant and is obtained by solving a Poisson equation.

On the stability of the method

The approximated velocity field is $O(\tau)$ in Ω_{obs} so the present algorithm is consistent of order 1 in time. To the author's knowledge, no stability analysis of this scheme has been provided in the literature so we propose to establish a stability inequality of this scheme without taking account of forcing and nonlinear terms. To do so we define the operator δ as follows:

$$\delta\mathbf{u}^{n+1} = \mathbf{u}^{n+1} - \mathbf{u}^n, \tag{2.4.10}$$

and introduce the following scheme:

$$\frac{\tilde{\mathbf{u}}^{n+1}-\chi\mathbf{u}^{n}}{\tau}-\frac{1}{R_e}\Delta\tilde{\mathbf{u}}^{n+1}+\nabla p^{n}=\chi\mathbf{f}^{n+1}, \tag{2.4.11}$$

$$\begin{cases}\dfrac{\mathbf{u}^{n+1}-\tilde{\mathbf{u}}^{n+1}}{\tau}+\nabla(\delta\phi^{n+1})=0,\\ \nabla\cdot\mathbf{u}^{n+1}=0,\end{cases} \tag{2.4.12}$$

$$-\Delta\delta\phi^{n+1}=-\frac{1}{\tau}\nabla\cdot\tilde{\mathbf{u}}^{n+1}, \tag{2.4.13}$$

$$\delta k^{n+1}=-\frac{1}{R_e}\nabla\cdot(\tilde{\mathbf{u}}^{n+1}), \tag{2.4.14}$$

$$p^{n+1}=\phi^{n+1}+k^{n+1}. \tag{2.4.15}$$

As pointed out in [41], it is interesting to note that the first scheme (2.4.3)–(2.4.8) is equivalent to the second scheme (2.4.11)–(2.4.15). Indeed by defining $\psi^{n+1}=\delta\phi^{n+1}$ and $q^{n+1}=\delta k^{n+1}$, we can notice by applying the delta operator, defined in (2.4.10), to equation (2.4.15) that the two schemes are identical. Thanks to this remark, we do not establish a stability estimate for the first scheme, as done in [104] by applying δ operator on scheme (2.4.3)–(2.4.8), and propose a stability inequality for the second scheme (2.4.11)–(2.4.15) inspired by [41].

Theorem 1. *Let χ be a penalty function such that $0\leq\chi\leq 1$. Let consider the sequence $(\mathbf{u}^n,p^n)$ solutions of the scheme* (2.4.11)–(2.4.15) *where we assume that $\tilde{\mathbf{u}}$ has homogeneous Dirichlet boundary conditions and neglect the forcing and nonlinear terms $\boldsymbol{f}$. Then the following inequality holds for all $n\geq 0$:*

$$\delta\|\mathbf{u}^{n+1}\|^2_{\mathbf{L}^2(\Omega)}+\frac{\tau}{R_e}\|\nabla\tilde{\mathbf{u}}^{n+1}\|^2_{\mathbf{L}^2(\Omega)}+\tau^2\delta\|\nabla\phi^{n+1}\|^2_{\mathbf{L}^2(\Omega)}+\frac{\tau}{R_e}\delta\|k^{n+1}\|^2_{\mathbf{L}^2(\Omega)}\leq 0.$$

Proof. Firstly we remind the equality $(\delta\mathbf{a}^{n+1},\mathbf{a}^n)=\delta\|\mathbf{a}^{n+1}\|^2_{\mathbf{L}(\Omega)^2}+\|\delta\mathbf{a}^{n+1}\|^2_{\mathbf{L}(\Omega)^2}$ where $(\cdot,\cdot)$ is the scalar product in $\mathbf{L}(\Omega)^2$ and $(\mathbf{a}^n)_n$ a sequence in $\mathbf{L}(\Omega)^2$. This relation will be used in the following without being referred to. We start to test equation (2.4.11) with $2\tau\tilde{\mathbf{u}}^{n+1}$ and integrate over Ω so we get:

$$\|\tilde{\mathbf{u}}^{n+1}\|^2_{\mathbf{L}^2(\Omega)}+\|\tilde{\mathbf{u}}^{n+1}-\chi\mathbf{u}^n\|^2_{\mathbf{L}^2(\Omega)}-\|\sqrt{\chi}\mathbf{u}^n\|^2_{\mathbf{L}^2(\Omega)}+\frac{2\tau}{R_e}\|\nabla\tilde{\mathbf{u}}^{n+1}\|^2_{\mathbf{L}^2(\Omega)}+2\tau(\tilde{\mathbf{u}}^{n+1},\nabla p^n)=0. \tag{2.4.16}$$

Then we multiply equation (2.4.15) at time t^n by $2\tau\tilde{\mathbf{u}}^{n+1}$ and integrate over Ω, so we obtain:

$$2\tau(\tilde{\mathbf{u}}^{n+1},\nabla p^n)=2\tau(\nabla(\phi^n+k^n),\tilde{\mathbf{u}}^{n+1}). \tag{2.4.17}$$

In one hand the term involving $\nabla\phi^n$ is controlled by multiplying equation (2.4.12) with $2\tau^2\nabla\phi^n$. So after integrating over Ω it gives:

$$2\tau(\tilde{\mathbf{u}}^{n+1},\nabla\phi^n)=\tau^2\delta\|\nabla\phi^{n+1}\|^2_{\mathbf{L}^2(\Omega)}-\tau^2\|\nabla\delta\phi^{n+1}\|^2_{\mathbf{L}^2(\Omega)}. \tag{2.4.18}$$

On the other hand the term in ∇k^n is handled by multiplying equation (2.4.14) with $2\tau k^n$, it gives:

$$2\tau(\tilde{\mathbf{u}}^{n+1},\nabla k^n)=\frac{\tau}{R_e}(\delta\|k^{n+1}\|^2_{\mathbf{L}^2(\Omega)}-\|\delta k^{n+1}\|^2_{\mathbf{L}^2(\Omega)}). \tag{2.4.19}$$

Eventually we sum the four previous equations (2.4.16)–(2.4.19) to get:

$$\|\tilde{\mathbf{u}}^{n+1}\|^2_{\mathbf{L}^2(\Omega)} + \|\tilde{\mathbf{u}}^{n+1} - \chi\mathbf{u}^n\|^2_{\mathbf{L}^2(\Omega)} - \|\sqrt{\chi}\mathbf{u}^n\|^2_{\mathbf{L}^2(\Omega)} + \frac{2\tau}{R_e}\|\nabla\tilde{\mathbf{u}}^{n+1}\|^2_{\mathbf{L}^2(\Omega)} + \tau^2\delta\|\nabla\phi^{n+1}\|^2_{\mathbf{L}^2(\Omega)} - \tau^2\|\nabla\delta\phi^{n+1}\|^2_{\mathbf{L}^2(\Omega)} + \frac{\tau}{R_e}(\delta\|k^{n+1}\|^2_{\mathbf{L}^2(\Omega)} - \|\delta k^{n+1}\|^2_{\mathbf{L}^2(\Omega)}) = 0. \tag{2.4.20}$$

To obtain the result of theorem 1 we note that equation (2.4.12) expresses an orthogonal decomposition, this is indeed the Helmholtz decomposition, so we can write:

$$\|\tilde{\mathbf{u}}^{n+1}\|^2_{\mathbf{L}^2(\Omega)} = \|\mathbf{u}^{n+1}\|^2_{\mathbf{L}^2(\Omega)} + \tau^2\|\nabla\delta\phi^{n+1}\|^2_{\mathbf{L}^2(\Omega)}. \tag{2.4.21}$$

Moreover equation (2.4.19) induces that $\|\delta k^{n+1}\|^2_{\mathbf{L}^2(\Omega)} = \|\nabla\cdot\tilde{\mathbf{u}}^{n+1}\|^2_{\mathbf{L}^2(\Omega)}$. As $\tilde{\mathbf{u}}$ is assumed to be in $\mathbf{H}^1_0$ we also have $\|\nabla\cdot\tilde{\mathbf{u}}^{n+1}\|^2_{\mathbf{L}^2(\Omega)} \leq \|\nabla\tilde{\mathbf{u}}^{n+1}\|^2_{\mathbf{L}^2(\Omega)}$. As a consequence equations (2.4.20) can be rewritten as follows:

$$\|\mathbf{u}^{n+1}\|^2_{\mathbf{L}^2(\Omega)} - \|\mathbf{u}^n\|^2_{\mathbf{L}^2(\Omega)} + \frac{\tau}{R_e}\|\nabla\tilde{\mathbf{u}}^{n+1}\|^2_{\mathbf{L}^2(\Omega)} + \tau^2\delta\|\nabla\phi^{n+1}\|^2_{\mathbf{L}^2(\Omega)} + \frac{\tau}{R_e}\delta\|k^{n+1}\|^2_{\mathbf{L}^2(\Omega)} \leq \|\sqrt{\chi}\mathbf{u}^n\|^2_{\mathbf{L}^2(\Omega)} - \|\mathbf{u}^n\|^2_{\mathbf{L}^2(\Omega)} \tag{2.4.22}$$

where we dropped the positive term $\|\tilde{\mathbf{u}}^{n+1} - \chi\mathbf{u}^n\|^2_{\mathbf{L}^2(\Omega)}$. The proof is completed thanks to the hypothesis $0 \leq \chi \leq 1$ so we have $\|\sqrt{\chi}\mathbf{u}^n\|^2_{\mathbf{L}^2(\Omega)} - \|\mathbf{u}^n\|^2_{\mathbf{L}^2(\Omega)} \leq 0$. □

Remark 2.4.1. As described in section 2.2, the SFEMaNS code approximates the velocity field $\tilde{\mathbf{u}}$ and not $\mathbf{u}$. However, thanks to equation (2.4.12) and the stability relation for $\mathbf{u}$, one can show that $\tilde{\mathbf{u}}$ is also stable in time.

Remark 2.4.2. The above stability inequality remains valid for any χ taking values in $[0, 1]$ so that a smooth penalty function χ can be used. By smooth we mean that the penalty function does not need to be a discontinuous function equal to 1 in the fluid and 0 in the obstacle, it can also go from 1 to 0 in a smooth way to avoid dealing with discontinuous functions. However, we will see in section 2.4.3 that it is more desirable to work with discontinuous penalty function, that we denote sharp penalty function.

Remark 2.4.3. In the frame of the previous remark, one can note that χ can also depend on time with the restrictions that it takes values in $[0, 1]$. Such a strategy is adopted in SFEMaNS code and requires to add a term taking into account the movement of the obstacle which is described in the following.

Implementation of the method in SFEMaNS

Before attesting of the correct behavior of the pseudo-penalization method with numerical test, we describe how this method is implemented in SFEMaNS. As the step of correction and update of the pressure remains the same as the one described in section 2.2, we refer to equations (2.2.9), (2.2.10) and (2.2.11) for the pressure correction step and focus on the equation solved by the predicted velocity $\tilde{\mathbf{u}}$. As mentioned earlier, we consider moving obstacles so we denote by $\mathbf{u}_{\text{obst}}$ the velocity of the obstacle and $\chi^n = \chi(t_n)$ the penalty function equal to 1 in the fluid and 0 in the solid at time t^n. We also abusively denote by $\mathbf{u}$ the predicted velocity $\tilde{\mathbf{u}}$ that is now solution of the equation:

$$\frac{3\mathbf{u}^{n+1}}{2\tau} - \frac{1}{R_e}\Delta\mathbf{u}^{n+1} = -\nabla p^n + \chi^{n+1}\left(\frac{4\mathbf{u}^n - \mathbf{u}^{n-1}}{2\tau} - \nabla(\frac{4\psi^n - \psi^{n-1}}{3})\right) + \chi^{n+1}\left(-(\nabla\times\mathbf{u}^{*,n+1})\times\mathbf{u}^{*,n+1} + \mathbf{f}^{n+1}\right) + (1-\chi^{n+1})\frac{3\mathbf{u}^{n+1}_{\text{obst}}}{2\tau}, \tag{2.4.23}$$

where $\mathbf{u}^{*,n+1} = 2\mathbf{u}^n - \mathbf{u}^{n-1}$. Apart from the use of backward differentiation formula of order 2 (BDF2) to approximate the time derivative, the main difference with the method of pseudo-penalization of Pasquetti et al. is the addition of the term $(1-\chi^{n+1})\frac{3\mathbf{u}_{\text{obst}}^{n+1}}{2\tau}$. As this term does not influence the approximation in the fluid domain, where $\mathbf{u}^{n+1}$ is solution of the Navier-Stokes equations, we note that the approximation is now solution in the solid domain of equation:

$$\frac{3\mathbf{u}^{n+1} - 3\mathbf{u}_{\text{obst}}^{n+1}}{2\tau} + \nabla p^n - \frac{1}{R_e}\Delta\mathbf{u}^{n+1} = 0. \tag{2.4.24}$$

As a consequence the approximated velocity $\mathbf{u}$ is equal in the solid domain to the velocity of the obstacle $\mathbf{u}_{\text{obst}}$ up to $O(\tau)$ so the scheme is still consistent of order 1 in time.

Eventually this pseudo-penalization method allows SFEMaNS code to take into account non axisymmetric geometries for the fluid domain which was one of the biggest restrictions of this code. After being tested with analytical solutions, details are given below, comparisons of VKS set-up numerical approximation with SFEMaNS and other codes have been done in D. Castanon-Quiroz thesis [18]. Other numerical computation results are presented in chapter 4 of this thesis in the goal to compare them with future experimental results that are currently being performed in CEA Saclay by B. Dubrulle et al.

2.4.2 Numerical test with manufactured solutions

The convergence in space and time of this pseudo-penalization technique is firstly investigated with manufactured solutions. This test consists in approximating on the domain $\Omega = \{(r,\theta,z) \mid 0.1 \le r \le 1; 0 \le \theta \le 2\pi; -1 \le z \le 1\}$ the functions:

$$\begin{cases} \chi(r,\theta,z,t) &= \mathbf{1}_{r\ge 0.5}, \\ u_r(r,\theta,z,t) &= (2r-1)^2\sin(z+t)\mathbf{1}_{r\ge 0.5}, \\ u_\theta(r,\theta,z,t) &= 0, \\ u_z(r,\theta,z,t) &= (2-\frac{1}{r})(6r-1)\cos(z+t)\mathbf{1}_{r\ge 0.5} + (r-0.5)\sin(2\theta)\mathbf{1}_{r\ge 0.5}, \\ p(r,\theta,z,t) &= r^2z^3\cos(t) + r\cos(\theta), \end{cases} \tag{2.4.25}$$

solutions of equations (2.4.23), (2.2.9) and (2.2.11) with Dirichlet boundary conditions for the velocity field. Figure 2.3 displays the profile of the pressure and velocity magnitude at time $t = 0.5$. We also set $R_e = 100$ and $\mathbf{u}_{\text{obst}} = 0$. In the same way of the test presented in 2.3.2, the source term $\mathbf{f}$ is equal to $\partial_t\mathbf{u} + (\nabla\times\mathbf{u})\times\mathbf{u} - \frac{1}{R_e}\Delta\mathbf{u} + \nabla p$, meaning we set:

$$\begin{aligned} f_r := (2r-1)^2\cos(z+t) + 2rz^3\cos(z+t)\cos(\theta) - {R_e}^{-1}\sin(z+t)(-4r^4+4r^3+11r^2-1)/r^2 \\ + (2r-1)/r^3(6r-1)cos(z+t)^2(4r^4-4r^3-11r^2+1) - \frac{r-0.5}{2}(\cos(\theta)-1) \\ + (4r^2-4r-11+1/r^2)(r-0.5)\cos(z+t)\sin(2\theta) - (2-1/r)(6r-1)\cos(z+t)\sin(2\theta), \end{aligned} \tag{2.4.26}$$

$$f_\theta := -(2-1/r)(6r-1)\sin(z+t) - \sin(4\theta), \tag{2.4.27}$$

$$\begin{aligned} f_z := -(2-1/r)(6r-1)\sin(z+t) + 3r^2z^2\cos(t) + {R_e}^{-1}\cos(z+t)(12r^4-8r^3-11r^2-1)/r^3 \\ -(2r-1)^2\sin(z+t)\cos(z+t)(4r^4-4r^3-11r^2+1)/r^2 + ({R_e}^{-1}(3/r-2/r^2) + (2r-1)^2\sin(z+t))\sin(2\theta). \end{aligned} \tag{2.4.28}$$

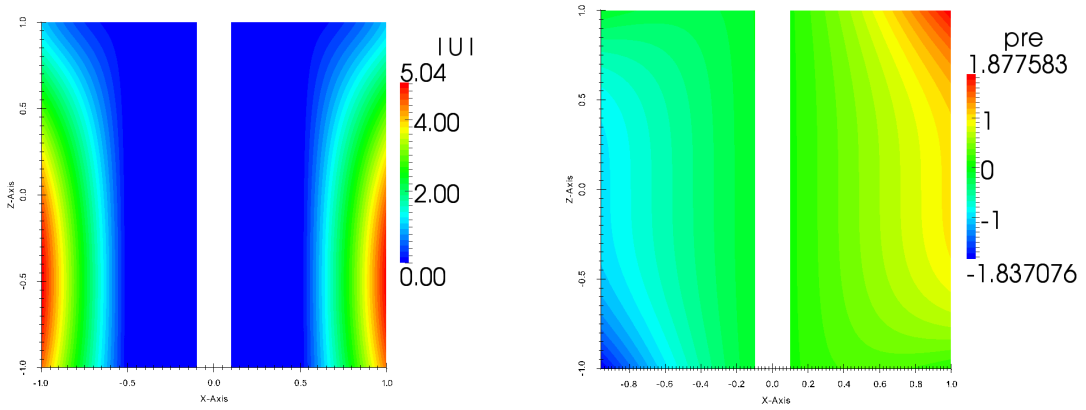

(a) Final velocity field (b) Final pressure

Figure 2.3: Profile of the velocity magnitude field and pressure in the meridian plane $\theta = 0$ and $\theta = \pi$ at $t = 0.5$.

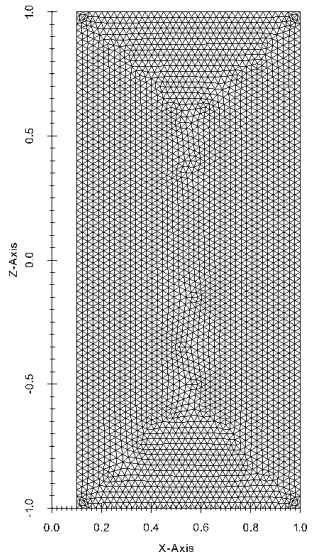

Figure 2.4: Finite element mesh of the meridian plane ($h = 1/20$ in $\mathbb{P}_1$).

The convergence of the method is studied with four different meshes of typical mesh-size: $h = 0.1$, $h = 0.05$, $h = 0.025$ and $h = 0.0125$, we refer to figure 2.4 for a representation of the discrete domain Ω. In order to the code to be stable, we test the time step $\tau = 0.002$, $\tau = 0.001$, $\tau = 0.0005$, $\tau = 0.00025$ and $\tau = 0.000125$. The error of the velocity and the error of the pressure outside the obstacle in $\mathbf{L}^2$-norm at the final time $T = 0.5$ are reported in tables 2.5 and 2.6. One can notice that errors do not always diminish with the time step, this behavior was already enhanced in [89] (see figure 1). Indeed setting a mesh size and varying the time step enhance an optimal time step where the error is minimal, for example with $h = 0.05$ the optimal time step is 5.10^{-4}. As enhanced in figure 1 of [89] for time steps smaller than this optimal value, the error will increase till an asymptotic value.

Despite this dependency of the error on the time step, we note that the error still converges, or at least remains stable, when working with constant CFL. Indeed when studying the convergence of the errors with CFL=0.25, first obtained with $h = 0.1$ and

time step τ / mesh size h	0.002	0.001	0.0005	0.00025	0.000125
0.1	2.12E-2	3.43E-2	5.22E-2	7.22E-2	9.15E-2
0.05	CFL	7.04E-3	6.95E-3	9.87E-3	1.38E-2
0.025	CFL	4.25E-3	2.37E-3	3.88E-3	7.44E-3
0.0125	CFL	CFL	4.31E-3	2.57E-3	1.75E-3

Table 2.5: $\mathbf{L}^2$-norm of the error on the velocity at time $t = 0.5$. The notation CFL means that the computations are not stable due to too large time step.

time step τ / mesh size h	0.002	0.001	0.0005	0.00025	0.000125
0.1	2.72E-2	4.60E-2	7.12E-2	9.92E-2	0.126
0.05	CFL	7.75E-3	5.73E-3	8.12E-3	1.22E-2
0.025	CFL	4.54E-3	1.91E-3	4.07E-3	8.58E-3
0.0125	CFL	CFL	4.17E-3	2.27E-3	1.65E-3

Table 2.6: $\mathbf{L}^2$-norm of the error on the pressure outside the obstacle at time $t = 0.5$. The notation CFL means that the computations are not stable due to too large time step.

$\tau = 1.10^{-3}$, the error will decrease with an order of convergence (in h and t all together) between 1 and 2. As a consequence when using this pseudo-penalization method to study physical problems, we will always work with a constant CFL between 0.25 and 0.5 since using smaller time step does not give better results.

2.4.3 Flow past a sphere and drag coefficient

After checking the behavior of the pseudo-penalization method with manufactured solutions, we now use it to study the well known physical problem of a flow past a sphere. We consider a solid sphere of diameter $d_{\text{sp}} = 2$ and of center $(r, z) = (0, 0)$ and define the Reynolds number as follows:

$$R_e = \frac{U_{\text{ref}} \mathrm{d}_{\text{sp}}}{\nu}, \tag{2.4.29}$$

where U_{ref} is the reference velocity and ν the reference viscosity. Then we split our study into the approximation of the flow for a low Reynolds number and the study of the evolution of the drag coefficient with larger Reynolds numbers.

Analytical Stokes flow with low Reynolds

At low Reynolds numbers, the flow is known to be stationary and is referred to as Stokes flow. Moreover the analytical expression of the velocity and the pressure are known and can be found for example in a lecture note of Chiang C. Mei about Stokes flow past a sphere based on [1] and [65]. To approximate the solutions of this problem we consider a solid sphere of radius 1 so we define the penalty function as follows:

$$\chi(r, \theta, z, t) = \mathbf{1}_{r^2+z^2 \geq 1}. \tag{2.4.30}$$

Then we introduce the domain of approximation $\Omega = \{(r,\theta,z) \mid 0 \leq r \leq 10; 0 \leq \theta \leq 2\pi; -8 \leq z \leq 12\}$, so the test consists in approximating on Ω the velocity field:

$$\begin{cases} u_r(r,\theta,z,t) &= \sin(\arctan(r/z))\cos(\arctan(r/z))\left(\dfrac{3}{4\sqrt{r^2+z^2}^3} - \dfrac{3}{4\sqrt{r^2+z^2}}\right)\mathbf{1}_{r^2+z^2\geq 1}, \\ u_\theta(r,\theta,z,t) &= 0, \\ u_z(r,\theta,z,t) &= \cos(\arctan(r/z))^2\left(1 + \dfrac{1}{2\sqrt{r^2+z^2}^3} - \dfrac{3}{2\sqrt{r^2+z^2}}\right)\mathbf{1}_{r^2+z^2\geq 1} \\ &\quad + \sin(\arctan(r/z))^2\left(1 - \dfrac{1}{4\sqrt{r^2+z^2}^3} - \dfrac{3}{4\sqrt{r^2+z^2}}\right)\mathbf{1}_{r^2+z^2\geq 1}, \end{cases} \tag{2.4.31}$$

and the pressure:

$$\begin{aligned} p(r,\theta,z,t) &= -\cos(\arctan(r/z))\frac{3}{2R_e(r^2+z^2)}\mathbf{1}_{r^2+z^2\geq 1} \\ &\quad +0.5\cos(\arctan(r/z))\left(1 + \frac{1}{2\sqrt{r^2+z^2}^3} - \frac{3}{2\sqrt{r^2+z^2}}\right)^2\mathbf{1}_{r^2+z^2\geq 1} \\ &\quad +0.5\sin(\arctan(r/z))\left(1 - \frac{1}{4\sqrt{r^2+z^2}^3} - \frac{3}{4\sqrt{r^2+z^2}}\right)^2\mathbf{1}_{r^2+z^2\geq 1} \\ &\quad -\cos(\arctan(r/z))\frac{3\sqrt{r^2+z^2}}{2R_e}\mathbf{1}_{r^2+z^2<1}, \end{aligned} \tag{2.4.32}$$

solutions of equations (2.4.23), (2.2.9) and (2.2.11) with Dirichlet boundary conditions for the velocity field. Although the pressure is not relevant inside the sphere, one can notice that it is a harmonic extension of the pressure inside the fluid which leads us to add the last term proportional to $\mathbf{1}_{r^2+z^2<1}$ in the above definition of the pressure. Figure 2.5 displays the profile of the pressure and velocity magnitude at time $t = 1$. We also set $R_e = 0.01$, $\mathbf{u}_{\text{obst}} = 0$ and $\mathbf{f} = 0$.

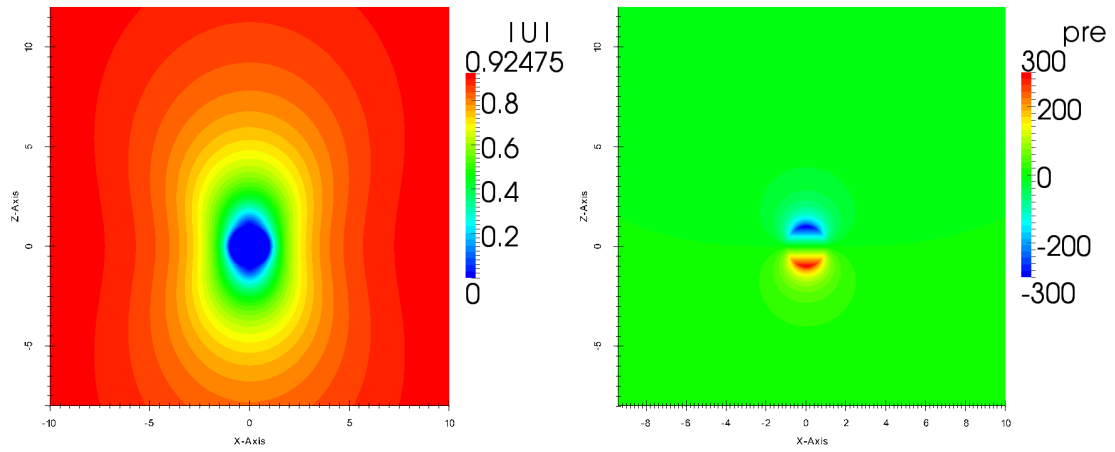

(a) Final velocity field (b) Final pressure

Figure 2.5: Profile of the velocity field magnitude and pressure in the meridian plane $\theta = 0$ and $\theta = \pi$ at $t = 1$.

The convergence of the method is studied with four different non uniform meshes of typical mesh size at the boundary of the domain h_{boundary} equal to 0.5, 0.25, and 0.125 and

of typical mesh size in and near the obstacle h_{obstacle} equal to $0.05, 0.025$, and 0.0125. We refer to figure 2.6 for a representation of the discrete domain Ω for the case $h_{\text{boundary}} = 0.5$ and $h_{\text{obstacle}} = 0.05$. As the error on the velocity inside the fluid is of order τR_e^{-1} and that $R_e = 0.01$, we decide to test the time step $\tau = 0.001$, $\tau = 0.0005$, $\tau = 0.00025$ and $\tau = 0.000125$. The relative error on the velocity and the relative error of the pressure in $\mathbf{L}^2$-norm at the final time $t = 1$ are reported in tables 2.7 and 2.8. By relative error, we mean that the $\mathbf{L}^2$-norm of the velocity error is divided by the $\mathbf{L}^2$-norm of the velocity while the $\mathbf{L}^2$-norm of the pressure error is divided by the $\mathbf{L}^2$-norm of the pressure. Unlike the previous test with manufactured solutions, here the error is mainly dominated by a error in time. Indeed increasing the space resolution does not improve the relative error on the velocity and the pressure. This behavior may be explained by the use of a small Reynolds number in order to be in the Stokes flow regime where an analytical expression of the flow is known. Since the pseudo-penalization method scales like τR_e^{-1} in the solid domain, the use of $R_e = 0.01$ induces a strong dependency of the numerical approximations with the time step used. However, the method remains convergent when fixing either the mesh or the CFL and the order of convergence is close to 0.5 which is suitable as the order of consistency of the method is equal to 1.

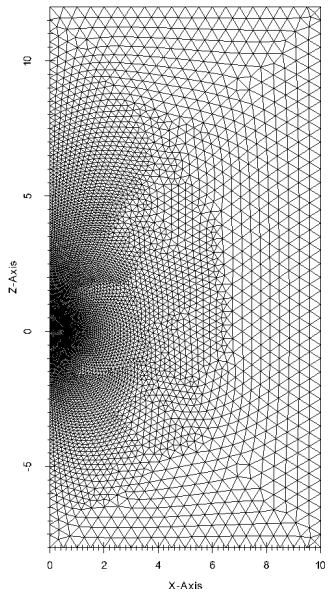

Figure 2.6: Finite element mesh of the meridian plane ($h = 0.5$ on boundary and $h = 0.05$ near the sphere in $\mathbb{P}_1$).

$h_{\text{boundary}} - h_{\text{obstacle}}$ \ time step τ	0.001	0.0005	0.00025	0.000125
0.5-0.05	3.129E-2	2.263E-2	1.586E-2	1.098E-02
0.25-0.025	3.128E-2	2.262E-2	1.585E-2	1.097E-2
0.125-0.0125	3.127E-2	2.261E-2	1.585E-2	1.096E-2

Table 2.7: Relative $\mathbf{L}^2$-norm of the error on the velocity at time $t = 1$

$h_{\text{boundary}} - h_{\text{obstacle}}$ \ time step τ	0.001	0.0005	0.00025	0.000125
0.5-0.05	1.331	8.614E-1	5.330E-1	3.347E-1
0.25-0.025	1.330	8.608E-1	5.324E-1	3.342E-1
0.125-0.0125	1.330	8.606E-1	5.323E-1	3.341E-1

Table 2.8: Relative $\mathbf{L}^2$-norm of the error on the pressure at time $t = 1$

Computation of Drag coefficient for various $R_e \in [1, 200]$

We now study the behavior of the method for a various range of Reynolds numbers by computing the drag coefficient C_d. While we use the same domain of computation Ω than previously, we use inflow boundary condition at $z = -8$, outflow boundary condition at $z = 12$ and homogeneous Neumann boundary condition at $r = 10$. As we refer to a lecture note of R. Shankar Subramanian, about drag on spherical particles and steady settling velocities based on correlation of experimental data from [19], to get an expression of the drag coefficient of the sphere in terms of kinetic Reynolds number, we remind that C_d is defined by:

$$C_d = \frac{8D}{\pi\rho {\mathrm{d}_{\mathrm{sp}}}^2 U_{\mathrm{ref}}^2}. \tag{2.4.33}$$

The previous definition involves the drag D which is defined as follows:

$$\begin{aligned} D &= \int_{\Gamma_{\mathrm{obs}}} \left(p\mathbf{n} - R_e^{-1}\nabla(\mathbf{u})\mathbf{n}\right)\cdot\mathbf{e}_z \\ &= \int_{\Omega_{\mathrm{obs}}} \nabla\cdot(p\mathcal{I} - R_e^{-1}\nabla\mathbf{u})\cdot\mathbf{e}_z, \end{aligned} \tag{2.4.34}$$

with Ω_{obs} the solid domain, Γ_{obs} the boundary of the solid domain, $\mathbf{n}$ the outward normal vector of the surface Γ_{obs} and $\mathbf{e}_z$ the unit vertical vector which is parallel to the direction of the flow. Thanks to equation (2.4.24) and the hypothesis $\mathbf{u}_{\mathrm{obst}} = 0$, we induce that the drag can be written:

$$D = \int_\Omega (1-\chi)\frac{-\mathbf{u}^n}{\tau}\cdot\mathbf{e}_z. \tag{2.4.35}$$

As we imposed $\rho = 1$, $d_{\mathrm{sp}} = 2$, $U_{\mathrm{ref}} = 1$, the drag coefficient is equal to:

$$C_d = \frac{-2}{\pi}\int_\Omega (1-\chi)\frac{\mathbf{u}^n}{\tau}\cdot\mathbf{e}_z. \tag{2.4.36}$$

The comparison between experimental and SFEMaNS numerical values of C_d is done for Reynolds numbers varying in $[1, 200]$ and results are summarized in table 2.9. The computations were done with meshes of typical mesh size at the boundary of the domain varying from 0.5 to 0.125 while the typical mesh size around the sphere is equal to 0.0125. Computations are axisymmetric for $R_e \leq 50$ while 4 to 8 Fourier modes are used for computations with $R_e \geq 100$. On the other hand the time steps used are such that the CFL is around 0.5 as we noticed that results are the best for this CFL value. Moreover the computations are done till the drag coefficient converges which is usually obtained after a code time of 20. The numerical results, displayed in the third column of table 2.9, are matching very well the experimental data as the relative error remains around 1%.

Eventually we can conclude that we adapt SFEMaNS code to non axisymmetric geometry for hydrodynamic problems. However, we note that all previous tests use a sharp

penalty function, meaning a discontinuous function that is equal to 1 in the fluid domain and 0 in the solid domain. So before describing another important development of this PhD thesis, that consists of adapting SFEMaNS code to variable fluid and solid properties, we propose to study the influence of the use of smooth penalty function.

R_e	$C_d^{\text{theoretical}}$	C_d^{SFEMaNS}	Rel. Error (%)
1	27.1560	27.1168	0.1
2	14.7569	14.7085	0.3
10	4.2584	4.2985	0.9
20	2.7147	2.7278	0.5
50	1.5743	1.5886	0.9
100	1.0870	1.1022	1.4
200	0.7756	0.7848	1.2

Table 2.9: Comparisons of theoretical and numerical value of Cd for various R_e

On the use of sharp (discontinuous) or smooth penalty function

In this section we propose to compare the influence of the use of sharp or smooth penalty function χ on the computation of the drag coefficient for $R_e = 100$. In that purpose, we consider a sharp and smooth penalty functions defined by:

$$\chi_{\text{sharp}}(r, \theta, z, t) = \mathbf{1}_{r^2+z^2 \geq 1} \tag{2.4.37}$$

and

$$\chi_{\text{smooth}}(r, \theta, z, t) = \frac{1}{2}\left(1 + \tanh(\frac{r^2 + z^2 - 1}{0.025})\right). \tag{2.4.38}$$

The comparisons are done by varying the time step from 0.01 to 0.00125 with a fixed mesh of typical mesh size 0.5 on boundary of the domain and 0.0125 around the sphere. We display in figure 2.7 the profile of both penalty functions around the sphere, one can note that the smooth function goes from 0 to 1 in a few mesh cells so it looks similar to the sharp function. The final values of the drag coefficient are represented in table 2.10 while the evolution of the drag coefficient along time for the different time steps used is displayed in figure 2.8. It is striking that even if the sharp and smooth penalty functions are relatively close, see figure 2.7, the resulting drag coefficients are on the contrary very different. First we can note that the sharp function allows to get a closer value of the expected C_d. Moreover reducing the time step does not influence very much the C_d obtained with the sharp penalty function as the relative errors stand around 2.5%. On the other hand reducing the time step while using the smooth penalty function increases the error with respect to the expected C_d. As a conclusion we can state that it is highly preferable to use a sharp penalty function equal to 1 in the fluid domain and 0 in the solid domain when using this pseudo-penalization method.

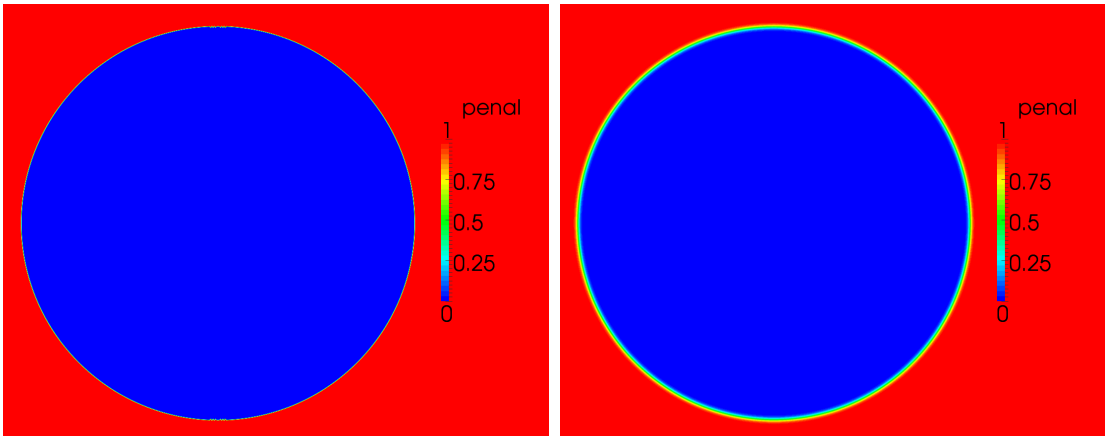

(a) Sharp penalty function (b) Smooth penalty function

Figure 2.7: Profiles of the penalty function for sharp and smooth cases near the obstacle ($h = 0.5$ on boundary and $h = 0.0125$ near the sphere in $\mathbb{P}_1$).

	Sharp penal function		Smooth penal function	
τ	C_d^{SFEMaNS}	Rel. Error (%)	C_d^{SFEMaNS}	Rel. Error (%)
10^{-2}	1.1154	2.6	1.1308	4.0
5.10^{-3}	1.1143	2.5	1.1336	4.3
$2,5.10^{-3}$	1.1151	2.6	1.1388	4.8

Table 2.10: Comparisons of C_d with $R_e = 100$ between sharp and smooth penalty functions for various time steps. $C_d^{\text{theoretical}} = 1.0870$

2.5 Extension to MHD problems with variable fluid and solid properties

During this PhD period we focused our investigations on three subjects: precession, VKS experiment and multiphase flow problems. While the precession only presents computational cost difficulties due to the Reynolds numbers involved, the other two problems involve the implementation of new approximation methods in the code. While the pseudo-penalization method described in section 2.4 extends the range of SFEMaNS code to hydrodynamic problems with non axisymmetric geometry, it remains to take into account magnetic problems with a given time and (r, θ, z) dependent magnetic permeability and hydrodynamic problems with variable density and viscosity.

In order to approximate such problems we have the choice to approximate the Maxwell equations either with the magnetic field $\mathbf{H}$ or the induction field $\mathbf{B} = \mu\mathbf{H}$ with μ the magnetic permeability. In the same way, the Navier-Stokes equations can either be approximated with the velocity field $\mathbf{u}$ or the momentum $\mathbf{m} = \rho\mathbf{u}$ with ρ the density. A first study, done with D. Castanon-Quiroz during the first part of a one year stay at Texas A&M University (College Station, Texas) thanks to an invitation of J.-L. Guermond, draws us to focus on the following simplified equations:

$$\partial_t(\mu\mathbf{u}) - \nabla\cdot\nabla\mathbf{u} = 0 \tag{2.5.1}$$

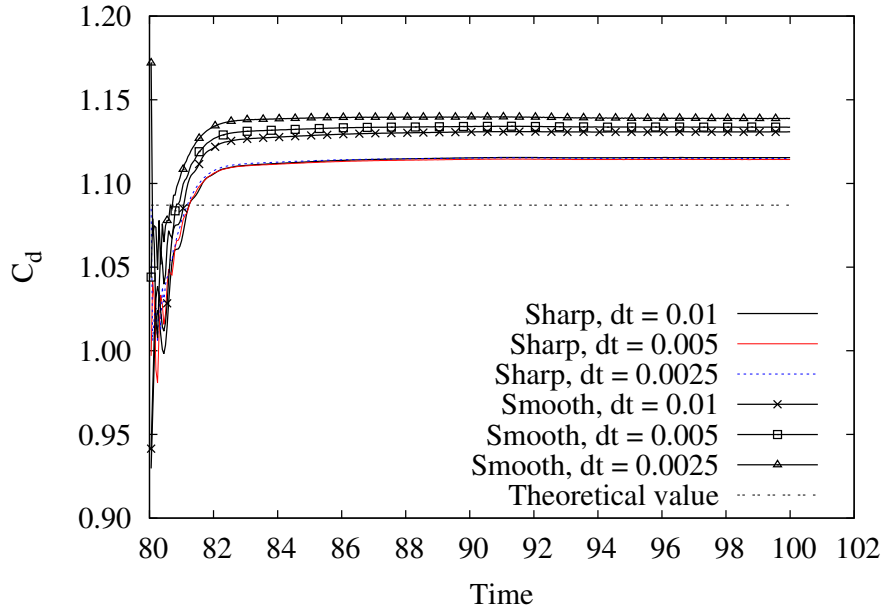

Figure 2.8: Evolution of C_d with $R_e = 100$ for sharp and smooth penalty functions.

and

$$\partial_t(\mathbf{v}) - \nabla\cdot\nabla(\frac{\mathbf{v}}{\mu}) = 0, \tag{2.5.2}$$

where $\mu\mathbf{u} = \mathbf{v}$. We note that the two previous equations are a simplification of the Maxwell and the Navier-Stokes equations where we drop the nonlinear term, source term and zero divergence condition (and so the pressure gradient). Since we want to work with time independent algebra for computational efficiency, the term $\partial_t(\mu\mathbf{u})$ or $\nabla\cdot\nabla(\frac{\mathbf{v}}{\mu})$ cannot be treated implicitly. To overcome this difficulty, we decide to introduce two constants $\tilde{\mu}$ and $\overline{\mu}$ such that $\overline{\mu} \leq \mu \leq \tilde{\mu}$ so we can rewrite the two previous terms as follows:

$$\partial_t(\mu\mathbf{u}) = \partial_t(\tilde{\mu}\mathbf{u}) + \partial_t((\mu - \tilde{\mu})\mathbf{u}) \tag{2.5.3}$$

and

$$\nabla\cdot\nabla(\frac{\mathbf{v}}{\mu}) = \nabla\cdot\nabla(\frac{\mathbf{v}}{\overline{\mu}}) + \nabla\cdot\nabla\left((\frac{1}{\mu} - \frac{1}{\overline{\mu}})\mathbf{v}\right). \tag{2.5.4}$$

The first term of these equations is then treated implicitly while the second one is made explicit with first or second order extrapolation. While these two models remain stable when using first order time extrapolation, only the second model with the variable $\mathbf{v} = \mu\mathbf{u}$ remains stable when using second order time extrapolation. We refer to D. Castanon-Quiroz thesis [18] for the numerical and theoretical analysis of these simplified models, the conclusions of this study motivate us to use the induction field $\mathbf{B} = \mu\mathbf{H}$ to approximate the Maxwell equations with variable magnetic permeability μ. By analogy we also decide to approximate the Navier-Stokes equations with the variable $\mathbf{m} = \rho\mathbf{u}$ when the density is variable. For a better understanding of the methods we develop to approximate problems with variable fluid and solid properties, the next two subsections give a short description of the methods we implement in SFEMaNS code to approximate such problems. We note that a full description of the method used to approximate the Navier-Stokes equations with variable density, but also viscosity, is provided in chapter 5.

2.5.1 Magnetic field based approximation for azimuthal dependent magnetic permeability

As the code allows variable permeability in r and z directions, the next obstacle to approximate solutions of VKS set-up is to take into account for variation of magnetic permeability in θ direction due to the counter-rotating impellers. This work was done in the frame of D. Castanon-Quiroz thesis [18] to which we refer for complete details on the method and its validation. As introduced previously, the main idea of this method is to use the induction field $\mathbf{B}$ as variable to approximate the Maxwell equations. Assuming the electrical conductivity is constant, we can rewrite equation (1.3.22) as follows:

$$\partial_t \mathbf{B} + \frac{1}{R_m} \nabla\times\nabla\times \left(\frac{\mathbf{B}}{\mu}\right) = \nabla\times(\mathbf{u}\times\mathbf{B}). \tag{2.5.5}$$

The main difficulty now relies on the approximation of the dissipative term $\nabla\times\nabla\times\frac{\mathbf{B}}{\mu}$. As the magnetic permeability μ is not constant along time, the implicit treatment of this term induces a time dependent algebra. For computational efficiency purposes, we want to use a numerical scheme with time independent algebra so the stiffness matrix of the problem only needs to be assembled and preconditioned at initialization. To fulfill this objective, we rewrite the dissipative term $\nabla\times\nabla\times\frac{\mathbf{B}}{\mu}$ as follows:

$$\nabla\times\nabla\times(\frac{\mathbf{B}}{\overline{\mu}}) + \nabla\times\nabla\times \left((\frac{1}{\mu} - \frac{1}{\overline{\mu}})\mathbf{B}\right) \tag{2.5.6}$$

with $\overline{\mu}$ a constant smaller than μ everywhere in the domain for all time. The first term is then treated implicitly while the second one is made explicit with second order extrapolation. As the time derivative is approximated with a second order backward differentiation formula (BDF2) and the nonlinear term is made explicit with second order extrapolation, we end up with a time independent algebra.

Combined to the pseudo-penalization technique described in section 2.4, this development allows SFEMaNS to fully approximate problem with a VKS set-up where the fluid is driven by non axisymmetric counter-rotating impellers with magnetic permeability different from that of the fluid. As this PhD thesis mainly focuses on hydrodynamic studies, we refer to D. Castanon-Quiroz's thesis [18] for a full MHD study of the VKS set-up. On the other hand we perform a study of the hydrodynamic regime of a VKS set-up for a large range of kinetic Reynolds numbers in order to compare our numerical results with future results of experiments that are currently carried out in CEA Saclay.

2.5.2 Momentum based approximation for multiphase flow problems

One of the main achievements of this PhD thesis has been to implement a new algorithm aiming at approximating multiphase flow problems with SFEMaNS code. This study is motivated by our group's interest in Liquid Metal Batteries (LMB) and their possible role in future energy storage. The main difficulties we face are to follow the evolution of the interface between two fluids and to approximate the Navier-Stokes equations with a time independent algebra algorithm. As this algorithm is exhaustively described in chapter 5, we give a short description of the methods we use to approximate multiphase flows and refer to chapter 5 for completeness.

We overcome the first difficulty by assuming the fluid is composed of two separate and immiscible phases and we use a level set technique to represent the evolution of the density

distribution. This method consists in introducing a level set ϕ taking value in $[0,1]$ and solution of:

$$\partial_t \phi + \mathbf{u} \cdot \nabla \phi = 0 \tag{2.5.7}$$

where the interface of the two fluids is localized in $\phi^{-1}(1/2)$ and ϕ equal to 0 in the first phase and 1 in the other. This level set is then used to reconstruct the density and the viscosity that unlike the magnetic permeability of the previous section are not given and need to be approximated.

After reconstructing the density and the viscosity, the Navier-Stokes equations are formulated as in (1.3.8) and approximated with the variable $\mathbf{m} = \rho\mathbf{u}$. Unlike the technique developed for the Maxwell equations with variable magnetic permeability μ that was of order 2 in time, the scheme developed for the Navier-Stokes equations is of order 1 in time. As a consequence the time derivative is approximated with a BDF1 formula and the nonlinear terms are made explicit with first time order extrapolation. To get a time independent algebra, the diffusive term is treated in a similar way as in the previous section by introducing the constant $\overline{\nu} \geq \eta/\rho$ and rewriting the diffusive term:

$$-\nabla\cdot(\overline{\nu}\epsilon(\mathbf{m})) + \nabla\cdot(\overline{\nu}\epsilon(\mathbf{m}) - \eta\epsilon(\mathbf{u})). \tag{2.5.8}$$

We note that a stabilization method involving the entropy viscosity, introduced in the following chapter, is used to stabilize both the momentum and the level set equations. This method is validated with many tests described in chapter 5 and allows to get preliminary results of LMB instabilities published in [46].

2.6 Outlook

After extending the range of SFEMaNS code to problems with non axisymmetric geometry or with variable fluid and solid properties, we end up with a code that can approximate most of hydrodynamic, magnetic or magnetohydrodynamic problems with the possibility of taking into account thermal effects. One of the biggest remaining constraints to approximate many physical or experimental problems is the computational cost of simulations. Although the SFEMaNS code presents a parallelization in three space directions and that the MHD equations are approximated with numerical schemes involving time independent algebra, the present computational power is not enough to compute the whole flow of many physical problems due to the kinetic and magnetic Reynolds numbers involved. As this difficulty is faced by all hydrodynamic and MHD codes, the scientific community developed models for the Navier-Stokes equations that allow to represent the influence of the smallest length scales of flows so only the large scales of flows are approximated. These models are referred to as Large Eddy Simulation (LES) models and allow to greatly reduce the computational cost of a numerical simulation as the small scales of the flow are not approximated, their influence is modeled.

In this frame a nonlinear stabilization method, called entropy viscosity and developed by J.-L. Guermond et al. [36, 37], is implemented in SFEMaNS code to allow us to approximate physical problems with realistic parameters. This method is introduced as a LES model in the following chapter where details on its numerical implementation and properties, such as its consistency with respect to the numerical scheme used, are also given. We plan to use in chapter 4 the entropy viscosity method on experimental set ups such as VKS and precession, studied by J.-L. Guermond and C. Nore for the past decade, to point

out the good results of this nonlinear stabilization method for the Navier-Stokes equations. Furthermore we note that the entropy viscosity is one of the keystones of our model to approximate multiphase flow problems. Indeed as we decide to adopt a continuous framework, solutions may present large gradients at the interface between two fluids so the use of the entropy viscosity method allows to stabilize our model. We refer to chapter 5 for more details.

Nonlinear stabilization method: entropy viscosity

Hydrodynamic problems with large R_e induce extremely complex flows, so present computational resources do not allow us to approximate all of the scales of the dynamics. Since many studies in aerodynamics and astrophysics involve large R_e, numerical models are developed to reduce the complexity of such problems. Some of these models are designed to approach average quantities, like the Reynolds Averaged Navier-Stokes method (RANS). However, we prefer to focus on models that approximate the solutions from their largest space scale to a given scale. Such methods, called Large Eddy Simulations (LES), consist of modeling the influence of the unresolved scales. After giving general descriptions of LES models, we introduce a nonlinear stabilization method called entropy viscosity as a LES model. A second section gives details on the numerical implementation of entropy viscosity in the SFEMaNS code. Numerical tests are also presented to check its consistency property.

Contents

3.1 Context and method

We start this section with comments on the necessity of using models for large R_e problems when Direct Numerical Simulations (DNS), that solve the whole dynamics of the flow, are not feasible. After giving details on present LES models, we describe the entropy viscosity technique of Guermond et al. [36, 37]. While we introduce this method as a LES model, we draw attention on its consistency and diffusive properties.

3.1.1 On the need of models

The first computational difficulty encountered when approximating the solutions of problems with large R_e is to take into account the full dynamics of the flow. By denoting $L_{\max}$ the largest and $L_{\min}$ the smallest space scales of the flow, the heuristic Kolmogorov criterion states that:

$$\frac{L_{\max}}{L_{\min}} \propto R_e^{3/4}. \tag{3.1.1}$$

Since the mesh size needs to report from all the scales, the number of degrees of freedom per dimension is proportional to ${R_e}^{3/4}$. So a three dimensional DNS requires a mesh with ${R_e}^{9/4}$ degrees of freedom to represent all of the dynamic spatial scales. The second difficulty lies in approximating the solutions on a sufficiently long time interval. For spin up problems like the Von Kármán Sodium (VKS) and precessing problems studied in chapter 4, the characteristic time scale, denoted by T_{car}, satisfies the relation:

$$T_{\text{car}} \propto R_e^{1/2}. \tag{3.1.2}$$

As the time step τ is controlled by a Courant-Friedrichs-Lewy condition, we get $\tau = O\left({R_e}^{-3/4}\right)$. Thus, the total number of time iterations required to approximate the problem over a characteristic time is proportional to ${R_e}^{5/4}$. Such restrictions combined to present computational resources make DNS not feasible when approximating problems with large R_e. Indeed the number of floating operations N required by a computation is proportional to the number of time iterations times the number of degrees of freedom of the mesh, so we get:

$$N \propto {R_e}^{7/2}. \tag{3.1.3}$$

Applications in aeronautics or astrophysics can involve R_e of the order 10^8 so N is proportional to 10^{28}. Present supercomputers have a peek speed of order 10^{16} floating operations per second (FLOPS) so these types of simulations are out of reach.

Since some problems are characterized by symmetries or some spatial frequencies, we note that these previous estimates can be reduced for DNS via a suitable decomposition, along Fourier modes for example. However, DNS remains infeasible for a general problem involving large R_e. In order to approximate the solutions of such problems, two main approaches can be distinguished:

- Reynolds Averaged Navier-Stokes (RANS) models that approximate mean quantities of the pressure and the velocity fields. These models are based on the idea that the characteristic time of the smallest space scale is much smaller than the one of the largest scale. As the mean flow is dominated by large scales, mean quantities can be approximated with lower computations cost. Such models use a Reynolds decomposition that consists in rewritting the variables in the form $\mathbf{u} = \overline{\mathbf{u}} + \mathbf{u}'$, where $\overline{\mathbf{u}}$ is a mean over time, and sometimes also over space, and $\mathbf{u}'$ is the fluctuating part that satisfies $\overline{\mathbf{u}'} = 0$. The mean quantities $\overline{\mathbf{u}}$ and $\overline{p}$ are then solutions of the dimensionless equations:

$$\partial_t \overline{\mathbf{u}} + \nabla\cdot(\overline{\mathbf{u}} \otimes \overline{\mathbf{u}}) - \frac{1}{R_e}\Delta(\overline{\mathbf{u}}) = -\nabla\overline{p} - \nabla\cdot(\overline{\mathbf{u}' \otimes \mathbf{u}'}), \tag{3.1.4}$$

$$\nabla\cdot(\overline{\mathbf{u}}) = 0. \tag{3.1.5}$$

  We note that RANS models were first designed for steady flows such that $\partial_t \overline{\mathbf{u}} = 0$. New methods for unsteady mean flows, called URANS, have been developed since

then. As $\mathbf{u}'$ is not approximated, many models were developed to consider the action of the term $-\nabla\cdot(\overline{\mathbf{u}'\otimes\mathbf{u}'})$. One of the most common methods is to use the Boussinesq approximation, thus this term is rewritten as a dissipative term (divergence of a strain rate tensor) associated to a turbulent, also called eddy, viscosity that needs to be modeled. We refer to [5, 91] for more descriptions of RANS models. We note that these models require accurate information on the flow to approximate, such as initial and boundary conditions or some hypothesis on the stationary or space invariance properties of the flow. These models present a low cost of computations, for example many 3D turbulent flows can be reduced to a 2D mean flow motion. RANS models are applied to several industrial studies, such as aeronautics, where numerous information can be obtained or compared with experiment results.

- Large Eddy Simulation (LES) models that approximate the solutions from their largest space scale to a given one. This restriction on the computed space scales, also called eddy, is based on Kolmogorov theory [57, 56]. It states that large scales are dependent to geometry and boundary conditions while the small scales of the flow have more universal structure. Moreover the main action of small scales is to dissipate energy so most of the energy is contained in the large scales of the flow. To avoid overly time consuming computations, due to the approximations of smallest scales, LES methods do not compute the small scales of the flow but they represent their action by the use of sub-grid-scale (SGS) models.

The main difference between these two methods is that LES methods only model the action of unresolved scales while RANS methods, by the use of time or space averages, model all the fluctuation of the flow. LES methods require less information on the flow and allow to grasp local behavior, such as instabilities, however they require more computational resources. The SFEMaNS code is developed to approximate the largest range of MHD-problems with the minimum information. Thus, we are more interested in LES methods, which we describe in the following.

3.1.2 Large Eddy Simulation models

Large Eddy Simulation models can be splitted into two main steps. Firstly, one needs to choose a level of space and time resolution so the Navier-Stokes equations are only solved for large scales of the flow. Secondly, we need to report from the action of the unresolved scales that are not taken into account when computing the nonlinear term of the Navier-Stokes equations. Furthermore, we give a general description of the "filters" used to separate the space scales and some information on the two main sub-grid-scale models. We refer to [71, 99] for more details on LES.

Use of "filters" to separate resolved and sub-grid scales

Since the goal of LES methods is to decrease the computational cost by approximating only the largest space scales of the dynamics, the scales of the flow need to be split into resolved and unresolved scales. This procedure is usually done by introducing a computational grid and a suitable time increment. A second step, involving convolution products, can also be implemented to induce a cut-off length bigger than the one of the grid. This second step induces extra implementation and is not the most used, however it allows to consider a larger range of sub-grid-scale models detailed later. The LES community usually differentiates this scale separation process into two kinds of "filtering":

- Implicit filters that are associated with the choice of a domain discretization and a time step τ. Thus, the resolved scales are bigger than the mesh size Δx, or bigger than a minimum wavelength $\frac{1}{k_{\max}}$ for spectral methods. Since a part of the scales is unresolved, the computation of the nonlinear term $\nabla\cdot(\mathbf{u}\otimes\mathbf{u})$ does not take into account their contribution. Their influence can be represented by the addition of the term $\nabla\cdot\tau^r$ where τ^r represents the interactions between resolved-unresolved scales and the interactions among unresolved scales.

- Explicit filters that introduce a function G, which is associated with a space cut off length $\overline{\Delta} \geq \Delta x$, and that focus on the approximation of the variables $\overline{\mathbf{u}} = G * \mathbf{u}$ and $\overline{p} = G * p$. We note that unlike the RANS model, or more generally Reynolds operator, $\overline{\overline{\mathbf{u}}} \neq \overline{\mathbf{u}}$. Explicit filters can also involve a time cut off length and are split into two groups: homogeneous and inhomogeneous filters. Homogeneous filters are designed for infinite or periodic domains and use fixed cut off length to commute with space or time derivative operators. Inhomogeneous filters are developed for bounded domains where small eddies arise near the walls and usually involve space and time dependent cut off lengths. The continuous problem is then rewritten as follows:

$$\partial_t\overline{\mathbf{u}} + \nabla\cdot(\overline{\overline{\mathbf{u}}\otimes\overline{\mathbf{u}}}) - \frac{1}{R_e}\Delta(\overline{\mathbf{u}}) = -\nabla\overline{p} - \nabla\cdot(\tau^r), \tag{3.1.6}$$

$$\nabla\cdot\overline{\mathbf{u}} = 0, \tag{3.1.7}$$

  with $\tau^r = \overline{\mathbf{u}\otimes\mathbf{u}} - \overline{\overline{\mathbf{u}}\otimes\overline{\mathbf{u}}}$ which is often rewritten with a Leonard decomposition [69]. The influence of $\nabla\cdot\tau^r$ then needs to be modeled by the use of a sub grid scale model or reconstruction of the solution $\mathbf{u}$. We note that inhomogeneous filters do not commute with space and time derivative operators and so induce commutation errors. These errors then need to be taken into account which increase again, compared to implicit filters alone, the complexity of the method.

Eventually the filtering processes leave us with resolved fields $\overline{\mathbf{u}}$ and $\overline{p}$, which are used to approximate the action of the sub-grid scales.

Modeling the action of sub-grid scales

As the solutions are only approximated on large scales, whose approximation is denoted $\overline{\mathbf{u}}$ independently of the use of explicit filters, the action of the sub-grid scales can only be represented with $\overline{\mathbf{u}}$. These models are usually referred to as SGS models. They can adopt various strategies that can be ordered into two kinds of models:

- functional models that focus on introducing an energy diffusion mechanism that represents the interactions between resolved and unresolved scales that are assumed to dissipate energy as in the Kolmogorov cascade energy scenario.

- structural models that aim to reconstruct the tensor τ^r from evaluation of $\overline{\mathbf{u}}$. These models are mainly based on a reconstruction of the unresolved scales $\mathbf{u}' = \mathbf{u} - \overline{\mathbf{u}}$ which are used to evaluate an approximation of τ^r.

Functional models are, to the author's knowledge, mainly based on statistical turbulence theory and usually introduce a turbulent viscosity, similar to the RANS model. For example, the widely used Smagorinsky model consists in approximating the term $-\nabla\cdot(\tau^r)$ of (3.1.6) by a diffusive term of the form $\nabla\cdot(\nu_t\epsilon(\overline{\mathbf{u}}))$ where ϵ is the strain rate tensor operator defined in section 1.3.1. The turbulent viscosity ν_t is then set proportional to

$\overline{\Delta}^2\|\epsilon(\overline{\mathbf{u}})\|$ with $\overline{\Delta}$ the cut off length of the filter or the mesh size for implicit filter. Since the cut off length $\overline{\Delta}$ is equal or bigger to the mesh size, we note that such a model may sacrifice the consistency of the numerical scheme to represent a dissipation mechanism. These functional models remain widely used due to their easy numerical implementation compared to structural models. Regarding the structural models, we can cite two main strategies: approximate deconvolution method (ADM) [66] and the more recent Residual Based Variational Multiscale (RBVM) method [10, 50]. ADMs are based on the fact that the Fourier transform of a convolution product $f * g$ is the product of the Fourier transform of f and g so the unresolved scales $\mathbf{u}'$ can be approximated by deconvolution method such as the Van-Cittert method. On the other hand RBVM methods separate resolved and unresolved scales with a projection method. Then the unresolved scales equation is modeled so the unresolved scales can be determined analytically and then used to approximate the resolved scales. We note that RBVM methods do not change the numerical scheme order of the resolved scales so they are consistent.

As we believe that consistency (with respect to the numerical scheme) and diffusive properties of sub grid scale models are essential to preserve the accuracy and to increase the stability of the numerical approximation, we propose to introduce a new LES functional models that satisfies these restrictions. This model, called entropy viscosity, consists in constructing an artificial viscosity based on an entropy residual and is described in the following section.

3.1.3 Entropy viscosity as LES method

The entropy viscosity method has been introduced in [36, 37, 38] by Guermond et al. This method is based on the notion of suitable solutions of Scheffer [101] and intends to introduce in the Navier-Stokes equations a consistent artificial viscosity proportional to the default of equilibrium of an energy equation. Before describing the entropy viscosity method, we propose to describe the mathematical frame and its connection to LES models under which this method has been developed.

Notion and interpretation of suitable solutions

While the existence of weak solutions to the Navier-Stokes equations has been enhanced by Leray [70], their uniqueness remains an open question. In order to study their uniqueness, Scheffer [101] worked on the regularity of Navier-Stokes solutions and introduced the notion of suitable weak solutions. We note that his work allowed to find an upper bound on the Hausdorff measure of the set of singularities of a suitable solution which was later improved by Caffarelli-Kohn-Nirenberg [17]. Although the study of uniqueness or regularity of Navier-Stokes solutions is out of the scope of this PhD thesis, we are still interested in the notion of suitable solution which can be defined as follows.

Definition Let $(\mathbf{u}, p)$ be a weak solution of the Navier-Stokes equations (1.3.5) with $\mathbf{u} \in L^2((0,T);\mathbf{H}^1(\Omega)) \cap L^\infty((0,T);\mathbf{L}^2(\Omega))$ and $p \in D'((0,T);L^2(\Omega))$. $(\mathbf{u}, p)$ is called suitable if the following inequality holds in $D'(Q_T, R^+)$:

$$\partial_t(\frac{1}{2}\mathbf{u}^2) + \nabla\cdot((\frac{1}{2}\mathbf{u}^2 + p)\mathbf{u}) - R_e^{-1}\Delta(\frac{1}{2}\mathbf{u}^2) + {R_e}^{-1}(\nabla\mathbf{u})^2 - \mathbf{f}\cdot\mathbf{u} \leq 0 \tag{3.1.8}$$

where $Q_t = \Omega \times [0,T]$.

The reader can notice the similarity of this notion with the entropy conditions for conservation laws where the kinetic energy plays the role of the entropy. Such conditions have

been introduced by Kružkov [61] to reduce the number of solutions of a conservation law problem to a unique solution that satisfies an entropy inequality. For example, we can consider the inviscid Burgers equations:

$$\partial_t u + \partial_x \frac{u^2}{2} = 0, \tag{3.1.9}$$

in one dimensional space with initial data $u_0(x) = 1 - H(x)$ where H is the Heaviside function. One can check that for every $\alpha > 1$, the following function is a weak solution of the problem:

$$u(x,t) = \begin{cases} 1 & \text{if } x < \frac{1-\alpha}{2}t \\ -\alpha & \text{if } \frac{1-\alpha}{2}t < x < 0 \\ \alpha & \text{if } 0 < x < \frac{\alpha}{2}t \\ 0 & \text{if } \frac{\alpha}{2}t < x. \end{cases} \tag{3.1.10}$$

However, $u(x,t) = 1 - H(x - \frac{t}{2})$ is the only entropy solution and satisfies the relation $\frac{1}{2}\partial_t u^2 + \frac{1}{3}\partial_x u^3 = -\frac{1}{12}\delta(x - \frac{t}{2}) \leq 0$ where the kinetic energy plays the role of the entropy and δ is the Dirac measure.

Since the definition of suitable solutions may not be meaningful as it is defined, we introduce the residual $\mathbf{R}$ of the Navier-Stokes equations defined by:

$$\mathbf{R}(\mathbf{x},t) := \partial_t \mathbf{u} + (\mathbf{u}\cdot\nabla)\mathbf{u} + \nabla p - R_e^{-1}\Delta\mathbf{u} - \mathbf{f}. \tag{3.1.11}$$

By denoting $\mathbf{u}^2 = \mathbf{u}\cdot\mathbf{u}$, we note that an incompressible flow with sufficient regularity hypothesis on the solutions satisfies the relations $(\partial_t\mathbf{u})\cdot\mathbf{u} = \frac{1}{2}\partial_t\mathbf{u}^2$, $((\mathbf{u}\cdot\nabla)\mathbf{u})\cdot\mathbf{u} = \nabla\cdot(\frac{1}{2}\mathbf{u}^2\mathbf{u})$, $(\nabla p)\cdot\mathbf{u} = \nabla\cdot(p\mathbf{u})$ and $(\Delta\mathbf{u})\cdot\mathbf{u} = \frac{1}{2}\Delta(\mathbf{u}^2) - (\nabla\mathbf{u})^2$. So under sufficient regularity hypothesis, a suitable weak solution of the Navier-Stokes equations is a solution that satisfies the following inequality:

$$\mathbf{R}\cdot\mathbf{u} \leq 0, \tag{3.1.12}$$

in the distribution sense. As a consequence, suitable solutions are such that the power of the residual is negative so they are dissipative. Eventually if singularities or shocks occur, they will dissipate energy.

Connection to LES methods and under-resolved simulations

We now consider the case of under-resolved computations where the numerical resolution used to approximate the solutions is not fine enough to capture all the scales of the flow. We denote by h the mesh size and $(\mathbf{u}_h, p_h)$ the numerical approximation of the solutions of the Navier-Stokes equations (1.3.5) so we can introduce the residual of the energy equation D_h defined by:

$$D_h(\mathbf{x},t) = \partial_t(\frac{1}{2}\mathbf{u}_h^2) + \nabla\cdot((\frac{1}{2}\mathbf{u}_h^2 + p)\mathbf{u}_h) - R_e^{-1}\Delta(\frac{1}{2}\mathbf{u}_h^2) + {R_e}^{-1}(\nabla\mathbf{u}_h)^2 - f\cdot\mathbf{u}_h. \tag{3.1.13}$$

Being under-resolved in a region $(\mathbf{x},t)$ means that large gradients cannot be represented by the grid and are going to perturb the approximation. Due to nonlinearity, these gradients may become larger and larger with time so energy is accumulating at the grid scale and energy balance is violated. As a consequence an under-resolved region can be defined as a region where the power of the residual $D_h(\mathbf{x},t)$ is larger than the consistency error of the method. It is then possible to distinguish two configurations: $D_h(\mathbf{x},t)$ negative or positive. If $D_h(\mathbf{x},t) \leq 0$, meaning the power of the singularity is negative, the energy is dissipated.

Eventually the energy is lost in subgrid scales as in the Kolmorogov cascade scenario so this situation does not pollute the approximations. On the other hand, if $D_h(\mathbf{x},t) > 0$, energy is produced and accumulated at the mesh scale so the approximations are polluted. This situation, by analogy with a shock that produces energy, is not physical. Eventually imposing the condition:

$$D_h(\mathbf{x},t) \leq 0, \tag{3.1.14}$$

would imply a diffusive mechanism that is in agreement with Kolmogorov cascade energy scenario, which is the base of many LES turbulent viscosity models. As such conditions cannot be imposed on the flow itself, the entropy viscosity method proposes to add an artificial viscosity to the Navier-Stokes equations that is proportional to D_h.

The main originality of this method is not the use of the entropy production, which was for example used in [4, 92] as an a posteriori error indicator that could be useful for adaptive methods, but the construction of an artificial viscosity based on the residual of the entropy production. We note that previous methods, described in [49, 52, 107], already constructed artificial viscosity based on the residual of the Navier-Stokes equations. However, the use of the residual of the entropy equation gives more information in the under-resolved regions since the residual of the Navier-Stokes equations is always of the same order as the consistency of the method. Eventually the entropy viscosity method can be classified as a LES functional model as it enforces a diffusive mechanism while disregarding the unresolved scales. We also note that this theory does not involve explicit filters so its numerical implementation is facilitated.

Definition of the entropy viscosity model

The first step of the entropy viscosity method consists in introducing a local artificial viscosity $\nu_{R,h}$ defined by:

$$\nu_{R,h}(\mathbf{x},t) = h(\mathbf{x})^2 \frac{|D_h(\mathbf{x},t)|}{\left\|\mathbf{u}_h^2\right\|_{L^\infty(\Omega)}} \tag{3.1.15}$$

where $h(\mathbf{x})$ is the local mesh size. While this artificial viscosity is expected to be smaller than the consistency error in smooth regions, it can be very large in regions where the equations are not well resolved. So the quantity $\nu_{R,h}$ may induce too much diffusion to be of practical use. As a result, the viscosity entropy method consists in adding the term $-\nabla\cdot(\nu_{E,h}\nabla\mathbf{u}_h)$ to the left hand side of the Navier-Stokes equations (1.3.5) where $\nu_{E,h}$, called entropy viscosity, is defined by:

$$\nu_{E,h}(\mathbf{x},t) := min\left(\mathrm{c_e} h(\mathbf{x})^2 \frac{|D_h(\mathbf{x},t)|}{\left\|\mathbf{u}_h^2\right\|_{L^\infty(\Omega)}}, \mathrm{c_{max}} h(\mathbf{x})|\mathbf{u}_h(\mathbf{x},t)|\right) \tag{3.1.16}$$

where $\mathrm{c_e}$, $\mathrm{c_{max}}$ are tunable constants. The term $\mathrm{c_{max}} h(\mathbf{x})|\mathbf{u}_h(\mathbf{x},t)|$, which we refer to as first order viscosity, is present to limit the diffusion of the entropy viscosity method. It finds its origin in an analogy with finite difference method for the advection equation in one space dimension:

$$\partial_t u + \beta \partial_x u = 0, \tag{3.1.17}$$

where we assume $\beta > 0$. As we denote by u_i^n, the approximation of $u(i\Delta x, n\tau)$ with a uniform grid of size Δx and time step τ, we remind that the first order up-wind scheme defined by:

$$\frac{u_i^{n+1} - u_i^n}{\Delta t} + \beta \frac{u_i^n - u_{i-1}^n}{\Delta x} = 0, \tag{3.1.18}$$

is known to be stable under the CFL condition $\beta\tau(\Delta x)^{-1} \leq 1$. It is then interesting to note that the first order up-wind scheme can be rewritten as follows:

$$\frac{u_i^{n+1} - u_i^n}{\Delta t} + \beta\frac{u_{i+1}^n - u_{i-1}^n}{2\Delta x} - |\beta|\frac{\Delta x}{2}\frac{u_{i+1}^n - 2u_i^n + u_{i-1}^n}{\Delta x^2} = 0. \tag{3.1.19}$$

As a consequence the first order up-wind scheme of the advection equation (3.1.17) is equivalent to use a centered second order finite difference to the equation:

$$\partial_t u + \beta\partial_x u - \beta\frac{\Delta x}{2}\partial_{xx} u = 0. \tag{3.1.20}$$

By analogy, we set $c_{\max} \leq \frac{1}{2}$ so the entropy viscosity does not induce more diffusion than the one induced by the first order up-wind scheme. As a consequence the entropy viscosity method should run with CFL of order $O(1)$ and not be too diffusive in under-resolved regions.

Before describing the tuning of constants $c_e, c_{\max}$ and the implementation of the entropy viscosity method in SFEMaNS code, we note that this method is consistent and only induces diffusion in under-resolved regions. Indeed, when using a mesh fine enough to resolve all of the scales of the flow, $|D_h(\mathbf{x}, t)|$ becomes of the same order as the consistency error. As a consequence $h(\mathbf{x})^2|D_h(\mathbf{x}, t)|$ is smaller than the consistency error and than the first order viscosity $\mathrm{c_{max}} h(\mathbf{x})|\mathbf{u}_h(\mathbf{x}, t)|$ which is of the order $O(h)$, so we can say that the entropy viscosity is a consistent method. On the other hand, if the mesh is not fine enough to resolve all the scales of the flow, the entropy viscosity is only active in under-resolved regions where $D_h \neq 0$. Eventually the entropy viscosity does not perturb the approximations in smooth regions. Moreover it adds the necessary diffusion in under-resolved regions, where energy is coming up from unresolved subgrid scales, so the energy is dissipated as in the Kolmogorov scenario.

Tuning of constants $\mathbf{c_e}$ and $\mathbf{c_{max}}$

As the couple $(\mathrm{c_e}, \mathrm{c_{max}}) = (1, \frac{1}{2})$ should induce enough diffusion for any kind of problems, a tuning is still required so the diffusion is not unnecessarily large. The idea of the tuning is to enhance a couple $(\mathrm{c_e}, \mathrm{c_{max}})$ such that our approximation remains smooth and stable over time. For a fixed problem, meaning initial/boundary conditions and body forces are fixed, the tuning is done on a coarse mesh over a hundred of time iterations by setting the kinetic Reynolds number to infinity, numerically we set $R_e = 10^{10}$. This strategy is adopted so the obtained couple is suitable for any under-resolved computations with smaller R_e. Firstly we set $\mathrm{c_e} = \infty$, so $\nu_{E,h}$ becomes a first order viscosity. Then we initialize $\mathrm{c_{max}} = \frac{1}{2}$ and diminish it till the approximation looses its regularity or stability. Once $\mathrm{c_{max}}$ is tuned, we set $\mathrm{c_e} = 1$ and repeat the same process that we use to tune $\mathrm{c_{max}}$. We note a typical range of $\mathrm{c_{max}}$ is $[0.15, 0.5]$, while $\mathrm{c_e}$ generally lies in $[0.1, 1]$. See [37] for more details.

3.2 Entropy viscosity and SFEMaNS code

As the previous section describes the theoretical frame in which the entropy viscosity method has been developed by J.-L. Guermond et al., we now focus on the use of this non-linear stabilization method with SFEMaNS code. Firstly we give details on its numerical implementation in SFEMaNS code such as the computation of the residual of the Navier-Stokes equations. In a second time, we present numerical tests to verify the consistency

of the method with manufactured solutions while its correct behavior for under-resolved simulations is checked in the next chapter on Von Kármán Sodium (VKS) and precessing cylinders problems.

3.2.1 Numerical Implementation

The implementation of the entropy viscosity method in SFEMaNS code can be splitted in two steps that we describe in the following. In a first step, the entropy viscosity is computed with the time and space discretized approximations $(\mathbf{u}^n, p^n)_n$. Then the stabilization term $-\nabla\cdot(\nu_{\mathrm{E}}\nabla\mathbf{u})$ is added in the Navier-Stokes equations weak formulation (2.2.8). In order to describe this implementation in SFEMaNS code we keep the same notation of section 2.2.2 where we defined the space of approximation $\mathbf{V}_h$ and a mesh $\mathcal{T}$ of disjoint cells K with respective diameters h_{loc}.

Residual and entropy viscosity computation

To compute the entropy viscosity defined in equation (3.1.16) we first need to compute the power of the residual $\mathbf{R}\cdot\mathbf{u}$ whose definition (3.1.13) involves time derivative and numerous nonlinear terms. Since SFEMaNS code is a hybrid spectral-finite element code, the computation of a nonlinear term requires the use of pseudo-spectral method and fast Fourier transform. To reduce the computation cost of this method we decide to compute the residual of the Navier-Stokes equations so we can later do a scalar product with $\mathbf{u}$ with fast Fourier transforms. To do so we define the residual $\mathbf{R}_{\mathrm{NS}}$ at time $t^n = \tau n$ as follows:

$$\mathbf{R}_{\mathrm{NS}}^n := \frac{\mathbf{u}^n - \mathbf{u}^{n-2}}{2\tau} - \frac{1}{R_e}\Delta\mathbf{u}^{n-1} + \nabla\times(\mathbf{u}^{*,n-1})\times\mathbf{u}^{*,n-1} + \nabla p^{n-1} - \mathbf{f}^{n-1}. \tag{3.2.1}$$

We note that second order space derivatives are not accessible in SFEMaNS code, so in practical we compute $\mathbf{R}_{\mathrm{NS}}^n$ as the solution for all $\mathbf{v}$ in $\mathbf{V}_h$, defined in section 2.2.2, of the formulation:

$$\begin{aligned}\int_\Omega \mathbf{R}_{\mathrm{NS}}^n\cdot\mathbf{v} = \int_\Omega \frac{\mathbf{u}^n - \mathbf{u}^{n-2}}{2\tau}\cdot\mathbf{v} + \frac{1}{R_e}\int_\Omega \nabla\mathbf{u}^{n-1} : \nabla\mathbf{v} - \frac{1}{R_e}\int_{\partial\Omega}(\nabla(\mathbf{u}^{n-1})\cdot\mathbf{n})\cdot\mathbf{v} \\ + \int_\Omega [(\nabla\times\mathbf{u}^{*,n-1})\times\mathbf{u}^{*,n-1} + \nabla p^{n-1} - \mathbf{f}^{n-1}]\cdot\mathbf{v},\end{aligned} \tag{3.2.2}$$

with $\mathbf{n}$ the outward normal vector of the surface $\partial\Omega$ and where we integrate by parts the term $(\Delta\mathbf{u}^{n-1})\cdot\mathbf{v}$ to remove the second order space derivatives. Eventually we define the entropy viscosity on a mesh cell K as follows:

$$\nu_{\mathrm{E|K}}^n := \min\left(c_{\max}h_{\mathrm{loc}}\|\mathbf{u}^{n-1}\|_{L^\infty(K)}, c_{\mathrm{e}}h_{\mathrm{loc}}^2\frac{\|\mathbf{R}_{\mathrm{NS}}^n\cdot\mathbf{u}^{n-1}\|_{L^\infty(K)}}{\|\mathbf{u}^{n-1}\|_{L^2(\Omega)}^2}\right) \tag{3.2.3}$$

where we normalize the power of the residual by $\|\mathbf{u}^{n-1}\|_{L^2(\Omega)}^2$.

Remark 3.2.1. To use the pseudo-penalization technique described in section 2.4, so the presence of solid obstacle can be taken into account, one needs to change the definition of the residual $\mathbf{R}_{\mathrm{NS}}$. Indeed the entropy viscosity method is designed to add the necessary diffusion such that the power of the residual is negative. Since the equations solved in the solid are no more the Navier-Stokes equations, when using the pseudo-penalization technique we modify definition (3.2.1) as follows:

$$\mathbf{R}_{\mathrm{NS}}^n := \frac{\mathbf{u}^n - \mathbf{u}^{n-2}}{2\tau} - \frac{1}{R_e}\Delta\mathbf{u}^{n-1} + \nabla p^{n-1} + \chi^{n-1}\left(\nabla\times(\mathbf{u}^{*,n-1})\times\mathbf{u}^{*,n-1} - \mathbf{f}^{n-1}\right), \tag{3.2.4}$$

where χ is the penalty function equal to 1 in the fluid and 0 in the solid.

Explicit treatment and resulting weak formulation

The entropy viscosity method consists of adding the term $-\nabla\cdot(\nu_{\mathrm{E}}\nabla\mathbf{u})$ in the left hand side of the Navier- Stokes so the implicit treatment of this stabilization term would induce a time dependent algebra. In order to keep a time independent algebra, so the stiffness matrix only needs to be assembled and preconditioned at initialization which reduces greatly the time of computation, we decide to explicit the stabilization term $-\nabla\cdot(\nu_{\mathrm{E}}\nabla\mathbf{u})$ with a first order time extrapolation. Eventually we approximate $\mathbf{u}^{n+1}$ solution of the following formulation for all $\mathbf{v}$ in $\mathbf{V}_{h,0}$:

$$\int_\Omega \frac{3\mathbf{u}^{n+1}}{2\tau}\cdot\mathbf{v} + \frac{1}{R_e}\int_\Omega \nabla\mathbf{u}^{n+1} : \nabla\mathbf{v} = \int_\Omega \left(\frac{4\mathbf{u}^n - \mathbf{u}^{n-1}}{2\tau} - \nabla p^n + \nabla(\frac{4\psi^n - \psi^{n-1}}{3})\right)\cdot\mathbf{v} + \int_\Omega \left(-(\nabla\times\mathbf{u}^{*,n+1})\times\mathbf{u}^{*,n+1} + \mathbf{f}^{n+1}\right)\cdot\mathbf{v} - \int_\Omega \nu_{\mathrm{E}}^n\nabla(\mathbf{u}^n) : \nabla\mathbf{v}, \quad (3.2.5)$$

with $\mathbf{u}^{n+1}$ matching the Dirichlet boundary conditions of the problem. The next steps of the prediction-correction algorithm for the Navier-Stokes equations described in section 2.2.2, see equations (2.2.9)–(2.2.11), remain the same.

Remark 3.2.2. Originally the explicit treatment of entropy viscosity was facilitated by adding a stabilization term of the form $-\nabla\cdot\left(c_1 h_{\mathrm{loc}}\nabla(\mathbf{u}^{n+1} - 2\mathbf{u}^n + \mathbf{u}^{n-1})\right)$ in the left hand side of equation (3.2.5) where c_1 was a tunable constant sastisfying $c_1 \geq c_{\max}\|\mathbf{u}\|_{L^\infty(\Omega)}$. However, many numerical tests and applications led us to note that the algorithm always remained stable, under a CFL condition, even when setting $c_1 = 0$. To avoid computing extra terms and adding error to the approximation, we decide to disable this term by approximating equation (3.2.5). We note that no theoretical demonstration of the stability of the above scheme has been given. Till now this method has only been proved stable for the case of the Euler equation in [13], theoretical proof of its stability when applied to the Navier-Stokes equations is still under investigation.

3.2.2 Numerical tests

To attest the correct behavior of the entropy viscosity as it is implemented in SFEMaNS code, we first propose to describe a test that enhances its consistency property. This test compares the error between computations with and without entropy viscosity so we can check that we get the same order of convergence. Next we propose to describe the action of the entropy viscosity with under resolved simulations by quoting recent pressed articles and studies led in this following chapter of this manuscript.

Consistency property

The consistency of the entropy viscosity with respect to the numerical scheme order of convergence in space and time is investigated with manufactured solutions to check its correct behavior. This test consists in approximating on the domain $\Omega = \{(r,\theta,z) \mid 0 \leq r \leq 1; 0 \leq \theta \leq 2\pi; 0 \leq z \leq 1\}$ (see figure 2.2) the functions:

$$\begin{cases} u_r(r,\theta,z,t) = \left((r^2z^3 - 3r^3z^2)\cos(\theta) - (r^2z^3 + 3r^3z^2)\sin(\theta)\right)\cos(t), \\ u_\theta(r,\theta,z,t) = 3(r^3z^2 - r^2z^3)(\cos(\theta) + \sin(\theta))\cos(t), \\ u_z(r,\theta,z,t) = (3r^2z^3\cos(\theta) + 5r^2z^3\sin(\theta))\cos(t), \\ p(r,\theta,z,t) = rz(\cos(\theta) + \sin(\theta))\sin(t), \end{cases} \quad (3.2.6)$$

solutions of the equations (3.2.5), (2.2.9) and (2.2.11) with Dirichlet boundary conditions for the velocity field. An illustration of the meridian finite element mesh can be found in figure 2.2 while the velocity and pressure fields at final time are represented in figures 3.1a and 3.1b. We also set $R_e = 1$, $c_1 = 0$, $c_e = 0.2$ and $c_{\max} = 0.125$. The source term $\mathbf{f}$ is computed accordingly and so does not take into account the viscosity entropy, so we can write:

$$\begin{aligned} f_r := &-\left((r^2z^3 - 3r^3z^2)\cos(\theta) - (r^2z^3 + 3r^3z^2)\sin(\theta)\right)\sin(t) + z(\cos(\theta) + \sin(\theta))\sin(t) \\ &- \frac{1}{R_e}\left((-4z^3 - 27rz^26r^2z - 6r^3)\cos(\theta) + (4z^3 - 27rz^2 - 6r^2z - 6r^3)\sin(\theta)\right)\cos(t) \\ &+ (3r^4z^6 - 61r^3z^6 - 3r^5z^5 + 60r^4z^5 - 60r^5z^4)\cos(t)^2 + (13r^3z^6 + 9r^5z^5 + 12r^4z^5 - 9r^6z^4 \\ &+ 6r^5z^4)\cos(2\theta)\cos(t)^2 + (3r^4z^6 - 57r^3z^6 - 3r^5z^5 + 66r^4z^5 - 60r^5z^4)\sin(2\theta)\cos(t)^2, \end{aligned} \tag{3.2.7}$$

$$\begin{aligned} f_\theta := &-3(r^3z^2 - r^2z^3)(\cos(\theta) + \sin(\theta))\sin(t) + z(-\sin(\theta) + \cos(\theta))\sin(t) \\ &- \frac{1}{R_e}\left((-8z^3 + 15rz^2 - 18r^2z + 6r^3)\cos(\theta) + (-8z^3 + 27rz^2 - 18r^2z + 6r^3)\sin(\theta)\right)\cos(t) \\ &- (9r^4z^5 + 12r^5z^4)\cos(t)^2 + (r^4z^6 - 24r^3z^6 + 21r^4z^5 - 9r^6z^4 - 6r^5z^4)\cos(2\theta)\cos(t)^2 \\ &- (8r^3z^6 + 6r^5z^5 + 9r^4z^5 + 12r^5z^4)\sin(2\theta)\cos(t)^2, \end{aligned} \tag{3.2.8}$$

$$\begin{aligned} f_z := &-(3r^2z^3\cos(\theta) + 5r^2z^3\sin(\theta))\sin(t) + r(\cos(\theta) + \sin(\theta))\sin(t) \\ &-\frac{1}{R_e}\left((9z^3 + 18r^2z)\cos(\theta) + (15z^3 + 30r^2z)\sin(\theta)\right)\cos(t) + (5r^3z^6 - 51r^4z^5 + 45r^5z^4 + 36r^6z^3)\cos(t)^2 \\ &+(-4r^3z^6 + 18r^4z^5 + 15r^5z^4)\cos(2\theta)\cos(t)^2 + (-r^3z^6 - 45r^4z^5 + 45r^5z^4 - 36r^6z^3)\sin(2\theta)\cos(t)^2. \end{aligned} \tag{3.2.9}$$

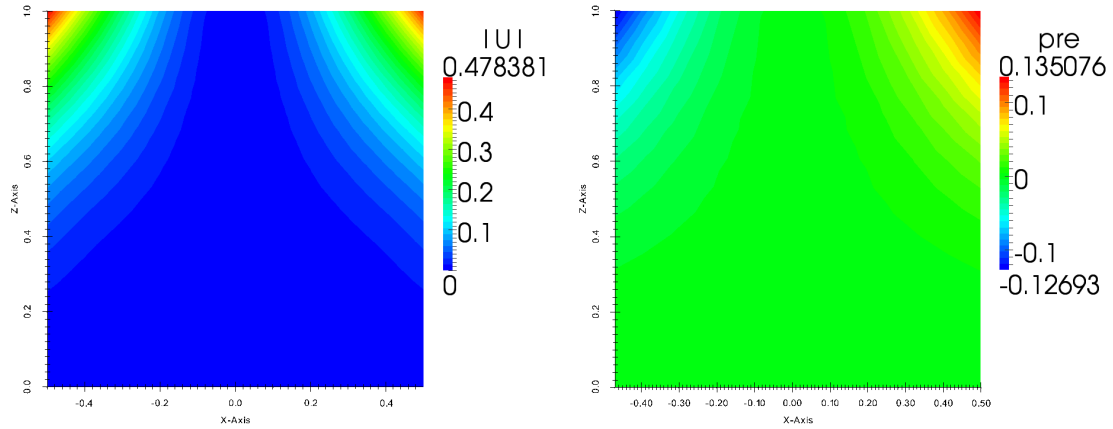

(a) Final velocity field

(b) Final pressure

Figure 3.1: Profile of the velocity field and pressure magnitude in the meridian plane $\theta = 0$ and $\theta = \pi$ at $t_{\text{end}} = 1$.

The convergence of the method is studied with four different meshes of typical mesh-size $h = 0.1$, $h = 0.05$, $h = 0.025$, and 0.0125 in $\mathbb{P}_1$. The time steps tested are $\tau = 0.01$, $\tau = 0.005$, $\tau = 0.0025$, $\tau = 0.00125$ and $\tau = 0.000625$. The error on the velocity and the

error of the pressure in $\mathbf{L}^2$-norm at the final time $t = 1$ are reported in tables 3.1 and 3.2. Since all the scales of the flow are resolved we expect the entropy viscosity simulations, denoted as LES, to behave like the simulations without entropy viscosity, denoted as DNS. As a consequence the errors on velocity and pressure should be similar, as shown by the two tables 3.1 and 3.2. This confirms the consistency of the entropy viscosity method. we notice that the velocity and pressure converge in time with second order by looking at the last two lines of these tables. We just note that the first time step $\tau = 0.01$ may be too large in respect of the mesh size $h = 0.0125$ and that the error on the pressure is dominated by a space error for $\tau = 6.25 \times 10^{-4}$. In addition the convergence with space for $\tau = 6.25 \times 10^{-4}$ is displayed in figure 3.2 where the theoretical orders of space convergence, 3 for the velocity and 2 for the pressure, are also represented. We deduce from this figure that we recover the theoretical order of convergence for both velocity and pressure. We note the rising of the error on the velocity is due to a time error which is in agreement with previous results on the time convergence of the velocity.

It results from this numerical test that LES computations give nearly the same result as DNS computations and that the theoretical orders of convergence in space for $\mathbf{u}$ and p are recovered. We can conclude that the entropy viscosity method is consistent with respect to the numerical scheme implemented in SFEMaNS code.

h \ τ	0.01		0.005		0.0025		0.00125		0.000625	
	DNS	LES	DNS	LES	DNS	LES	DNS	LES	DNS	LES
0.1	1.85E-5	2.02E-5	1.70E-5	1.83E-5	1.70E-5	1.82E-5	1.71E-5	1.82E-5	1.71E-5	1.82E-5
0.05	9.67E-6	1.00E-5	3.16E-6	3.68E-6	1.59E-6	2.22E-6	1.43E-6	2.03E-6	1.44E-6	2.01E-6
0.025	9.72E-6	9.74E-6	3.00E-6	3.02E-6	8.71E-7	9.02E-7	2.65E-7	3.10E-7	1.41E-7	1.92E-7
0.0125	9.73E-6	9.73E-6	3.00E-6	3.00E-6	8.73E-7	8.75E-7	2.43E-7	2.45E-7	6.59E-8	6.83E-8

Table 3.1: $\mathbf{L}^2$-norm of the error on the velocity at time 1.

h \ τ	0.01		0.005		0.0025		0.00125		0.000625	
	DNS	LES	DNS	LES	DNS	LES	DNS	LES	DNS	LES
0.1	6.31E-4	1.16E-3	6.63E-4	1.10E-3	6.79E-4	1.09E-3	6.84E-4	1.07E-3	6.85E-4	1.07E-3
0.05	1.60E-4	3.27E-4	9.90E-5	2.50E-4	1.08E-4	2.31E-4	1.14E-4	2.26E-4	1.16E-4	2.25E-4
0.025	1.77E-4	1.88E-4	5.29E-5	6.74E-5	2.09E-5	3.56E-5	2.21E-5	3.16E-5	2.41E-5	3.14E-5
0.0125	1.89E-4	1.89E-4	6.14E-5	6.23E-5	1.77E-5	1.88E-5	5.39E-6	6.53E-6	4.95E-6	5.45E-6

Table 3.2: $\mathbf{L}^2$-norm of the error on the pressure at time 1.

Action in the context of under resolved computations

Originally the entropy viscosity method was tested in [36, 37, 38] with Burgers and Euler equations for problems involving shocks. It allowed to enhance the correct behavior of this method to approximate solutions that present singularities. A study of its action for approximating the Navier-Stokes equations has been recently proposed by Guermond et al [34]. A DNS, entropy viscosity and Smagorinsky model approaches are used to approximate in a periodic box the solution of the Navier-Stokes equations with initial data $u_x = \cos(8\pi x)\sin(8\pi y)$, $u_y = -\sin(8\pi x)\cos(8\pi y)$ and $u_z = 0$. The entropy viscosity is

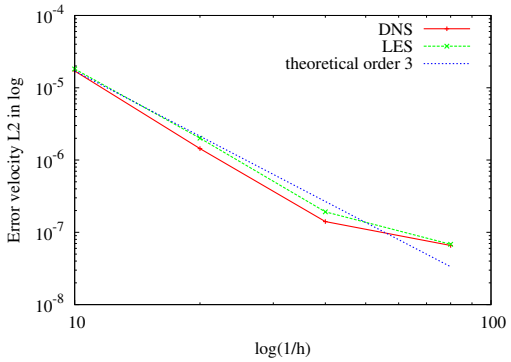

(a) Space convergence on velocity

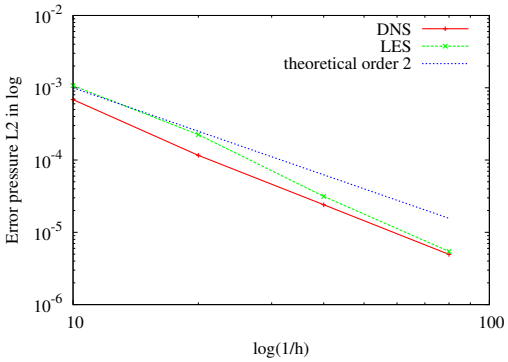

(b) Space convergence on pressure

Figure 3.2: Evolution in log scale of $\mathbf{L}^2$ error of velocity and pressure with mesh size h for DNS and LES computations with fixed time step $\tau = 6,25.10^{-4}$

shown to be consistent. Moreover when fixing a space resolution, it scales better than the Smagorinsky model with respect to a well resolved DNS.

In that frame the following chapter, see section 4.1.4, provides comparisons between DNS and LES computations of a Von Kármán problem. The set-up consists of driving an incompressible fluid in a cylindrical container with counter-rotating lids. These tests are done with $R_e \in \{500, 1000, 2500\}$ and enhance the correct behavior of the entropy viscosity method. For example we give comparisons between under resolved DNS and entropy viscosity computations with a full resolved DNS. It shows that the entropy viscosity results match the ones of the full resolved DNS and even allows to grasp the bifurcation in the energy spectrum that under resolved DNS cannot catch. Moreover, we also compare DNS results and under resolved computations with entropy viscosity ones for a cylinder precessing problem with $R_e = 4000$. We refer to chapter 4 for more details on these studies.

3.2.3 Outlook

The implementation of the entropy viscosity method in SFEMaNS code now allows us to consider studying problems that DNS could not approximate due to the computations of the smallest scales of the flow and the resulting high computational cost. Thanks to this, we firstly intend to use the entropy viscosity method as a LES method to approximate the experimental set-ups of the Von Kármán Sodium (VKS) experiment and of precessing cylinders. This study is done in the following chapter and falls within the scope of previous studies performed by J.-L. Guermond and C. Nore. On one hand they investigated magnetodynamics of the VKS experiment with *prescibed velocity fields* in simplified geometries [28, 29, 35]. On the other hand they studied the generation of magnetic field in a precessing cylinder for kinetic Reynolds numbers up to 1200 [83]. In this frame, chapter 4 first presents hydrodynamic numerical studies of a VKS set-up that is currently experimented in CEA Saclay by the team of B. Dubrulle. Thanks to the pseudo-penalization technique of Pasquetti et al., described in section 2.4, we can now represent correctly the rotating impellers that drive the fluid. Moreover the use of the entropy viscosity method enables us to study a larger range of kinetic Reynolds numbers so more comparisons with ongoing experiments in CEA Saclay can be done in the future. The entropy viscosity is also used to study hydrodynamic set-up of a precessing cylinder that will be experimented in the Dresden Sodium facility (DRESDYN) by the team of F. Stefani in the coming years.

The study is performed up to a kinetic Reynolds number of 15000. Implications in view of the generation of the magnetic field are discussed. We also study another way of forcing the precession than the one used in Dresden coming experiment and we compare the benefit of two precessing driven forces.

To conclude we note that this chapter focuses on introducing the entropy viscosity method as a LES method to approximate problems with large R_e, however we remind that the main idea of the method is to add the appropriate diffusion such that the approximations do not produce energy in regions where they present large gradients and may be under-resolved. This remark finds echo in chapter 5 where we approximate multiphase flow problems with continuous density and viscosity that may present large gradients at the interface between two fluids. While we combine a level set method and a momentum based approximation of the Navier-Stokes equations introduced in [41], the entropy viscosity is used to stabilize both mass and momentum equations. This stabilization technique is inspired by the one presented in [41] that states that stabilizing the mass and momentum equations with the same viscosity helps the stability of the global algorithm. Since the entropy viscosity is based on a residual of the momentum equation, that also contains information of the mass equation, we believe it is a good candidate to stabilize both equations. The corect behavior of the method is confirmed with numerous numerical tests involving gravity, rotational, surface tension and magnetic forces. We refer to chapter 5 for more details on the use of entropy viscosity in the frame of multiphase flow computations.

Large Eddy Simulation with entropy viscosity

In answer to the previous chapter, we propose to validate the entropy viscosity method as a LES method on two experimental configurations. First we intensively use the entropy viscosity method, often denoted as LES, to study the hydrodynamic regime of a Von Kármán Sodium (VKS) set up with under resolved meshes. While on going experiments in CEA Saclay may provide future comparisons with numerics for a large range of R_e, we give comparisons between DNS and LES results at moderate Reynolds numbers (smaller than 2500) to enhance the correct behavior of the entropy viscosity. Next we present, in the form of an article in preparation, a study on two different set ups of precessing cylinders. This method is validated with DNS comparisons at $R_e = 4000$ before being used to extend the range of kinetic Reynolds numbers studied of a set up that will be soon experimented in Dresden [105]. As precession may take part in the Earth dynamo action (conversion of kinetic energy into magnetic energy), a MHD study with DNS of the two set ups is also given to enhance the most favourable one to the generation of a magnetic field.

Contents

4.1 Hydrodynamic study of a Von Kármán Sodium set-up

The flow produced in a cylindrical cavity driven by the rotation of the upper and lower lids has long been the focus of experimental, numerical and theoretical investigations during the past decades. The original problem, consisting of the analysis of the flow of a viscous fluid over an infinite rotating disk, was studied by von Kármán [54] in 1921. While Batchelor [9] in 1951 was the first one to consider an upper rotating disk, these types of flow were called 'von Kármán swirling flows' in 1987 by Zandbergen and Dijkstra [112] in reference of Von Kármán studies. These flows occur frequently in geophysical and in industrial applications involving impellers. As we plan to study a specific set-up, that is currently the subject of experiments in CEA Saclay by the team of B. Dubrulle, we do not present exhaustively the vast literature on von Kármán flows but rather focus on relevant articles that led to the configuration we study.

The flow depends strongly on the height-to-radius aspect ratio (H/R_{cyl} with H the distance between the lids and R_{cyl} the radius of the cylinder), on the ratio of the angular velocities of the upper and lower lids as well as on the geometry of the lids (disks or impellers). Here we will focus on order one aspect ratios and on exactly counter-rotating lids. Using flat smooth disks, Nore et al. [87, 86, 84] carried out both experimentally and numerically a study of the symmetry breakings and transitions. They introduced the R_π symmetry which is the symmetry by rotation of π about any equatorial axis and found for a cylinder of height-to-radius ratio of 2 a dynamical system involving the competition of two modes. However, flat disks can only drive the flow through viscous boundary layers. To reach high kinetic Reynolds numbers, the lids are made of disks fitted with blades (called impellers) and drive the flow inertially: turbulence in such configurations has been the subject of numerous experimental investigations. Many teams in France have used different working fluids such as water (Cadot et al [16]) or helium (Saint-Michel et al [100]). Liquid Sodium was used by the Von Kármán Sodium team in view of studying the generation of magnetic field by dynamo effect (for example see Monchaux et al [80]). Most impellers dealt with straight blades until the VKS team (Bourgoin et al. [14], Ravelet [94]) intensively studied the influence of the geometry of the impeller (called TM for Turbine Métallique, meaning Metal Impeller in French) on the flow properties: they varied the curvature of the blades, the number of blades, their height, the disk radius and the sense of rotation. They called the unscooping sense of rotation (the fluid is pushed by the convex side of the blade) the (+) sense while the scooping sense (the fluid is pushed by the concave side of the blade) was designated as the (-) sense.

As a VKS set-up with specific TM has demonstrated the generation of magnetic field [80], the study of the hydrodynamic regime with such impellers may help to determine a favourable set up to the generation of a magnetic field. In that frame Ravelet et al. [95] performed a thorough investigation of the transition from laminar flow to fully developed turbulence in the two senses of rotation for curved impellers called TM60 (16 blades with a 72^o degree of curvature, a disk radius 0.925 of the cylinder radius and a blade height 0.2 of the cylinder radius). They used visualization, temporal velocity signals and torque measurements to characterize the dynamics. They showed that the flows are similar for small Reynolds numbers but are very different for high Reynolds numbers: the (-) forcing leads to multiple states (with one or two recirculation cells) while the (+) forcing shows only one state demanding less torque. Kreuzahler et al [60] numerically studied this set up with TM28 impellers (8 blades with a 64^o degree of curvature, a disk radius 0.9 of

the cylinder radius and a blade height 0.2 of the cylinder radius) rotating with both senses (+) and (-) and also considered straight blades with $R_e = 2430$ (2700 with SFEMaNS nondimensionalization). Moreover they extended their study of the rotating sense (+) up to $R_e = 4860$ (5400 with SFEMaNS nondimensionalization). While comparisons with water experiment data give good agreement and allow to validate their numerical approach, they also show that the mean flow structures are very similar for $2430 \leq R_e \leq 4860$ with rotating sense (+). Unlike experiment data, e.g. Ravelet et al [95], they can also get information on the velocity in the blade area. It allows them to emphasize different vortex topology around the blade area between the sense of rotation (+), (-) and rotating straight blades at a moderate Reynolds number $R_e = 2400$.

In the following we propose to simulate the flow driven by other impellers (TM87, see figure 4.3) for moderate Reynolds numbers as it is currently performed in CEA Saclay (B. Dubrulle et al.). As the experiments can involve very large Reynolds numbers we plan to use the entropy viscosity as a LES method, described in chapter 3, to extend the range of Reynolds numbers we can study with SFEMaNS code. To describe this hydrodynamic study, the followings sections give information on the experimental set up and the numerical methods used to approximate the problem with SFEMaNS code. Then we study the problem for Reynolds numbers smaller than 2500 with DNS simulations. After providing comparisons between DNS and LES simulations for $R_e \in \{500, 1000, 2500\}$, we present numerical results obtained at Reynolds numbers 5000 with the entropy viscosity method.

4.1.1 Experimental set-up

In this section we give information of the experimental set-up (TM87) currently used in CEA Saclay by B. Dubrulle et al. that we plan to study in the following. Before giving qualitative information on this set-up, we give general information on a VKS set up. Such a configuration consists of two counter rotating impellers (disk and blades) embedded in a cylindrical container filled with fluid. A 3D representation of this configuration is displayed in figure 4.1a. We note the disks are not directly into contact with the top and bottom walls and are indeed embedded in the fluid. Moreover the impellers have a hole in their center of radius R_{int}, meaning that fluid is present in the area $0 \leq r \leq R_{\text{int}}$. For simplification we do not consider, and so we do not represent, the shafts that connect the brushless motors driving the impellers in rotation. To get a better idea of the shape and the definition of the blades, we display in figure 4.1b a 2D representation of the bottom blades with an angle of curvature α supported by a disk of radius R_b viewed from top. We note the blades can be generated as a section of a circle of radius R_g called gauss radius which is represented in figure 4.1b.

The set-up studied in this section and by the team of B. Dubrulle in CEA Saclay, referred to as TM87, uses a cylindrical container of radius $R_{\text{cyl}} = 100$mm and of heigh $H = 248$mm. The impellers are composed of two disks each supporting 8 blades. The disks have a radius $R_b = 92.5$mm, an interior radius $R_{\text{int}} = 10$mm and thickness of 12mm. The blades have an angle of curvature equal to 72^o, a height of 20mm and a thickness of 2.5mm. Eventually the distance between the disks is set to 180mm as in the TM28 that are numerically studied in [60]. As a consequence the respective disks and the top-bottom walls of the cylinder are spaced by a layer of fluid of 22mm height. While we display a vertical slice of this set up in figure 4.2, which summarizes the previous characteristics

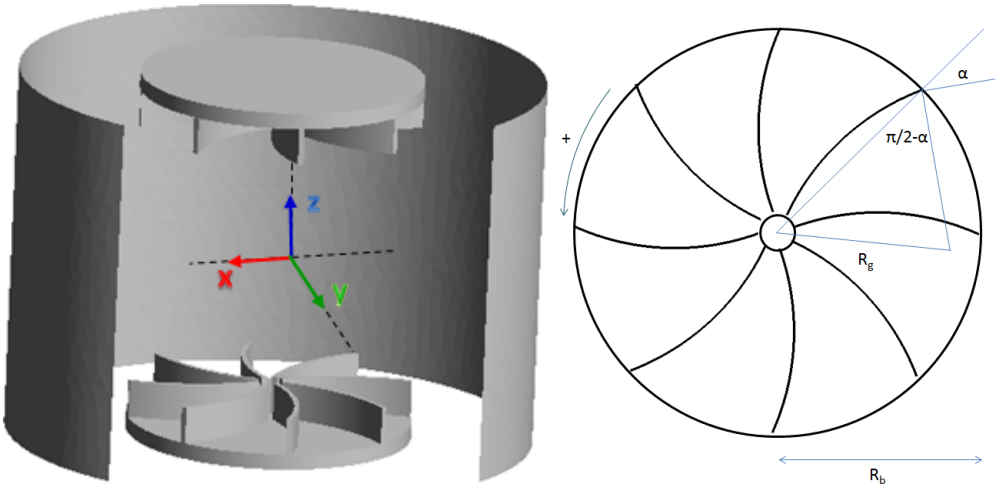

(a) 3D representation of a VKS set-up (b) 2D representation of the bottom blades.

Figure 4.1: 3D and 2D representations of a VKS set up for an arbitrary angle of curvature α. The sense of rotation studied (+) is displayed in (b). (both figures courtesy of H. Zaidi)

lengths of the problem, we refer to the following section and figure 4.3 for a 3D visualisation of the impellers and a discussion on the required space geometry to represent correctly the blades. In order to compute relevant quantities that allow comparisons with experiments,

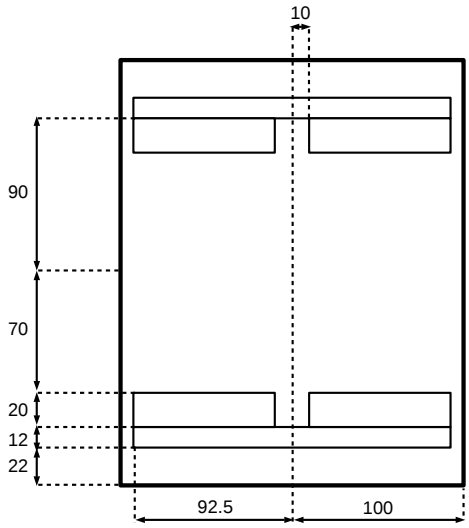

Figure 4.2: 2D representation (vertical slice) of the VKS set up with TM87. Length unit is the millimeter.

we note experimentalists can characterize the dynamics by performing measurements of the velocity field with Laser Doppler Velocimetry (LDV). This technique allows to get local information on components of the velocity field while the mean velocity field can also be visualized in meridian section. Thanks to this technique, experimentalists get information on the mean poloidal and toroidal fields but also on the root mean square velocity, denoted U_{RMS}. Moreover the torque can be measured by recording the current injected to the bruthless motors. We refer to [94, 95] for more details on the technique used to characterize the dynamics in the frame of VKS laboratory experiments.

4.1.2 Numerical approximation

We want to investigate the hydrodynamic regime of the above experimental set-up. The reference length L_{ref} is set to R_{cyl} so the domain of computation is $\Omega = \{(r,\theta,z) \in [0,1]\times[0,2\pi)\times[-1.22,1.22]\}$. The cylinder Ω can be split into a solid domain Ω_{solid}, composed of the rotating impellers, and a fluid domain Ω_{fluid} that are both time dependent due to the impellers rotation. The resulting main difficulty is to approximate the Navier-Stokes equations in a time and θ dependent domain while forcing the velocity in the solid domain Ω_{solid} to be a solid body rotation. On the other hand the study of the problem for large Reynolds numbers cannot be performed with Direct Numerical Simulation, due to limited computational resources, and requires the use of a stabilization technique so the action of the unresolved small scales of the flow can be represented.

In the following we describe the numerical methods implemented in SFEMaNS code to overcome these difficulties and present the time discretized algorithm used to approximate the problem. In a second time we give general information on the space discretization in SFEMaNS code and discuss the minimum space resolution required to correctly represent the problem. Eventually we introduce the quantities of interest, such as the kinetic energy or torque, that we compute to study the hydrodynamic regime of this experimental set-up.

Time discretized algorithm

The experimental set-up is approximated by combining a prediction-correction method of J.-L. Guermond et al [43] and a pseudo-penalization technique of R. Pasquetti et al [89]. These methods allow respectively to approximate the solutions of the Navier-Stokes equations in the fluid domain Ω_{fluid} and to penalize the velocity in the solid domain Ω_{solid} so it matches the velocity of the impeller. These methods led to the introduction of pressure increment ψ to split the time marching of the velocity-pressure couple and a penalty function χ defined by:

$$\chi(r,\theta,z,t) = \begin{cases} 1 & \text{if } (r,\theta,z) \in \Omega_{\text{fluid}} \\ 0 & \text{if } (r,\theta,z) \in \Omega_{\text{solid}}. \end{cases} \tag{4.1.1}$$

While we refer to sections 2.2.2 and 2.4.1 for a thorough description of these methods, we write the resulting time discretized algorithm for completeness. We introduce a time step τ and denote by f^n the approximation of $f(n\tau)$, the velocity is then updated by solving the following scheme:

$$\begin{aligned} \frac{3\mathbf{u}^{n+1}}{2\tau} - \frac{1}{R_e}\Delta\mathbf{u}^{n+1} = -\nabla p^n + \chi^{n+1}\left(\frac{4\mathbf{u}^n - \mathbf{u}^{n-1}}{2\tau} - \nabla(\frac{4\psi^n - \psi^{n-1}}{3})\right) \\ + \chi^{n+1}\left(-(\nabla\times\mathbf{u}^{*,n+1})\times\mathbf{u}^{*,n+1} + \mathbf{f}^{n+1}\right) + (1-\chi^{n+1})\frac{3\mathbf{u}^{n+1}_{\text{obst}}}{2\tau}, \end{aligned} \tag{4.1.2}$$

where $R_e = \frac{U_{\text{ref}}L_{\text{ref}}}{\nu}$ with ν the viscosity of the fluid, $U_{\text{ref}} = R_{\text{cyl}}\omega$ the angular velocity of the impellers and $L_{\text{ref}} = R_{\text{cyl}}$. Moreover we set $\mathbf{u}^{*,n+1} = 2\mathbf{u}^n - \mathbf{u}^{n-1}$ and $\mathbf{u}_{\text{obs}}$ represents the velocity inside the disk and blades defined for all $n \geq 0$ by:

$$\mathbf{u}^n_{\text{obs}}(r,\theta,z) = \begin{cases} -r\mathbf{e}_\theta & \text{if } z > 0, \\ r\mathbf{e}_\theta & \text{if } z \leq 0. \end{cases} \tag{4.1.3}$$

On the other hand the increment of pressure ψ is solution of the following Poisson problem:

$$-\Delta\psi^{n+1} = \frac{3}{2\tau}\nabla\cdot\mathbf{u}^{n+1}, \tag{4.1.4}$$

so the pressure can be updated as follows:

$$p^{n+1} = p^n + \psi^{n+1} - \frac{1}{R_e}\nabla\cdot\mathbf{u}^{n+1}. \tag{4.1.5}$$

We note that the velocity and the pressure are solutions of the Navier-Stokes equations when $\chi = 1$, meaning in the fluid domain. On the other hand in Ω_{solid} the pressure is not relevant and is determined by solving a Poisson problem while the velocity field satisfies $\mathbf{u} = \mathbf{u}_{\text{obs}} + O\left(\frac{\tau}{R_e}\right)$. Consequently the resulting algorithm is of order 1 in time.

Eventually we use a nonlinear stabilization method called entropy viscosity, introduced by J.-L. Guermond et al [36, 37] and described in chapter 3, to approximate solutions of the problem with large R_e. The entropy viscosity method consists in adding the term $-\nabla\cdot(\nu_{\text{E}}^n\nabla\mathbf{u}^n)$ in the left hand side of equation (4.1.2) where we define the entropy viscosity ν_{E} on a mesh cell K as follows:

$$\nu_{\text{E|K}}^n := \min\left(c_{\max}h_{\text{loc}}\|\mathbf{u}^{n-1}\|_{L^\infty(K)}, c_{\text{e}}h_{\text{loc}}^2\frac{\|\mathbf{R}_{\text{NS}}^n\cdot\mathbf{u}^{n-1}\|_{L^\infty(K)}}{\|\mathbf{u}^{n-1}\|_{L^2(\Omega)}}\right), \tag{4.1.6}$$

with $c_{\max}$, c_{e} tunable constants and $\mathbf{R}_{\text{NS}}$ the residual of Navier-Stokes defined by:

$$\mathbf{R}_{\text{NS}}^n := \frac{\mathbf{u}^n - \mathbf{u}^{n-2}}{2\tau} - \frac{1}{R_e}\Delta\mathbf{u}^{n-1} + \nabla p^{n-1} + \chi^{n-1}\left(\nabla\times(\mathbf{u}^{*,n-1})\times\mathbf{u}^{*,n-1} - \mathbf{f}^{n-1}\right). \tag{4.1.7}$$

Thanks to its definition the entropy viscosity is smaller than the order of consistency of the method in regions where the solution is smooth and well resolved and does not perturb the approximation. On the other hand in regions where the solution is not well approximated due to the presence of large gradients that cannot be represented by the coarse mesh, the entropy viscosity adds a diffusion proportional to the unbalance in the energy equation so the resulting approximation dissipates energy. We refer to previous chapter 3 for details on theory and numerical implementation in SFEMaNS code of this nonlinear stabilization method.

Space discretization and solid representation

SFEMaNS code uses a hybrid spatial discretization which involves spectral and finite elements. A full description of its spatial discretization and the resulting weak formulation of the Navier-Stokes equations is given in section 2.2.2 and in [33]. In a nutshell we use a Fourier decomposition in the azimuthal direction so the problem can be approximated independently, modulo the computations of nonlinear terms, for each Fourier mode in a meridian plane with Taylor-Hood Lagrange elements $\mathbb{P}_1$-$\mathbb{P}_2$.

A proper representation of the impellers, and so their actions, requires to use a refined grid around them. Indeed the thickness of the blades is equal to 2.5% of the radius of the cylinder set to 1. As a consequence all numerical computations reported in this study use a mesh size smaller than 0.01 in $\mathbb{P}_1$ (so 5.10^{-3} for the velocity). Moreover the strong azimuthal dependency of the problem, due to the presence of 8 blades rotating in the azimuthal direction, leads us to approximate the problem with at least 64 Fourier modes. To justify this choice figure 4.3 displays the shape of the bottom impellers, for mesh sizes $h_{\text{imp}} = 0.04$, $h_{\text{imp}} = 0.01$ in $\mathbb{P}_1$ around the blades and with 32 to 64 Fourier modes. It shows off the necessity to use more than 32 Fourier modes as the resulting blades in figures 4.3a and 4.3c are not even in one piece. The use of a mesh size $h = 0.01$ around the impellers is motivated so their shape is regular enough from the interior to lateral boundaries of the disk.

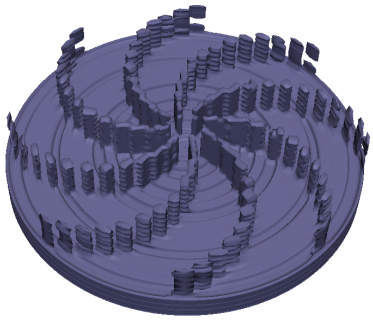

(a) 32 Fourier modes and $h_{\text{imp}} = 0.025$ in $\mathbb{P}_1$

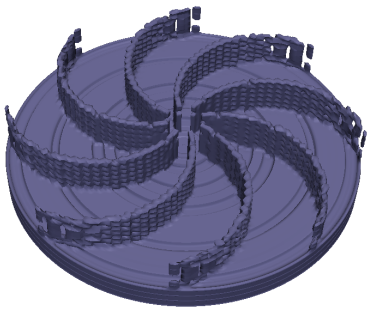

(b) 64 Fourier modes and $h_{\text{imp}} = 0.025$ in $\mathbb{P}_1$

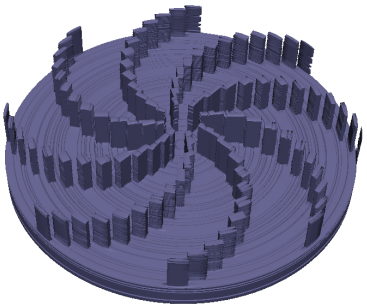

(c) 32 Fourier modes and $h_{\text{imp}} = 0.01$ in $\mathbb{P}_1$

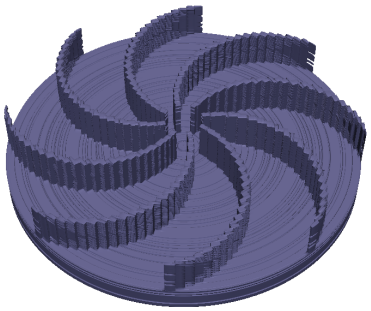

(d) 64 Fourier modes and $h_{\text{imp}} = 0.01$ in $\mathbb{P}_1$

Figure 4.3: Representation of the bottom impeller for different spatial resolutions

Eventually we end up using 64 Fourier modes and two different meridional meshes of mesh size equal to 0.01 in $\mathbb{P}_1$ near the blades and of respective sizes 0.04 and 0.02 in $\mathbb{P}_1$ near the boundaries of the cylinder and the plane $z = 0$. The refined mesh is used to approximate the solutions for Reynolds number in $[500, 2500]$ with DNS computations while the coarser mesh is used for DNS computations with $R_e \leq 208$ and LES computations with $R_e \geq 500$.

Quantities of interest

In addition to representations of the mean or instantaneous components of the velocity field, we also propose to characterize the structure of the flow by computing various time averaged physical quantities. For that purpose we define the notion of the time average $\overline{f}$ of a quantity f as follows:

$$\overline{f} = \frac{1}{n} \sum_{1 \leq m \leq n} f^m, \tag{4.1.8}$$

where f^m is the approximation of f at time $t^m = m\tau$ with τ the time step. It allows us to compute the time average of the kinetic energy E and of an indicator of the fluctuation level δ that are respectively defined as follows:

$$E = \frac{1}{2}\|\mathbf{u}\|_{L^2(\Omega)}, \quad \delta(\mathbf{u}) = \frac{\|\mathbf{u}\|^2_{L^2(\Omega)}}{\|\overline{\mathbf{u}}\|^2_{L^2(\Omega)}}. \tag{4.1.9}$$

As these quantities may not be accessible to experimentalists, we also propose to compute five other quantities that will allow future comparisons between experimental and numerical results. First we introduce the poloidal and toroidal components, respectively denoted by

$P(\mathbf{u})$ and $T(\mathbf{u})$, of the velocity fields that we define as Ravelet in [94]. So we end up computing the time average of the following quantities:

$$P(\mathbf{u}) = \frac{1}{|\Omega|}\int_\Omega \sqrt{\mathbf{u}_{r,0}^2 + \mathbf{u}_{z,0}^2}d\Omega, \quad T(\mathbf{u}) = \frac{1}{|\Omega|}\int_\Omega |\mathbf{u}_{\theta,0}|d\Omega \tag{4.1.10}$$

where $\mathbf{u}_{r,0}$, $\mathbf{u}_{\theta,0}$ and $\mathbf{u}_{z,0}$ are the radial, azimuthal and vertical component associated to the Fourier mode 0 of the velocity $\mathbf{u}$. We also consider the ratio of the poloidal and toroidal components denoted as $\Gamma(\mathbf{u})$ and defined by:

$$\Gamma(\mathbf{u}) = \frac{P(\mathbf{u})}{T(\mathbf{u})}. \tag{4.1.11}$$

Eventually we consider two other quantities which are the root mean square velocity defined by:

$$U_{\text{RMS}} = \overline{\sqrt{\frac{2E}{|\Omega|}}}, \tag{4.1.12}$$

and the time average of the torque K_p defined by:

$$K_p = \frac{1}{2\omega^2}\int_{\Omega_{\text{solid}}} |(\mathbf{r}\times\mathbf{F})\cdot\mathbf{e}_z|d\Omega, \tag{4.1.13}$$

where F is the force that induces a rotating motion in the impellers and ω is the angular velocity speed. Due to the dimensionalization of the problem we have $\omega = 1$. In the same way of section 2.4.3 where we compute the drag coefficient for the flow past a sphere, we end up computing K_p as follows:

$$K_p = \frac{1}{2}\int_\Omega r(1-\chi)\text{sign}(z)\frac{3}{2\tau}(\mathbf{u}-\mathbf{u}_{\text{obs}})\cdot\mathbf{e}_\theta d\Omega \tag{4.1.14}$$

with $sign(z)$ equal to 1 if $z > 0$ and -1 if $z < 0$. The function χ and $\mathbf{u}_{\text{obs}}$ are respectively defined in equations (4.1.1)and (4.1.3).

4.1.3 Hydrodynamic regimes for $R_e \leq 2500$

In this section we describe the numerical results we obtain without the use of the entropy viscosity method for $R_e \in [10, 2500]$. We split this study in two sets of R_e, first we present results for $R_e \leq 208$ where the flow is stationary in the sense that the kinetic energy tends asymptotically to a constant value. Next we study the flow structure for $R_e \in \{500, 1000, 2500\}$. The flow is not any more stationary and bifurcations in the energy spectrum appear with a growing Fourier mode $m = 2$ or $m = 3$ depending on the Reynolds number.

Stationary flow with $R_e \leq 208$

In this range of low Reynolds numbers the global structure of the flow is not influenced by the Reynolds number. As a consequence we first propose to describe the flow we numerically approximate for $R_e = 208$. Next we present the value of the torque K_p we get for $R_e \leq 100$ and discuss on the time resolution required by the pseudo-penalization technique to find a scaling law in R_e^{-1} as enhanced in [95].

In this regime of Reynolds numbers the flow is stationary and axisymmetric, see figure 4.4 which displays the evolution of the total kinetic energy with time and the final energy spectrum of the flow for $R_e = 208$. Apart from the Fourier mode 0, that contains

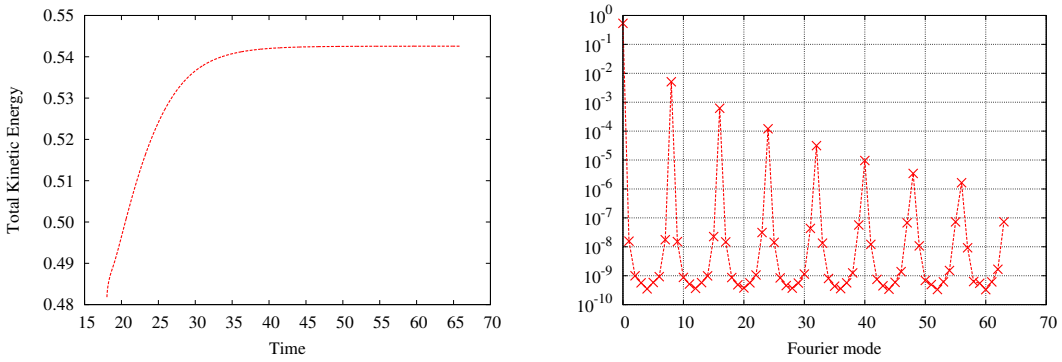

(a) Total kinetic energy. (b) Modal kinetic energy.

Figure 4.4: Kinetic energy at $R_e = 208$ (a) Evolution in time of the total kinetic energy. (b) Modal kinetic energy of each Fourier mode ($0 \leq m \leq 63$) at final time.

98.9% of the total kinetic energy, we note that the presence of 8 blades on both disks induces peaks in the energy spectrum every mode multiple of 8. A 2D representation of the mean axisymmetric velocity field is displayed in figure 4.5. We infer that the flow is also R_π symmetric. Its main structure consists of two toric recirculation cells separated by the shear layer $z = 0$. The fluid is driven on the lateral boundary of the cylinder to the plane $z = 0$ and is then driven back to the impellers around the vertical axis $r = 0$. We confirm the presence of the shear layer by representing the vertical component of the final velocity in $z = 0$, see figure 4.6, which is zero modulo weak echoes of the 8 blades. We can also note the presence of two recirculations in the areas between the disks and the bottom-upper boundaries of the cylinder ($|z| > 1$). However, these recirculations are not interacting with the main structure of the flow. Eventually we refer to table 4.1 for a summary of the numerical outputs of the computations. They allow, for example, to confirm the stationary state of the flow as $\overline{\delta}$ is around 1.01.

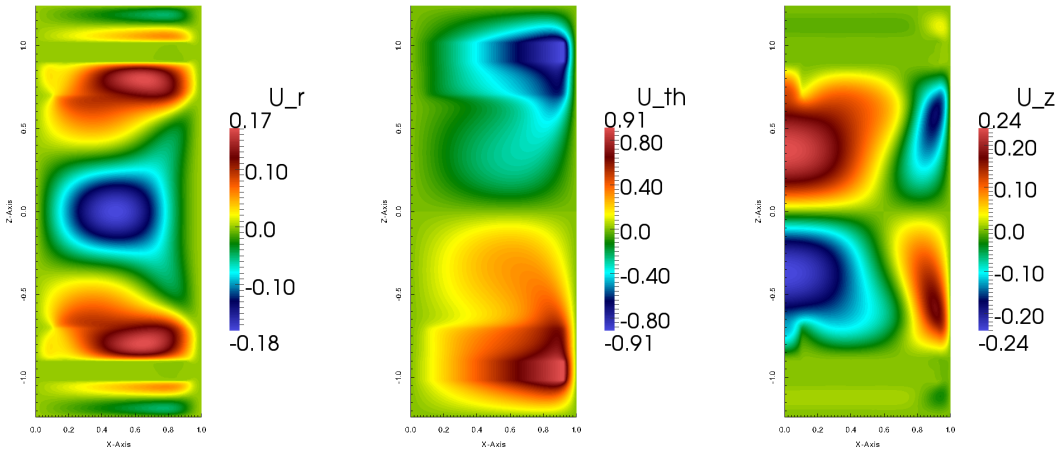

(a) U_r (b) U_θ (c) U_z

Figure 4.5: Mean profile of the mode 0 of the velocity field with $R_e = 208$ in the meridian plane $\theta = 0$.

Before studying the evolution of K_p for $R_e \in [10, 100]$, we note the pseudo-penalization technique we implemented in SFEMaNS induces an error in the solid domain of the order $O\left(\frac{\tau}{R_e}\right)$. As a consequence this study cannot be done with constant τ or would require a

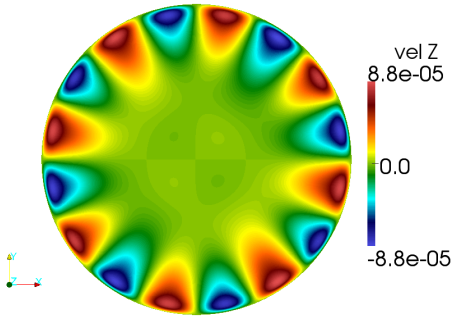

Figure 4.6: Vertical velocity at final time in the plane $z = 0$ viewed from the top with $R_e = 208$.

really small time step which is not of practical use. To illustrate our tells we display in figure 4.7 the evolution of K_p for two configurations. In one hand we fix the ratio $\frac{\tau}{R_e}$ to 5.10^{-5} so the error in the solid domain does not depend of the Reynolds numbers. The expected scaling law in R_e^{-1} is recovered with a multiplying factor 30 for $R_e \leq 60$, see figure 4.7a. On the other hand we display in figure 4.7b the evolution of K_p when working with constant CFL. In that purpose we set the time step τ to 2.5×10^{-3}. We note the torque is no more scaling as R_e^{-1} due to the error depending on the Reynolds numbers.

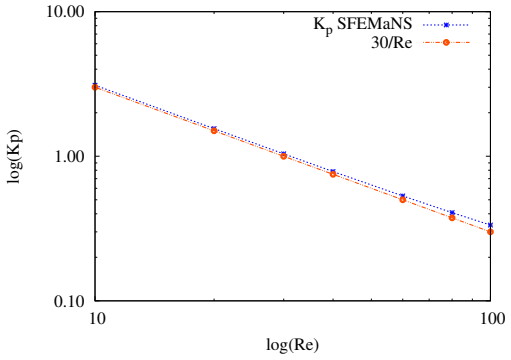

(a) $\frac{\tau}{R_e} = 5.10^{-5}$.

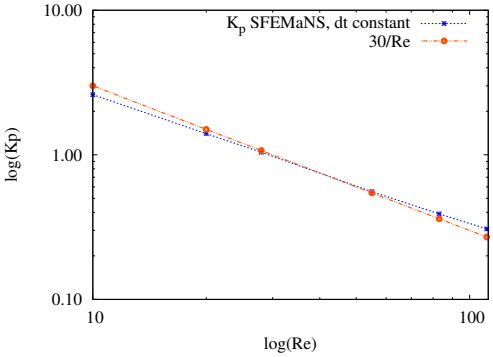

(b) $\tau = 2.5 \times 10^{-3}$.

Figure 4.7: Evolution of the torque K_p with the kinetic Reynolds number R_e (a) constant error for the pseudo-penalization method, (b) constant time step τ.

Eventually our numerical method manages to recover the main structure of the flow and a scaling law of K_p in R_e^{-1} for small values of Reynolds which were both known thanks to previous experimental and numerical studies. Before studying the flow for larger Reynolds numbers we note that unlike in the study of the K_p, we will always work with a constant CFL set to 0.4 for stability purposes. This choice allows us to deal with reasonable time step. Moreover it is consistent with the fact that we deal with Reynolds number of order 10^3 so the time error in $O\left(\frac{\tau}{R_e}\right)$ remains small in all configurations.

Non stationary flow for $R_e = 500 \leq R_e \leq 2500$

We now present DNS results for three Reynolds numbers from 500 up to 2500 where the flow becomes unsteady. First we increase the space resolution by setting the mesh size h to 0.02 in $\mathbb{P}_1$ near the cylinder boundaries and the area $z = 0$ while we keep using 64 Fourier modes and $h_{\text{imp}} = 0.01$ in the region where the impellers rotate. We note this resolution may not be sufficient to approximate the flow with a DNS for $R_e = 2500$, but it is the

best resolution we can afford with our computational resources. The study starts with a discussion on our numerical outputs and a description of the mean average velocity that lead us to conclude the flow loses its axisymmetry and becomes non stationary. Moreover the R_π symmetry is broken and exchanges of fluid between the upper and bottom parts of the cylinder appear. Eventually we study the energy spectrum of each computed flow to enhance bifurcation in the energy repartition such like a dominant mode 2 (modulo the mode 0) for $R_e = 500$.

In this range of Reynolds numbers the flow becomes non stationary thus the total kinetic energy presents fluctuations as shown in figure 4.8. This behavior is also emphasized in table 4.2, which displays the numerical outputs of our computations. Indeed the value of $\overline{\delta}$ keeps increasing with the Reynolds number to reach the value 1.239 for $R_e = 2500$ which confirms the presence of a non stationary flow. Moreover the level of kinetic energy and U_{RMS} also increase with the Reynolds number while the torque keeps decreasing. Even though the value of the torque is decreasing with R_e, we note the difference in level of K_p seems to be less pronounced as the Reynolds number grows. Such behavior was already emphasized in Ravelet et al [95] and will be discussed in the next section where a study of the problem for $R_e = 5.10^3$ is performed with the entropy viscosity method. Eventually

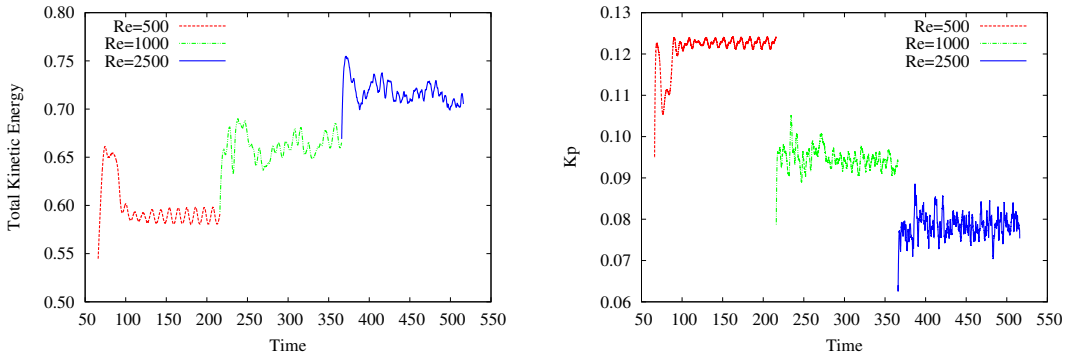

(a) Evolution of total kinetic energy.

(b) Evolution of Kp.

Figure 4.8: Evolution in time of total kinetic energy and torque for $R_e \in \{500, 1000, 2500\}$.

R_e	$\overline{E}$	$\overline{\delta(\mathbf{u})}$	$\overline{P(\mathbf{u})}$	$\overline{T(\mathbf{u})}$	$\overline{\Gamma(\mathbf{u})}$	U_{RMS}	$\overline{K_p}$
208	0.543	1.011	0.081	0.288	0.281	0.373	0.190
500	0.598	1.043	0.093	0.274	0.339	0.392	0.123
1000	0.662	1.131	0.109	0.288	0.378	0.412	0.093
2500	0.719	1.239	0.121	0.282	0.429	0.430	0.079

Table 4.1: Numerical results of DNS computations for $R_e = 208, 500, 1000, 2500$.

table 4.1 also shows that the ratio of the poloidal over the toroidal component of the mean axisymmetric velocity field is growing with the Reynolds number. Indeed the poloidal component is increasing while the toroidal one remains mainly constant which induces a more intense flow in the radial and vertical directions inside the cylinder. However, these quantities alone cannot provide a correct idea of the flow inside the cylinder. For example the toroidal component mainly reports from the action of the rotating disks while the poloidal component, see figure 4.9 for its representation in the meridian plane $\theta = 0$, lets

guess a recirculation where the fluid is driven to the plane $z = 0$ near the boundaries of the cylinder and driven back to the impellers near the vertical axis $r = 0$. Nevertheless the poloidal component of the mean axisymmetric flow is close to zero in the area $z = 0$. This implies that these recirculations also involve Fourier modes different from 0. Consequently the mean flow is not only supported by the Fourier mode 0 and cannot be considered as axisymmetric anymore.

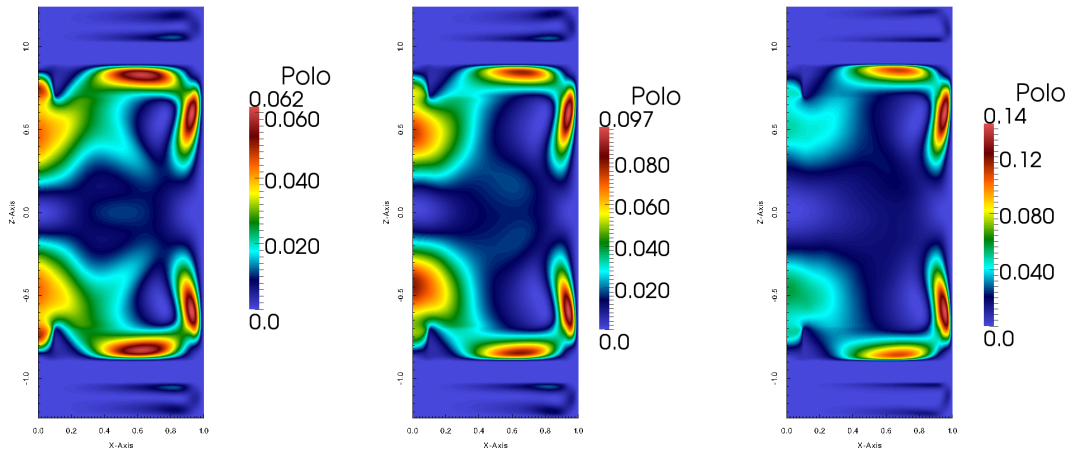

(a) $R_e = 500$. (b) $R_e = 1000$. (c) $R_e = 2500$.

Figure 4.9: Mean profile of the mode 0 of the poloidal component $\sqrt{\mathbf{u}_r^2 + \mathbf{u}_z^2}$ for various Reynolds numbers in the meridian plane $\theta = 0$.

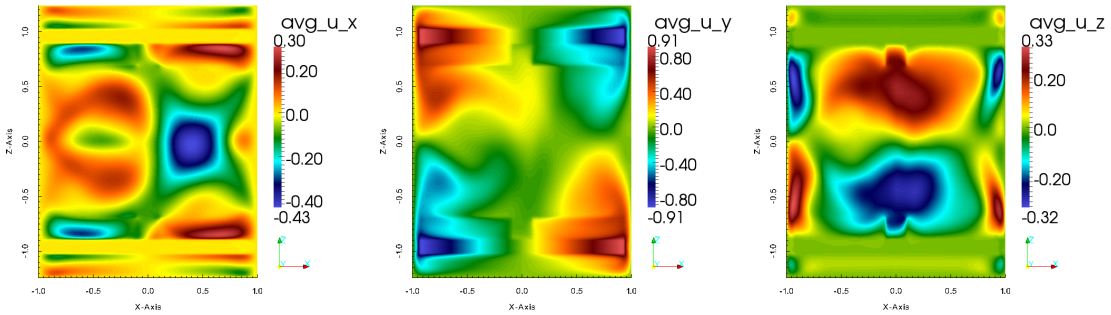

(a) $\overline{\mathbf{u}_x}$. (b) $\overline{\mathbf{u}_y}$. (c) $\overline{\mathbf{u}_z}$.

Figure 4.10: Representation of the mean Cartesian components of the velocity field in a plane (x, z) at $R_e = 1000$.

To enhance this behavior, we display the time average Cartesian components of the velocity field for $R_e = 1000$ in figure 4.10. It allows to confirm that the mean flow is not axisymmetric. It also reports the presence of a recirculation in the radial direction in the area $z = 0$ that was not possible to grasp with the poloidal component of the mean axisymmetric flow. As shown in past experimental studies with other metal impeller and figure 4.10, the flow also breaks the R_π symmetry. Moreover the flow crosses the section $z = 0$ so exchanges of fluid between the upper and bottom parts of the cylinder take place. These exchanges are highlighted in figure 4.11 which displays the final vertical velocity in the plane $z = 0$. Unlike for $R_e = 208$, the norm of the vertical velocity is non negligible. For $R_e = 500$ it even enhances the presence of a dominant Fourier mode equal to 2. This

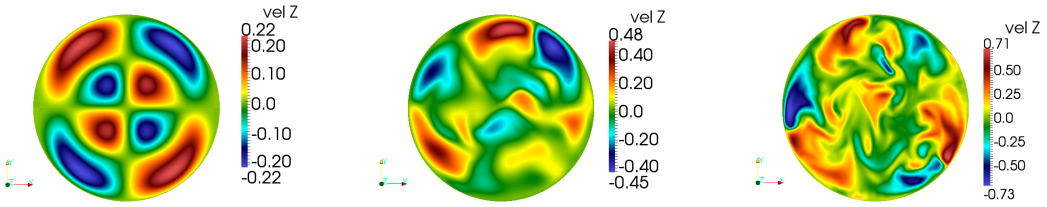

(a) $R_e = 500$. (b) $R_e = 1000$. (c) $R_e = 2500$.

Figure 4.11: Vertical velocity at final time in the plane $z = 0$ viewed from the top for $R_e \in \{500, 1000, 2500\}$.

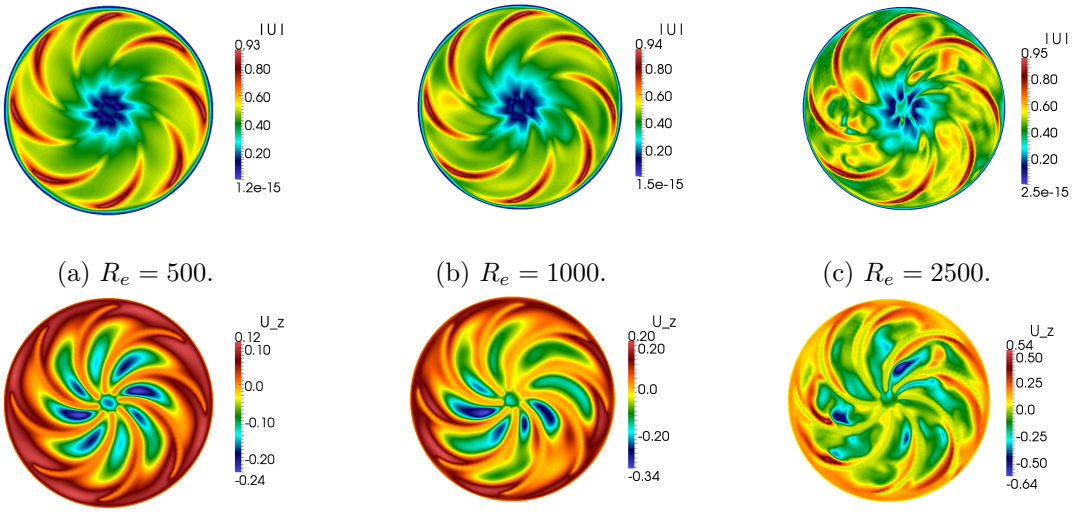

(a) $R_e = 500$. (b) $R_e = 1000$. (c) $R_e = 2500$.

(d) $R_e = 500$. (e) $R_e = 1000$. (f) $R_e = 2500$.

Figure 4.12: Instantaneous snapshot of the velocity at final time near the bottom blades in the plane $z = -0.8$ viewed from the top for $R_e \in \{500, 1000, 2500\}$. (a)-(b)-(c) Velocity magnitude. (d)-(e)-(f) Vertical velocity.

symmetry-breaking by the mode $m = 2$ is in agreement with a previous experimental study [95] that uses TM60. Before studying the repartition of energy between the different Fourier modes, we display in figure 4.12 an instantaneous visualization of the velocity magnitude and vertical component in the blades area $z = -0.8$. In one hand for $R_e = 500$ the flow seems to be dominated by the rotation of the impellers that expel the fluid toward the lateral boundaries of the cylinder. On the other hand for $R_e = 2500$ we note peaks in the velocity magnitude and vertical component between the impellers meaning some vortical structures appear between the blades. The existence of in-blades vortices in the von Kármán swirling flow has been evidenced experimentally and numerically by Ravelet et al [96] and numerically by Kreuzahler et al [60]. As we do not plan to study these vortices, we just note they seem to appear for a Reynolds number of the order 10^3 and refer to [96, 60] for more details.

To conclude this study we propose to display the evolution of the Fourier modes $m = 1$, $m = 2$ and $m = 3$ in figure 4.13 and the final energy spectrum in figure 4.14 for the three Reynolds numbers studied (500, 1000 and 2500). A first bifurcation appears for $R_e = 500$ where the Fourier mode $m = 2$ is growing and becomes dominant together with the $m = 0$

and $m = 8$ modes due to the rotating impellers. This result is in agreement with previous experimental data with TM60 rotating in the sense (-) where a mode 2 was found in [95] for Reynolds numbers in the range $[200, 300]$. As a consequence the energy spectrum, see figure 4.14a, presents peak for all even modes. A second bifurcation appears for a Reynolds number of 1000 and 2500 as the Fourier modes 1, 2 and 3 enter in competition with a little dominance of the mode 3. This behavior was also observed in the numerical study using TM73 performed by D. Castanon [18]. As a consequence the energy spectrum mainly presents peaks for the first three modes and every multiple of 8 due to the presence of the blades. We note on the figure 4.14 that the computation with $R_e = 2500$ is a little under-resolved and suffers from aliasing effect for the largest modes so it may require the use of more than 64 Fourier modes. Despite this under resolution our numerical results give coherent results with respect to experimental [94, 95] and numerical [18] studies and so will be used to validate the entropy viscosity model in the following section.

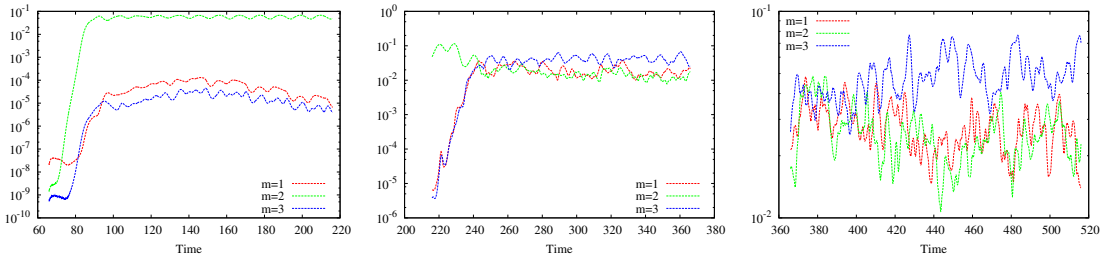

(a) $R_e = 500$. (b) $R_e = 1000$. (c) $R_e = 2500$.

Figure 4.13: Time evolution of the kinetic energy of the Fourier modes $m = 1, 2$, and 3 for $R_e \in \{500, 1000, 2500\}$. Note the different ordinate scales of the plots.

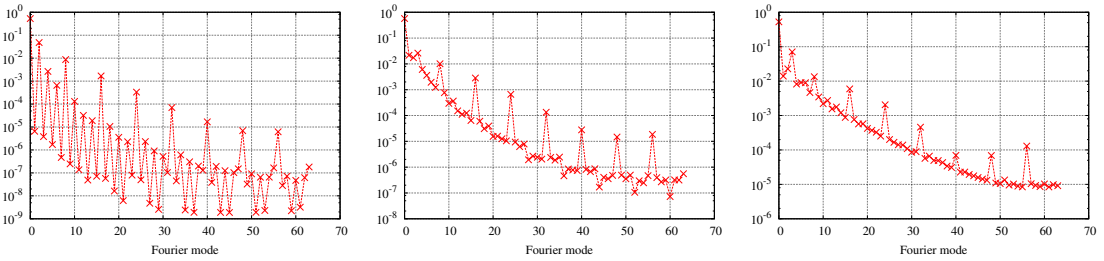

(a) $R_e = 500$. (b) $R_e = 1000$. (c) $R_e = 2500$.

Figure 4.14: Modal kinetic energy of each Fourier mode ($0 \leq m \leq 63$) at final time for $R_e \in \{500, 1000, 2500\}$.

4.1.4 Numerical results with entropy viscosity method

In this section we propose to approximate the previous VKS set up with the entropy viscosity method so we can study a larger range of Reynolds numbers with under resolved computations. First we validate our LES model by comparing results obtained with LES and DNS for Reynolds numbers in $[500, 2500]$. Next we present a preliminary study of the flow for a moderate Reynolds number equal to 5.10^3. This second study is done over 10 turns of the impellers and is a first step of a future study that aims to compare experimental data of B. Dubrulle's team in CEA Saclay with entropy viscosity computations involving

larger time integration and also larger Reynolds numbers. We note in the following all LES computations have been done with 64 to 96 (for $R_e = 5000$) Fourier modes and a meridional with a mesh size $h = 0.01$ in $\mathbb{P}_1$ near the impellers to represent correctly the impeller geometry, see figure 4.3. The mesh size near the cylinders boundaries and the area $z = 0$ is set to $h = 0.04$ in $\mathbb{P}_1$ and so it is twice less refined than the one used with previous DNS computations. Moreover the viscosity entropy is computed by setting $c_{\mathrm{e}} = 0.2$ and $c_{\max} \in \{0.04, 0.0625\}$, see definition 4.1.6.

DNS and LES comparisons with $R_e = 500, 1000$ and 2500

We validate the entropy viscosity model to approximate this VKS set up by doing comparisons with DNS computations presented in the previous section for $R_e = 500, 1000$ and 2500. The outputs of the LES computations for this set of Reynolds numbers is summarized in table 4.2 and can be compared to the DNS results in table 4.1. All these mean values are in agreement with an error of 1% or less which confirms that the entropy viscosity method manages to approximate the mean flow correctly even with a coarser mesh. As these values are not sufficient to report on all the flow dynamics, we propose to compare the final energy spectrum and the evolution of quantities such as the total kinetic energy of DNS and LES computations for each kinetic Reynolds number.

R_e	$\overline{E}$	$\overline{\delta(\mathbf{u})}$	$\overline{P(\mathbf{u})}$	$\overline{T(\mathbf{u})}$	$\overline{\Gamma(\mathbf{u})}$	U_{RMS}	$\overline{K_p}$
500	0.599	1.043	0.093	0.274	0.339	0.392	0.123
1000	0.671	1.145	0.110	0.293	0.375	0.414	0.094
2500	0.718	1.229	0.119	0.281	0.423	0.429	0.078

Table 4.2: Numerical results of LES computations for $R_e = 500, 1000, 2500$.

First we focus on comparisons between LES and DNS computations with $R_e = 500$. To do so we display in figure 4.15 the evolution of the modes 1, 2 and 3 of the LES computations and a comparison of the energy spectrum of LES and DNS computations. The entropy viscosity method allows to grasp the bifurcation in the energy repartition as the mode 2 grows and becomes dominant modulo the mode 0 due to the rotation of the impellers. Figure 4.15a can be compared to figure 4.13a. We note that the evolution of these modes for the LES computations matches perfectly the one of the DNS that resolves all the scales of the dynamics (the DNS was performed with a mesh satisfying the Kolmogorov criterion). Moreover the correct behavior of the method is checked by comparing the energy azimuthal spectrum at final time $t = 216$ that matches for every Fourier modes computed. As a consequence the entropy viscosity allows to approximate the correct flow for $R_e = 500$ even with a coarser mesh.

To enhance the benefit of the entropy viscosity with a coarser mesh we now performe comparisons between previous DNS computations with LES and under resolved DNS computations for $R_e = 1000$. We denote by under resolved DNS, a DNS computation performed with the same mesh used in the LES computations. For this purpose figure 4.16 displays the evolution of the total kinetic energy and the final energy spectrum for the DNS and LES computations. In one hand the kinetic energy presents differences but similar level of flucturations as they both takes values in $[0.64, 0.70]$. This is in agreement with the previous remark on their mean kinetic energies which present a 1% difference. On the other hand the energy spectra of DNS and LES computations present peaks every mode

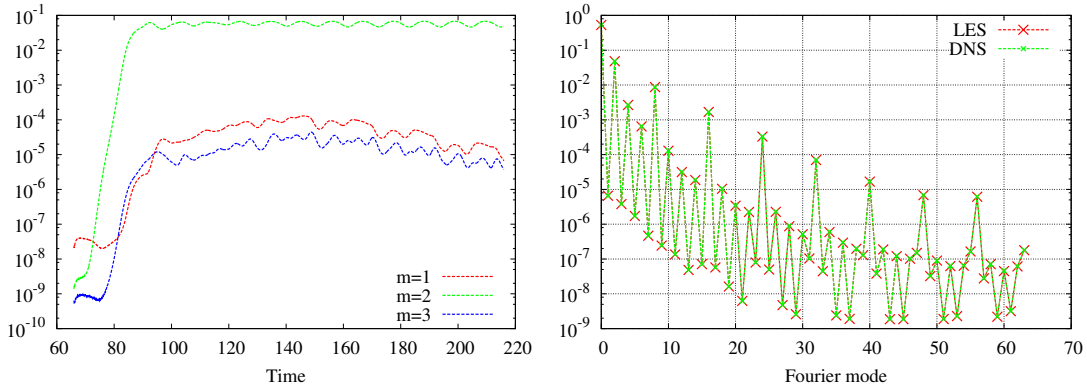

(a) Evolution of Kinetic energy of modes 1, 2 and 3 with time.

(b) Comparison of final modal kinetic energy of each 64 Fourier mode with LES and DNS.

Figure 4.15: Evolution of the kinetic energy of various Fourier modes with $R_e = 500$ with LES. Figure (a) can be compared to figure 4.13a.

multiple of 8 of same intensity. However, we note the rest of the LES spectrum is a little above the one of the DNS. This could be explained by the fact that the final kinetic energy of the LES computation is at a higher level than the one of the DNS. We conclude the analysis of this spectrum by noting that as with the DNS computations, the Fourier modes 1, 2 and 3 enter in competition with a little dominance of the mode 3, see figure 4.18a. To confirm the correct behavior of the entropy viscosity we display the mean average of

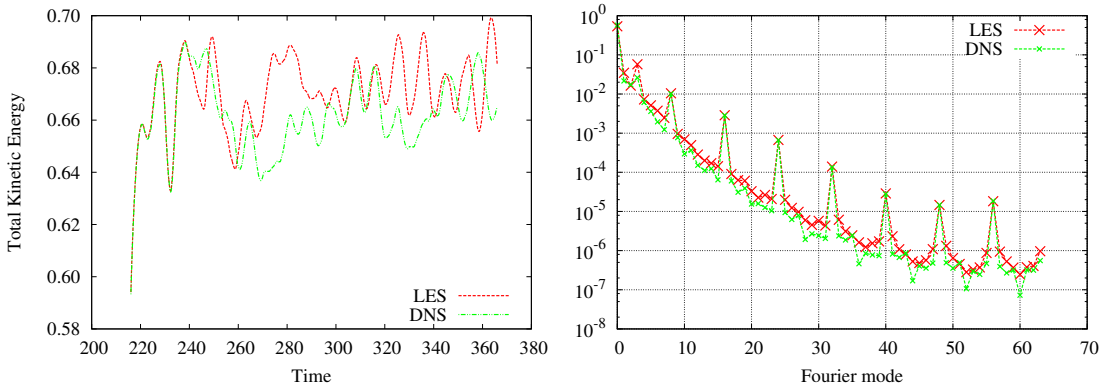

(a) Time evolution of total kinetic energy.

(b) Kinetic energy azimuthal spectrum.

Figure 4.16: Kinetic energy with $R_e = 1000$ for LES and previous DNS computations.

the Cartesian components of the velocity field in figure 4.17. This figure can be compared to figure 4.10 which shows that the mean flows are very close. Indeed all three Cartesian components of the velocity field present similar structure apart from a little difference in the x component in the area $r = 0$ near the impellers. We draw the attention of the reader that the level zero of these components may be represented by different colors (light orange for the x component and light green for the others).

As the entropy viscosity method with a coarser mesh gives satisfying results compared to the previous DNS computations with $R_e = 1000$, we now show that a DNS performed with the same coarser mesh would not be as satisfying. To support this claim we display in figure 4.18 the time evolution of the kinetic energy of the Fourier modes $m = 1, 2$ and 3 of the LES and under resolved DNS computations. While both computations emphasize a

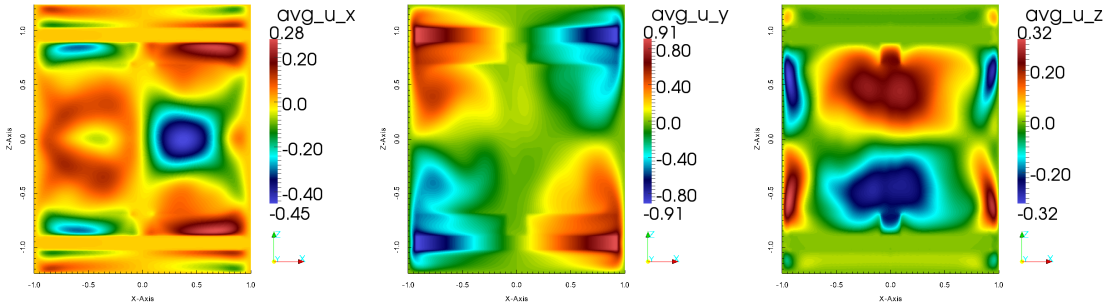

(a) $\overline{\mathbf{u}_x}$. (b) $\overline{\mathbf{u}_y}$. (c) $\overline{\mathbf{u}_z}$.

Figure 4.17: Representation of the mean Cartesian components of the velocity field in a plane (x, z) at $R_e = 1000$ with LES.

competition between the Fourier modes $m = 1, 2$ and 3, we note the under resolved DNS fails to capture a bifurcation in the spectrum energy. Indeed the energy level of the mode 3 saturates around 10^{-2} which is nearly 10 times smaller than the value obtained with the LES and previous DNS with a refined mesh. As a consequence the Fourier mode 2 remains dominant and the under resolved DNS, unlike the LES, does not manage to capture the bifurcation in the energy spectrum.

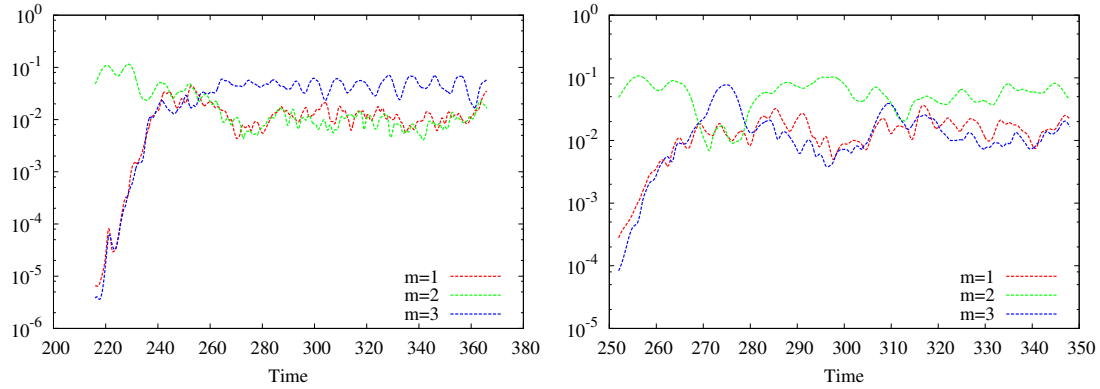

(a) LES. (b) Under resolved DNS.

Figure 4.18: Evolution of the kinetic energy of Fourier modes 1, 2 and 3 with $R_e = 1000$ for LES and DNS computations with the same space resolution. See figure 4.13b for comparisons.

We end the validation of our LES method by doing comparisons with previous DNS computation at $R_e = 2500$. In that purpose figure 4.19 displays the time evolution of the kinetic energy and the energy spectrum at final time of each computation. We note the LES computation has only been performed over 10 turns of the disk to save computational time for a computation with $R_e = 5000$ presented in the following. The kinetic energy of the LES computation varies in the same range as the one with DNS and as mentioned earlier their time averaged values match up to 1-2% of relative error, see tables 4.1 and 4.2. Although the DNS and LES computations are not performed on the same time integration range (20 turns against 10), we note their respective kinetic energies at final time are close to 0.71. It leads us to compare their energy spectrum at final time in figure 4.19b. The LES computation manages to recover correctly the spectrum of the DNS for the large scales of

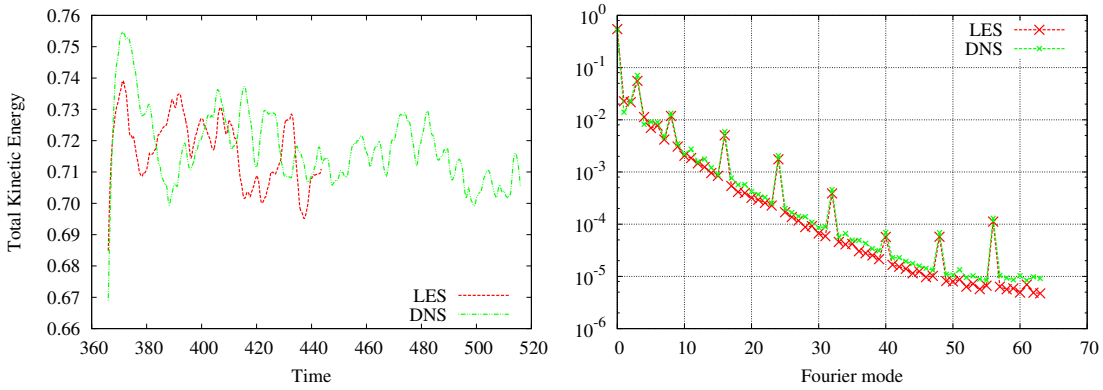

(a) Time evolution of total kinetic energy.

(b) Kinetic energy azimuthal spectrum.

Figure 4.19: Kinetic energy with $R_e = 2500$ for LES and previous DNS computations.

the flow while the small scales, ie large modes, are a little dissipated due to the entropy viscosity action.

LES results with $R_e = 5.10^3$

As the entropy viscosity method has proved to be efficient to approximate this VKS set-up in the frame of under resolved computations, we now describe a preliminary study of the problem with larger Reynolds numbers which we restrain to $R_e = 5000$ for the time being. Since both DNS and LES computations at $R_e = 2500$ suffer of aliasing effect at the largest Fourier modes multiple of 8, meaning $m = 48$ and $m = 56$, this study is performed with 96 Fourier modes. Furthermore it is done over 11 turns of impellers. We note this time of integration is rather small so future investigations will pursue this study with longer time integration. However, in the same way as previous computations, the transient time is reduced by initializing the computations with the final velocity field obtained with the LES computation at $R_e = 2500$. To show off the benefit of using 96 Fourier modes we display the energy spectrum at the final time in figure 4.20. As expected the spectrum is reduced for the largest mode multiple of 8 and presents less aliasing effect for the largest modes whose levels of energy remain under 10^{-4}.

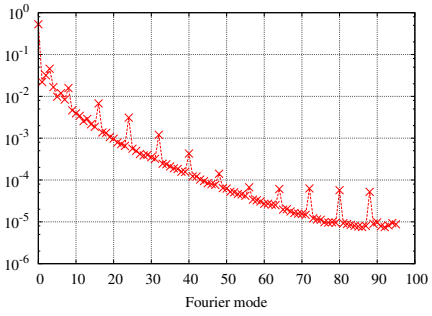

Figure 4.20: Modal kinetic energy of each Fourier mode ($0 \leq m \leq 95$) at final time for $R_e = 5000$ with LES.

As a published experimental study [95] shows that the torque value saturates as the Reynolds number grows beyond a few thousand and a previous numerical study [60] enhances that many other quantities of interest such as the root mean square velocity U_{RMS} or the mean kinetic energy remain nearly constant when the Reynolds number goes from 2430 to 4860, we display in figure 4.21 the evolution of the kinetic energy and the torque

with time for LES computations at $R_e = 2500$ and 5000. In one hand one can note that the torque varies in the same range of values for both computations. On the other hand the kinetic energy increases slightly but the average value of these quantities are close. To support this tell table 4.3 gives a summary of the outputs of the computation at $R_e = 5000$ and can be compared with the last line of table 4.2. It confirms that the torque and the

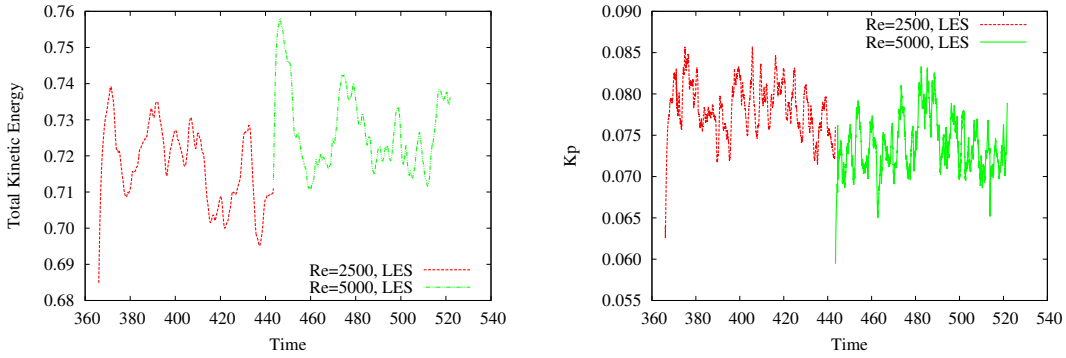

(a) Evolution of total kinetic energy.

(b) Evolution of Kp.

Figure 4.21: Evolution in time of total kinetic energy and torque for $R_e \in \{2500, 5000\}$ with LES.

R_e	$\overline{E}$	$\overline{\delta(\mathbf{u})}$	$\overline{P(\mathbf{u})}$	$\overline{T(\mathbf{u})}$	$\overline{\Gamma(\mathbf{u})}$	U_{RMS}	$\overline{K_p}$
5.10^3	0.726	1.268	0.123	0.268	0.459	0.431	0.074

Table 4.3: Numerical results of LES computations at $R_e = 5.10^3$.

mean kinetic energy start to saturate with the Reynolds numbers. As in [60] the mean fluctuation of kinetic energy $\overline{\delta}$ and the ratio of poloidal and toroidal velocity components $\overline{\Gamma}$ increase slightly little which can be explained by a more efficient local pumping of the impellers.

While we keep the study of the flow structure for future investigations with larger time integration and extended range of Reynolds numbers, we end this study with a representation of the mean Cartesian components of the velocity field displayed in 4.22. As enhanced previously, the flow is pushed towards the sides of the cylinder in the blades area and is then driven to the area $z = 0$ along the sides of the cylinder. The exchange of fluid between the upper and bottom parts of the cylinder is enhanced when the mean vertical velocity differs from zero in the area $z = 0$, see figure 4.22c.

4.1.5 Conclusion

The hydrodynamic study of this VKS set up with TM87 for low Reynolds numbers $R_e \leq 208$ manages to recover the expected laminar flow, axisymmetric and mainly composed of two toric recirculation cells, and a scaling law of the torque in R_e^{-1} for Reynolds numbers smaller than 60. This first study validates the implementation in SFEMaNS code of the pseudo-penalization technique of Pasquetti et al [89] in the frame of solid obstacle in motion, represented by the counter rotating impellers.

In order to consider large Reynolds numbers, so comparisons between experiments and numerical results can be led, a second study of the problem with $R_e \in [500, 2500]$ enhances

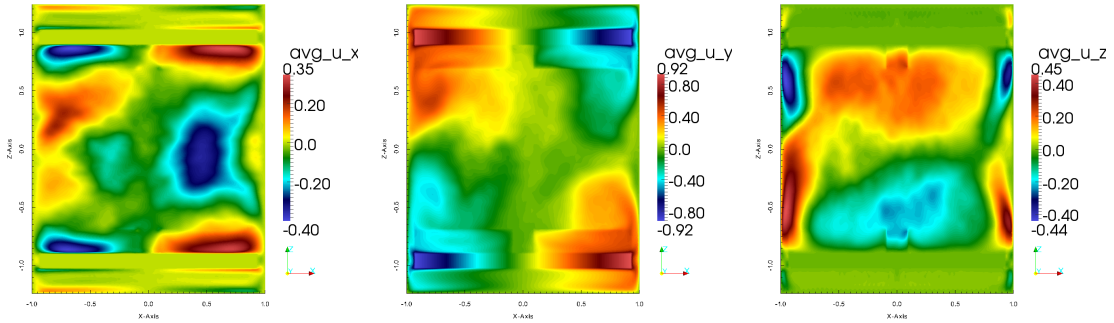

(a) $\overline{\mathbf{u}_x}$. (b) $\overline{\mathbf{u}_y}$. (c) $\overline{\mathbf{u}_z}$.

Figure 4.22: Representation of the mean Cartesian components of the velocity field in a plane (x, z) at $R_e = 5000$ with LES.

the good results of the entropy viscosity method (LES) with under resolved simulations. First DNS computations on a refined grid and LES computations on a coarser grid are proved to give similar results. Moreover these computations show off bifurcations in the energy spectrum already pointed out with other TM experimentally in [95] for $R_e = 500$ and numerically in [18] for $R_e = 500$ and 1000. Finally the correct behavior of the entropy viscosity is confirmed with a computation at $R_e = 5000$ that enhances an asymptotic value in kinetic energy and torque K_p as the Reynolds number grows which is consistent with previous studies done in [95, 60].

As the entropy viscosity proves efficient to approximate this problem for moderate Reynolds numbers in the frame of under resolved computations, the next step of this hydrodynamic investigation would be to validate it for larger Reynolds numbers. Since comparisons with DNS computations may be limited to a Reynolds number of the order 10^4 due to present computational power limits, we plan to do comparisons with coming results of experiments using TM87 led in CEA Saclay by B. Dubrulle et al.

The extension of SFEMaNS code to problem with variable magnetic permeability in all space directions, see section 2.5 and D. Castanon thesis [18] for more details, opens a second perspective: the magnetohydrodynamic study of a VKS set up. Since the VKS experiment of Cadarache [80], where a strong axisymmetric magnetic field was generated, a study of Miralles et al [78] showed the importance of using impellers with high magnetic permeability to generate an axisymmetric magnetic field. However, the mechanism behind this dynamo effect is not fully understood and numerical studies may bring light on some aspect of this dynamo. In that frame SFEMaNS code is used in [85] to show preliminary results of the magnetic problem with a given velocity field. A full MHD study of this problem with TM73 is currently performed by D. Castanon [18] with SFEMaNS code and could be feasible with TM87.

4.2 Two spinning ways for precession dynamo

In the frame of previous studies of Nore et al [83] we propose to analyze, in the form of an article in preparation, two configurations of precessing cylinder. The problem consists of driving a cylindrical container with a main rotation and a second rotation, called precession, about a different axis and with a smaller intensity. First we study an axial spin case of precession that will be experimented in Dresden [105]. The problem involves a

main rotation around the symmetry axis of the cylinder and a precession around a radial axis. We extend the hydrodynamic study of [83] by using the entropy viscosity method so larger kinetic Reynolds numbers are considered. After checking its correct behavior with DNS comparisons at $R_e = 4000$, the entropy viscosity is used to perform a study of the hydrodynamic regime for $4000 \leq R_e \leq 15000$. It allows to suggest a scaling law of the kinetic energy in the precession frame as $R_e^{-0.48}$. Moreover the flow is shown to tend to a solid rotation in the wall frame which is in agreement with experimental results for larger Reynolds numbers [82] and the fact that in the limit of zero viscosity the rotation does not force the flow. In addition comparisons with an equatorial spin case, where the main rotation is radial and the precession is around the vertical axis, are provided. This second set-up proves to be more efficient at breaking the symmetry of the flow. However, a MHD study of both configurations enhances that the axial spin case remains more favorable to the generation of magnetic field, referred as dynamo action. Eventually the presence of a container with conducting or ferromagnetic walls is also investigated to check their influence on the dynamo threshold. While the use of ferromagnetic walls raises the dynamo threshold, we show that conducting lateral walls allow to reduce the threshold. As a consequence the addition of a copper layer in lateral wall would help the dynamo, this result may find echoes in the preparation of an axial spin case precession experiment in Dresden [105].

Two spinning ways for precession dynamo

L. Cappanera[1], J.-L. Guermond[1,2], J. Léorat[3] and C. Nore[1]

Abstract It is numerically demonstrated by means of a magnetohydrodynamic (MHD) code that precession can trigger dynamo action in a cylindrical container. Fixing the angle between the spin and the precession axis to be $\pi/2$, two limit configurations of the spinning axis are explored: either the symmetry axis of the cylinder is parallel to the spin axis (this configuration is henceforth referred to as the axial spin case), or it is perpendicular to the spin axis (this configuration is referred to as the equatorial spin case). In both cases, when the kinetic Reynolds number, based on the radius of the cylinder, its spin angular velocity and the kinematic viscosity of the fluid, increases, the flow breaks its centro-symmetry. The equatorial spin case is more efficient in breaking the symmetry of the flow. In the axial spin case, we propose a scaling law for the kinetic average energy as a function of Reynolds. We also study the influence of conducting or ferromagnetic walls on the dynamo threshold. In the equatorial spin case, the unsteady and asymmetric flow is shown to be capable of sustaining dynamo action in the linear and nonlinear regimes. The magnetic field thus generated is mainly dipolar in the equatorial spin case while it is is mainly quadrupolar in the axial spin case. These numerical evidences of dynamo action in a precessing cylindrical container may be useful for the design of new dynamo experiments, such as the one planned at the DRESDYN facility in Germany.

4.2.1 Introduction

The idea that precession can be a potent mechanism to drive dynamo action for the Earth has long been debated (see for example [75]). Modern astrophysical observations of some planetary dynamos can contribute to resolve this issue but definite evidence is still lacking [67].

The quest for experimental dynamo action is currently pursued in Europe. Precession driving provides a potential promising way to generate experimental fluid dynamos since it involves large scale forcing and does not require any pump or impellers. For example, an ambitious project at the DREsden Sodium facility for DYNamo and thermohydraulic studies (DRESDYN) [105] is to build a precession-driven dynamo experiment composed of a large cylinder: the diameter and the height of the cylinder are equal to 2 metres. The cylinder will be filled with liquid sodium and will undergo rotation about its axis and precession about another axis (which can be the equator). The planned maximum rotation and precession frequencies are 10 Hz and 1 Hz, respectively, leading to a magnetic Reynolds number of a few hundreds.

Even though numerical simulations of the Dresden experiment with very large kinetic Reynolds numbers (at least 10^6) are out of reach with present day computers, we think that numerical simulations are useful complements and can shed some light on specific aspects of this experiment. Because of the large computing resources required, it is only recently that numerical computations have demonstrated that dynamo action occurs in different

[1]Laboratoire d'Informatique pour la Mécanique et les Sciences de l'Ingénieur, CNRS UPR 3251, Rue John von Neumann, 91403 Orsay cedex, France and Université Paris-Sud

[2]Department of Mathematics, Texas A&M University 3368 TAMU, College Station, TX 77843-3368, USA

[3]Luth, Observatoire de Paris-Meudon, place Janssen, 92195-Meudon, France.

precessing containers: spherical [109] and spheroidal [111] ones. Since neither spheres nor spheroids are convenient for large-scale experiments, it is instructive to investigate whether similar results can be obtained in cylindrical containers. Many experiments have been conducted in cylinders (full or with an inner cylinder, see e.g. [26, 82, 62, 72]) with varying aspect ratios, various angles between the precession and the spin axis (always assumed to be the symmetry axis) and varying ratios of precession to spin frequencies. In contrast, very few numerical studies have been performed [83, 59, 58].

The main motivation of the present paper is to present new hydrodynamic and magnetohydrodynamic results in a precessing cylinder. We have developed for this purpose a nonlinear magnetohydrodynamic (MHD) code called SFEMaNS (for Spectral/Finite Elements for the Maxwell and Navier-Stokes equations). This code solves the nonlinear incompressible MHD equations in heterogenous cylindrical domains. The spatial approximation is done with Fourier expansions in the azimuthal direction and Lagrange finite elements in the meridional section (see [31, 33, 35] for more details). The spatial distribution of the electrical conductivity and the magnetic permeability is allowed to be discontinuous in the meridional section and highly heterogeneous (but continuous) in the azimuthal direction; the magnetic domains can be composed of conducting and non-conducting parts. The code has been thoroughly validated on numerous manufactured solutions and against other MHD codes on linear [27, 29, 28] and nonlinear magnetohydrodynamic problems [33].

The paper is organized as follows. The numerical settings are defined in section §4.2.2 together with the two spinning ways for precession forcing, namely the axial and the equatorial spin forcings. Section §4.2.3 presents hydrodynamic studies in relation with the precession-driven experiment at the DRESDYN facility. Extended range of kinetic Reynolds numbers up to 15000 is reached for the axial spin case thanks to the entropy viscosity stabilization method summarized in appendix §4.2.6. The two spinning ways for precession forcing are investigated and compared. Section §4.2.4 contains new results of dynamo action in the axial spin case with varying properties of the vessel walls. It is shown that using lateral walls made of copper helps the dynamo effect. It is also numerically demonstrated in this section that, if strong enough, precession can generate dynamo action in a rotating cylinder filled with a conducting fluid in the equatorial spin forcing. Section §4.2.5 contains our discussion.

4.2.2 Numerical settings

Let us consider a cylindrical vessel $\mathcal{C}$ of radius R and height L. The vessel contains a conducting fluid and is embedded in vacuum. The container rotates about its spin axis with constant angular velocity $\Omega_s \mathbf{e}_s$ and is assumed to precess about a second axis spanned by the unit vector $\mathbf{e}_p$ forming an angle α with $\mathbf{e}_s$ ($0 < \alpha < \pi$). The constant precession angular velocity is $\Omega_p \mathbf{e}_p$.

We use the cylindrical coordinate system centered at the center of mass of the cylinder, say O; the Oz axis is the line passing through O and parallel to $\mathbf{e}_z$ the cylinder axis of symmetry; the origin of the angular coordinate θ ($0 \leq \theta < 2\pi$) is the half plane passing through O, spanned by $\mathbf{e}_s$ and $\mathbf{e}_p$. The third coordinate, denoted r, is the distance to the Oz axis.

Let R and $U = R\Omega_s$ be the reference length and velocity scales, respectively. The fluid density, ρ, is assumed to be constant and the reference pressure scale is $P := \rho U^2$. The magnetic permeability and the electric conductivity of the conducting fluid are constant,

μ_0 (the vacuum permeability) and σ_0 respectively. These quantities are used as reference magnetic permeability and electric conductivity, respectively. The reference scale for the magnetic induction is chosen so that the reference Alfvén speed is 1, i.e., $B := U\sqrt{\mu_0\rho}$.

Six parameters govern the flow: the aspect ratio of the container L/R, the precession angle α (angle between the spin axis $\mathbf{e}_s$ and the precession axis $\mathbf{e}_p$), the spin angle (angle between the symmetry axis $\mathbf{e}_z$ and the spin axis $\mathbf{e}_s$), the precession rate $\varepsilon = \Omega_p/\Omega_s$ (ratio of the precession and spin angular velocity, also called the Poincaré number), the kinetic Reynolds number $R_e = R^2\Omega_s/\nu$ (where ν is the kinematic viscosity) and the magnetic Reynolds number $R_m = \mu_0\sigma_0 R^2\Omega_s$ (where μ_0 is the magnetic permeability of the vacuum and σ_0 the electrical conductivity of the fluid). Note that R_e is in fact the inverse of the Ekman number and differs from the actual effective Reynolds number of the flow.

Choosing the container height equal to its diameter (i.e., $L/R = 2$), the precession axis orthogonal to the spin axis (i.e., $\alpha = \pi/2$) and the precession rate $\varepsilon = 0.15$, we are left with two limit configurations: one called *axial spin* for which the spin angle is 0 and the symmetry axis of the cylinder remains fixed in the precession frame and another one called *equatorial spin* for which the spin angle is $\pi/2$ and the symmetry axis rotates in the precession frame (see figure 4.23). We focus our attention on these two configurations because, in the axial spin case, the wall speed is tangent to the wall and only the viscous stress on the wall drives the flow while, in the equatorial spin case, the flow is put into motion by the pressure on the wall and is therefore inertially driven.

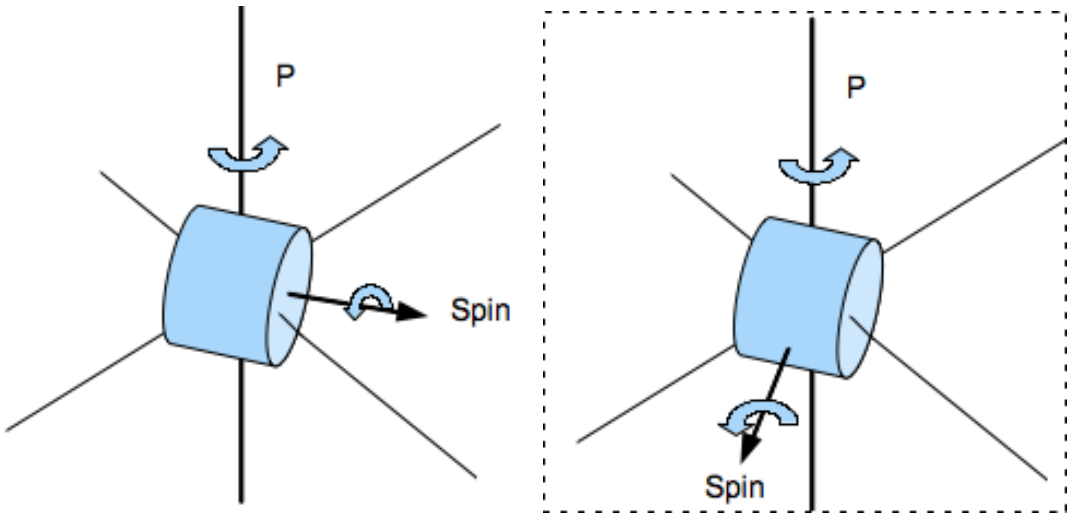

(a) (b)

Figure 4.23: Schematic representation of the *axial spin* (a) and the *equatorial spin* (b) configurations.

The non-dimensional set of equations can be written in two frames of reference. For the axial spin case, since the geometry of the container is fixed in the precession frame of

reference, computations can be performed in this frame where equations are:

$$\partial_t \mathbf{u} + (\mathbf{u}\cdot\nabla)\mathbf{u} + 2\varepsilon \mathbf{e}_p \times \mathbf{u} + \nabla p = \frac{1}{R_e}\Delta \mathbf{u} + \left[\nabla \times \left(\frac{\mathbf{B}}{\mu_r}\right)\right] \times \mathbf{B}, \tag{4.2.1}$$

$$\nabla \cdot \mathbf{u} = 0, \tag{4.2.2}$$

$$\partial_t \mathbf{B} = \nabla \times (\mathbf{u} \times \mathbf{B}) - \frac{1}{R_m}\nabla \times \left(\frac{1}{\sigma_r}\nabla \times \left(\frac{\mathbf{B}}{\mu_r}\right)\right), \tag{4.2.3}$$

$$\nabla \cdot \mathbf{B} = 0, \tag{4.2.4}$$

where $\mathbf{u}$, p, and $\mathbf{B}$ are the velocity field, the reduced pressure including the centrifugal term, and the induction field, respectively, and σ_r and μ_r are the relative conductivity and permeability of the various materials. The spin axis coincides with the symmetry axis i.e., $\mathbf{e}_s = \mathbf{e}_z$ and the precession axis $\mathbf{e}_p = \mathbf{e}_x$ is fixed in the precession frame. In the lhs of equation (4.2.1), the term depending on ε is the Coriolis acceleration. The no-slip boundary condition on the velocity field is written as follows in the precession frame of reference: $\mathbf{u} = \mathbf{e}_\theta$ at $r = 1$ and $\mathbf{u} = r\mathbf{e}_\theta$ at $z = \pm 1$.

For the equatorial spin case, to avoid dealing with moving boundaries, computations must be performed in the wall frame of reference attached to the container (also called the *mantle* frame) where the momentum equation is changed to:

$$\partial_t \mathbf{u} + (\mathbf{u}\cdot\nabla)\mathbf{u} + 2\boldsymbol{\Omega}(t) \times \mathbf{u} + \nabla p = \frac{1}{R_e}\Delta \mathbf{u} + \left[\nabla \times \left(\frac{\mathbf{B}}{\mu_r}\right)\right] \times \mathbf{B} - \frac{d\boldsymbol{\Omega}}{dt} \times \mathbf{r}. \tag{4.2.5}$$

where $\mathbf{e}_s = \mathbf{e}_x$ is fixed in this frame while $\mathbf{e}_p$ rotates around $\mathbf{e}_s$. Hence, the Coriolis acceleration in the lhs depends on the total angular velocity $\boldsymbol{\Omega}(t) = \mathbf{e}_x + \varepsilon \mathbf{e}_p(t) = \mathbf{e}_x + \varepsilon(\sin t \mathbf{e}_y + \cos t \mathbf{e}_z)$ while the Poincaré force $-\frac{d\boldsymbol{\Omega}}{dt} \times \mathbf{r}$ appears in the rhs. The no-slip boundary condition on the velocity field is $\mathbf{u} = 0$ at $r = 1$ and $\mathbf{u} = 0$ at $z = \pm 1$.

4.2.3 Hydrodynamic study

In this section we examine the two configurations in the hydrodynamic regime, where R_e is the control parameter. At low Reynolds number, the flow is steady and centro-symmetric for the axial spin case, meaning that $\mathbf{u}(\mathbf{r}) = -\mathbf{u}(-\mathbf{r})$, while it is unsteady and centro-symmetric for the equatorial spin case. At larger Reynolds numbers, the loss of centro-symmetry can be monitored by inspecting the symmetric and antisymmetric components of the velocity field: $\mathbf{u}_s(r,t) = (\mathbf{u}(\mathbf{r},t) - \mathbf{u}(-\mathbf{r},t))/2$ and $\mathbf{u}_a(\mathbf{r},t) = (\mathbf{u}(\mathbf{r},t) + \mathbf{u}(-\mathbf{r},t))/2$. All computations have been done on centrosymmetric grids, but centrosymmetry has not been otherwise enforced.

4.2.3.1 Energy scaling with Reynolds number in the axial spin case

For the axial spin case, equations (4.2.1)-(4.2.2) are integrated with $\mathbf{B} = 0$ in the precessing reference frame. We start our investigations with a Navier-Stokes run at $R_e = 1200$ as in [83]. The initial velocity field in the precessing frame is the solid rotation: $\mathbf{u}_0 = \mathbf{e}_z \times \mathbf{r}$. The onset of the axial circulation induced by precession is monitored by recording the time evolution of the normalized total kinetic energy $K(t) = \frac{1}{2}\int_{\mathcal{C}} \mathbf{u}^2(\mathbf{r},t)\,\mathrm{d}\mathbf{r}/K_0$ where $K_0 = \frac{1}{2}\int_{\mathcal{C}} \mathbf{u}_0^2\,\mathrm{d}\mathbf{r}$ is the kinetic energy of the initial solid body rotation. This computation is the same as in [83] where it was shown that the time evolution of the total kinetic energy exhibits doubly periodic oscillations. To enrich the dynamics we increase the Reynolds

number as reported in figure 4.24. Usually, for saving computing time, we use computed velocity fields obtained at smaller R_e to restart computations at higher R_e. Note that a rotation period is 2π in our units. For $R_e \leq 4000$, we perform Direct Numerical Simulations (DNS) while, for $R_e \geq 4000$, we use a stabilization method to reach higher Reynolds numbers with similar spatial and time resolutions (see Appendix for an explanation of this method). The parameters for the stabilization method (LES in short) are tuned at $R_e = 4000$: figure 4.24b shows for $0 \leq t \leq 300$ the kinetic energy computed in DNS from figure 4.24a and shifted in time and, for $300 \leq t \leq 430$, the kinetic energy computed in LES at $R_e = 4000$. Dynamical behaviours are similar and validate the LES coefficients which are kept for increased R_e number computations. Note that the time-averaged kinetic energy K decreases with R_e at ε fixed.

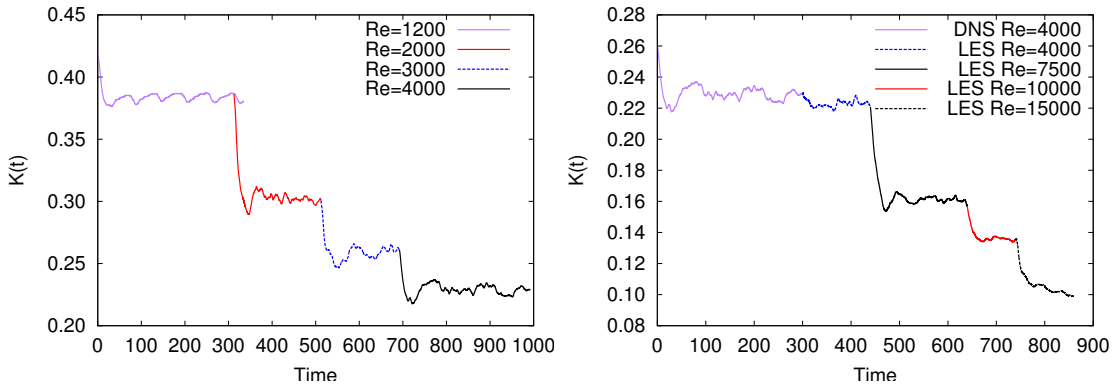

(a) (b)

Figure 4.24: (Color online) Time evolution of the total kinetic energy $K(t)$ in the precession frame for different Reynolds numbers as indicated: (a) DNS at $R_e = 1200, 2000, 3000, 4000$; (b) DNS computation at $R_e = 4000$ and LES computations at $R_e = 4000, 7500, 10000, 15000$.

Using our LES method, the range of Reynolds numbers that we have explored is wide enough to suggest a scaling law for the time-averaged kinetic energy, K, as a function of the Reynolds number R_e for the precession rate $\varepsilon = 0.15$. To substantiate this claim we show in figure 4.25a the time-averaged kinetic energy K as a function of R_e. Values for $R_e < 1200$ are extracted from our previous article [83]. The log-log representation of the data suggests that in range $R_e \in [400 : 15000]$ the energy scales like $K \simeq R_e^{-0.48}$ (see figure 4.25b), which in turn suggests the following scaling law for the temporally averaged velocity $\overline{u} \simeq R_e^{-1/4} = Ek^{1/4}$ (where Ek is the Ekman number). This scaling predicts that the average flow vanishes at large R_e. This property is not paradoxical since, in an axisymmetric container with a rotation axis parallel to its symmetry axis, the azimuthal flow is driven only by viscous forces at the wall. Since in the limit of zero viscosity the rotation does not force the flow, one expects to get at the inviscid limit a static fluid in the precession frame and a solid body motion around the rotation axis in the mantle frame at $\mathbf{\Omega} = -\mathbf{e}_z$ (note that it is a counter-rotation with respect to the spin rotation). In the precession frame (i.e., the turntable frame), the inhibition of the mean rotation has been observed in the ATER experiment [82]. In the mantle frame, the corresponding nearly rigid-body rotation has been discussed in [58] where it was called geostrophic flow: it was shown that its size and amplitude gradually grow as ε increases from 0.075 to 0.25 at $R_e = 10000$.

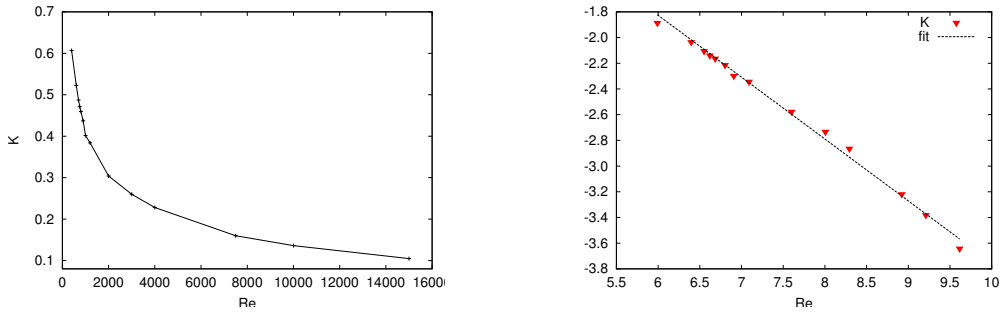

(a) (b)

Figure 4.25: (Color online) Total (time-averaged) kinetic energy K in the precession frame as a function of the Reynolds number R_e: (a) in linear scale and (b) in log-log scale with the fit $R_e^{-0.48}$.

We observe the same behavior in the precession frame when we increase R_e at fixed Poincaré number $\varepsilon = 0.15$: figure 4.26 shows that the highest values of the axial velocity are more and more localized near the lateral wall. As R_e increases, the central part of the flow is nearly static and all the small scales, highly intermittent, are pushed towards the wall. For all Reynolds numbers, we observe a central S-shaped vortex deformed by the precession and connected to the walls through viscous boundary layers (see figure 4.27). With increasing R_e, the vorticity lines are more entangled and the central part of the vortex is more aligned with the x-axis (the precession axis).

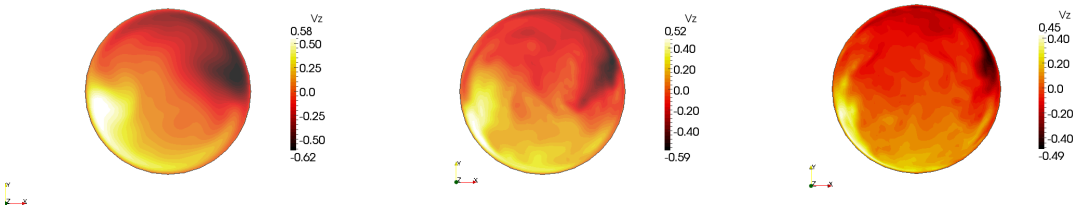

(a) (b) (c)

Figure 4.26: (Color online) Snapshots of contours of the axial velocity in the equatorial plane in the precession frame: (a) at $t = 302$ and $R_e = 1200$, (b) at $t = 235$ and $R_e = 4000$ and (c) at $t = 850$ and $R_e = 15000$.

This tendency to alignment with the precession axis is also apparent on the time-averaged velocity and vorticity fields as displayed on figure 4.28. A similar three-dimensional structure is observed at $\varepsilon = 0.1$ and $R_e = 10^4$ in a precessing sphere in the axial spin case, where it is attributed to a pair of large-scale energetic vortex tubes (see figure 16 in [30]). For a precessing cylinder, this structure can be attributed to the trace of the S-shape vortex observed at all Reynolds numbers.

Another way to interpret our scaling based on this wall-localization is to consider that velocity of order 1 is concentrated in a small layer δ on the lateral wall (within the volume $2\pi R\delta H$). The scaling gives $\delta/R \approx 1/\sqrt{R_e}$ reminiscent of the usual width of a boundary layer.

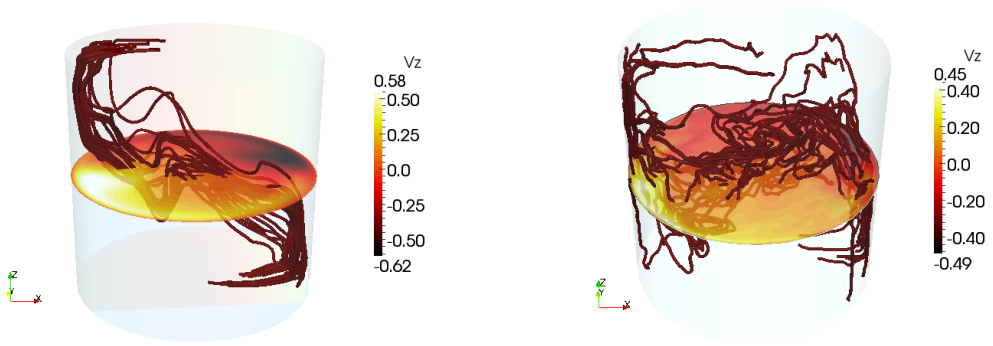

(a) (b)

Figure 4.27: (Color online) Streamlines of the instantaneous vorticity field (in red/dark grey) from a perspective point of view and contours of the axial velocity in the equatorial plane: (a) $R_e = 1200$ and (b) $R_e = 15000$.

(a) $R_e = 1200$, top view (b) $R_e = 1200$ from the side

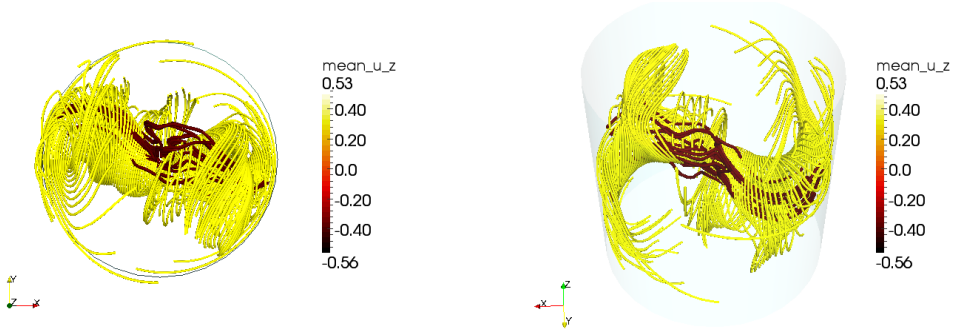

(c) $R_e = 4000$, top view (d) $R_e = 4000$ from the side

Figure 4.28: (Color online) Streamlines of the mean velocity field (in yellow/light grey) and of the mean vorticity field (in red/dark grey). Illustrated are 100 streamlines for $\mathbf{u}$ with endpoints distributed uniformly on the Ox axis and 20 streamlines for $\nabla\times\mathbf{u}$ with endpoints distributed uniformly on a sphere of radius 0.2: (a-b) $R_e = 1200$ and (c-d) $R_e = 4000$.

4.2.3.2 Comparison between equatorial and axial spin forcing

For the equatorial spin case, equation (4.2.5) is integrated with $\mathbf{B} = 0$. We use a different normalization for the total kinetic energy for the equatorial spin case, namely the kinetic energy of the solid rotation around the equatorial axis $\mathbf{e}_x$, $\mathbf{u}_0^\perp = \mathbf{e}_x \times \mathbf{r}$ denoted as $E_0^\perp = 0.5 \int (\mathbf{u}_0^\perp)^2 dV$. We define the normalized total kinetic energy in the wall frame as $E^\perp(t) = 0.5 \int \mathbf{u}^2 dV / E_0^\perp$, the asymmetric kinetic energy $E_a^\perp(t) = 0.5 \int \mathbf{u}_a^2 dV / E_0^\perp$ and the asymmetry ratio $r_a^\perp(t) = E_a^\perp(t)/E^\perp(t)$.

Figure 4.29a shows the time evolution of the total kinetic energy in the mantle frame which rapidly increases with R_e for moderate Reynolds numbers and then seems to saturate at large Reynolds numbers. The asymmetric ratio of figure 4.29b fluctuates in time and the flow is clearly asymmetric for $R_e \geq 1000$. This ratio seems also to saturate around 6%.

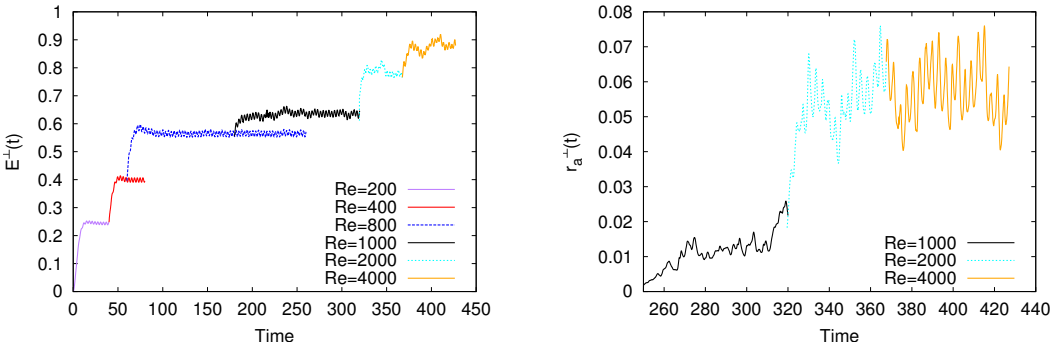

(a) (b)

Figure 4.29: (Color online) Time evolution of (a) the total kinetic energy $E^{\perp}(t)$ and (b) the asymmetry ratio $r_a^{\perp}(t) = E_a^{\perp}(t)/E^{\perp}(t)$ in the mantle frame at different Reynolds numbers R_e in the equatorial spin case.

To compare the efficiency of energy injection according to the two ways of spin forcing, we need to use a shared reference frame. We perform a change of reference frame for the axial spin data: velocities are simply transformed from the precession frame to the wall frame with $\mathbf{u}(\mathbf{r},t) = \mathbf{u}^{\parallel}(\mathbf{r},t) + \mathbf{e}_z \times \mathbf{r}$. Note that K and $E^{\parallel}$ have the same normalization factor which is different from that of $E^{\perp}$. For example, we display the time evolution of the kinetic energy of the axial spin case at $R_e = 1200$ in the two reference frames in figure 4.30a.

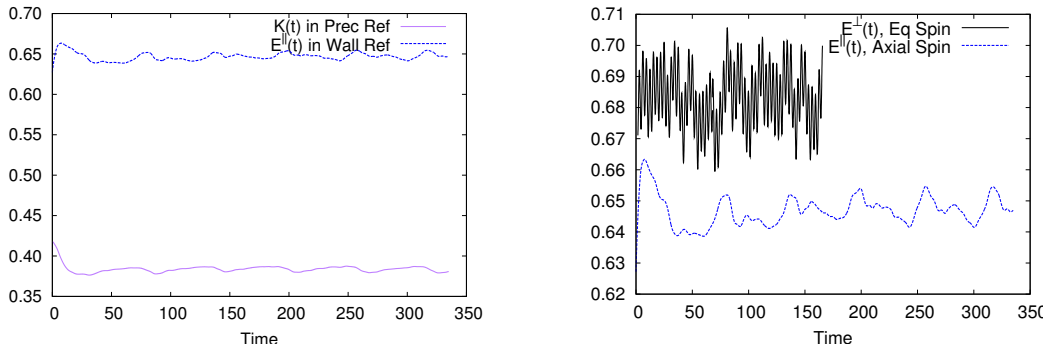

(a) Axial spin case at $R_e = 1200$ recorded in the two frames

(b) Axial and equatorial spin cases in the wall frame

Figure 4.30: (Color online) (a) Time evolution at $R_e = 1200$ of the kinetic energy $K(t)$ in the precession frame as in figure 4.24a and of the transformed kinetic energy $E^{\parallel}(t)$ in the wall frame for the axial spin case. (b) Comparison of the kinetic energy in the wall frame for the axial and the equatorial spin cases at $R_e = 1200$.

We plot in figure 4.30b the normalized kinetic energy of the two configurations in the wall frame at $R_e = 1200$. Note that both the time-averaged value of the kinetic energy and the fluctutations are larger in the equatorial spin case than in the axial spin case.

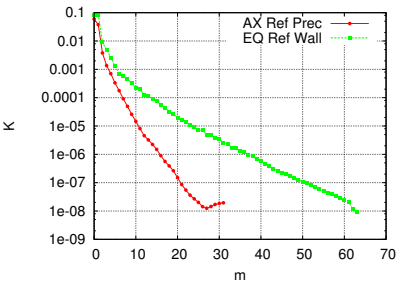

(a) Energy spectra

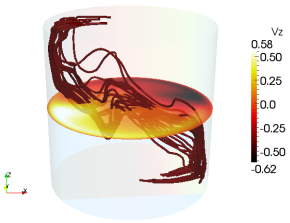

(b) axial spin case

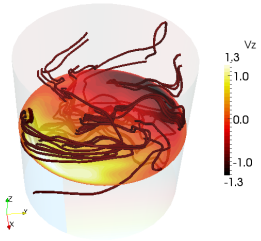

(c) equatorial spin case

Figure 4.31: (Color on line) Comparison between the axial and equatorial spin cases: kinetic energy azimuthal spectra as a function of the azimuthal mode m (a) and snapshot at $R_e = 1200$ of the vorticity field lines (red/dark grey) and contours of the axial velocity component in the equatorial plane: (b) axial spin case (same as figure 4.27a), (c) equatorial spin case.

We compare in figure 4.31 kinetic energy azimuthal spectra as a function of the azimuthal mode m (defined around the symmetry axis of the cylinder) at the same Reynolds number $R_e = 1200$ for the two forcings as well as snapshots of instantaneous vorticity and velocity fields. Note that the equatorial spin case needs twice Fourier modes as much as the axial spin case, therefore the computations are more demanding. We see also different features in the two flows: the spin axis case displays a deformed S-shape vortex approximately contained in a meridian plane and a velocity field localized near the side wall; the equatorial spin case shows no coherent vortical structure with small-scales localized near the wall.

It is then interesting to compare the time-averaged value of the total kinetic energy $E^{\parallel}$ and $E^{\perp}$ as in figure 4.32a as a function of R_e: for the axial spin case, the efficiency of the viscous forcing decreases when R_e increases; for the equatorial spin case, the kinetic energy is slightly larger and saturation is nearly achieved at $R_e = 4000$. We know that (see previous section), at large R_e, in the axial spin case, the system tends to a nearly rigid body rotation around the rotation axis $\mathbf{e}_z$ in the mantle frame corresponding to the value 1 for the normalized time-averaged kinetic energy $E^{\parallel}$. By analogy, we expect that, in the equatorial spin case, the system should also nearly rigidly rotate around the rotation axis $\mathbf{e}_x$ since the kinetic energy $E^{\perp}$ seems to converge also to 1.

The difference between the two spin forcings is made apparent with the asymmetry ratio: it becomes positive for similar Reynolds numbers $R_e \gtrsim 800$ but its value is much larger in the equatorial spin case than in the axial spin case by a factor of three at large Reynolds numbers (see figure 4.32b). The equatorial spin case is therefore more efficient in breaking the centro-symmetry than the axial spin case.

Based on the phenomenological argument that dynamo action is favored by symmetry breaking, it could be anticipated that the equatorial spin case would generate dynamo action at a lower threshold than the axial spin case. However, it is shown in section 4.2.4.2 that this intuitive argument is incorrect.

4.2.4 Dynamo action

We now investigate the MHD regime, where R_e and R_m are the two control parameters. The nonlinear MHD simulations use a small magnetic seed field as initial data or restart

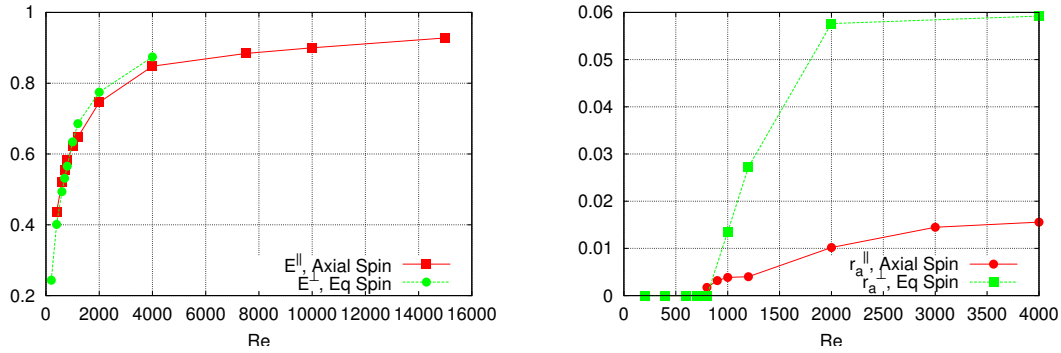

(a) (b)

Figure 4.32: (Color on line) Comparisons between the axial and equatorial spin cases in the wall frame (also called the mantle frame): (a) time-averaged total kinetic energy $E^{\parallel}$ and $E^{\perp}$ as a function of R_e; (b) time-averaged asymmetry ratio $E_a^{\parallel}/E^{\parallel}$ and $E_a^{\perp}/E^{\perp}$ as a function of R_e.

from a state computed at neighboring parameters. As already observed for spherical and spheroidal dynamos, dynamo action occurs after symmetry breaking of the flow when the magnetic dissipation is small enough, i.e. for magnetic Reynolds numbers R_m above a critical value $R_{\rm m}^c(R_e)$.

4.2.4.1 Axial spin case

4.2.4.1.1 Reminder from [83] In [83], we have explored the range of the kinetic and magnetic Reynolds numbers and found dynamo action for $R_e = 1200$ and $R_m \geq R_{\rm m}^c \approx 775$ when the solid walls of the vessel were assumed to be insulating. The growing magnetic field that is observed rotates in the precession frame of reference and is dominated by the $m = 2$ mode: as shown in figure 4.33b, the magnetic field lines show a mainly quadrupolar structure in the vacuum when seen from the top of the cylinder.

4.2.4.1.2 Numerical results with thick walls We now present new results about thresholds and growing magnetic fields when using conducting or ferromagnetic walls of relative thickness $w = 0.1$ at different places. The relative conductivity of these walls is chosen to be that of copper i.e., $\sigma_r = 4.5$ or the relative magnetic permeability is taken to be that of soft iron i.e., $\mu_r = 65$ [110].

Conducting walls. We study the influence of the conducting walls with $\sigma_r = 4.5$ and $\mu_r = 1$. We keep $R_e = 1200$ and vary R_m to find the threshold when the growth rate of the magnetic energy is zero. We define four cases as follows. We call 'insulating' case the configuration studied in [83], the 'side' case corresponds to adding conducting walls on the cylindrical side of the vessel, the 'lid' case corresponds to adding conducting walls at the top and bottom of the vessel, and the 'wall' case corresponds to adding conducting walls everywhere.

We first show in figure 4.34a a series of dynamo simulations done with $R_m = 300, 400$ and 900 for the 'side' case. The figure shows the time evolution of the magnetic energy $M(t) = \int_{\Omega_c} \frac{1}{2}\mathbf{B}^2/\mu_0\mu_r dV$ where Ω_c is the fluid domain and the walls. We start the $R_m = 900$ run with a magnetic seed and integrate long enough to get a decrease or an increase of M. Dynamo action occurs when $M(t)$ is an increasing function of time as is the case for

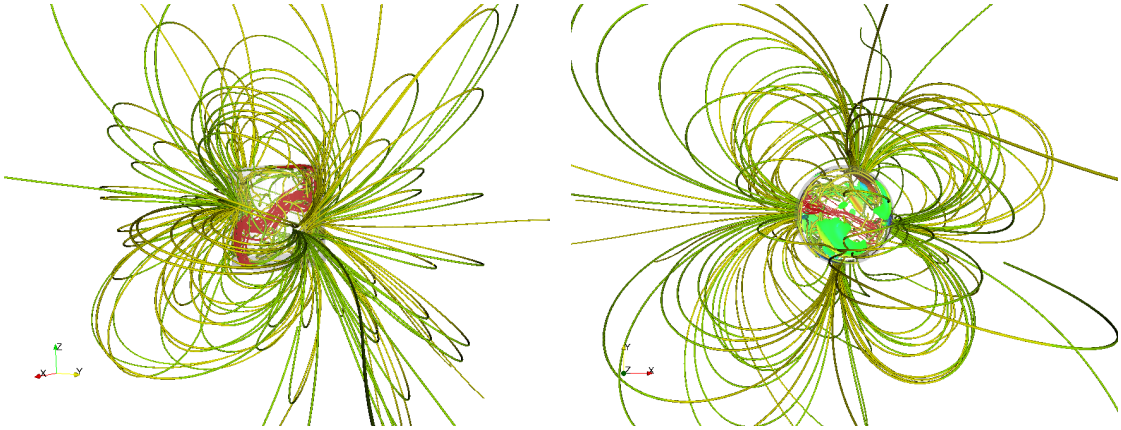

(a) 'insulating' case in perspective (b) 'insulating' case from the top

Figure 4.33: Snapshot at $R_e = 1200$, $R_m = 2400$ for the 'insulating' case showing vorticity field lines (red lines inside the cylinder) and magnetic field lines colored by the axial component [yellow (green) for positive (negative) h_z component]: (a) perspective view, (b) from the top of the cylinder. From [83].

$R_m = 900$ and $R_m = 400$ but not for $R_m = 300$. The initial velocity and magnetic field for the runs at $R_m = 400$ are the velocity and the magnetic fields obtained from the run at $R_m = 900$ at time $t = 47$. For $R_m = 300$, we restart from $R_m = 400$ at time $t = 107$. Linear interpolation of the growth rates gives an estimate of the critical magnetic Reynolds number $R_{\mathrm{m}}^c \approx 365$ for the 'side' case.

We perform two other series of simulations and collect the growth rates in figure 4.34b. The thresholds are $R_{\mathrm{m}}^c(\text{'side'}) \approx 365 < R_{\mathrm{m}}^c(\text{'wall'}) \approx 650 < R_{\mathrm{m}}^c(\text{'insulating'}) \approx 775 < R_{\mathrm{m}}^c(\text{'lid'}) \approx 965$. We observe that the 'lid' walls are highly detrimental to the dynamo action while adding the 'side' walls helps it. That is reminiscent to the results found in [106, 64] for the von Kármán Sodium experiment.

Conducting walls enable currents to loop on longer scales but also lead to different growing magnetic field structures (see figure 4.35). The 'lid' configuration as the 'insulating' configuration lead to a mainly quadrupolar magnetic field while the 'side' case gives rise to a mainly equatorial dipolar growing magnetic field. The 'wall' configuration shows an oblique dipolar growing magnetic field (data not shown).

Ferromagnetic walls. We now study the influence of the ferromagnetic walls with $\mu_r = 65$ and $\sigma_r = 1$. We keep $R_e = 1200$ and vary R_m to find the threshold when the growth rate of the magnetic energy is zero. We define four cases as before. We call 'insulating' case the configuration studied in [83], the 'side' case corresponds to adding ferromagnetic walls on the cylindrical side of the vessel, the 'lid' case corresponds to adding ferromagnetic walls at the top and bottom of the vessel, and the 'wall' case corresponds to adding ferromagnetic walls everywhere. We perform linear dynamo simulations and collect the growth rates in figure 4.36a. The thresholds are $R_{\mathrm{m}}^c(\text{'insulating'}) \approx 775 < R_{\mathrm{m}}^c(\text{'side'}) \approx 800 < R_{\mathrm{m}}^c(\text{'wall'}) \approx 840 < R_{\mathrm{m}}^c(\text{'lid'}) \approx 880$. We can note that adding ferromagnetic walls increases the threshold in any case. In the 'wall' case the magnetic energy is dominated by the $m = 1$, 2 modes and the growing magnetic field is an equatorial dipole (see figure 4.36b).

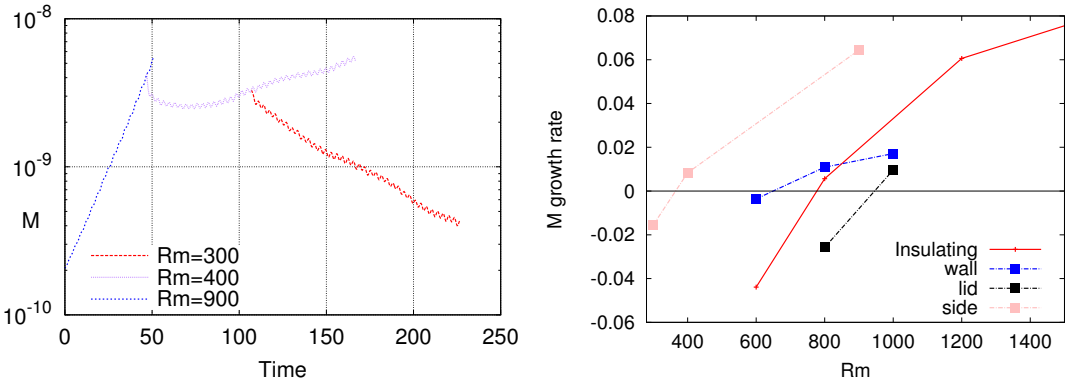

(a) $M(t)$ for the 'side' case

(b) Growth rates vs. R_m

Figure 4.34: Conducting walls: (a) Time evolution of the magnetic energy $M(t)$ in the conducting fluid at $R_e = 1200$ and various R_m as indicated (in lin-log scale) for the 'side' case; (b) Growth rates of the magnetic field energy as a function of R_m for various configurations. The values are for $R_e = 1200$ and the thickness of either conducting wall type is taken as $0.1R$, with a relative conductivity $\sigma_r = 4.5$ and relative magnetic permeability $\mu_r = 1$.

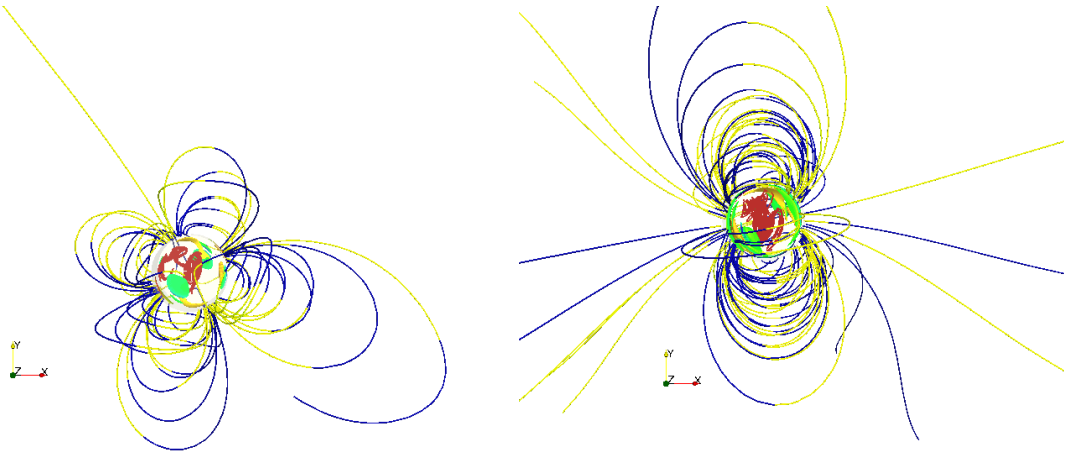

(a) From the top for the 'lid' case

(b) From the top for the 'side' case

Figure 4.35: Conducting walls: Snapshots at (a) $R_e = 1200$, $R_m = 1000$ for the 'lid' case and (b) $R_e = 1200$, $R_m = 900$ for the 'side' case showing vorticity field lines (red lines inside the cylinder) and magnetic field lines colored by the axial component [yellow (blue) for positive (negative) h_z component].

Although a predictive explanation of the variation of the dynamo threshold is still lacking at the present time, the impact of the nature of the walls seems crucial for the design of experimental fluid dynamos. For conducting walls, the increase of $R_{\mathrm{m}}^{\mathrm{c}}$ from the 'side' case to the 'lid' case suggests to diminish the influence of the lid by lowering its conductivity: for example, it would be interesting to consider an inner copper layer attached to the outer stainless steel shell of the dynamo vessel in the DRESDYN precession experiment. In any configuration ferromagnetic walls seem to be detrimental to the dynamo action.

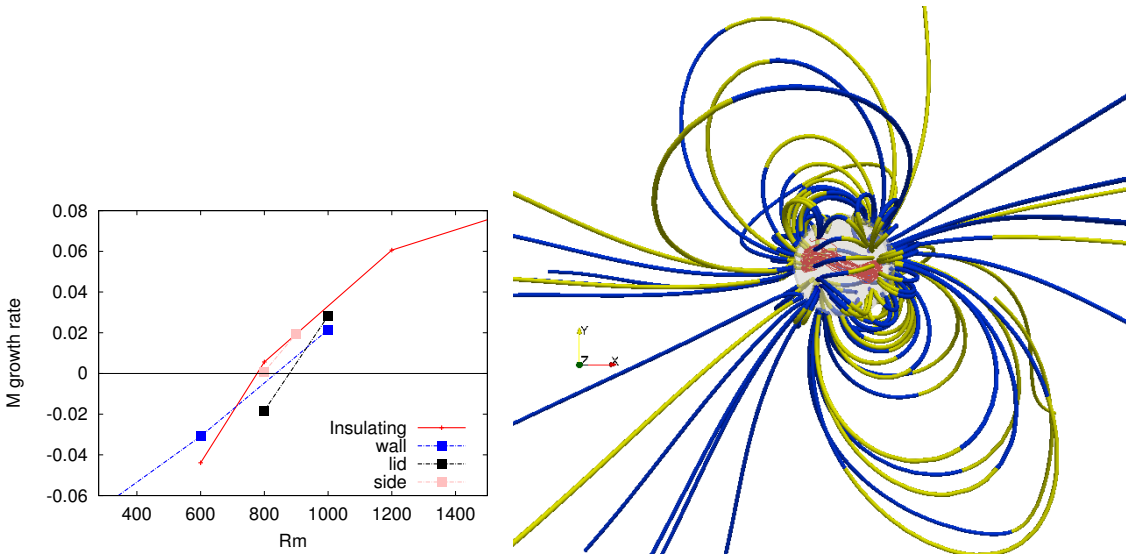

(a) Growth rates vs. R_m (b) Snapshot for the 'wall' case with $\mu_r = 65$

Figure 4.36: Ferromagnetic walls: (a) Growth rates of the magnetic field energy as a function of R_m for various configurations. The values are for $R_e = 1200$ and the thickness of either ferromagnetic wall type is taken as $0.1R$, with a relative conductivity $\sigma_r = 1$ and relative magnetic permeability $\mu_r = 65$. (b) Snapshot at $R_e = 1200$, $R_m = 1000$ for the 'wall' case showing vorticity field lines (red lines inside the cylinder) and magnetic field lines colored by the axial component [yellow (blue) for positive (negative) h_z component]. View from the top.

4.2.4.2 Equatorial spin case

We now want to test if the equatorial spin case with a higher level of asymmetric energy is more efficient for dynamo action than the axial case. For that purpose, various MHD runs are performed at $R_e = 1200$ for different values of the magnetic Reynolds numbers R_m as in [83]. The onset of dynamo action is monitored by recording the time evolution of the magnetic energy in the conducting fluid $M(t)$. Two types of simulations are done: linear dynamo runs are first performed by imposing $\mathbf{B} = 0$ in equation (4.2.5), i.e., the retroaction of the Lorentz force on the velocity field is disabled; then the Lorentz force is restored to observe the nonlinear saturation and the full system of equations (4.2.5,4.2.2,4.2.3,4.2.2) is integrated.

4.2.4.2.1 Linear regime A first series of linear dynamo simulations is done with $R_m = 1200, 2000$ and 2400. The time evolution of $M(t)$ is shown in figure 4.37a. The initial velocity and magnetic field for the runs at $R_m = 2000$ and 2400 are the velocity and the magnetic fields obtained from the run at $R_m = 1200$ at time $t = 282$. Dynamo action occurs when $M(t)$ is an increasing function of time for large times with a positive growthrate (as is the case for $R_m = 2400$). Linear interpolation of the growthrates gives the critical magnetic Reynolds number $R_{\mathrm{m}}^c \approx 2130$ at $R_e = 1200$, i.e., the critical magnetic Reynolds number is almost three times larger than that in the axial spin case (see section 4.2.4.1.1).

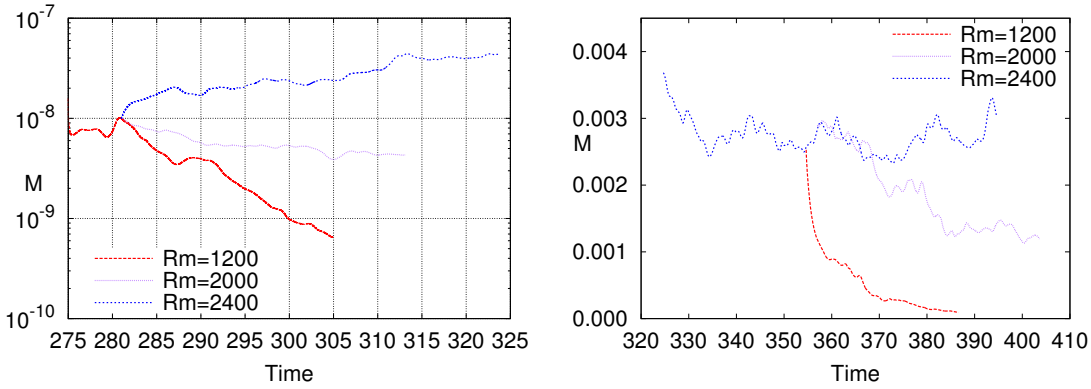

(a) $M(t)$ in linear regime (b) $M(t)$ in nonlinear regime

Figure 4.37: Equatorial spin case: Time evolution of the magnetic energy $M(t)$ in the conducting fluid (a) in the linear regime from $t = 275$ at $R_e = 1200$ and various R_m as indicated (in lin-log scale) and (b) in the nonlinear regime.

4.2.4.2.2 Nonlinear regime To observe the nonlinear saturation, we use as initial data the velocity and magnetic fields from the linear MHD run at $t = 323$ for $R_m = 2400$ (see figure 4.37a). The amplitude of the initial magnetic field is multiplied arbitrarily by 200 to reach saturation faster; the initial velocity field is kept unchanged. Figure 4.37b shows that $M(t)$ decreases rapidly over a time period corresponding to one turnover time, i.e., until $t = 329$, and begins to oscillate thereafter. After restarting the MHD run at $t = 357$ with $R_m = 2000$ and running it until $t = 405$, we observe that $M(t)$ decreases with time. After restarting the MHD run at $t = 355$ with $R_m = 1200$ and running it until $t = 387$, we observe that the dynamo dies in a short time lapse. A snapshot of the vorticity and the magnetic field lines at $R_e = 1200$ and $R_m = 2400$ is shown on figure 4.38. We observe a central S-shaped vortex deformed by the precession and connected to the walls through viscous boundary layers. The magnetic energy is dominated by the azimuthal modes $m = 1, 2, 3$ and the magnetic field lines exhibit a complex shape.

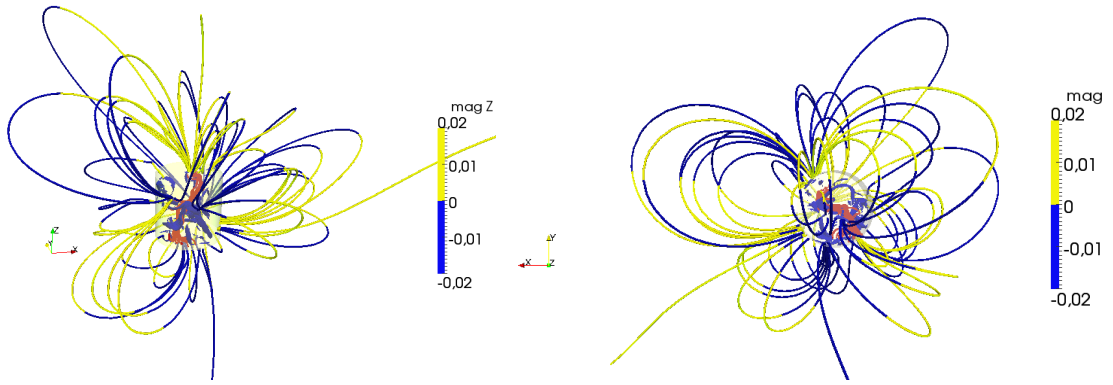

(a) from the side (b) from the top

Figure 4.38: (Color on line) Equatorial spin case: snapshot at $t = 395$ at $R_e = 1200$ and $R_m = 2400$ of the vorticity field lines (grey/red) and the magnetic field lines colored by the axial component (light grey/yellow for positive axial magnetic field component and black/blue for negative axial magnetic field component). (a) The view is seen from the side (Ox is the spin axis, Oz the precession axis), (b) from the top.

4.2.4.3 Discussion about mean flows induced by the two spinning ways at $R_e = 1200$

Since the two spinning ways for precession forcing lead to different dynamo properties, it seems discerning to compare the mean flows at play in these two cases. Figure 4.31a shows that the kinetic energy azimuthal spectra at $R_e = 1200$ are different for the two forcings, with much more energy in the high azimuthal modes for the equatorial spin case. Although comparing unidirectional spectra is straightforward with our hybrid code, this comparison is limited since the symmetry axis for the equatorial spin case may not be relevant (as is clearly seen in a stratified medium when the reference axis is chosen perpendicular to the effective gradient). Moreover comparing the flows in the physical space is not an easy task since it needs to take into account their full 3D geometry and time dependence. Figure 4.30b shows indeed that the two forcings lead to highly different time regimes of the total kinetic energy. Another possibility is to resort to the time-averaged flows over several turns from figure 4.30b. Figure 4.39 reveals a rather structured large-scale flow for the axial spin case while no coherent feature is apparent in the equatorial spin case. This lack of large coherent scale flow may contribute to enhance the dynamo threshold in the equatorial spin case.

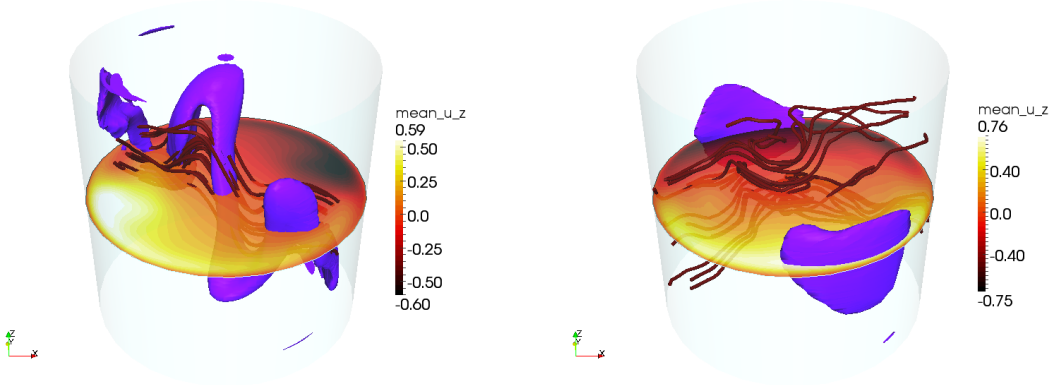

(a) axial spin (b) equatorial spin

Figure 4.39: (Color on line) Time-averaged velocity field at $R_e = 1200$ for the axial and equatorial spin cases: vorticity field lines (red/dark grey), contours of the axial velocity component in the equatorial plane and isosurface of $|\mathbf{u}|^2$: (a) axial spin case (with $|\mathbf{u}|^2$ at 0.3% of maximum in the precession frame), (b) equatorial spin case (with $|\mathbf{u}|^2$ at 70% of maximum in the wall frame).

4.2.5 Conclusion

Using numerical simulations, we have extended the scope of precession forcing in hydrodynamic and magnetohydrodynamic regimes by assuming that the symmetry axis of a cylindrical container does not coincide necessarily with the spin axis. To reduce the parameter space, we have fixed the Poincaré number, the ratio of precession to spin rotation, to $\varepsilon = 0.15$ and chosen a container length equal to its diameter. We have considered only equatorial spin forcing besides the more conventional axial spin case, with a spin axis orthogonal to the precession axis. In the axial spin case, the kinetic energy in the precession frame decreases when the Reynolds number increases. It verifies a scaling law,

$R_e^{-0.48}$, which suggests that the dominant kinetic energy lies in a viscous boundary layer. Thus the numerical approach is in agreement with the experimental inhibition of the spin motion [82] observed at Reynolds numbers hundred times larger the ones computed in the present paper. In the resulting flow, the azimuthal speed decreases rapidly in the viscous boundary layer attached to the wall, while a 3D bulk flow involving axial velocities is formed. In the wall frame, kinetic energy appears to increase with the Reynolds number, since the bulk flow is nearly in counter-rotation with respect to the container frame.

Using equatorial spin forcing, kinetic energy is also increasing with the Reynolds number in the wall frame, indicating that the flow also tends to the rotation opposite to the spin motion. This fact suggests that the precession acts efficiently against the inertial forcing by the moving walls. At $R_e = 4000$, for example, kinetic energy is close to 90% of the one of solid body spin motion.

In the perspective of studying dynamo action, comparison of asymmetry ratio shows a saturation at rather low values, although different in the axial spin case (around 1.8%) and in the equatorial spin case (around 6%). Contrary to what could be expected from these results, the critical magnetic Reynolds number is found to be lower for the axial spin configuration than for the equatorial spin case. This result contradicts the intuition that wall-normal stress would enhance symmetry breaking and would favor dynamo action. Inspection of flows at $R_e = 1200$ reveals different features like more small-scales in the equatorial spin case with a less coherent large-scale flow.

Our results of varying wall properties of a cylinder precessing in the axial spin configuration are encouraging for the optimization of the critical magnetic Reynolds number for the planned experiment at DRESDYN, where magnetic Reynolds number as large as 700 are expected to be reached: it could be interesting to add an inner copper layer inside the stainless steel container. The question of self-excitation in a real precession experiment is far from being settled though.

4.2.6 Appendix: Stabilization method

As the Reynolds number is chosen beyond a few thousands, due to a lack of computational resources, dynamical scales smaller than the mesh scale appear in the flow. So large gradients, which produce even smaller scales by the action of nonlinearity, are not correctly represented by the mesh. As a consequence, numerical approximations accumulate energy that should have been dissipated. In order to expand the range of Reynolds numbers the code SFEMaNS can approximate, a stabilization method called entropy viscosity is implemented. This method was developed by J.-L. Guermond [37], [38], and consists of adding a local artificial viscosity made proportional to the residual of the Navier-Stokes equation 4.2.1 or 4.2.5. This artificial viscosity induces a diffusion proportional to the energy imbalance such that the action of unresolved scales is better represented.

To give technical details on the entropy viscosity definition, we consider a mesh $\mathcal{K}_\mathrm{h}$ of the domain made of cells K with local mesh-size h_K. We introduce a time-step $\tau > 0$ and set $\phi^n = \phi(n\tau)$ for any time-dependent function ϕ. Then we define the residual of the Navier-Stokes equation as follows:

$$\mathrm{Res}_{\mathrm{NS}}^n = \frac{\mathbf{u}^n - \mathbf{u}^{n-2}}{2\tau} + (\mathbf{u}^{n-1} \cdot \nabla)\mathbf{u}^{n-1} - \frac{1}{R_e}\Delta\mathbf{u}^{n-1} + \nabla p^{n-1} - \mathbf{f}^{n-1}, \tag{4.2.6}$$

where $\mathbf{f}$ takes into account the Coriolis, Poincaré and Lorentz forces depending of the problem setting (axial or equatorial spin cases). This residual is computed at each time

step and over every mesh cell. It allows us to introduce a local artificial viscosity, defined on each cell K by:

$$\nu^n_{R|K} = \frac{h_K^2 \|\mathrm{Res}^n_{\mathrm{NS}} \cdot \mathbf{u}^{n-1}\|_{\mathbf{L}^\infty(K)}}{\|\mathbf{u}^{n-1}\|^2_{\mathbf{L}^\infty(\Omega)}}. \tag{4.2.7}$$

The quantity $\nu^n_{R|K}$ is expected to be as small as the consistency error in smooth regions and to be large in the regions where the PDE is not well resolved. To avoid excessive dissipation and to be able to run with CFL numbers of order $\mathcal{O}(1)$, we define the entropy viscosity as follows:

$$\nu^n_{E|K} = \min\left(c_{\max} h_K \|\mathbf{u}^n\|_{\mathbf{L}^\infty(K)}, c_{\mathrm{e}} \nu^n_{R|K}\right), \tag{4.2.8}$$

with $c_{\max} \in (0, \frac{1}{2}]$ and $c_{\mathrm{e}} \in (0, 1]$ tunable constants. Technical details about $c_{\max}$ and c_{e} tuning are given in section 2.7 of [37]. Thus defined, the entropy viscosity does not perturb the approximations in smooth regions and is first order in regions with large gradients.

R_e	DNS/LES	τ	N_F	h_{bdy}	h_{int}
4000	DNS	10^{-3}	32	0.008	0.024
4000	LES	10^{-3}	24	0.0125	0.05
7500	LES	10^{-3}	32	0.008	0.04
10000	LES	10^{-3}	48	0.008	0.04
15000	LES	5.10^{-4}	64	0.005	0.02

Table 4.4: Space and time resolutions used for DNS and LES computations in the axial spin case. N_F represents the number of Fourier modes, τ the time step, h_{bdy} the mesh size near the walls of the cylinder and h_{int} the mesh size along the axis $r = 0$ used to approximate the pressure (the velocity field is approximated with cells twice smaller).

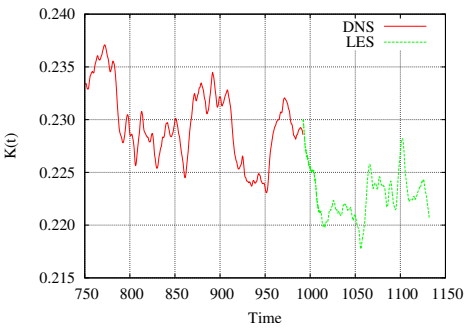

(a) Kinetic energy K

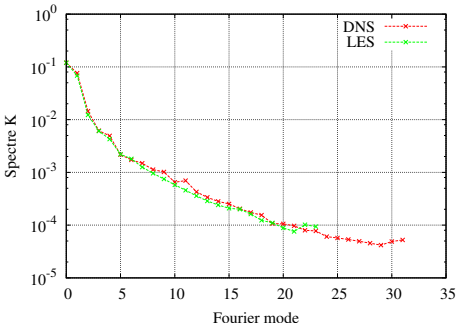

(b) Energy spectra at final time

Figure 4.40: Comparisons of DNS and LES results at $R_e = 4000$. (a) Evolution of total kinetic energy $K(t)$ (zoom of figure 4.24b), (b) kinetic erngy azimuthal spectra at final time as a function of the Fourier modes ($0 \leq m \leq 31$ with DNS and $0 \leq m \leq 23$ with LES).

For completeness we report in table 4.4 information on the spatial and time resolutions used for the hydrodynamic study of the axial spin case with $R_e \geq 4000$. We also provide a comparison of the kinetic energy and energy spectrum at final time of DNS and

LES computations with $R_e = 4000$ in figure 4.40 to enhance the correct behavior of the entropy viscosity method. As pointed out previously the kinetic energies of DNS and LES computations match up to a 2% relative error. Moreover the entropy viscosity manages to approximate correctly the energy spectrum of the DNS computation. It confirms that LES recovers a similar dynamics to the one approximated with DNS.

Acknowledgments The HPC resources for SFEMaNS were provided by GENCI-IDRIS (grant 2015-0254) in France and BRAZOS at TAMU. J.-L. Guermond acknowledges support from University Paris Sud and the National Science Foundation grant NSF DMS-1015984.

Momentum-based approximation of incompressible multiphase fluid flows

This chapter aims at extending the range of SFEMaNS code to multiphase flow problems. With that objective we present, in the form of an article in preparation, a new approximation method of such problems that we implement and numerically test with SFEMaNS code. This method combines a level set method, used to follow the evolution of the interface between two fluids that are assumed immiscible, and an approximation of the Navier-Stokes equations inspired of [41]. The method relies on the use of the momentum $\mathbf{m}$, equal to the density ρ times the velocity field $\mathbf{u}$, as a variable for the Navier-Stokes equations. As a consequence the mass matrix becomes time independent and can be treated implicitly. We note this would not be possible when using the velocity field as variable due to the evaluation of the product ρ with $\partial_t \mathbf{u}$. However the diffusive term, which involves the velocity, needs to be treated explicitly such that we can work with time independent algebra for computational efficiency purposes. While the treatment of the dissipation operator is described in section 2.5.1 and the following, we note that the main novelty of this method is to use the entropy viscosity to stabilize both the momentum and the mass (i.e level set) equations. As the energy equation associated to the momentum equation also contains information on the mass equation, we believe the entropy viscosity to be a perfect candidate to stabilize our equations and to reduce spurious oscillations generated when large ratios of density or viscosity are involved. After describing the method and presenting theoretical arguments to legitimate it under reasonable simplifying assumptions, the method is tested with numerous tests involving either gravity, rotational container, surface tension or MHD effects. Eventually we note that this method allowed us to perform a preliminary study of Liquid Metal Battery instability in Herreman et al [46].

Momentum-based approximation of incompressible multiphase fluid flows

L. Cappanera[1], J.-L. Guermond[1,2], W. Herreman[1] and C. Nore[1]

Abstract We introduce a time stepping technique using the momentum as dependent variable to solve incompressible multiphase problems. The main advantage of this approach is that the mass matrix is time-independent making this technique suitable for spectral methods. The method is validated by solving a wide range of problems going from manufactured solutions to a MHD problem with a liquid metal.

5.1 Introduction

Variable density flows and multi-fluid models are important in many applications ranging from geophysical flows to magnetohydrodynamics. Almost every solution method for incompressible flows currently available in the literature uses the velocity as dependent variable. As a consequence, when using finite elements, the mass matrix associated with the term $\rho\partial_t\mathbf{u}$ must be assembled at each time step, since the density, ρ, depends on time and space. Evaluating the product of ρ by $\partial_t\mathbf{u}$ can be expensive when using high-order elements, or cannot be made implicit when using spectral methods. We propose in the present paper to investigate an alternative formulation which consists of using the momentum as dependent variable, as routinely done in compressible fluid mechanics. This change of dependent variable is not simple, since the viscous dissipation depends on the velocity and thereby must be treated implicitly to avoid unreasonable time step restrictions. This obstacle is overcome by re-writing the dissipation appropriately and by accounting for the fact that the range of variation of the kinematic viscosity of many fluids and gases is smaller than that of the dynamic viscosity. In particular, denoting the momentum $\mathbf{m} := \rho\mathbf{u}$, we will rely on the fact that the dominating part of the viscous dissipation operator $-\nabla\cdot(\eta(\rho)\nabla^s\frac{\mathbf{m}}{\rho})$ can be re-written $-\nabla\cdot(\nu_{\max}\nabla^s\mathbf{m})+\nabla\cdot(\nu_{\max}\nabla^s\mathbf{m}-\eta(\rho)\nabla^s\mathbf{u})$. Under reasonable simplifying assumptions, it can be shown that provided $-\nabla\cdot(\nu_{\max}\nabla^s\mathbf{m})$ is made implicit, the correction $\nabla\cdot(\nu_{\max}\nabla^s\mathbf{m}-\eta(\rho)\nabla^s\mathbf{u})$ can be made explicit without compromising unconditional stability too much. This approach has also been used in [24]. The objectives of the present paper are to present this new method and to validate it against referenced cases mainly on hydrodynamic cases. We present also a magnetohydrodynamic case for a generalization to conducting fluids of our method.

The paper is organized as follows. We formulate the multiphase problem and introduce the level set technique in §5.2. The semi-discretization using the momentum as dependent variable is introduced in §5.3. A stability result in a simplified setting is given. The full discretization is described in §5.4. We show in particular in this section how the level set equation is stabilized by using an entropy-viscosity technique. The proposed technique is validated against analytical and manufactured solutions in §5.5. We solve Newton's bucket problem and a variation thereof in §5.6 and §5.7. The modeling of the

[1]Laboratoire d'Informatique pour la Mécanique et les Sciences de l'Ingénieur, CNRS UPR 3251, Rue John von Neumann, 91403 Orsay cedex, France and Université Paris-Sud

[2]Department of Mathematics, Texas A&M University 3368 TAMU, College Station, TX 77843-3368, USA

surface tension effects is validated in §5.8 by solving various classical benchmark problems involving bubbles. Finally we solve a multiphase MHD problem in §5.9.

5.2 The model problem

We introduce in this section the model problem and describe the level-set representation of the two phases composing the fluid.

5.2.1 The Navier-Stokes system

Consider a domain $\Omega \subset \mathbb{R}^d$, where $d = 2$ or 3, occupied by a variable density incompressible fluid. Denoting by ρ, $\mathbf{m}$ and p the density, momentum and pressure, the conservations of mass and momentum are expressed as follows:

$$\partial_t \rho + \nabla\cdot\mathbf{m} = 0 \tag{5.2.1a}$$

$$\partial_t \mathbf{m} + \nabla\cdot(\mathbf{m}\otimes\mathbf{u}) - \frac{2}{R_e}\nabla\cdot(\eta(\rho)\varepsilon(\mathbf{u})) + \nabla p = \frac{1}{W_e}\nabla\cdot\mathcal{S} - \frac{1}{F_r}\rho\mathbf{e}_z + \mathbf{f}, \tag{5.2.1b}$$

$$\nabla\cdot\mathbf{u} = 0, \tag{5.2.1c}$$

where $\mathbf{u} = \frac{1}{\rho}\mathbf{m}$ is the velocity, $\varepsilon(\mathbf{u}) = \nabla^s\mathbf{u} = \frac{1}{2}(\nabla\mathbf{u} + (\nabla\mathbf{u})^\mathsf{T})$ is the strain rate tensor and $\mathcal{S}$ is the volume distribution of surface tension. The scalar field $\eta(\rho)$ is the distribution of dynamic viscosity, which we assume to depend on ρ. The term $-\frac{1}{F_r}\rho\mathbf{e}_z$ is the buoyancy force; the unit vector $\mathbf{e}_z$ conventionally gives the upward direction. The quantity $\mathbf{f}$ is a yet undefined source term. The above equations are written in non-dimensional form. The reference length scale is denoted L_{ref}, the reference velocity is denoted U_{ref}; the reference time scale is then $L_{\text{ref}}/U_{\text{ref}}$. The reference density, dynamic viscosity, and surface tension coefficients are denoted ρ_{ref}, η_{ref}, and σ_{ref}, respectively. The Reynolds, Froude and Weber numbers are defined by

$$R_e = \frac{\rho_{\text{ref}}U_{\text{ref}}L_{\text{ref}}}{\eta_{\text{ref}}}, \qquad F_r = \frac{U_{\text{ref}}^2}{gL_{\text{ref}}}, \quad W_e = \frac{\rho_{\text{ref}}U_{\text{ref}}^2L_{\text{ref}}}{\sigma_{\text{ref}}}. \tag{5.2.2}$$

The above system is supplemented with initial and boundary conditions

$$\mathbf{u}_{|\Gamma} = \mathbf{v}, \qquad \mathbf{u}_{|t=0} = \mathbf{u}_0, \tag{5.2.3}$$

where Γ is the boundary of Ω. The initial velocity field $\mathbf{u}_0$ is assumed to be divergence free.

5.2.2 Level-set representation

We henceforth assume that the fluid is composed of two separate phases of (non-dimensional) density ρ_0, ρ_1 and dynamic viscosity η_0, η_1, and we propose to represent the density distribution by using a level set technique. Compared to front tracking techniques, level-set methods have the advantage of handling topology changes of interfaces easily, see e.g. [3, 73, 44, 103]. We then introduce the level-set function $\phi : \Omega \times [0, \mathrm{T}] \longrightarrow [0, 1]$ satisfying the following transport equation:

$$\partial_t\phi + \mathbf{u}\cdot\nabla\phi = 0, \qquad \phi_{|t=0} = \phi_0. \tag{5.2.4}$$

The domain is assumed to be closed and Γ is assumed to be a characteristics boundary, i.e., $\mathbf{u}\cdot\mathbf{n}|_\Gamma = 0$, which implies that there is no boundary condition on the level set function ϕ. The initial data ϕ_0 conventionally takes values in $[0,1]$. The density and the dynamical viscosity are reconstructed by means of the level set function as follows:

$$\rho = \rho_0 + (\rho_1 - \rho_0)F(\phi), \qquad \eta = \eta_0 + (\eta_1 - \eta_0)F(\phi). \tag{5.2.5}$$

Depending on the physical situation to be modeled, the user-defined reconstruction function F is either the identity, $F(\phi) = \phi$, or the piecewise polynomial function defined by

$$F(\phi) = \begin{cases} 0 & \text{if } \phi - 0.5 \le -c_{\text{reg}}, \\ \frac{1}{2}\left(1 + \frac{(\phi-0.5)((\phi-0.5)^2 - 3c_{\text{reg}}^2)}{-2c_{\text{reg}}^3}\right) & \text{if } |\phi - 0.5| \le c_{\text{reg}}, \\ 1 & \text{if } c_{\text{reg}} \le \phi - 0.5. \end{cases} \tag{5.2.6}$$

The user-defined coefficient c_{reg} is selected in the interval $(0, \frac{1}{2}]$; $c_{\text{reg}} = 0.4$ is a typical value regularly used. Note that these definitions imply that $\rho(\mathbf{x},t) \in [\rho_0, \rho_1]$ and $\eta(\rho) \in [\eta_0, \eta_1]$ for all $\mathbf{x} \in \Omega$ and all $t \in [0, \mathrm{T}]$, since (5.2.4) satisfies the maximum principle $\phi(\mathbf{x},t) \in [0,1]$ for all $\mathbf{x} \in \Omega$, $t \ge 0$.

The surface tension tensor $\mathcal{S}$ appearing in the momentum equation (5.2.1b) is expressed in terms of the level set function as follows:

$$\mathcal{S} = \frac{\nabla\phi \otimes \nabla\phi}{\|\nabla\phi\|} - \|\nabla\phi\|\mathcal{I}, \tag{5.2.7}$$

where $\mathcal{I}$ is the $d \times d$ identity matrix and $\|\cdot\|$ is the Euclidean norm.

Remark 5.2.1. The above setting can be generalized for stratification or inclusion of n fluids, $n \ge 3$, by considering $n-1$ level set functions $\phi_0, \ldots \phi_{n-2}$. In this case the density and viscosity are reconstructed by setting

$$\rho = \rho_0 + \sum_{i=0}^{n-2} (\rho_{i+1} - \rho_i)F(\phi_i), \qquad \eta = \eta_0 + \sum_{i=0}^{n-2} (\eta_{i+1} - \eta_i)F(\phi_i). \tag{5.2.8}$$

In case of surface tension effects, the volumic force $\mathcal{S}$ is rewritten $\mathcal{S} = \sum_{i=0}^{n-2} \mathcal{S}_i$ with $\mathcal{S}_i$ defined as in 5.2.7 with level set ϕ_i. This extension has been used to study the Tayler instability of Liquid Metal Batteries in [46].

5.3 Semi-discretization in time

We present in this section two time stepping algorithms, both inspired from [41]. The first one addresses the question of replacing the velocity by the momentum as dependent variable. The second shows a pressure splitting technique that requires solving a constant coefficient Poisson equation for the pressure correction instead of solving a variable coefficient Poisson equation as usually done in the literature.

5.3.1 Constant matrix diffusion on a model problem

We motivate the approach that we are going to adopt latter by considering the following model problem where the pressure is absent:

$$\partial_t \mathbf{m} + \tfrac{1}{2}\mathbf{m}\nabla\cdot\mathbf{u} + \mathbf{u}\cdot\nabla\mathbf{m} - \nabla\cdot(\eta\varepsilon(\mathbf{u})) = \mathbf{g}, \qquad \mathbf{m}_{|\Gamma} = 0, \qquad \mathbf{m}_{|t=0} = \mathbf{m}_0, \tag{5.3.1}$$

where ρ is a given scalar field that may depend on time and space. This equation is the prototype for the momentum equation where $\mathbf{g}$ collects the pressure gradient and other source terms from (5.2.1b). Note that the term $\frac{1}{2}\mathbf{m}\nabla\cdot\mathbf{u}$ is consistent since $\nabla\cdot\mathbf{u}=0$ a priori. The question that we want to address now is that of approximating (5.3.1) in time. Let $\tau>0$ be a time step, and let us set $t_n=n\tau$ for $n\geq 0$. For any time-dependent function $\phi(t)$ we set $\phi^n=\phi(t_n)$, and discrete time sequences are denoted by $\phi^\tau=\{\phi^n\}_{n\geq 0}$. Also to simplify notation, we define the following time-increment operators:

$$\delta^0\phi^n:=\phi^n;\quad \delta^1\phi^n:=\delta\phi^n:=\phi^n-\phi^{n-1};\quad \delta^k\phi^n:=\delta^{k-1}\phi^n-\delta^{k-1}\phi^{n-1},\quad k\geq 1. \tag{5.3.2}$$

We then propose the following discretization of (5.3.1): Set $\mathbf{m}^0=\mathbf{m}_0$, and for $n\geq 0$ set

$$\mathbf{m}^{\#n}:=\rho^{n+1}\mathbf{u}^n,\qquad \text{and}\qquad R^{n+1}:=\frac{1}{\rho^{n+1}}\left(\frac{\delta\rho^{n+1}}{\tau}+\mathbf{u}^n\cdot\nabla\rho^{n+1}\right), \tag{5.3.3}$$

and let $\mathbf{m}^{n+1}$ be the solution of

$$\frac{\delta\mathbf{m}^{n+1}}{\tau}+\tfrac{1}{2}\mathbf{m}^{n+1}(\nabla\cdot\mathbf{u}^n-R^{n+1})+\mathbf{u}^n\cdot\nabla\mathbf{m}^{n+1}-\bar\nu\nabla\cdot(\varepsilon(\mathbf{m}^{n+1}-\mathbf{m}^{\#n}))=\nabla\cdot(\eta^{n+1}\varepsilon(\mathbf{u}^n))+\mathbf{g}^{n+1}, \tag{5.3.4}$$

where $\bar\nu$ is a time-independent constant yet to be defined. We assume that the density is computed in such a way that the residual R^{n+1} is small, i.e., the term $\frac{1}{2}\mathbf{m}^{n+1}(\nabla\cdot\mathbf{u}^n-R^{n+1})$ is consistent. We also assume that the algorithm that produces the approximate density satisfies the maximum principle. More precisely, upon defining $\rho_{\min}=\operatorname{ess\,inf}_{\mathbf{x}\in\Omega}\rho_0(\mathbf{x})$ and $\rho_{\max}=\operatorname{ess\,sup}_{\mathbf{x}\in\Omega}\rho_0(\mathbf{x})$, we assume that

$$\rho_{\min}\leq\rho^n\leq\rho_{\max},\quad \forall n\geq 0. \tag{5.3.5}$$

As the dynamical viscosity is seen as a function of the density, we also assume that an analogous inequality can by written for η^n, $n\geq 0$.

In the rest of the paper we denote $\sigma=\sqrt{\rho}$. Note that the key adavantage of using the momentum as dependent variable is that the mass matrix becomes time-independent. Note also that the stiffness matrix associated with the fully discrete version of the algorithm (5.3.4) is time-independent.

Theorem 2. Let $\bar\nu:=\|\eta(\rho_0)/\rho_0\|_{L^\infty(\Omega)}$. Let $\gamma\in(0,1)$ be a constant. Assume that the time step is such that $\tau^{\frac{1}{2}}\bar\nu\|\frac{1}{\sqrt{\rho^n\eta^{n+1}}}\nabla\rho^{n+1}\|_{\mathbf{L}^\infty(\Omega)}\leq\gamma<1$ for all $n\geq 0$ and that the sequence ρ^τ is such that $\bar\nu\|\frac{\delta\rho^{n+1}}{\eta^{n+1}}\|_{L^\infty(\Omega)}\leq 1$ for all $n\geq 0$. Under the above assumptions, the sequence defined by the scheme (5.3.4) satisfies the following energy inequality for all $n\geq 0$:

$$\begin{aligned}\|\sigma^{n+1}\mathbf{u}^{n+1}\|^2_{\mathbf{L}^2(\Omega)}+\tau(1-\gamma^2)\|\sqrt{\eta^{n+1}}\varepsilon(\mathbf{u}^{n+1})\|^2_{\mathbf{L}^2(\Omega)}+\tau\bar\nu\|\sigma^{n+1}\varepsilon(\mathbf{u}^{n+1})\|^2_{\mathbf{L}^2(\Omega)}\\ \leq\|\sigma^n\mathbf{u}^n\|^2_{\mathbf{L}^2(\Omega)}+\tau\bar\nu\|\sigma^n\varepsilon(\mathbf{u}^n)\|^2_{\mathbf{L}^2(\Omega)}+2\tau\|\mathbf{g}^{n+1}\|_{\mathbf{L}^2(\Omega)}\|\mathbf{u}^{n+1}\|_{\mathbf{L}^2(\Omega)},\end{aligned} \tag{5.3.6}$$

and there is a constant $c>0$, that only depends on the shape of Ω, $\eta_{\min}$ and γ, such that

$$\|\sigma^{n+1}\mathbf{u}^{n+1}\|^2_{\mathbf{L}^2(\Omega)}\leq\|\sigma_0\mathbf{u}_0\|^2_{\mathbf{L}^2(\Omega)}+\tau\bar\nu\|\sigma^0\varepsilon(\mathbf{u}^0)\|^2_{\mathbf{L}^2(\Omega)}+c\tau\sum_{k=0}^{n}\|\mathbf{g}^{k+1}\|^2_{\mathbf{L}^2(\Omega)}. \tag{5.3.7}$$

Proof. Let us test the equation with $2\tau\mathbf{u}^{n+1}$. Upon noticing that $\varepsilon(\rho\mathbf{u}):\varepsilon(\mathbf{v})\leq\rho\varepsilon(\mathbf{u}):\varepsilon(\mathbf{v})+\|\mathbf{u}\|_{\ell^2}\|\nabla\rho\|_{\ell^\infty}\|\varepsilon(\mathbf{v})\|_{\ell^2}$ where $\|\mathbf{u}\|_{\ell^2}$ is the Euclidean norm of $\mathbf{u}$, $\|\varepsilon(\mathbf{v})\|_{\ell^2}$ is the induced

matrix norm of $\epsilon(\mathbf{v})$, and $\|\mathbf{w}\|_{\ell^\infty}$ is the max-norm of $\mathbf{w}$, we infer that

$$
\begin{aligned}
&2\int_\Omega \bar\nu\varepsilon(\mathbf{m}^{n+1}-\mathbf{m}^{\#n}):\epsilon(\mathbf{u}^{n+1})\,\mathrm{d}\Omega = 2\int_\Omega \bar\nu\varepsilon(\rho^{n+1}(\mathbf{u}^{n+1}-\mathbf{u}^n)):\epsilon(\mathbf{u}^{n+1})\,\mathrm{d}\Omega\\
&\geq 2\int_\Omega \bar\nu\rho^{n+1}\varepsilon(\delta\mathbf{u}^{n+1}):\epsilon(\mathbf{u}^{n+1})\,\mathrm{d}\Omega - 2\bar\nu\|\sigma^n\delta\mathbf{u}^{n+1}\|_{\mathbf{L}^2(\Omega)}\|\tfrac{1}{\sqrt{\rho^n\eta^{n+1}}}\nabla\rho^{n+1}\|_{\mathbf{L}^\infty(\Omega)}\|\sqrt{\eta^{n+1}}\varepsilon(\mathbf{u}^{n+1})\|_{\mathbf{L}^2(\Omega)}\\
&\qquad\geq \bar\nu\|\sigma^{n+1}\varepsilon(\mathbf{u}^{n+1})\|^2_{\mathbf{L}^2(\Omega)} - \bar\nu\|\sigma^{n+1}\varepsilon(\mathbf{u}^n)\|^2_{\mathbf{L}^2(\Omega)} + \bar\nu\|\sigma^{n+1}\varepsilon(\delta\mathbf{u}^{n+1})\|^2_{\mathbf{L}^2(\Omega)}\\
&\qquad\qquad - 2\bar\nu\|\sigma^n\delta\mathbf{u}^{n+1}\|_{\mathbf{L}^2(\Omega)}\|\tfrac{1}{\sqrt{\rho^n\eta^{n+1}}}\nabla\rho^{n+1}\|_{\mathbf{L}^\infty(\Omega)}\|\sqrt{\eta^{n+1}}\varepsilon(\mathbf{u}^{n+1})\|_{\mathbf{L}^2(\Omega)}.
\end{aligned}
$$

Moreover, using the following identities

$$
\begin{aligned}
&2\int_\Omega \delta\mathbf{m}^{n+1}\cdot\mathbf{u}^{n+1}\,\mathrm{d}\Omega = \|\sigma^{n+1}\mathbf{u}^{n+1}\|^2_{\mathbf{L}^2(\Omega)} - \|\sigma^n\mathbf{u}^n\|^2_{\mathbf{L}^2(\Omega)} + \|\sigma^n\delta\mathbf{u}^{n+1}\|^2_{\mathbf{L}^2(\Omega)} + \int_\Omega \|\mathbf{u}^{n+1}\|^2_{\ell^2}\delta\rho^{n+1}\,\mathrm{d}\Omega,\\
&\int_\Omega \big(\rho^{n+1}\mathbf{u}^{n+1}(\nabla\cdot\mathbf{u}^n - R^{n+1}) + 2\mathbf{u}^n\cdot\nabla\mathbf{m}^{n+1}\big)\cdot\mathbf{u}^{n+1}\,\mathrm{d}\Omega = \int_\Omega \|\mathbf{u}^{n+1}\|^2_{\ell^2}(\mathbf{u}^n\cdot\nabla\rho^{n+1} - \rho^{n+1}R^{n+1})\,\mathrm{d}\Omega,\\
&2\int_\Omega \eta^{n+1}\varepsilon(\mathbf{u}^n)\varepsilon(\mathbf{u}^{n+1})\,\mathrm{d}\Omega = -\|\sqrt{\eta^{n+1}}\varepsilon(\delta\mathbf{u}^{n+1})\|^2_{\mathbf{L}^2(\Omega)} + \|\sqrt{\eta^{n+1}}\varepsilon(\mathbf{u}^{n+1})\|^2_{\mathbf{L}^2(\Omega)} + \|\sqrt{\eta^{n+1}}\varepsilon(\mathbf{u}^n)\|^2_{\mathbf{L}^2(\Omega)},
\end{aligned}
$$

we obtain

$$
\begin{aligned}
&\|\sigma^{n+1}\mathbf{u}^{n+1}\|^2_{\mathbf{L}^2(\Omega)} + \|\sigma^n\delta\mathbf{u}^{n+1}\|^2_{\mathbf{L}^2(\Omega)} + \tau\|\sqrt{\eta^{n+1}}\varepsilon(\mathbf{u}^{n+1})\|^2_{\mathbf{L}^2(\Omega)} + \tau\|\sqrt{\eta^{n+1}}\varepsilon(\mathbf{u}^n)\|^2_{\mathbf{L}^2(\Omega)}\\
&\quad + \tau\bar\nu\|\sigma^{n+1}\varepsilon(\mathbf{u}^{n+1})\|^2_{\mathbf{L}^2(\Omega)} + \tau\bar\nu\|\sigma^{n+1}\varepsilon(\delta\mathbf{u}^{n+1})\|^2_{\mathbf{L}^2(\Omega)} \leq 2\tau\|\mathbf{g}\|_{\mathbf{L}^2(\Omega)}\|\mathbf{u}^{n+1}\|_{\mathbf{L}^2(\Omega)}\\
&\qquad + \|\sigma^n\mathbf{u}^n\|^2_{\mathbf{L}^2(\Omega)} + \tau\|\sqrt{\eta^{n+1}}\varepsilon(\delta\mathbf{u}^{n+1})\|^2_{\mathbf{L}^2(\Omega)} + \tau\bar\nu\|\sigma^{n+1}\varepsilon(\mathbf{u}^n)\|^2_{\mathbf{L}^2(\Omega)}\\
&\qquad\quad + 2\bar\nu\|\sigma^n\delta\mathbf{u}^{n+1}\|_{\mathbf{L}^2(\Omega)}\|\tfrac{1}{\sqrt{\rho^n\eta^{n+1}}}\nabla\rho^{n+1}\|_{\mathbf{L}^\infty(\Omega)}\|\sqrt{\eta^{n+1}}\varepsilon(\mathbf{u}^{n+1})\|_{\mathbf{L}^2(\Omega)},
\end{aligned}
$$

where we used that $\int_\Omega \|\mathbf{u}^{n+1}\|^2_{\ell^2}(\delta\rho^{n+1} + \tau\mathbf{u}^n\cdot\nabla\rho^{n+1} - \tau\rho^{n+1}R^{n+1})\,\mathrm{d}\Omega = 0$, owing to the definition of R^{n+1}. The assumed restriction on the time step, $\tau^{\frac12}\bar\nu\|\frac{1}{\sqrt{\rho^n\eta^{n+1}}}\nabla\rho^{n+1}\|_{\mathbf{L}^\infty(\Omega)} \leq \gamma < 1$, implies that

$$
\begin{aligned}
&2\tau\bar\nu\|\sigma^n\delta\mathbf{u}^{n+1}\|_{\mathbf{L}^2(\Omega)}\|\tfrac{1}{\sqrt{\rho^n\eta^{n+1}}}\nabla\rho^{n+1}\|_{\mathbf{L}^\infty(\Omega)}\|\sqrt{\eta^{n+1}}\varepsilon(\mathbf{u}^{n+1})\|^2_{\mathbf{L}^2(\Omega)}\\
&\qquad\leq \|\sigma^n\delta\mathbf{u}^{n+1}\|^2_{\mathbf{L}^2(\Omega)} + \tau^2\bar\nu^2\|\tfrac{1}{\sqrt{\rho^n\eta^{n+1}}}\nabla\rho^{n+1}\|^2_{\mathbf{L}^\infty(\Omega)}\|\sqrt{\eta^{n+1}}\varepsilon(\mathbf{u}^{n+1})\|^2_{\mathbf{L}^2(\Omega)}\\
&\qquad\qquad\leq \|\sigma^n\delta\mathbf{u}^{n+1}\|^2_{\mathbf{L}^2(\Omega)} + \gamma^2\tau\|\sqrt{\eta^{n+1}}\varepsilon(\mathbf{u}^{n+1})\|^2_{\mathbf{L}^2(\Omega)}.
\end{aligned}
$$

Note finally that the definition of $\bar\nu = \|\eta(\rho_0)/\rho_0\|_{L^\infty(\Omega)}$ together with the assumption $\rho_{\min} \leq \rho^{n+1} \leq \rho_{\max}$ implies that

$$
\|\sqrt{\eta^{n+1}}\varepsilon(\delta\mathbf{u}^{n+1})\|_{\mathbf{L}^2(\Omega)} \leq \bar\nu\|\sigma^{n+1}\varepsilon(\delta\mathbf{u}^{n+1})\|_{\mathbf{L}^2(\Omega)}.
$$

Using the assumption $\bar\nu\|\frac{\delta\rho^{n+1}}{\eta^{n+1}}\|_{L^\infty(\Omega)} \leq 1$, we infer that

$$
\begin{aligned}
\bar\nu\|\sigma^{n+1}\varepsilon(\mathbf{u}^n)\|^2_{\mathbf{L}^2(\Omega)} &\leq \bar\nu\|\sigma^n\varepsilon(\mathbf{u}^n)\|^2_{\mathbf{L}^2(\Omega)} + \bar\nu\|\tfrac{\delta\rho^{n+1}}{\eta^{n+1}}\|_{L^\infty(\Omega)}\|\sqrt{\eta^{n+1}}\varepsilon(\mathbf{u}^n)\|^2_{\mathbf{L}^2(\Omega)}\\
&\leq \bar\nu\|\sigma^n\varepsilon(\mathbf{u}^n)\|^2_{\mathbf{L}^2(\Omega)} + \|\sqrt{\eta^{n+1}}\varepsilon(\mathbf{u}^n)\|^2_{\mathbf{L}^2(\Omega)}.
\end{aligned}
$$

The inequality (5.3.6) follows readily by combining the above estimates. The estimate (5.3.7) is a consequence of a standard telescopic argument, the first Korn inequality $c_1\|\nabla\mathbf{u}^{n+1}\|_{\mathbf{L}^2(\Omega)} \leq \|\varepsilon(\mathbf{u}^{n+1})\|_{\mathbf{L}^2(\Omega)}$, the Poincaré inequality $c_2\|\mathbf{u}^{n+1}\|_{\mathbf{L}^2(\Omega)} \leq \|\nabla\mathbf{u}^{n+1}\|_{\mathbf{L}^2(\Omega)}$ and Young's inequality $2\|\mathbf{g}\|_{\mathbf{L}^2(\Omega)}\|\mathbf{u}^{n+1}\|_{\mathbf{L}^2(\Omega)} \leq \frac{1}{c_3}\|\mathbf{g}\|^2_{\mathbf{L}^2(\Omega)} + c_3\|\mathbf{u}^{n+1}\|^2_{\mathbf{L}^2(\Omega)}$ which holds for all $c_3 > 0$. The constant c in (5.3.7) can be chosen to be equal to $(c_1^2c_2^2\eta_{\min}(1-\gamma^2))^{-1}$. □

Remark 5.3.1. While the hypothesis $\tau^{\frac{1}{2}}\bar{\nu}\|\frac{1}{\sqrt{\rho^n\eta^{n+1}}}\nabla\rho^{n+1}\|_{\mathbf{L}^\infty(\Omega)} \leq \gamma < 1$ may be seen as a CFL-like condition on the time step τ, the hypothesis $\bar{\nu}\|\frac{\delta\rho^{n+1}}{\eta^{n+1}}\|_{L^\infty(\Omega)} \leq 1$ is far less restrictive. In principle both conditions can be checked a posteriori and the step $t_n \to t_{n+1}$ can be redone with a smaller time step if they are not satisfied.

5.3.2 Pressure splitting

In order to avoid the saddle point structure induced by the velocity-pressure coupling, we adopt a splitting technique *à la* Chorin-Temam. However, traditional extension of projection methods, i.e., those based on the Helmholtz decomposition $\mathbf{L}^2(\Omega) = \{\mathbf{v} \in \mathbf{L}^2(\Omega) \mid \nabla\cdot\mathbf{v} \in L^2(\Omega),\ \mathbf{v}\cdot\mathbf{n}_{|\Gamma} = 0\} \oplus \nabla H^1(\Omega)$, have the disadvantage that the pressure must be computed by solving at each time step an equation of the form

$$-\nabla\cdot\left(\frac{1}{\rho^k}\nabla\Phi\right) = \Psi, \tag{5.3.8}$$

which is more time consuming than solving a Poisson problem, see e.g. [11, 2, 39, 93]. The algebraic complexity of solving the discrete version of problem (5.3.8) is higher than that of a Poisson problem for two reasons: (i) the matrix associated with the discrete problem is time-dependent and thus must be re-assembled at each time step; (2) the linear system becomes ill-conditioned when the density contrast is high. It is possible to overcome this difficulty without sacrificing stability and accuracy by abandoning the standard projection paradigm as proposed in [40, 42], and this is the strategy that we now adopt.

The scheme, inspired from [41] consists of working with the level set sequence ϕ^τ plus four dependent variables: $(\mathbf{m}^\tau, \psi^\tau, p^\tau)$, where the sequence ρ^τ approximates the density, $\mathbf{m}^\tau$ the momentum, ψ^τ the pressure increment, and p^τ the pressure. The density ρ^τ and the dynamic viscosity η^τ are computed from the level set function, and the velocity is defined to be the ratio $\mathbf{m}^\tau/\rho^\tau$. We introduce the parameters

$$\bar{\nu} := \|\eta(\rho_0)/\rho_0\|_{L^\infty(\Omega)}, \quad \chi \in [0,1] \tag{5.3.9}$$

The scheme begins with a standard initialization step: $\mathbf{u}^0 = \mathbf{u}_0$, $p^0 = p_0$, $\psi^0 = p_0$, $\delta\psi^0 = 0$, and proceeds as follows:

Level set: Set $\phi^0 = \phi_0$ and for $n \geq 0$ compute ϕ^{n+1} by solving

$$\frac{\delta\phi^{n+1}}{\tau} + \mathbf{u}^n\cdot\nabla\phi^{n+1} = 0, \tag{5.3.10}$$

and reconstruct ρ^{n+1} and η^{n+1} by setting

$$\rho^{n+1} = \rho_0 + (\rho_1 - \rho_0)F(\phi^{n+1}), \qquad \eta^{n+1} = \eta_0 + (\eta_1 - \eta_0)F(\phi^{n+1}). \tag{5.3.11}$$

Momentum: Set $\mathbf{m}^0 = \mathbf{m}_0$ and for $n \geq 0$ set

$$\mathbf{m}^{\#n} := \rho^{n+1}\mathbf{u}^n, \quad p^{\sharp,n+1} = p^n + \psi^n \quad \text{and} \quad R^{n+1} := \frac{1}{\rho^{n+1}}\left(\frac{\delta\rho^{n+1}}{\tau} + \mathbf{u}^n\cdot\nabla\rho^{n+1}\right), \tag{5.3.12}$$

and let $\mathbf{m}^{n+1}$ be the solution of

$$\begin{aligned}&\frac{\delta\mathbf{m}^{n+1}}{\tau} + \frac{1}{2}\mathbf{m}^{n+1}(\nabla\cdot\mathbf{u}^n - R^{n+1}) + \mathbf{u}^n\cdot\nabla\mathbf{m}^{n+1} - 2\frac{\bar{\nu}}{R_e}\nabla\cdot(\varepsilon(\mathbf{m}^{n+1} - \mathbf{m}^{\#n})) + \nabla p^{\sharp,n+1}\\ &= \mathbf{f}^{n+1} + 2\frac{1}{R_e}\nabla\cdot(\eta^{n+1}\varepsilon(\mathbf{u}^n)) + \frac{1}{W_e}\nabla\cdot\left(\frac{\nabla\phi^{n+1}\otimes\nabla\phi^{n+1}}{\|\nabla\phi^{n+1}\|_{\ell^2}} - \|\nabla\phi^{n+1}\|_{\ell^2}\mathcal{I}\right) - \frac{1}{F_r}\rho^{n+1}\mathbf{e}_z,\end{aligned} \tag{5.3.13}$$

with appropriate boundary conditions on $\mathbf{m}^{n+1}$.
Penalty: Compute ψ^{n+1} by solving

$$\Delta\psi^{n+1} = \frac{\varrho_{\min}}{\tau}\nabla\cdot\mathbf{u}^{n+1}, \quad \partial_n\delta\psi^{n+1}_{|\Gamma} = 0. \tag{5.3.14}$$

Pressure update: Update the pressure

$$p^{n+1} = p^n + \psi^{n+1} + \chi\eta_{\min}q^{n+1}. \tag{5.3.15}$$

The above algorithm (minus the surface tension and buoyancy terms) has been investigated in [41] and shown therein to be stable under the time step restriction stated in Theorem 2 provided $\chi \leq \frac{1}{2}$. The restriction $\chi \leq \frac{1}{2}$ seems to be purely technical, and in practice we use $\chi = 1$.

5.4 Full discretization and stabilization

We describe the space discretization and the corresponding stabilization techniques in this section.

5.4.1 Space discretization

Let $(\mathcal{K}_h)_{h>0}$ be a mesh sequence for the domain $\Omega \subset \mathbb{R}^d$ that we assume to be affine and shape-regular in the sense of Ciarlet. The reference elements are denoted $\widehat{K}$, and the affine diffeomorphism mapping $\widehat{K}$ to an arbitrary element $K \in \mathcal{K}_h$ is denoted $\Phi_K : \widehat{K} \longrightarrow K$. In the simulation reported at the end of the paper are done with triangular elements, i.e., $\widehat{K} = \{(x_1, x_2) \in \mathbb{R}^2 \mid 0 \leq x_1;\ 0 \leq x_2;\ x_1 + x_2 \leq 1\}$. For each mesh cell $K \in \mathcal{K}_h$, we define the local mesh size h_K to be the smallest height of K. Let $k \geq 1$ be an integer. We define the following spaces:

$$X_h = \{\phi \in \mathcal{C}^0(\Omega;\mathbb{R}) \mid \phi_{|K}\circ\Phi_K \in \mathbb{P}_k,\ \forall K \in \mathcal{K}_h\}, \tag{5.4.1}$$

$$\mathbf{X}_h = \{\mathbf{v} \in \mathcal{C}^0(\Omega;\mathbb{R}^d) \mid \mathbf{v}_{|K}\circ\Phi_K \in \mathbb{P}_k,\ \forall K \in \mathcal{K}_h\}, \tag{5.4.2}$$

$$M_h = \{q \in \mathcal{C}^0(\Omega;\mathbb{R}) \mid q_{|K}\circ\Phi_K \in \mathbb{P}_{k-1},\ \forall K \in \mathcal{K}_h\}, \tag{5.4.3}$$

where $\mathbb{P}_k$ is the vector space of polynomials of total degree at most k. The spaces X_h and M_h are composed of scalar-valued functions whereas $\mathbf{X}_h$ is composed of vector fields. The pair $(\mathbf{X}_h, M_h)$ is the so-called Taylor-Hood approximation space, which is known to be stable to approximate the incompressible Navier-Stokes equations. The system of equations (5.3.10) to (5.3.15) are discretized by approximating $\phi^\tau, \rho^\tau, \eta^\tau$ in X_h, $\mathbf{m}^\tau, \mathbf{u}^\tau$ in $\mathbf{X}_h$, and $\psi^\tau, p^\tau, q^\tau$ in M_h.

5.4.2 Stabilization by entropy viscosity

In order to make the matrices in the level set equation (5.3.10) and the momentum equation (5.3.13) fully time-independent, the nonlinear terms are made explicit and the resulting equations are stabilized by adding some artificial viscosity that we call entropy viscosity, [37]. More precisely we compute at each time step and over each mesh cell the residual of the Navier-Stokes equations 5.3.13 by setting

$$\mathrm{Res}^n_{\mathrm{NS}} = \frac{\mathbf{m}^n - \mathbf{m}^{n-2}}{2\tau} + \nabla\cdot(\mathbf{m}^n \otimes \mathbf{u}^n) - \frac{2}{R_e}\nabla\cdot(\eta^n\varepsilon(\mathbf{u}^n)) + \nabla p^n - \mathbf{g}^n,$$

where $\mathbf{g}$ takes into account gravity, surface tension and all other possible source terms. We introduce a local artificial viscosity defined on each cell K by setting

$$\nu_{R|K}^n = \frac{h_K^2 \|\mathrm{Res}_{\mathrm{NS}}^n\|_{\mathbf{L}^\infty(K)}}{\|\mathbf{m}^n\|_{\mathbf{L}^\infty(\Omega)}}. \tag{5.4.4}$$

The quantity $\eta_{R|K}^n$ is expected to be as small as the consistency error in the smooth regions and to be large in the regions where the PDEs are not well resolved. To avoid excessive dissipation and to be able to run with CFL numbers of order $\mathcal{O}(1)$, we define the entropy viscosity as follows:

$$\nu_{E|K}^n = \min\left(c_{\max} h_K \|\mathbf{u}^n\|_{\mathbf{L}^\infty(K)}, c_{\mathrm{e}} \nu_{R|K}^n\right). \tag{5.4.5}$$

with $c_{\max} \in (0, \frac{1}{2}]$ and $c_{\mathrm{e}} \in (0, 1]$ tunable constants. In practice we take $c_{\max} = \frac{1}{2}$ for $\mathbb{P}_1$ finite elements and $c_{\max} = \frac{1}{8}$ for $\mathbb{P}_2$ finite elements. The entropy viscosity is small in smooth regions and is first-order in regions with large gradients.

The level set equation and the momentum equation are stabilized by adding the same artificial viscosity. We explain in §5.4.3 how it is done for the level set equation. The fully discrete momentum equation is reformulated as follows. Find $\mathbf{m}^{n+1} \in \mathbf{X}_h$ such that:

$$\begin{aligned}
&\int_\Omega \left(\frac{1}{\tau}(\mathbf{m}^{n+1} - \mathbf{m}^n)\cdot\mathbf{v} + 2\frac{\overline{\nu}}{R_e}\varepsilon(\mathbf{m}^{n+1} - \mathbf{m}^n):\varepsilon(\mathbf{v})\right) \mathrm{d}\Omega \\
&\quad = \int_\Omega \left(-\mathbf{v}\cdot\nabla(p^n + \psi^n) - \nabla\cdot(\mathbf{m}^n \otimes \mathbf{u}^n)\cdot\mathbf{v} - 2\frac{\eta^n}{R_e}\varepsilon(\mathbf{u}^n):\varepsilon(\mathbf{v}) - \nu_{\mathrm{E}}^n \nabla\mathbf{m}^n:\nabla\mathbf{v}\right) \mathrm{d}\Omega \\
&\quad + \int_\Omega \left(\left(\mathbf{f}^{n+1} - \frac{1}{F_r}\rho^{n+1}\mathbf{e}_z\right)\cdot\mathbf{v} - \frac{1}{W_e}\left(\frac{\nabla\phi^{n+1}\otimes\nabla\phi^{n+1}}{\|\nabla\phi^{n+1}\|_{\ell^2}} - \|\nabla\phi^{n+1}\|_{\ell^2}\mathcal{I}\right):\varepsilon(\mathbf{v})\right) \mathrm{d}\Omega,
\end{aligned} \tag{5.4.6}$$

for all $\mathbf{v} \in \mathbf{X}_h$. The fields ψ^{n+1}, p^{n+1} are computed by solving the discrete weak form (5.3.14) as follows. Find $\psi^{n+1} \in M_h$ such that:

$$\int_\Omega \nabla\psi^{n+1}\cdot\nabla r \,\mathrm{d}\Omega = \frac{\rho_{\min}}{\tau}\int_\Omega r\nabla\cdot\mathbf{u}^{n+1} \,\mathrm{d}\Omega, \quad \forall r \in M_h, \tag{5.4.7}$$

and find $p^{n+1} \in M_h$ such that:

$$\int_\Omega p^{n+1} r \,\mathrm{d}\Omega = \int_\Omega (p^n + \psi^{n+1} - \frac{\eta_{\min}}{R_e}\nabla\cdot\mathbf{u}^{n+1}) r \,\mathrm{d}\Omega, \quad \forall r \in M_h. \tag{5.4.8}$$

5.4.3 Compression technique for the level-set

In order to illustrate the efficiency of the entropy viscosity stabilization, we show in Figure 5.1 solutions of the transport equation $\partial_t\phi + \partial_x\phi = 0$ over the periodic domain $(0, 1)$ using $\mathbb{P}_1$ finite elements and the following approximation

$$\int_0^1 (\frac{\delta\phi^{n+1}}{\tau} + \partial_x\phi^{n+1}) r \,\mathrm{d}x + \int_0^1 \nu_{\mathrm{E}}\partial_x\phi^n\partial_x r \,\mathrm{d}x = 0, \qquad \forall r \in X_h \tag{5.4.9}$$

where $\nu_{E|K} = \min(\frac{1}{2}h_K, \frac{1}{2}\nu_{R|K}^n)$, and $\nu_{R|K}^n = \|\frac{\delta E(\phi^n)}{\tau} + \partial_x E(\phi^n))\|_{L^\infty(K)}$ with the entropy $E(\phi) = \log(|\phi(1-\phi)|)$. The initial data is $\phi_0(x) = 1$ if $0.4 \le x \le 0.7$ and $\phi_0(x) = 0$ otherwise. The mesh is composed of 100 cells, i.e., 100 grid points. Three solutions are computed at times $T = 1$, $T = 10$, and $T = 100$ in each panel. We show in the left

panel the solutions obtained by using the first-order viscosity only, i.e., $\nu_{E|K} = \frac{1}{2}h_K$, which corresponds to the upwind approximation in the finite difference and finite volume literature. The method is monotone but very diffusive; actually it is $\mathcal{O}(h^{\frac{1}{2}})$ accurate in the L^1-norm with this particular initial data. The solution computed with the entropy viscosity, i.e., $\nu_{E|K} = \min(\frac{1}{2}h_K, \frac{1}{2}\nu^n_{R|K})$, is shown in the central panel. The superiority of the entropy viscosity method over the first-order viscosity solution is clear. Note that, although the entropy viscosity is mainly localized in the two regions where the graph of the solution goes from 0 to 1, the dissipation accumulates in time and the graph of the approximate solution is eventually flattened.

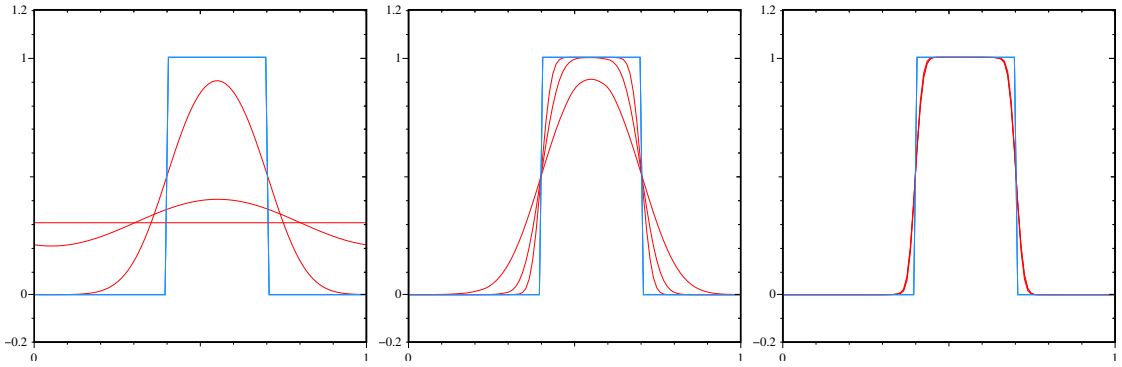

(a) First-order Visc. (b) Entropy visc. (c) Entropy visc. + comp.

Figure 5.1: Linear transport: exact and approximate solutions at $T = 1$, 10, 100.

To limit the flattening effect we introduce a nonlinear compression effect in the spirit of the artificial compression methods proposed by [45]. The original idea was to add an artificial compression step using a false-time iteration after every time step. This anti-diffusion step is called re-initialization in the level set literature and is often done by enforcing the level set function to be a signed distance function measuring the distance to the interface of interest. The compression mechanism then consists of making sure that $\|\nabla\phi\|_{\ell^2} = 1$ after each time step. Solution methods for Hamilton-Jacobi equations are usually employed to achieve this goal, see e.g. [102]. Since it is not really necessary that ϕ be a distance function, we prefer to adopt an approach coming from the shock-capturing literature, such as the artificial compression method of [88], and to combine the advection and the so-called re-initialization step into one single time step as done in [21, 22]. Assuming that the level set of interest is $\phi = \frac{1}{2}$, we propose to augment the level set equation with a term proportional to $\nabla\cdot(\phi(1-\phi)\mathbf{n})$, where $\mathbf{n}$ is the unit normal on the interface aligned with the gradient of ϕ. Since the gradient of ϕ is sensitive to $\mathcal{O}(h)$ errors, we compute a smooth version of the gradient by solving $\phi^n_{\text{reg}} \in X_h$ so that

$$\int_\Omega (w\phi^n_{\text{reg}} + 3h_{\text{reg}}\nabla\phi^n_{\text{reg}}\cdot\nabla w)\,\mathrm{d}\Omega = \int_\Omega w\phi^n\,\mathrm{d}\Omega, \quad \forall w \in X_h, \tag{5.4.10}$$

where $h_{\text{reg}} \in X_h$ is a regularized version of the mesh size. Denoting by $\{\mathbf{a}_i\}_{1\le i\le I}$ the collection of the Lagrange nodes associated with the space X_h, and $\Delta_i = \{K \in \mathcal{K}_h \mid \mathbf{a}_i \in K\}$ the collection of cells containing $\mathbf{a}_i$, we define $h_{\text{reg}} \in X_h$ so that $h_{\text{reg}}(\mathbf{a}_i) = \frac{1}{\text{card}(\Delta_i)}\sum_K h_K$. We then approximate the normal $\mathbf{n}$ by $\nabla\phi^n_{\text{reg}}/\|\nabla\phi^n_{\text{reg}}\|_{\ell^2}$. The level set $\phi^{n+1} \in X_h$ is computed

by solving

$$\int_\Omega \frac{\delta\phi^{n+1}}{\tau} r \,\mathrm{d}\Omega = \int_\Omega \left(-r\mathbf{u}^n\cdot\nabla\phi^n - \nu_{\mathrm{E}}^n \left(\nabla\phi^n - \frac{\mathrm{c_{comp}}}{h_{\mathrm{reg}}}\phi^n(1-\phi^n)\frac{\nabla\phi^n_{\mathrm{reg}}}{\|\nabla\phi^n_{\mathrm{reg}}\|}\right)\cdot\nabla r\right) \mathrm{d}\Omega, \tag{5.4.11}$$

where $\mathrm{c_{comp}}$ is a tunable constant that we choose in the interval $[0, 0.5]$.

Let us interpret the effect of the compression on the PDE corresponding to (5.4.11). Let $\mathbf{x}_0(t)$ be a point on the moving interface and assume that $\phi = \phi_{\mathrm{reg}}$, the velocity is locally constant in a neighborhood of $\mathbf{x}_0$, and $\phi(\mathbf{x}-\mathbf{u}t)$ is time-independent. Then denoting $\varphi(\mathbf{x}) = \phi(\mathbf{x}-\mathbf{u}t)$ and letting s be the signed distance along the normal direction, φ solves the following ODE, $\partial_s\varphi + \alpha\varphi(1-\varphi) = 0$, $\varphi(0) = \frac{1}{2}$, where $\alpha = \mathrm{c_{comp}}h_{\mathrm{reg}}^{-1}$. The solution is

$$\varphi(s) = \frac{1}{2}\left(1 + \tanh\left(\mathrm{c_{comp}}\frac{s}{h_{\mathrm{reg}}}\right)\right). \tag{5.4.12}$$

Hence at equilibrium, the compression balances exactly the artificial viscosity, and the level set adopts the classical hyperbolic tangent profile of width $h_{\mathrm{reg}}/\mathrm{c_{comp}}$.

Once ϕ^{n+1} is computed, the fluid's physical properties are updated by setting:

$$\rho^{n+1} = \rho_0 + (\rho_1-\rho_0)F(\phi^{n+1}), \qquad \eta^{n+1} = \eta_0 + (\eta_1-\eta_0)F(\phi^{n+1}), \tag{5.4.13}$$

where F is defined in 5.2.6.

5.4.4 Extension of the algorithm to the MHD setting

The MHD system is as follows:

$$\partial_t\rho + \nabla\cdot\mathbf{m} = 0 \tag{5.4.14a}$$

$$\nabla\cdot\mathbf{u} = 0, \tag{5.4.14b}$$

$$\partial_t\mathbf{m} + \nabla\cdot(\mathbf{m}\otimes\mathbf{u}) - \frac{2}{R_e}\nabla\cdot(\eta\varepsilon(\mathbf{u})) + \nabla p = \frac{1}{W_e}\nabla\cdot\mathcal{S} - \frac{1}{F_r}\rho\mathbf{e}_z + S\,(\nabla\times\mathbf{b})\times\mathbf{b}, \tag{5.4.14c}$$

$$\nabla\cdot\mathbf{b} = 0, \tag{5.4.14d}$$

$$\partial_t\mathbf{b} + \frac{1}{R_e^m}\nabla\times(\frac{1}{\sigma}\nabla\times\mathbf{b}) = \nabla\times(\mathbf{u}\times\mathbf{b}), \tag{5.4.14e}$$

where $\mathbf{b}$ is the magnetic induction and $S\,(\nabla\times\mathbf{b})\times\mathbf{b}$ the Lorentz force. Two new non-dimensional parameters appear: the magnetic Reynolds number $R_e^m = \mu_0\sigma_{\mathrm{ref}}L_{\mathrm{ref}}U_{\mathrm{ref}}$, which characterizes the ratio of the magnetic advection to the magnetic diffusion, and the coupling parameter $S = \frac{B_{\mathrm{ref}}^2}{\mu_0\rho_{\mathrm{ref}}U_{\mathrm{ref}}^2}$, which measures the ratio of the magnetic energy to the kinetic energy. Note that we only consider problems with constant magnetic permeability $\mu = \mu_0$. The electrical conductivity σ in the fluids is allowed to vary. The conductivity is reconstructed like the density and the dynamic viscosity with the level set and the function F defined in 5.2.6. As in the Navier-Stokes equations 5.2.1b, the diffusive term of Maxwell equations is rewritten: $\nabla\times(\frac{1}{\bar\sigma}\nabla\times\mathbf{b}) - \nabla\times((\frac{1}{\bar\sigma}-\frac{1}{\sigma})\nabla\times\mathbf{b})$ with $\bar\sigma \le \sigma_{\min}$. The term $\nabla\times(\frac{1}{\bar\sigma}\nabla\times\mathbf{b})$ is made explicit, whereas the term with variable conductivity $-\nabla\times((\frac{1}{\bar\sigma}-\frac{1}{\sigma})\nabla\times\mathbf{b})$ is made explicit in order to make the stiffness matrix of the problem time-independent.

5.4.5 Finite elements/Fourier expansion

The algorithms described above are implemented in a code called SFEMaNS, which the authors have been developing since 2003 in the context of a collaborative research program in MHD. The space discretization is hybrid and specialized to axisymmetric domains. It uses a Fourier decomposition in the azimuthal direction and the standard Taylor-Hood Lagrange elements $\mathbb{P}_1$-$\mathbb{P}_2$ in the meridian section (with $\mathbb{P}_1$ for the pressure, $\mathbb{P}_2$ for the velocity field and level-set, and either $\mathbb{P}_1$ or $\mathbb{P}_2$ for the magnetic field). The meridian mesh is composed of quadratic triangles.

The level set is approximated by using (5.4.11). The physical properties are reconstructed by using (5.4.13). The momentum and the pressure are computed by solving (5.4.6)–(5.4.8). The nonlinear terms are made explicit and approximated using second-order extrapolation in time. The code is parallelized in the Fourier space by using MPI and it is parallelized in the meridian sections by using the code METIS from [55] for the domain decomposition, and PETSC (Portable, Extensible Toolkit for Scientific Computation) [6] for the parallel linear algebra. The nonlinear terms are computed using a pseudo-spectral method and the fast Fourier transform subroutines from the FFTW3 package from [25]. The zero-padding technique (2/3-rule) is applied to prevent aliasing. We refer to [32, 33, 35] for more details on SFEMaNS.

5.5 Analytical tests

We test the accuracy of above algorithm (5.4.6)–(5.4.8), (5.4.11), (5.4.13), using either manufactured solutions or problems with analytical solutions.

5.5.1 Manufactured solution

In the first test we use a manufactured solution to evaluate the convergence properties of the above algorithm with respect to the time step and the mesh size. Using the cylindrical coordinates, (r, θ, z), the computational domain is the cylinder $\Omega = \{(r, \theta, z) \in [0, 1] \times [0, 2\pi) \times [0, 1]\}$ and the analytical solution is defined by

$$\phi(r, \theta, z, t) = r^2 + z^2, \qquad \mathbf{u}(r, \theta, z, t) = (0, r^2 \sin(t - z), 0)^{\mathsf{T}}, \qquad p = 0.$$

The source term $\mathbf{f}$ is computed accordingly. The surface tension and the buoyancy effects are not accounted for, i.e., $W_e = F_r = \infty$.

The tests are performed on three different grids composed of triangular meshes of typical mesh size $h = 0.1$, $h = 0.05$ and $h = 0.025$, respectively, (130, 478, 1850 triangles and 291, 1017, 3821 $\mathbb{P}_2$ grid points in the meridian section, respectively). Three time steps are tested: $\tau = 0.01$, $\tau = 0.005$, $\tau = 0.0025$. We use $R_e = 250$, $\rho_1 = 1$, $\rho_2 = 2$ and $\eta_1 = \eta_2 = 1$. The reconstruction is linear, i.e., $F(\phi) = 0$ if $\phi < 0$, $F(\phi) = \phi$ if $0 \leq \phi \leq 1$, and $F(\phi) = 1$ if $1 < \phi$. The error on the velocity in the $\mathbf{L}^2$-norm and $\mathbf{H}^1$-norm and on the level set and the pressure in the $\mathbf{L}^2$-norm are reported in Table 5.1 at time $t = 1$. We note that the error on the velocity and the pressure is mainly dominated by a time error as fixing the time step and refining the grid does not allow to improve errors. On the other hand the error in time is of order 1 which is consistent with our algorithm that uses BDF1 and first-order time extrapolation.

The above algorithm can be made second-order in time by using BDF2. We omit the details for brevity. We report the corresponding convergence tests in Table 5.2.

h \ τ	0.01	0.005	0.0025
0.1	1.806E-04	9.085E-05	4.557E-05
0.05	1.814E-04	9.115E-05	4.570E-05
0.025	1.817E-04	9.129E-05	4.575E-05

(a) $\mathbf{L}^2$-error on velocity.

h \ τ	0.01	0.005	0.0025
0.1	2.220E-03	1.119E-03	5.647E-04
0.05	2.253E-03	1.134E-03	5.691E-04
0.025	2.264E-03	1.139E-03	5.712E-04

(b) $\mathbf{H}^1$-error on velocity.

h \ τ	0.01	0.005	0.0025
0.1	1.309E-04	6.552E-05	3.281E-05
0.05	5.228E-05	2.581E-05	1.285E-05
0.025	2.566E-05	1.265E-05	6.289E-06

(c) $\mathbf{L}^2$-error on level set

h \ τ	0.01	0.005	0.0025
0.1	3.813E-05	1.920E-05	9.708E-06
0.05	3.813E-05	1.911E-05	9.575E-06
0.025	3.817E-05	1.913E-05	9.575E-06

(d) $\mathbf{L}^2$-error on pressure.

Table 5.1: Convergence tests using BDF1.

h \ τ	0.01	0.005	0.0025
0.1	2.925E-06	1.503E-006	1.362E-06
0.05	2.582E-06	6.573E-007	2.004E-07
0.025	2.579E-06	6.463E-007	1.612E-07

(a) $\mathbf{L}^2$-error on velocity.

h \ τ	0.01	0.005	0.0025
0.1	9.690E-05	8.949E-05	8.881E-05
0.05	3.880E-05	1.678E-05	1.426E-05
0.025	3.609E-05	9.297E-06	3.185E-06

(b) $\mathbf{H}^1$-error on velocity.

h \ τ	0.01	0.005	0.0025
0.1	3.483E-07	3.013E-07	2.9781E-07
0.05	1.657E-07	4.0411-08	1.5378E-08
0.025	1.691E-07	4.191E-08	1.0037E-08

(c) $\mathbf{L}^2$-error on level set

h \ τ	0.01	0.005	0.0025
0.1	2.341E-07	2.547E-07	2.760E-07
0.05	2.062E-07	4.308E-08	1.703E-08
0.025	2.206E-07	5.478E-08	1.299E-08

(d) $\mathbf{L}^2$-error on pressure.

Table 5.2: Convergence tests using BDF2.

5.5.2 Gravity waves

We test the BDF1 version of the above algorithm on a gravity wave problem with an exact solution. We consider a cylinder filled with two immiscible fluids of density $\rho_2 > \rho_1$. The light fluid of density ρ_1 is on top of the heavier fluid of density ρ_2. The two fluids are initially at rest with interface $z = 0$. The height of the top and bottom layers of fluid are H_1 and H_2, respectively. In the regime of infinitesimal displacements and zero viscosity ($R_e \to +\infty$), the motion of the fluid is described by the system

$$\rho\partial_t\mathbf{u} + \nabla P = -\rho g\mathbf{e}_z, \quad \nabla\cdot\mathbf{u} = 0, \quad \mathbf{u}\cdot\mathbf{n}|_\Gamma = 0$$

The pressure can be decomposed into its hydrostatic $-\rho gz$ and its fluctuating part p, i.e., $P = -\rho gz + p$. It is possible to find an exact solution of the problem in the limit of infinitesimal perturbations of the interface. For instance we define the following setting:

$$\mathbf{u}_j = \nabla\Phi_j, \text{ in fluids } j = 1, 2, \tag{5.5.1}$$

$$\Phi_1 = C_1(e^{-kH_1}e^{kz}+e^{kH_1}e^{-kz})J_m(kr)e^{im\theta}e^{i\omega t}, \quad \Phi_2 = C_2(e^{kH_2}e^{kz}+e^{-kH_2}e^{-kz})J_m(kr)e^{im\theta}e^{i\omega t}.$$

where J_m is the Bessel function of the first kind. So we can write:

$$\Phi_1 = C_1 \sinh(k(-H_1+z))J_m(kr)e^{im\theta}e^{i\omega t}, \quad \Phi_2 = C_2 \sinh(k(H_2+z))J_m(kr)e^{im\theta}e^{i\omega t}. \tag{5.5.2}$$

Radial boundary condition implies that k is a root of J'_m whose first values are reported in Table 5.3.

m	0	1	2	3	4
k_1	3.8317	1.8412	3.0542	4.2012	5.3176
k_2	7.0156	5.3314	6.7061	8.0152	9.2824

Table 5.3: First two roots of J'_m for various azimuthal Fourier modes.

The continuity of the normal component of the stress tensor across the fluids' interface gives the following dispersion relation:

$$\omega^2 = \frac{(\rho_2-\rho_1)gk}{\rho_1 \coth(kH_1)+\rho_2 \coth(kH_2)}. \tag{5.5.3}$$

We perform computations with perturbations on modes $m = 0, 1, 2$ with parameter $k = k_1, k_2$ for two sets of density ratio $\frac{\rho_2}{\rho_1}$. All the tests are done with the parameters

$$H_1 = H_2 = 1, \quad R = 1, \quad g = 9.81, \quad \rho_1 = 1, \quad R_e = 2{\times}10^4, \quad \eta_1 = \eta_2 = 1.$$

We use the time step $\tau = 5.10^{-3}$ and the mesh is locally refined in the vicinity of the interface: the mesh size is 1/320 at $z = 0$ and 0.1 at $z = \pm 1$ (19105 $\mathbb{P}_2$ grid points in the meridian section). Note that we use g rather that F_r because there is no reference velocity. The time evolution of the kinetic energy, which we use to estimate the frequency of the fluid motion, is plotted in Figure 5.2. Theoretical and numerical frequencies are reported in Table 5.4. We recover the theoretical values up to a relative error of order 1% to 3%.

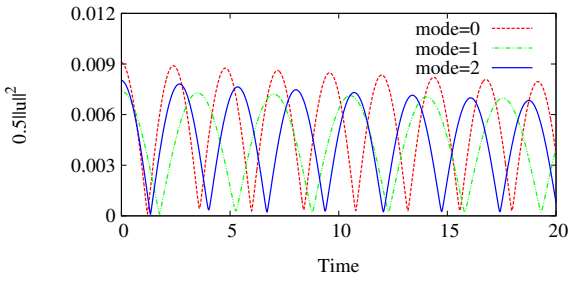

Figure 5.2: Time evolution of the kinetic energy for density ratio $\frac{\rho_2}{\rho_1} = 1.1$, using wave number k_1 and $R_e = 2{\times}10^4$.

5.6 Newton's bucket

We study the flow driven by a rotating cylindrical cavity with a free surface. Without surface tension, the free surface is governed by the equilibrium between gravity and the centrifugal force leading to the famous upward paraboloid profile. In the inertial frame,

m		0			1			2		
		Exact	Num.	Rel. Err	Exact	Num.	Rel. Err	Exact	Num.	Rel. Err
$\frac{\rho_2}{\rho_1} = 1.1$	$\omega(k_1)$	1.3373	1.309	2.1E-2	0.9044	0.896	1.E-2	1.1918	1.173	1.6E-2
	$\omega(k_2)$	1.8103	1.749	3.4E-2	1.5781	1.538	2.5E-2	1.7699	1.713	3.2E-2
$\frac{\rho_2}{\rho_1} = 2$	$\omega(k_1)$	3.5381	3.472	1.9E-2	2.3927	2.36	1.3E-2	3.1533	3.096	1.8E-2
	$\omega(k_2)$	4.7897	4.638	3.2E-2	4.1753	4.065	2.6E-2	4.6828	4.530	3.3E-2

Table 5.4: Frequencies for density ratio $\frac{\rho_2}{\rho_1} \in \{1.1, 2\}$ for azimuthal Fourier modes $m = 0, 1, 2$. Computations done with $R_e = 2\times10^4$.

the velocity is purely toroidal. In this section, we examine the influence of the modelling of the viscous term, i.e., by making the stress tensor proportional either to the gradient of the velocity $\nabla\mathbf{u}$ alone and or to the symmetric strain rate tensor $\nabla^s\mathbf{u}$. We also study the influence of the surface tension.

5.6.1 Physical setting

The equilibrium solution is axisymmetric, therefore we restrict our spectral computations to the $m = 0$ mode. We model this configuration by using two immiscible fluids of density $\rho_{\text{bot}} \gg \rho_{\text{top}}$ contained in a cylinder of radius R rotating at angular velocity Ω constant with respect to an inertial frame. The light fluid of density ρ_{top} is on top of the heavier fluid of density ρ_{bot}. Using the cylinder radius R as the characteristic length, ΩR as the characteristic velocity and the physical properties of the bottom fluid, the Froude, Reynolds and Weber numbers are defined by:

$$R_e = \frac{\rho_{\text{bot}}\Omega^2 R}{\eta_{\text{bot}}}, \qquad F_r = \frac{\Omega^2 R}{g}, \quad W_e = \frac{\rho_{\text{bot}}\Omega^3 R^2}{\sigma_{\text{bot}}} \tag{5.6.1}$$

In the following, all the quantities and equations are non-dimensional. We define $\rho_1 = \rho_{\text{top}}/\rho_{\text{bot}}$ and $\eta_1 = \eta_{\text{top}}/\eta_{\text{bot}}$.

5.6.2 Influence of Strain rate tensor

The two fluids are at rest at time $t = 0$ and their respective heights are H_1 and H_2. Therefore the initial interface is flat and located at $z = H_2$.

With no surface tension and $\rho_1 \longrightarrow 0$, the velocity field is purely toroidal with $\mathbf{u} = r\mathbf{e}_\theta$. The minimum water height is positive for small angular velocities ($F_r \leq F_r^c$), but a dry zone appears for higher angular velocities ($F_r > F_r^c$). The free surface elevation in non-dimensional units is given by:

$$\zeta(r) = \begin{cases} H_2 + \frac{F_r}{2}\left(r^2 - \frac{1}{2}\right) & \text{for} \quad F_r < F_r^c, \\ \max\left(0, \sqrt{H_2 F_r} + \frac{F_r}{2}(r^2 - 1)\right) & \text{for} \quad F_r \geq F_r^c. \end{cases} \tag{5.6.2}$$

In our setting the critical Froude number for no dry zone to appear is $F_r^c = 4H_2$. Note that this elevation does not depend on R_e since the viscosity only impacts the relaxation time needed to reach the equilibrium.

We use the following parameters: $H_2 = 0.5$, $\rho_1 = 1/1000$, $\eta_1 = 1/1000$, $R_e = 10^3$ and we perform two series of computations: one series with $F_r = 1 < F_r^c$ (wet case, i.e., no dry zone appear) and one series with $F_r = 2.5 > F_r^c$ (dry case, i.e., a dry zone is created). For

$F_r < F_r^c$ we set $H_1 = 0.5$ and we set $H_1 = 0.7$ otherwise. We have chosen $\rho_1 = \eta_1$ to have the same R_e in the two fluids. The wet case computations are performed with the time step $\tau = 10^{-3}$ and the $\mathbb{P}_1$ mesh size equal to 1/50 (11745 $\mathbb{P}_2$ grid points in the meridian section). The dry case computations are done with the time step $\tau = 10^{-3}$ and the $\mathbb{P}_1$ mesh size equal to 1/100 (58183 $\mathbb{P}_2$ grid points in the meridian section).

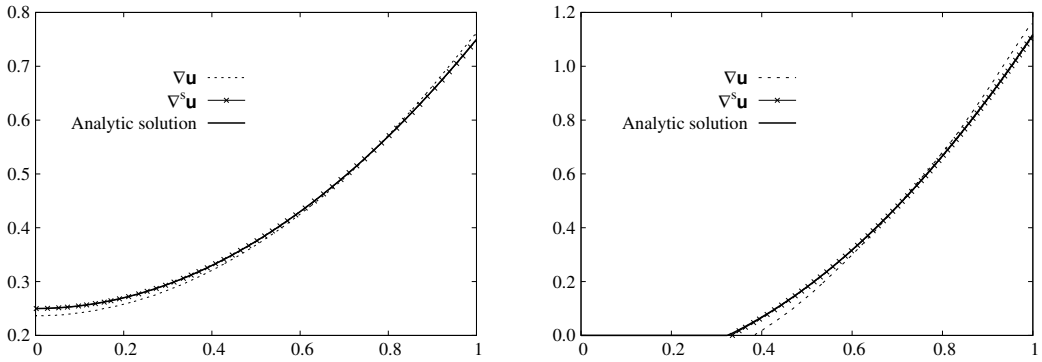

(a) $F_r = 1$ (b) $F_r = 2.5$

Figure 5.3: Free surface elevation $\zeta(r)$ for the Newton's bucket configuration: analytical solution (solid line), numerical solution with $\nabla \mathbf{u}$ (dotted line), numerical solution with $\nabla^s \mathbf{u}$ (symbol $\times$): (a) wet case, (b) dry case.

We compare in Figure 5.3 the analytical solution with the two numerical solutions obtained with $\nabla \mathbf{u}$ or $\nabla^s \mathbf{u}$ in equation (5.2.1b). The solution using $\nabla \mathbf{u}$ is below the analytical solution for $r < 0.6$ and above for $r > 0.6$ (the total mass is preserved). The solution using $\nabla^s \mathbf{u}$ is in excellent agreement with the analytical solution even near the rim of the cylinder. These results and the ones of section 5.7.2 show that it is necessary to use the symmetric strain rate tensor when η is variable.

5.6.3 Influence of the surface tension

In this section, we explore the effects of the surface tension on the surface elevation in the wet cases. The surface tension enters into the non-dimensional system via the Weber number only. We set $R_e = 10^3$, $F_r = 1.815$, $\eta_1 = 0.5284$, $\rho_1 = 0.5284$, $H_1 = H_2 = 0.75$ (corresponding to the two-fluid system considered in [15] except for the viscosity ratio which is $\eta_1 = 6.9124$ in their case). We consider four different values of the Weber number $W_e = 50, 114, 550$ and $W_e = \infty$ (zero surface tension). The analytical free surface profile for $W_e = \infty$ is given in (5.6.2). The computations are done with $\tau = 10^{-3}$ and the $\mathbb{P}_1$ mesh size is 1/50 at $r = 0$ and 1/100 at $r = 1$ (36110 $\mathbb{P}_2$ grid points in the meridian section).

The Results are shown in Figure 5.4. The agreement with the results reported in Figure 9 of [15] is excellent. The action of the surface tension significantly modifies the profile of the free surface. The free surface flattens as the surface tension increases and a meniscus appears at the rim of the cylinder.

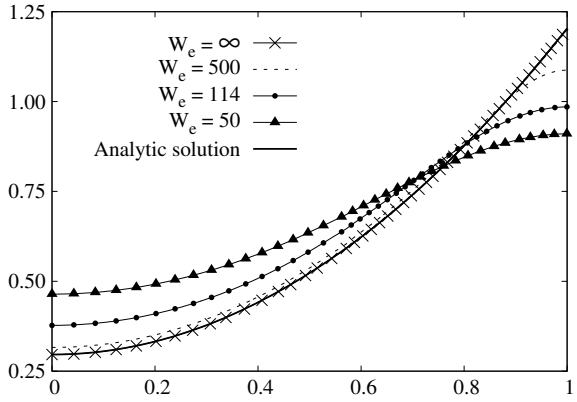

Figure 5.4: Free surface elevation $\zeta(r)$ for the Newton's bucket configuration using $\nabla^s\mathbf{u}$: analytical solution (solid line), no surface tension (symbol $\times$), with surface tension as indicated $W_e = 50, 114, 550$. Parameters are $R_e = 10^3$, $F_r = 1.815$, $\eta_1 = 0.5284$, $\rho_1 = 0.5284$, $H_1 = H_2 = 0.75$.

5.7 Free surface flow in an open cylinder

5.7.1 Physical setting

We study the flow driven by a rotating disk at the bottom of an open stationary cylindrical vessel. The steady axisymmetric solution is different from Newton's bucket paraboloid studied in the previous section since the lateral wall is motionless. We numerically compute the axisymmetric solution (i.e., using on the Fourier mode $m = 0$) and compare it with published numerical and experimental results.

5.7.2 Numerics vs. experiment

The free surface flow problem in an open cylinder with large free surface deformation has been investigated numerically and experimentally in [53]. We compare our numerical results to the numerical and experimental results obtained by [53]. The numerical method used therein consists of solving the steady axisymmetric Navier-Stokes equation projected onto a curvilinear coordinate system using a Newton-Raphson algorithm. In the experiment reported in [53] the vessel is filled with car engine oil and the surface elevation is measured by using a vertical needle reflected by the free surface acting as a mirror (see details in [53] and Figure 5.5a).

We model this flow using two immiscible fluids filling a cylinder of radius R with a large density ratio. We use the following parameters: $H_1 = 0.432$, $H_2 = 0.568$, $\rho_1 = 1.4\times10^{-3}$, $\eta_1 = 4\times10^{-2}$, $F_r = 1.435$ and $R_e = 1026$. The computations are performed with the time step $\tau = 10^{-3}$ and a $\mathbb{P}_1$ meshsize equal to 1/50 (11745 $\mathbb{P}_2$ grid points in the meridian section). The central panel in Figure 5.5 shows the free interface obtained by SFEMaNS using either $\nabla\mathbf{u}$ or $\nabla^s\mathbf{u}$ in the expression of the stress tensor; the symbol $*$ represent measurements. We compare in the right panel of Figure 5.5 the results from SFEMaNS with those from [53] . The agreement between SFEMaNS's numerical profile computed with $\nabla^s\mathbf{u}$ in the stress tensor and both the experimental data and the numerical profile obtained in [53] is excellent.

Figure 5.6 compares the axial profiles of the velocity at $r = 0.5$ obtained numerically in [53] with those obtained with SFEMaNS (using $\nabla^s\mathbf{u}$). As expected the azimuthal velocity

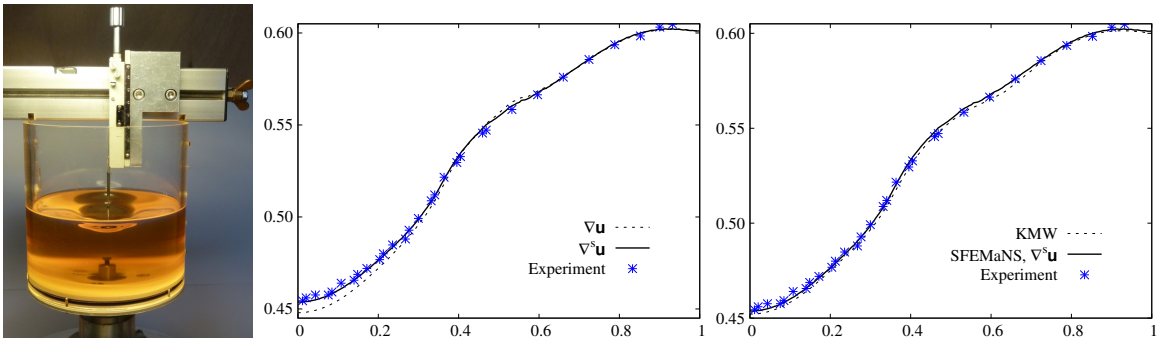

Figure 5.5: (a) Experimental set up with the needle measuring the free surface elevation (courtesy of L. Martin Witkowski); (b) Free surface elevation by SFEMaNS with $\nabla \mathbf{u}$ (dotted line) and $\nabla^s \mathbf{u}$ (solid line) and experimental results (symbol $*$); (c) Numerical solution by SFEMaNS with $\nabla^s \mathbf{u}$ (solid line), numerical (KMW, dotted line) and experimental (symbol $*$) results by [53].

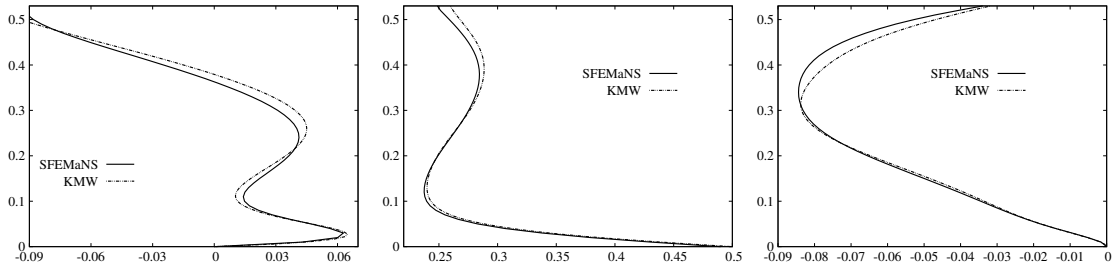

(a) $u_r(z)$ (b) $u_\theta(z)$ (c) $u_z(z)$

Figure 5.6: Velocity profiles at $r = \frac{1}{2}$ as a function of z: (a) $u_r(z)$, (b) $u_\theta(z)$, (c) $u_z(z)$. Comparisons between results from SFEMaNS, using the symmetric strain rate tensor $\nabla^s \mathbf{u}$, and numerical results by [53].

component dominates the other two components and the spatial distribution of the velocity field is non trivial. The maximum difference on the azimuthal profiles between the two computations is 1.5×10^{-2}; the relative difference is about 6% is the maximum norm

5.8 Bubbles

We investigate in this section the influence of the surface tension. We begin by studying the evolution of an axisymmetric bubble under the influence of the gravity with various ratios of density and dynamical viscosity. Then we study the behaviour of an oscillating bubble perturbed with a Fourier mode $m = 0$ or $m = 1$ without gravity.

5.8.1 Rising bubbles

To validate the surface tension effects implemented in SFEMaNS, we start with an axisymmetric rising bubble test case. We consider a spherical droplet of density ρ_2, initially at rest and of radius R, in an immiscible heavier surrounding fluid of density ρ_1. We follow the evolution of the bubble under the effect of gravity. This test is important because it is well documented (see [68, 48]).

We start with some test cases from [48] where various density and viscosity ratios are investigated. The reference parameters used in the following computations are $L_{\text{ref}} = R$

and $U_{\text{ref}} = \sqrt{gR}$ giving

$$R_e = \frac{\rho_1 g^{1/2} R^{3/2}}{\eta_1}, \qquad W_e = \frac{\rho_1 g R^3}{\sigma} \qquad F_r = 1. \tag{5.8.1}$$

Table 5.5 shows how to convert our definitions of R_e, W_e and F_r into those from [48] . The computational domain is a cylinder of height 24 and radius 8; the $\mathbb{P}_1$ meshsize is 1/20 for $0 \leq r \leq 2$ and $0.5in$ for $r = 8$ (121247 $\mathbb{P}_2$ grid points in the meridian section); the time step used for the computations is $\tau = 10^{-3}$. We use only the Fourier mode $m = 0$ since the solution is axisymmetric.

Reference parameters	L_{ref}	U_{ref}	Computation parameters	R_e		W_e	F_r
SFEMaNS	R	$\sqrt{gR}$	SFEMaNS	4.93	3.09	29	1
Hua-Lou	D=2R	$\sqrt{gD}$	Hua-Lou	13.95	8.75	116	1

Table 5.5: Reference parameters used for non-dimensionalization in SFEMaNS and [48] and comparison of computation parameters.

The first test is done by setting $R_e = 4.93$, $W_e = 29$ and using the large ratios $\rho_1/\rho_2 = 10^3$ and $\eta_1/\eta_2 = 10^2$. The time evolution of the velocity of the bubble and its final shape, shown in Figure 5.7, are qualitatively very similar to those reported in Figure 4 of [48]. The relative difference on the terminal velocity of the bubble is 1.4% (0.7 versus $0.502 \times \sqrt{2} = 0.71$) and the shape of the bubble matches in height and width the results from [48].

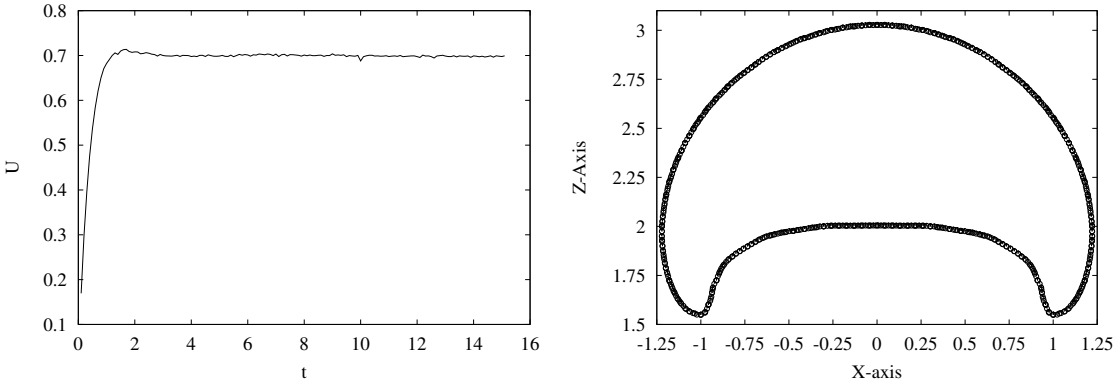

(a) Time evolution of the bubble velocity (b) final profile of the bubble

Figure 5.7: Computation with $\frac{\rho_1}{\rho_2} = 10^3$, $\frac{\eta_1}{\eta_2} = 10^2$, $R_e = 4.93$ and $W_e = 29$ corresponding to $R_e = 13.95$ and $W_e = 116$ in [48].

In the second test we set $R_e = 3.09$ and $W_e = 29$, and we investigate the influence of the density and viscosity ratios. The density and viscosity ratios studied are $\{2, 10^3\}$ and $\{2, 10^2\}$, respectively. The final shape of the bubble is shown in Figure 5.8 and the final velocity of the bubble is reported in Table 5.6. These results can be compared to Figures 17 and 19, and Figure 18 and 20 of [48]. The overall shape (height and width) is well recovered. The differences on the final velocity are between 1.4% and 5%. We conclude that our method correctly approximates axisymmetric problems with surface tension effects.

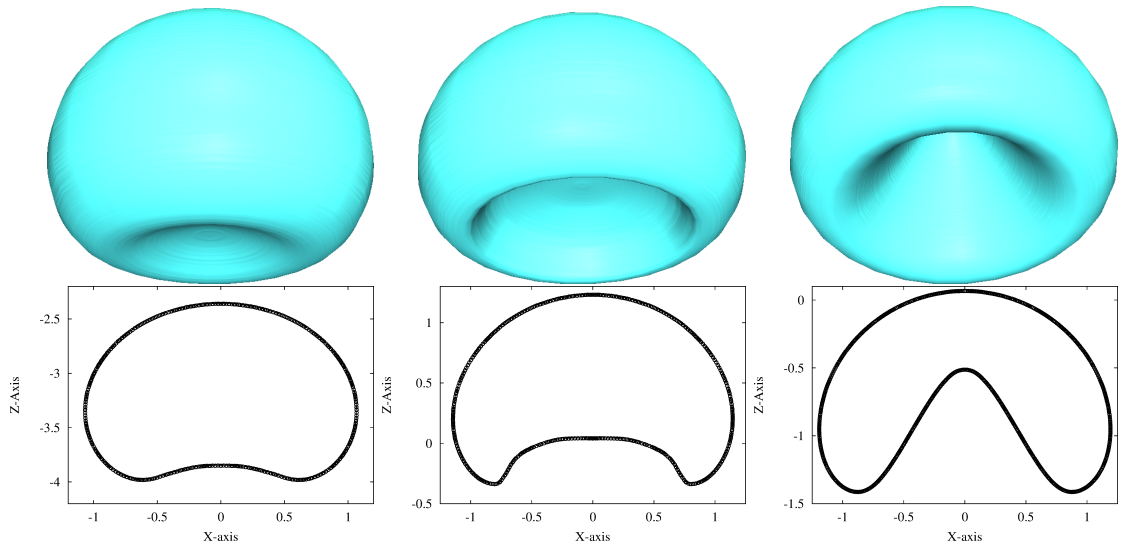

(a) $\frac{\rho_1}{\rho_2} = 2, \frac{\eta_1}{\eta_2} = 10^2$ (b) $\frac{\rho_1}{\rho_2} = 10^3, \frac{\eta_1}{\eta_2} = 10^2$ (c) $\frac{\rho_1}{\rho_2} = 10^3, \frac{\eta_1}{\eta_2} = 2$

Figure 5.8: (Top) 3D isocontour of level set ($\phi = 0.5$). (Bottom) Bubble profiles along r and z axis. Computations done with $R_e = 3.09$ and $W_e = 29$ and various density and viscosity ratio

Fluid parameters	$\frac{\rho_1}{\rho_2} = 2, \frac{\eta_1}{\eta_2} = 10^2$	$\frac{\rho_1}{\rho_2} = 10^3, \frac{\eta_1}{\eta_2} = 10^2$	$\frac{\rho_1}{\rho_2} = 10^3, \frac{\eta_1}{\eta_2} = 2$
final bubble velocity (SFEMaNS)	0.339	0.576	0.487
final bubble velocity (Hua-Lou)	0.346	0.585	0.513
Relative difference	2%	1.5%	5.1%

Table 5.6: Final velocity $\frac{U}{(gR)^{1/2}}$ with $R_e = 3.09$ and $W_e = 29$.

5.8.2 Oscillating bubbles

We now study how a bubble immersed in a quiescent fluid with no gravity oscillates. It is again a classical test case (number 5 in [68]). The inner and outer fluids are immiscible and of density ρ_i and ρ_o, respectively. The initial perturbations of the spherical shape of radius R are supposed to be small and, in the case of inviscid fluids, the analytical formula for the oscillation frequency and shape of the interface are given by [65]:

$$\omega_n^2 = \frac{n(n+1)(n-1)(n+2)}{(n+1)\rho_i + n\rho_o} \frac{\sigma}{R^3} \tag{5.8.2}$$

$$r_s(\theta, \chi, t) = R[1 + \epsilon\, Y_{mn} sin(\omega_n t)], \tag{5.8.3}$$

ϵ is the amplitude of the perturbation and Y_{mn} are the spherical harmonics:

$$Y_{mn}^o = \sin(m\theta) P_n^m(\cos\chi) \tag{5.8.4}$$

$$Y_{mn}^e = \cos(m\theta) P_n^m(\cos\chi), \tag{5.8.5}$$

where $n \in \mathbb{N}$, m is the azimuthal Fourier mode, θ the azimuth, χ the colatitude and P_n^m the Legendre functions.

We neglect gravity and use the radius of the undeformed bubble R as the characteristic length and the physical properties of the inner fluid as reference properties. We define a

Reynolds number that compares the surface tension and the viscosity effects:

$$Re_{\rm st} = \sqrt{\rho_i R \sigma_i}/\eta_i. \tag{5.8.6}$$

Not that viscosity effects decrease when $Re_{\rm st}$ increases.

We set $\rho_1 = \rho_o/\rho_i = 1$, $\eta_1 = \eta_o/\eta_i = 1$ and focus on perturbations with the mode $n = 2$. We perform axisymmetric computations with various values of $Re_{\rm st} \in \{20, 50, 100, 500, 1000\}$ and a perturbation on the Fourier $m = 0$ with $\epsilon = \{0.1, 0.5\}$. The computations are done with the time step $\tau = 10^{-3}$ and the $\mathbb{P}_1$ meshsize is $1/25$ in the bubble ($r^2 + z^2 \leq 1$) and 10 at the boundary of the computational domain $r^2 + z^2 = 40^2$ (51877 $\mathbb{P}_2$ grid points in the meridian section).

The theoretical period from (5.8.2) is $T = 2.9$. We show in the left panel of Figure 5.9 the time evolution of the L^2-norm of the velocity Fourier mode $m = 0$ computed in SFEMaNS with $Re_{\rm st} \in \{20, 50, 100, 500, 1000\}$. We observe that the signal varies in time with the half-period as expected. Note that we recover the theoretical value of the frequency only for $500 \leq Re_{\rm st}$; for smaller Reynolds numbers the oscillations are slower due to viscous effects, e.g. for $Re_{\rm st} = 20$ the period is around 3.3 which is 13% higher than the theoretical one.

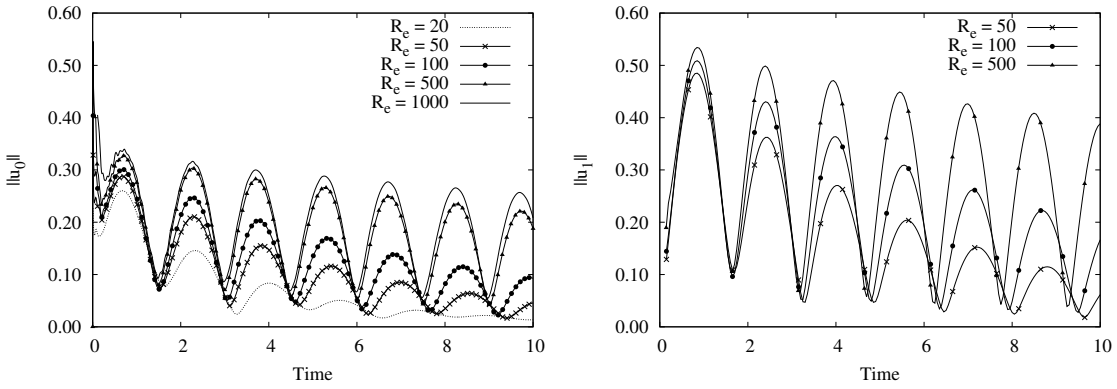

(a) Axisym. computations with Y_{02} perturbation. (b) 3D computations with Y_{12} perturbation.

Figure 5.9: Time evolution of the L^2-norm of (a) velocity mode $m = 0$ and (b) velocity mode $m = 1$ for $\epsilon = 0.1$ at different Reynolds numbers.

We also do fully 3D computations using 32 Fourier modes with the perturbation $\epsilon = 0.1$ on the Fourier mode $m = 1$ on the spherical harmonics Y_{12}. Since the theoretical frequency (5.8.2) does not depend on the azimuthal mode number we should recover the period $T = 2.9$ obtained in the axisymmetric computations. We show in the right panel of Figure 5.9 the time evolution of the L^2-norm of the Fourier $m = 1$ of the velocity for $Re_{\rm st} \in \{50, 100, 500\}$. As expected we observe that the period is close to 2.9 for $Re_{\rm st} = 500$. This tests validates or 3D computations.

We now investigate the effect of a large initial deformation $\epsilon = 0.5$ in the axisymmetric configuration, i.e., the perturbation is done on the spherical harmonics Y_{02}. We show in Figure 5.10 the time evolution of the radial velocity obtained with $\epsilon = 0.5$ and $\epsilon = 0.1$. The nonlinear effects are large when $\epsilon = 05$; as a result, the period and the amplitude of the oscillations are increased. Snapshots of the bubble are shown in the top right and bottom panels of Figure 5.10.

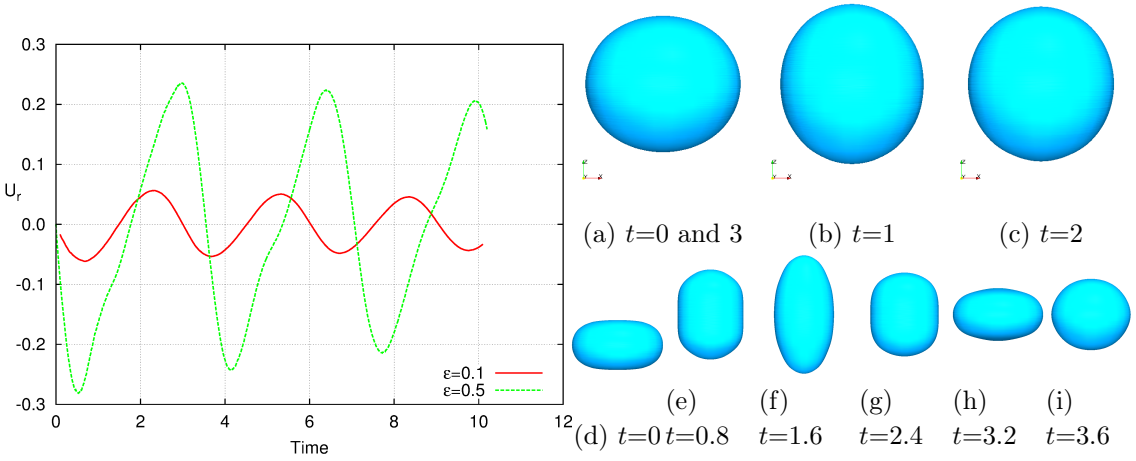

Figure 5.10: Left: Time evolution of the radial velocity of the $m = 0$ mode for $\epsilon = 0.1$ and $\epsilon = 0.5$ at $Re_{\text{st}} = 500$. Right: Snapshots of the bubble for $\epsilon = 0.1$ ((a) to (c)) and $\epsilon = 0.5$ ((d) to (i))

5.9 Liquid metal droplet falling in a vertical magnetic field

We now consider a two-phase flow in the presence of a magnetic field. We first reproduce published results of [108] based on the Navier-Stokes equations with a simplified Lorentz force, then we consider the full magnetohydrodynamic (MHD) problem. We assume that the problem is axisymmetric and compute only the Fourier mode $m = 0$.

5.9.1 Physical configuration

We study the influence of an imposed vertical magnetic field on a liquid metal droplet submitted to gravity. We use the same configuration as [108]: a spherical liquid metal droplet of radius R is released in the air from the height $4R$ above a pool of liquid metal contained in a cylindrical container of radius $R_c = 6R$ and height $H = 6R$. The thickness of the liquid layer at the bottom of the vessel is $3R/8$. The droplet has no initial velocity and is accelerated downwards by gravity (see Figure 5.11). It is also submitted to a vertical magnetic field which slows its fall.

We perform three series of computations to compare the dynamics of the falling droplet. In the first two cases, we only solve the Navier-Stokes equations (5.2.1) and in the third case we solve the full MHD equations (5.4.14). The reference length scale is the initial radius of the droplet $L_{\text{ref}} = R$ and the reference velocity is the falling speed $U_{\text{ref}} = \sqrt{gR}$. The reference density and dynamic viscosity are chosen to be those of the liquid phase. Therefore $F_r = 1$ for us and the relations with the nondimensional parameters used in [108] are

$$R_e = \frac{1}{2^{3/2}} \frac{\rho_L}{\rho_G} \frac{\eta_G}{\eta_L} G^{1/2}, \qquad W_e = \frac{\rho_L}{4\rho_G} \frac{G}{\Gamma}, \tag{5.9.1}$$

where ρ_G, ρ_L are the gas and liquid densities, η_G, η_L are their dynamic viscosities, G is the Galilei number characterizing the ratio of the gravitational and viscous forces, and Γ is the ratio of the surface tension and viscous forces. Using the parameters of [108] , $G = 3\times10^6, \Gamma = 2\times10^5, \rho_L/\rho_G = 10^2$ and $\eta_L/\eta_G = 55.6$, we get $R_e = 1101.4$ and $W_e = 375$. We have used two meshes: one with uniform $\mathbb{P}_1$ meshsize $h = 1/40$ (66941 $\mathbb{P}_2$ grid points in the

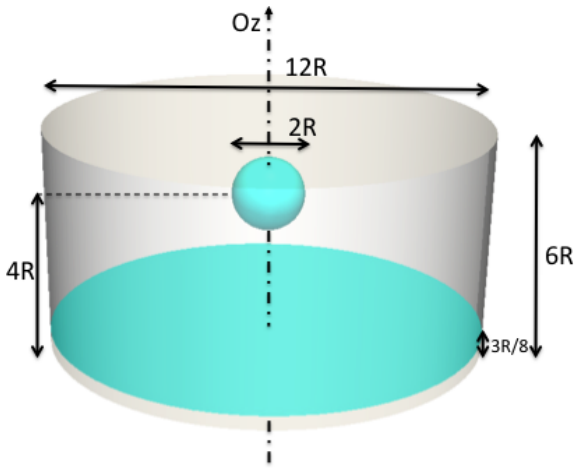

Figure 5.11: Schematic model for a liquid metal droplet falling under the action of gravity in a pool of liquid metal.

meridian section) and another one with a non-uniform $\mathbb{P}_1$ mesh-size ranging from $h = 1/200$ near the vertical axis to $h = 1/40$ on the lateral side ($253983\mathbb{P}_2$ grid points in the meridian section). The time-step is $\tau = 10^{-3}$. We have not observed any noticeable differences on the results between the two meshes. Supplementary nondimensional parameters are introduced in each case as needed.

5.9.2 Falling droplet under gravity

For the first case, the additional force $\mathbf{f}$ in (5.2.1b) is zero and no magnetic field is imposed. We let the liquid droplet fall in the pool under the sole action of gravity. The spherical droplet accelerates downward and then collides the flat liquid surface at the bottom of the vessel. The impact of the droplet on the flat liquid surface occurs at $t = 3$. Surface waves are created and these waves bounce back and forth on the lateral side of the pool as seen on the left panel of Figure 5.12, (only a quarter of the total domain is shown). The profile of the free surface at $t = 4$ and $t = 8$ is shown in the center and right panels of Figure 5.12. Dewetting occurs approximately at $t = 8$.

The time evolution of the square of the L^2-norm of the velocity field is reported in Figure 5.13a, see label 'Grav'.

5.9.3 Lorentz force as an external force

We now add a vertical magnetic field which induces a Lorentz force in the right-hand side of (5.2.1b):

$$\mathbf{f} = (\nabla\times\mathbf{b})\times\mathbf{b} = \sigma(\mathbf{E} + \mathbf{u}\times\mathbf{b})\times\mathbf{b}, \tag{5.9.2}$$

where $\mathbf{b}$ is the applied magnetic induction, σ is the electrical conductivity of the fluid and $\mathbf{E}$ is the electric field. As in [108], we first neglect the induced magnetic field and the force is simplified into

$$\mathbf{f}_{\text{Lo}} = -\sigma u_r b_0^2 \mathbf{e}_r. \tag{5.9.3}$$

This force is only radial and depends on the amplitude of the applied magnetic field b_0. With our nondimensional units, we need to define a new nondimensional parameter denoted

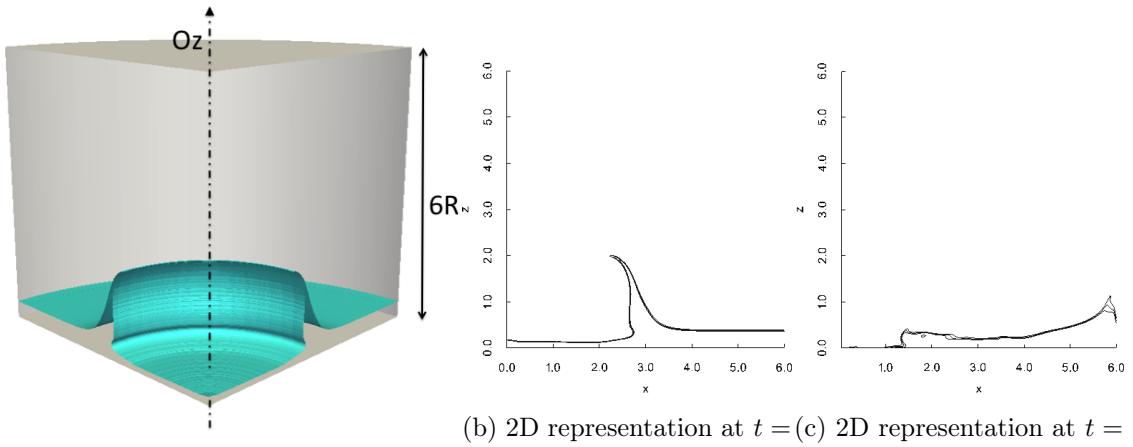

(a) 3D representation at $t = 4$

(b) 2D representation at $t = 4$

(c) 2D representation at $t = 8$

Figure 5.12: Droplet falling under the sole action of gravity with $R_e = 1101.4$ and $W_e = 375$ at time $t = 4$ and $t = 8$. Density varies between 10^{-2} (in white) to 1 (in black). (a) shows a 3D representation of the isocontour $\phi = 0.5$, while (b) and (c) display only a meridional plane with the vertical axis on the left and the lateral side of the box on the right.

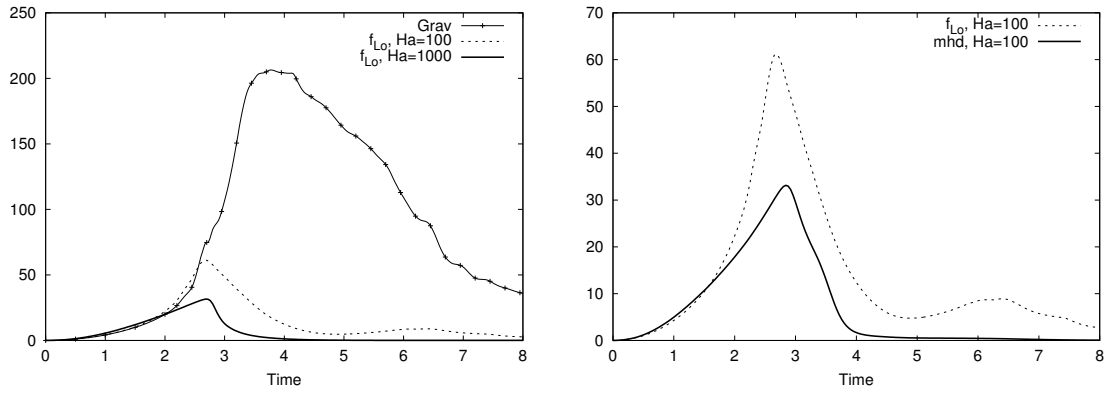

Figure 5.13: Time evolution of the L^2-norm of the velocity field under different conditions: 'Grav' with gravity only, '$f_{\mathrm{Lo}}, Ha = 100$' and '$f_{\mathrm{Lo}}, Ha = 1000$' for the simplified Lorentz force with $Ha = 100$ or 1000, 'mhd, $Ha = 100$' for the MHD system with $Ha = 100$.

Lo:

$$\mathrm{Lo} = \frac{\sigma_{\mathrm{ref}} b_0^2 L_{\mathrm{ref}}}{\rho_{\mathrm{ref}} U_{\mathrm{ref}}} = \frac{Ha^2}{4R_e}, \qquad \mathrm{Ha} = \sqrt{\frac{\sigma_{\mathrm{ref}}}{\eta_{\mathrm{ref}}}} b_0 L_{\mathrm{ref}}. \tag{5.9.4}$$

Ha is the Hartmann number which characterizes the ratio of the electromagnetic and viscous forces.

We choose the liquid electrical conductivity and the liquid dynamic viscosity as references. In [108] two values of Hartmann number are investigated, Ha = 100 and 1000, which correspond to Lo = 2.27 and Lo = 227 respectively. We model the gas as a weakly conducting fluid such that $\sigma_G/\sigma_L = 10^{-2}$. The time evolution of $\frac{1}{2}\int \|\mathbf{u}\|^2 \, \mathrm{d}x$ is reported in Figure 5.13a. The snapshots of the free surface shown in Figure 5.14 are similar to Figures 3 and 4 of [108]. the braking effect of the Lorentz force for Ha = 100 is less pronounced than for Ha = 1000. The action of the Lorentz force is so strong when Ha = 1000 that no surface wave is generated and the droplet forms a bulge which slowly disappears in time. Note that a gas pocket is captured under the droplet for Ha = 1000.

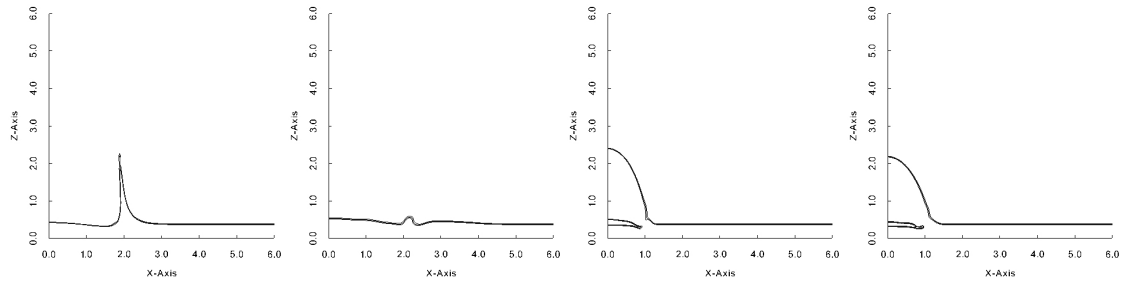

(a) Ha = 100 and $t = 4$ (b) $Ha = 100$ and $t = 8$ (c) $Ha = 10^3$ and $t = 4$ (d) $Ha = 10^3$ and $t = 8$

Figure 5.14: Falling droplet under gravity and magnetic field with $R_e = 1101.4$, $W_e = 375$ and Ha = 100 (a,b) or Ha = 1000 (c,d) at time $t = 4$ and $t = 8$. Density varies between 10^{-2} (in white) to 1 (in black).

5.9.4 Full MHD setting

We now investigate a full MHD configuration using 5.4.14. In this setting, we take into account the retroaction of the velocity field on the magnetic induction and the induced current. We change the reference scale for $\mathbf{b}$ in order to take into account the imposed magnetic field $\mathbf{b}_0$. The coupling parameter becomes $S = \frac{\mathrm{Lo}}{R_e^m}$. We choose $R_e^m = 1$ and Lo = 2.27 (corresponding to the imposed magnetic field with Ha = 100).

The time evolution of $\frac{1}{2}\int \|\mathbf{u}\|^2 \, \mathrm{d}x$ is reported in Figure 5.13b. The downwards motion of the droplet is damped by the induced current which was neglected in the previous section. The two snapshots of Figure 5.15(a,b) are similar to the previous ones. The time evolution of $\int \|\mathbf{b}\|^2 \, \mathrm{d}x$ is shown in Figure 5.15c. A peak is observed at $t = 3.5$ when the azimuthal current is enhanced (see vectors on Figure 5.15d). Note that, with the simplified Lorentz force, no time variation of the current is possible since the magnetic field is prescribed.

5.10 Conclusion

A new time stepping technique using the momentum as dependent variable to solve incompressible multiphase problems has been introduced and validated. The method is inspired from [41], where its full stability analysis is performed. The key advantage of this approach is that the mass matrix is time-independent, which makes this technique suitable for spectral methods. The method has been validated by solving a wide range of problems going from manufactured solutions to a MHD problem with a liquid metal.

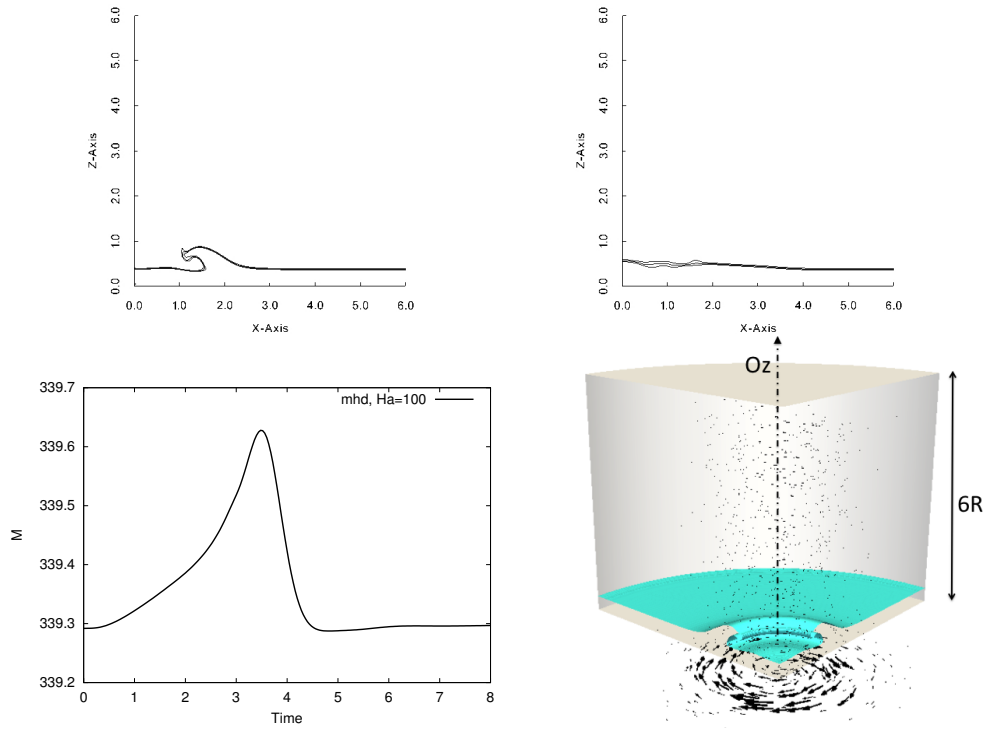

Figure 5.15: Full MHD setting plus gravity for the falling droplet with $R_e = 1101.4$, $W_e = 375$, Ha $= 100$ and $R_e^m = 1$ at $t = 4$ (a) and $t = 8$ (b). Density varies between 10^{-2} (in white) to 1 (in black) and is represented in a meridional plane with the vertical axis on the left and the lateral side of the box on the right. (c) Time evolution of the magnetic energy $M = \frac{1}{2}\int \|\mathbf{b}\|^2 \, \mathrm{d}x$. (d) Level-set isocontour $\phi = 0.5$ in blue (dark) and electric current vector fields at $t = 4$.

Conclusion and prospects

6.1 Outcome

All of the studies carried out in this PhD period have been motivated by upgrading the SFEMaNS MHD code. This project is in the continuity of the previous PhD thesis of R. Laguerre [63], A. Ribeiro [97], F. Luddens [74] that allowed the birth of SFEMaNS MHD code and its development into a massivelly parallel code that can approximate MHD problems involving thermodynamic effects or discontinuous magnetic permeability in the radial and vertical directions. In this content one of the objectives of this PhD was to add a stabilization method such that computations with parameters closer to the ones encountered in experiments can be considered. The other main goal consisted of extending the range of action of the SFEMaNS code to multiphase flow problems.

Our first objective was reached by implementing in SFEMaNS code a nonlinear stabilization method called entropy viscosity that induces a diffusion proportional to the unbalance of an energy equation. In order to attest the correct behavior of this method we performed studies of a Von Kármán Sodium (VKS) set up and precession cylinder problems that are both the subject of current or future experiments respectively in CEA Saclay (France) and Dresden (Germany). In one hand we showed the benefit of the entropy viscosity to approximate flows with under resolved meshes on a VKS set up by comparing LES and DNS results for moderate $R_e \leq 2500$. The entropy viscosity managed to match correctly the results of the DNS (performed on a finer mesh) while a computation with the same coarse grid without stabilization missed bifurcation in the energy spectrum. The numerical study of the problem for $R_e \leq 2500$ allowed to recover a scaling law of the torque in R_e^{-1} for low Reynolds numbers and known bifurcations in the energy spectrum for $R_e \in \{500, 1000\}$. Furthermore a preliminary study of the flow at $R_e = 5000$ recovers similar behavior of experimental and numerical studies [95, 96, 60]. As a consequence the entropy viscosity ended up to be a good candidate for LES computations and could be used to pursue this study at larger kinetic Reynolds numbers with under resolved meshes. On the other hand a previous hydrodynamical study of Nore et al [83] on an axial spin case precession problem has been expanded to a larger range of Reynolds numbers by using the entropy viscosity. After a validation of the model with DNS comparisons at $R_e = 4000$, LES computations for $R_e \leq 15000$ combined to previous results at smaller R_e enhanced a scaling law of the kinetic energy in the precession frame in $R_e^{-0.48}$. The flow was shown to tend to a solid body rotation in the wall frame which matches experimental results obtained for larger R_e in [82]. As a complement a second set up of precession, the equatorial spin

case, was also analyzed and a MHD study of both configurations with DNS was proposed to determine the most favorable one to the generation of magnetic field (dynamo effect). Although the equatorial spin case was proved to break the symmetry of the flow more easily, it was less favorable to dynamo effect. We also showed that the dynamo threshold may be reduced by using container with lateral walls in copper which may find echo in the preparation of future precession experiments in Dresden [105].

The extension of SFEMaNS code to multiphase flow problems involved the development of a new method of approximation for the Navier-Stokes equations with variable density. While we implemented a level set method to describe the evolution of the interface between two fluids, a few obstacles remained to approximate the Navier-Stokes equations. Since the density and viscosity are time and space dependent, using the velocity as variable would have induced a mass matrix and a diffusive operator depending on time and space. To work with time independent algebra, so the stiffness matrix of the problem is only assembled at initialization, we developed a method inspired of [41] that uses the momentum as variable. Thanks to this the mass matrix becomes time independent and the diffusive term is rewritten adequately so it can be treated explicitly. The main innovation of the method consisted in stabilizing both the momentum and the mass (level set) equations with the same viscosity entropy. As a consequence large ratios of density and viscosity can be taken into account. We note the addition of diffusion in the level set equation led us to add a compressive tool so it does not get flatten with time. Unlike many approaches which induce an extra step in the algorithm, this anti diffusion step is done when approximating the advection equation as in [21]. This method was then implemented in SFEMaNS code and validated with numerous tests cases involving comparisons with analytical solutions or experimental results. On the side it was also used to perform a preliminary analysis of Liquid Metal Battery instability. This study, not reported in this manuscript, was published in Journal of Fluid Mechanics (W. Herreman, C. Nore, L. Cappanera and J.-L. Guermond, vol. 771, p79-114, 2015 [46]).

Eventually we note the study of VKS set ups in chapter 4 required to model the action of non axisymmetric impellers that are driving the fluid by counter rotation. As the code SFEMaNS uses a Fourier expansion in the azimuthal direction and approximates the Navier-Stokes equations in a meridian plane with finite elements, a pseudo-penalization technique [89] has been adapted to prediction-correction schemes for the Navier-Stokes equations. Its implementation in SFEMaNS code, validated with manufactured solutions and a study of the flow past a sphere, now allows us to consider non axisymmetric geometries. Combined to previous extension to multiphase flow problems and the addition of the entropy viscosity stabilization method, we conclude that SFEMaNS code is now able to consider most of problems involving magnetohydrodynamics with physical parameters closer to the ones used in experiments.

6.2 Outlook

After a satisfying study of the hydrodynamical regime of a VKS set up with TM87 for moderate kinetic Reynolds numbers, the next logical step would be to use the entropy viscosity to study the flow with even larger R_e. Since DNS would not be feasible, such a study could be validated by comparisons with experiments that are currently carried out in CEA Saclay by the team of B. Dubrulle. Moreover in parallel of the studies led in this PhD period, SFEMaNS code was extended to problems with variable magnetic permeability in

time and all space directions (including the azimuthal direction) by D. Castanon in the frame of his PhD [18]. This extension now allows SFEMaNS to study MHD configurations of VKS set ups that have already been shown to generate magnetic field when the impellers present a high magnetic permeability.

Regarding the extension of SFEMaNS to multiphase flow problems, we note our algorithm is of order 1 in time which could be improved. As the introduction of BDF2 formula or second order in time extrapolation perturbs the stability of the algorithm when using large ratios of densities, we are investigating on the combination of our method with a technique of Guermond and Minev (SIAM J. Sci. Comput., 2015 in print). This technique may allow us to raise the convergence order in time to 2 for any ratio of densities by the successive use of order 1 algorithms. Furthermore the study of LMB, that may play a role in the storage of energy and that will be the subject of future experiments in Dresden [105], will be pursued. In order to get closer to a realistic set-up, thermodynamics effects should be considered and will require some modifications of SFEMaNS code.

Eventually all these previous investigations make SFEMaNS one of the most complete MHD codes. The next step is to make it available to teams working on MHD. A full documentation has been started and should be completed in 2016.

Résumé en français

7.1 Introduction

7.1.1 Contexte et motivations

Les équations de la magnétohydrodynamique (MHD) décrivent les interactions entre un fluide conducteur de l'électricité et un champ magnétique ambiant. L'évolution du champ magnétique est gouvernée par les équations de Maxwell dans la limite quasi-statique et celle du champ de vitesse par les équations de Navier-Stokes. Le couplage s'effectue par la force de Lorentz et la loi d'Ohm. L'adimensionnement de ces équations fait apparaître deux nombres sans dimension : le nombre de Reynolds cinétique R_e et le nombre de Reynolds magnétique R_m qui comparent respectivement le temps convectif avec les temps de diffusion cinétique et Ohmique. La magnétohydrodynamique intervient dans une large gamme de problèmes tels que des procédés industriels (production d'aluminium dans des cellules de Hall-Héroult ou développement des batteries à métaux liquides pour le stockage d'énergie), des phénomènes naturels (génération de champ magnétique en astrophysique) ou des expériences de laboratoire. L'approximation numérique de ces problèmes peut apporter des informations utiles pour améliorer l'efficacité de montages industriels ou de laboratoire, de plus elle présente un avantage majeur : les calculs numériques sont *a priori* plus faciles à réaliser. Cependant, la plupart de ces applications font intervenir soit des grands nombres de Reynolds cinétique, qui induisent une dynamique trop riche pour être entièrement simulée avec les capacités de calcul actuelles, soit des écoulements multiphasiques qui nécessitent de rendre compte de l'évolution de la densité, solution d'une loi de conservation qui présente des singularités dues à des discontinuités de la densité à l'interface entre deux fluides. Pour surmonter ces difficultés, la communauté scientifique développe des méthodes de stabilisation qui se concentrent sur l'approximation des grandes échelles d'un écoulement turbulent, appelées Simulation des Grandes Echelles (ou LES pour Large Eddy Simulation), ou bien sur la réduction des fortes oscillations (phénomène de Gibbs) générées par l'approximation de solutions discontinues.

Dans ce cadre, ce manuscrit de thèse propose de faire face à ces difficultés en utilisant une méthode de stabilisation non linéaire appelée viscosité entropique. Cette méthode a été développée par Guermond et al. [36, 37, 38] et consiste à ajouter une viscosité artificielle proportionnelle au résidu d'une équation d'énergie. Cette méthode permet de dissiper l'énergie accumulée par les approximations numériques due à la présence de gradients importants qui ne peuvent être représentés correctement par le maillage. Elle peut aussi

être vue comme un moyen de sélectionner l'unique solution entropique de Kružkov [61] d'une loi de conservation ou d'approcher une solution "pertinente" (suitable) des équations de Navier-Stokes au sens de Scheffer [101]. Dans tous les cas, cette méthode permet d'approcher des solutions physiques, dans le sens où elles ne produisent pas d'énergie. Dans un premier temps, nous proposons d'attester du bon comportement de la viscosité entropique comme méthode LES pour approcher des problèmes caractérisés par des grands nombres de Reynolds cinétique. A la suite de précédents travaux réalisés par l'équipe qui a encadré cette thèse, cette étude a porté sur deux problèmes physiques où le fluide est entraîné par des turbines contra-rotatives au sein d'une cavité cylindrique ou bien par un récipient cylindrique en précession. Ces problèmes sont actuellement le sujet d'expériences au CEA Saclay et à Dresden (Allemagne) ce qui permettra dans le futur des comparaisons avec nos résultats numériques. La simulation numérique de ces problèmes se fait avec le code SFEMaNS (Spectral/Finite Element for Maxwell and Navier-Stokes), développé depuis plus de dix ans par Guermond et Nore dans le système des coordonnées cylindriques. Comme ce code utilise une décomposition de Fourier dans la direction azimutale et des éléments finis de Lagrange dans un plan méridien, la représentation de turbines contra-rotatives (composées de disques munis de pales courbées ou droites) n'a été possible que par l'adaptation d'une technique de Pasquetti et al. [89] dite de pseudo-pénalisation. Dans un second temps, nous avons étendu la portée du code SFEMaNS à des problèmes d'écoulements multiphasiques. De tels problèmes présentent deux difficultés majeures : il faut suivre l'évolution de l'interface entre deux fluides immiscibles et utiliser un algorithme avec une algèbre indépendante du temps pour réduire le temps de calcul. Nous proposons de suivre l'évolution des interfaces avec une méthode de level set et nous présentons une nouvelle méthode d'approximation d'écoulements multiphasiques inspirée de Guermond et al. [41]. Cette méthode utilise la quantité de mouvement, égale à la densité fois le champ de vitesse, comme variable d'approximation des équations de Navier-Stokes. Cette méthode trouve aussi son originalité en stabilisant les équations de la masse et de la quantité de mouvement avec la même viscosité entropique ce qui réduit les oscillations qui émergent lorsque des rapports importants de densité et de viscosité sont considérés. Le bon comportement de cette méthode est vérifié sur de nombreux tests numériques. Finalement les travaux effectués durant cette thèse étendent l'action du code SFEMaNS à de nombreuses applications géophysiques ou MHD. L'utilisation de la viscosité entropique permet d'augmenter les paramètres de nos simulations numériques dans le but de se rapprocher des paramètres expérimentaux.

Avant de fournir un résumé de chaque chapitre de ce manuscrit de thèse, nous proposons de décrire brièvement son organisation. Tout d'abord, un premier chapitre est dédié au code SFEMaNS et aux différentes possibilités et récentes extensions qu'il propose. Ensuite, nous décrivons la méthode de viscosité entropique et son implémentation dans le code SFEMaNS. Cette méthode de stabilisation est alors dans un premier temps validée comme une méthode LES pour approcher des problèmes à grands nombres de Reynolds cinétique. Cette validation se fait sur des configurations expérimentales de problèmes de Von Kármán Sodium (VKS) et de cylindre en précession. Enfin, le dernier chapitre présente une nouvelle méthode d'approximation d'écoulements multiphasiques qui utilise la quantité de mouvement comme variable d'approximation et la viscosité entropique comme méthode de stabilisation.

7.1.2 Rappel des équations adimensionnées de la MHD

Pour décrire les équations de la MHD adimensionnée, on introduit une échelle de longeur de référence L_{ref}, une vitesse caractéristique U_{ref}, un temps caractéristique $T_{\text{ref}} := L_{\text{ref}}/U_{\text{ref}}$ et une pression de référence $P_{\text{ref}} := \rho U_{\text{ref}}^2$. En définissant le nombre de Reynolds cinétique $R_e := \frac{U_{\text{ref}} L_{\text{ref}}}{\nu}$ avec ν la viscosité du fluide, les équations de Navier-Stokes peuvent alors s'écrire :

$$\partial_t \mathbf{u} + (\nabla \times \mathbf{u}) \times \mathbf{u} - \frac{1}{R_e} \Delta \mathbf{u} = -\nabla p + \mathbf{f}, \tag{7.1.1}$$

$$\nabla \cdot \mathbf{u} = 0, \tag{7.1.2}$$

où $\mathbf{u}$ est le champ de vitesse, p la pression et $\mathbf{f}$ le terme source. Dans un domaine conducteur de l'électricité et sous l'approximation quasi-statique, les équations de Maxwell, qui régissent l'évolution du champ magnétique, peuvent s'écrire sous la forme adimensionnée suivante :

$$\partial_t (\mu \mathbf{H}) = -\frac{1}{R_m} \nabla \times (\frac{1}{\sigma} \nabla \times \mathbf{H}) + \nabla \times (\mathbf{u} \times (\mu \mathbf{H})), \tag{7.1.3}$$

$$\nabla \cdot (\mu \mathbf{H}) = 0. \tag{7.1.4}$$

où $\mathbf{H}$ est le champ magnétique et $R_{\text{m}} := \mu_0 \sigma_0 L_{\text{ref}} U_{\text{ref}}$ le nombre de Reynolds magnétique avec μ_0 la perméabilité magnétique de référence et σ_0 la conductivité électrique de référence et μ et σ les perméabilité et conductivité relatives.

7.2 Le code SFEMaNS

Cette section propose un résumé du chapitre 2 de ce manuscrit qui donne une description du code SFEMaNS, code MHD développé en Fortran 90 depuis 2002 par Guermond et al. [31, 33, 35]. Dans un premier temps, nous décrivons le fonctionnement du code et certaines de ses possibilités. Enfin, nous donnons des informations sur les développements plus récents réalisés durant cette thèse.

7.2.1 Description du code

Cadre de travail

Le code SFEMaNS est un code MHD qui permet d'approcher les solutions de problèmes hydrodynamique, magnétique (avec un champ de vitesse donné) et magnétohydrodynamique. SFEMaNS utilise au départ le champ de vitesse $\mathbf{u}$ comme variable d'approximation des équations de Navier-Stokes et le champ magnétique $\mathbf{H}$ comme variable pour les équations de Maxwell.

Ce code est écrit en coordonnées cylindriques (r, θ, z), par conséquent les géométries des problèmes considérés se doivent d'être axisymétriques (c'est-à-dire 2π périodiques dans la direction azimutale). Cette hypothèse d'axisymétrie réduit le champ d'action du code qui ne peut par exemple pas considérer des turbines contra-rotatives comme dans les configurations expérimentales de l'expérience von Kármán Sodium (VKS) décrite plus loin. Cependant, cette restriction a pu être surmontée par l'implémentation d'une méthode de pseudo-pénalisation de Pasquetti et al. [89] décrite par la suite.

Finalement, on peut noter que le domaine de calcul Ω est décomposé en 3 sous domaines : un domaine fluide conducteur $\Omega_{c,f}$, un domaine solide conducteur $\Omega_{c,s}$ et un domaine isolant (vide) Ω_v qui sont tous supposés axisymétriques. De plus, le domaine

isolant est supposé simplement connexe pour que le champ magnétique $\mathbf{H}$ puisse s'écrire sous la forme du gradient d'un scalaire ϕ dans Ω_v, solution de l'équation $\mu_0 \partial_t \Delta\phi = 0$ avec μ_0 la perméabilité magnétique du vide.

Approximation numérique

Le code SFEMaNS présente une méthode hybride de Fourier et d'éléments finis. L'utilisation des coordonnées cylindriques permet de faire une décomposition de Fourier dans la direction azimutale avec M le nombre de modes de Fourier complexes. Le problème 3D peut alors être découpé en M problèmes 2D indépendants (modulo les termes non linéaires) pour chaque mode $m \in [|0, M|]$. Chaque problème 2D est approché par des éléments finis de Lagrange sur un plan méridien. Les termes non linéaires sont toujours traités de façon explicite avec des extrapolations d'ordre 2 ce qui permet de travailler avec une algèbre indépendante du temps et donc de réduire le temps de calcul. On peut noter que la formulation éléments finis du problème fait intervenir des éléments de Taylor-Hood ($\mathbb{P}_2/\mathbb{P}_1$ pour le couple vitesse-pression, des polynômes d'ordre $l_{\mathbf{H}}$ pour le champ magnétique et l_ϕ pour le potentiel ϕ avec $2 \geq l_\phi \geq l_{\mathbf{H}} \geq 1$.). De plus, les équations de Maxwell et de Navier-Stokes ne sont pas approchées simultanément, c'est-à-dire que l'avancée en temps se déroule selon le schéma suivant :

- initialisation des champs de vitesse $\mathbf{u}^0, \mathbf{u}^1$ et des champs magnétiques $\mathbf{H}^0$ et $\mathbf{H}^1$,
- calcul de $\mathbf{u}^{n+1}$ et p^{n+1} (force de Lorentz calculée avec des extrapolations d'ordre 2 du champ magnétique),
- calcul de $\mathbf{H}^{n+1}$ et ϕ^{n+1} après avoir calculé les termes non linéaires avec des extrapolations en $\mathbf{u}^{n+1}$, $\mathbf{H}^n$ et $\mathbf{H}^{n-1}$.

Étant donné que cette thèse se concentre sur l'approximation des équations de Navier-Stokes, l'approximation des équations de Maxwell n'est pas décrite et peut être trouvée dans [31, 33]. L'approximation des équations de Navier-Stokes se fait avec une méthode de projection dite de prédiction-correction détaillée dans [43]. L'avancée en temps consiste à résoudre pour tout $\mathbf{v} \in \mathbf{V}_{h,0}$ et $q \in M_h$, espaces d'approximation définis dans 2.2.2, les formulations faibles suivantes :

$$\int_\Omega \frac{3}{2\tau}\mathbf{u}^{n+1}\cdot\mathbf{v} + \frac{1}{R_e}\nabla\mathbf{u}^{n+1} : \nabla\mathbf{v} = -\int_\Omega \left(\frac{-4\mathbf{u}^n + \mathbf{u}^{n-1}}{2\tau} + \nabla(p^n + \frac{4\psi^n - \psi^{n-1}}{3})\right)\cdot\mathbf{v} + \int_\Omega (\mathbf{f}^{n+1} - (\nabla\times\mathbf{u}^{*,n+1})\times\mathbf{u}^{*,n+1})\cdot\mathbf{v}, \quad (7.2.1)$$

$$\int_\Omega \nabla\psi^{n+1}\cdot\nabla q = \frac{3}{2\tau}\int_\Omega \mathbf{u}^{n+1}\cdot\nabla q, \quad (7.2.2)$$

$$\int_\Omega q\delta^{n+1} = \int_\Omega q\nabla\cdot\mathbf{u}^{n+1}, \quad (7.2.3)$$

La pression est alors actualisée en posant :

$$p^{n+1} = p^n + \psi^{n+1} - \frac{1}{R_e}\delta^{n+1}. \quad (7.2.4)$$

Quelques possibilités du code SFEMaNS

Au cours des années, le code SFEMaNS a été développé pour pouvoir prendre en compte un plus large éventail de problèmes tout en réduisant le coût de calcul. Ces travaux ont principalement permis au code de :

- présenter une parallélisation massive qui se fait sur la distribution des modes de Fourier (chaque processeur va résoudre le problème pour un groupe de modes de Fourier fixé) et aussi en décomposant le plan méridien en N_S sous domaines. Ainsi un processeur résout le problème sur un sous domaine du plan méridien pour un nombre de modes de Fourier donné. Une étude des scalabilités faible et forte est présentée dans la section 2.3.

- prendre en compte des problèmes de thermique en ajoutant l'équation de la chaleur (advection-diffusion). Cette extension a été validée avec de nombreux tests numériques et a permis de participer à un benchmark [51] comparant des codes spectraux et pseudo-spectraux.

- étudier des problèmes où la perméabilité magnétique et/ou la conductivité électrique présentent des discontinuités dans les directions radiale et verticale.

7.2.2 Développements récents

Au cours de cette thèse, nous avons décidé d'améliorer le code SFEMaNS en nous concentrant sur trois développements : l'utilisation de nombres de Reynolds cinétique plus élevés, l'extension à des géométries non axisymétriques et la prise en compte de problèmes avec des fluides à propriétés physiques (densité, viscosité) variables. Tandis que le premier développement consiste à implémenter une méthode de stabilisation, dite de viscosité entropique, décrite et validée dans les deux prochaines sections, nous nous limitons à quelques informations sur les deux autres développements.

Extension à des géométries non axisymétriques

Pour étendre le champ d'action du code SFEMaNS à des géométries non axisymétriques, nous avons adapté une technique dite de pseudo-pénalisation de Pasquetti et al. [89] à des schémas numériques des équations de Navier-Stokes de type prédiction-correction. Le domaine de calcul Ω est supposé être l'union disjointe d'un domaine fluide Ω_{fluid}, où l'évolution du champ de vitesse est régie par les équations de Navier-Stokes, et d'un domaine solide Ω_{obs} (obstacle) où la vitesse est nulle. Cette technique consiste à modifier les équations de Navier-Stokes pour que le champ de vitesse soit de l'ordre de τR_e^{-1} dans Ω_{obs} avec τ le pas de temps. Après avoir modifié la méthode, pour que celle-ci soit consistante avec des schémas de type prédiction-correction, nous avons démontré sa stabilité (voir théorème 1). Enfin, nous avons modifié le modèle pour que le solide puisse être animé d'une vitesse non nulle. Finalement, l'avancée en temps du champ de vitesse et de la pression requiert uniquement de modifier l'équation 7.2.1 par :

$$\frac{3\mathbf{u}^{n+1}}{2\tau} - \frac{1}{R_e}\Delta\mathbf{u}^{n+1} = -\nabla p^n + \chi^{n+1}\left(\frac{4\mathbf{u}^n - \mathbf{u}^{n-1}}{2\tau} - \nabla(\frac{4\psi^n - \psi^{n-1}}{3})\right) + \chi^{n+1}\left(-(\nabla\times\mathbf{u}^{*,n+1})\times\mathbf{u}^{*,n+1} + \mathbf{f}^{n+1}\right) + (1-\chi^{n+1})\frac{3\mathbf{u}_{\text{obst}}^{n+1}}{2\tau}, \quad (7.2.5)$$

avec χ une fonction de pénalisation égale à 1 dans le fluide et 0 dans le solide et où $\mathbf{u}_{\text{obst}}^{n+1}$ représente la vitesse du solide au temps $t = (n+1)\tau$.

L'implémentation de cette méthode dans SFEMaNS a été validée avec des solutions manufacturées (le terme source est pris égal au reste des termes de l'équation) et sur un problème plus connu d'écoulement autour d'une sphère. Après avoir vérifié que nous retrouvions le bon écoulement autour de la sphère à faibles nombres de Reynolds, nous avons

étudié l'évolution du coefficient de traînée C_d pour $R_e \in [1, 200]$. Le tableau 2.9 compare les valeurs de C_d théorique et obtenues avec SFEMaNS qui correspondent à moins de 1.5% d'erreur relative. Après avoir validé cette méthode, nous avons aussi étudié l'influence de l'utilisation d'une fonction de pénalisation continue (qui croît de 0 à 1 très rapidement au niveau de l'interface solide/fluide). Pour ce faire nous avons comparé les valeurs de C_d obtenues avec une fonction de pénalisation sharp (discontinue) et smooth (continue) à $R_e = 100$ et maillage fixé pour différents pas de temps. La figure 7.1 et le tableau 2.10 nous

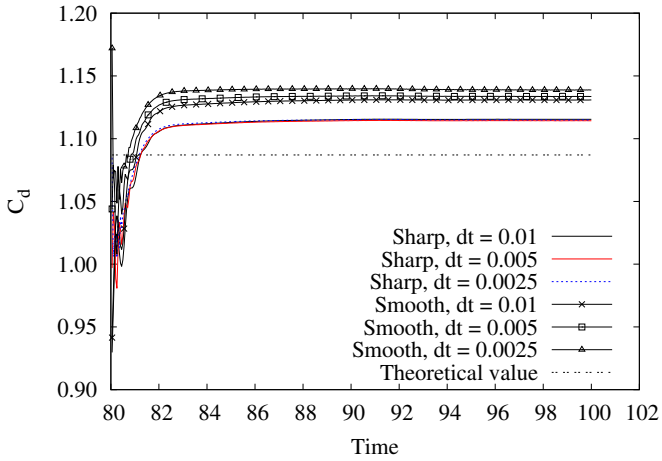

Figure 7.1: Evolution temporelle du C_d pour $R_e = 100$ avec des fonctions de pénalisation "sharp" et "smooth" pour différents pas de temps dt.

montrent le bon comportement de la méthode avec une fonction de pénalisation sharp. En revanche, l'utilisation d'une fonction smooth entraîne des erreurs plus grandes (2% contre 4%) qui augmentent lorsque le pas de temps diminue. On en conclut qu'il est préférable de travailler avec des fonctions χ discontinues (égale à 0 dans le solide et 1 dans le fluide).

Extension à des problèmes avec des fluides et solides à propriétés variables

Le dernier développement majeur du code réalisé au cours de cette thèse a consisté à prendre en compte des problèmes avec des fluides et solides à propriétés variables, c'est-à-dire des problèmes où la densité, la viscosité, la conductivité électrique et la perméabilité magnétique peuvent varier dans le temps et selon toutes les directions de l'espace. Cette étude a été motivée par notre intérêt pour les batteries à métaux liquides (ou Liquid Metal Batteries, LMB) et les problèmes de configuration VKS où le fluide est entraîné par des turbines contra-rotatives à forte perméabilité magnétique. Pour approcher la partie magnétique de tels problèmes, nous pouvions utiliser comme variable d'approximation le champ magnétique $\mathbf{H}$ ou bien le champ d'induction $\mathbf{B} := \mu\mathbf{H}$ avec μ la perméabilité magnétique. De même, les équations de Navier-Stokes font intervenir soit le champ de vitesse $\mathbf{u}$ soit la quantité de mouvement $\mathbf{m} := \rho\mathbf{u}$ avec ρ la densité. Une étude préliminaire sur des équations simplifiées, effectuée avec D. Castanon à Texas A&M University (College Station, Texas), nous a mené à utiliser le champ d'induction $\mathbf{B}$ et la quantité de mouvement $\mathbf{m}$ comme variables d'approximation des équations de la MHD. Tandis que le problème lié à l'évolution de la perméabilité magnétique a été traité par D. Castanon dans le cadre de sa thèse [18], ce manuscrit se concentre sur des problèmes à variation de densité ou viscosité et propose une nouvelle méthode d'approximation des équations de Navier-Stokes pour des écoulements multiphasiques. Cette méthode est décrite et validée dans le chapitre 5

résumé en français dans la section 7.5. On note que notre algorithme fait intervenir une même viscosité entropique pour stabiliser les équations de la masse et de la quantité de mouvement.

7.3 Viscosité entropique

Le chapitre 3 introduit la méthode de viscosité entropique comme un nouveau modèle LES. Afin de synthétiser les informations qu'on y donne, nous proposons de rappeler pourquoi il est nécessaire de développer des modèles pour approcher des écoulements à grands nombres de Reynolds cinétique. Après quelques généralités sur les modèles LES, nous introduisons la viscosité entropique comme modèle LES et décrivons son implémentation dans le code SFEMaNS.

7.3.1 Nécessité de modélisation

La simulation numérique de toutes les échelles d'un écoulement, appelée Direct Numerical Simulation (DNS), est soumise à des restrictions qui ne permettent pas sa mise en oeuvre pour des problèmes à grands R_e du fait de capacités de calcul insuffisantes. En effet, le critère de Kolmogorov dit que le rapport de la plus grande échelle d'espace sur la plus petite est proportionnel à $R_e^{3/4}$. Le maillage doit donc posséder $R_e^{3/4}$ degrés de liberté par dimension d'espace, soit $R_e^{9/4}$ en 3 dimensions. Combinée à une condition sur le pas de temps de type CFL, la simulation d'un problème 3D sur un temps code de 1 présente donc une complexité en R_e^3. Étant donné que de nombreux problèmes font intervenir des R_e de l'ordre de 10^8, la puissance de calcul des ordinateurs actuels ne permet pas de réaliser des simulations DNS. La communauté scientifique a donc développé des modèles pour réduire le coût d'approximation de tels problèmes. Deux approches principales se distinguent :

- les modèles RANS (Reynolds Averaged Navier-Stokes) qui se concentrent sur l'approximation de quantités moyennées en temps et/ou en espace. Ces modèles requièrent souvent une bonne connaissance du problème pour mettre en place des hypothèses d'invariance temporelle ou spatiale.

- les modèles LES (Large Eddy Simulation ou Simulations des Grandes Échelles) qui approchent l'écoulement de la plus grande échelle d'espace jusqu'à une échelle donnée. Ces modèles se basent sur la théorie de Kolmogorov [57, 56] qui affirme que les petites échelles, qui servent principalement à dissiper l'énergie, ont des structures plus universelles que celles des grandes échelles, qui dépendent de la géométrie et des conditions de bord du problème. Ainsi les modèles LES se concentrent sur l'approximation des grandes échelles de l'écoulement et modélisent l'action des petites échelles (aussi appelées échelles de sous maille car non représentées par le maillage) par des modèles de sous maille. Ces modèles ont pour but d'introduire un mécanisme de diffusion qui représente l'interaction entre les grandes et les petites échelles comme le scénario de cascade d'énergie de Kolmogorov.

Afin de modéliser le plus grand éventail de problèmes possibles (avec le minimum d'information) avec le code SFEMaNS, nous proposons de décrire un nouveau modèle LES développé par Guermond et al. [36, 37] dénommé viscosité entropique.

7.3.2 La viscosité entropique comme modèle LES

Le modèle de la viscosité entropique se base sur la notion de solution "pertinente" (suitable) de Scheffer [101] et se propose d'introduire une viscosité artificelle prise proportionnelle au défaut d'équilibre de l'équation d'énergie cinétique. On peut noter qu'une solution suitable est une solution dont le résidu de l'équation de l'énergie cinétique est négatif au sens des distributions. Sous certaines hypothèses de régularité, cette condition peut se ré-écrire:

$$\mathbf{R} \cdot \mathbf{u} \leq 0, \tag{7.3.1}$$

au sens des distributions avec $\mathbf{R}$ le résidu des équations de Navier-Stokes défini par $\mathbf{R}(\mathbf{x}, t) := \partial_t \mathbf{u} + (\mathbf{u}.\nabla)\mathbf{u} + \nabla p - R_e^{-1}\Delta\mathbf{u} - \mathbf{f}$. Ainsi les solutions "pertinentes" dissipent les chocs ou singularités si ceux-ci apparaissent.

Afin de définir la viscosité entropique, nous proposons d'interpréter la notion de solution pertinente dans le cadre de simulations sous résolues. Pour ce faire on considère un couple d'approximation $(\mathbf{u}_h, p_h)$ des équations de Navier-Stokes et on définit le résidu de l'équation d'énergie cinétique D_h comme suit :

$$D_h(\mathbf{x}, t) = \partial_t(\frac{1}{2}\mathbf{u}_h^2) + \nabla\cdot((\frac{1}{2}\mathbf{u}_h^2 + p)\mathbf{u}_h) - R_e^{-1}\Delta(\frac{1}{2}\mathbf{u}_h^2) + {R_e}^{-1}(\nabla\mathbf{u}_h)^2 - f \cdot \mathbf{u}_h. \tag{7.3.2}$$

Être sous résolu dans une région $(\mathbf{x}, t)$ signifie que des gradients élevés ne sont pas représentés par le maillage. Dus à des non linéarités, ces gradients vont devenir de plus en plus grands et l'énergie va s'accumuler à l'échelle du maillage. Par conséquent, l'équilibre énergétique est brisé et $D_h(\mathbf{x}, t)$ est non nul. On peut alors dire qu'une région sous résolue est une région où $D_h(\mathbf{x}, t)$ est plus grand que l'erreur de consistance du schéma numérique. Si D_h est négatif, l'énergie sera dissipée mais, si D_h est positif, l'énergie va s'accumuler et perturber notre approximation. Ainsi imposer au sens des distributions la condition :

$$D_h(\mathbf{x}, t) \leq 0 \tag{7.3.3}$$

permet d'induire un mécanisme de diffusion en accord avec celui de Kolmogorov à la base de nombreux modèles LES. Dans cet esprit, Guermond et al. [36, 37] ont introduit la méthode de viscosité entropique qui consiste à ajouter $-\nabla\cdot(\nu_{E,h}\nabla\mathbf{u}_h)$ dans le terme de gauche des équations de Navier-Stokes avec :

$$\nu_{E,h}(\mathbf{x}, t) := min\left(\mathrm{c}_{\max} h(\mathbf{x})|\mathbf{u}_h(\mathbf{x}, t)|, \mathrm{c}_\mathrm{e} h(\mathbf{x})^2 \frac{|D_h(\mathbf{x}, t)|}{\left\|\mathbf{u}_h^2\right\|_{L^\infty(\Omega)}}\right) \tag{7.3.4}$$

où h_{loc} représente la taille locale du maillage et $c_{\max}$ et c_e des constantes à régler. Ainsi définie, la viscosité entropique induit de la diffusion uniquement dans les régions sous résolues où D_h est très grand (le premier terme de la viscosité entropique est présent pour limiter la diffusion lorsque D_h devient trop grand). De plus, cette méthode est consistante. En effet, lorsque le maillage est assez fin pour résoudre toutes les échelles, D_h est de l'ordre de consistance du maillage (car $D_h = \mathbf{R}\cdot\mathbf{u}$ avec $\mathbf{R}$ le résidu des équations de Navier-Stokes). Ainsi la viscosité entropique ν_E est plus petite que l'ordre de consistance du schéma et l'on peut parler de méthode consistante.

7.3.3 La viscosité entropique dans SFEMaNS

Pour implémenter cette méthode de stabilisation non linéaire dans le code SFEMaNS, nous introduisons le résidu des équations de Navier-Stokes défini par:

$$\mathbf{R}_{\mathrm{NS}}^n := \frac{\mathbf{u}^n - \mathbf{u}^{n-2}}{2\tau} - \frac{1}{R_e}\Delta\mathbf{u}^{n-1} + \nabla\times(\mathbf{u}^{*,n-1}) \times \mathbf{u}^{*,n-1} + \nabla p^{n-1} - \mathbf{f}^{n-1}. \tag{7.3.5}$$

Ensuite nous définissons la viscosité entropique sur une maille K de taille h_{loc} comme suit:

$$\nu^n_{\text{E|K}} := \min\left(c_{\max} h_{\text{loc}} \|\mathbf{u}^{n-1}\|_{L^\infty(K)}, c_{\text{e}} h^2_{\text{loc}} \frac{\|\mathbf{R}^n_{\text{NS}} \cdot \mathbf{u}^{n-1}\|_{L^\infty(K)}}{\|\mathbf{u}^{n-1}\|^2_{L^2(\Omega)}}\right) \tag{7.3.6}$$

Finalement on ajoute le terme $\nabla\cdot(\nu^n_{\text{E}}\nabla\mathbf{u}^n)$ dans le terme de droite de l'équation 7.2.1. Le lecteur pourra remarquer que la viscosité entropique est traitée de façon explicite pour garder une algèbre indépendante du temps et ainsi un temps de calcul raisonnable. Après avoir implémenté cette méthode dans le code SFEMaNS, nous avons vérifié sa propriété de consistance avec un test analytique qui est détaillé dans la section 3.2.2. D'un autre côté, le bon comportement de la viscosité entropique dans le cadre de simulations sous résolues est étudié sur deux configurations expérimentales (VKS et cylindre en précession) dans le chapitre 4 résumé dans la prochaine section. On peut noter que de précédentes études [36, 37, 38] ont déjà permis de mettre en valeur le bon comportement de cette méthode pour approcher des solutions singulières des équations de Burgers et d'Euler. Plus récemment, dans [34], il a été montré que la viscosité entropique est plus efficace que le modèle classique LES de Smagorinsky pour approcher des solutions analytiques des équations de Navier-Stokes. Bien que cette section introduise la viscosité entropique comme modèle LES, nous utilisons aussi cette méthode dans le chapitre **??** pour stabiliser un nouvel algorithme d'approximation des équations de Navier-Stokes à densité variable.

7.4 Application aux Simulations des Grandes Echelles (LES)

Dans cette section, nous proposons de résumer le chapitre 4 qui a pour but de valider la viscosité entropique comme modèles LES. Avec cet objectif, nous étudions deux configurations expérimentales qui ont fait l'objet de précédentes études par Guermond et Nore. Tout d'abord, nous étudions le régime hydrodynamique d'un problème de VKS. Nous validons notre modèle LES pour $R_e \leq 2500$ par des comparaisons avec des simulations DNS. De futurs calculs à plus grands R_e pourraient voir le jour et être comparés à des résultats expérimentaux en cours d'acquisition au CEA Saclay. Dans un second temps nous étudions, sous la forme d'un article en préparation, deux configurations différentes de cylindre en précession. Étant donné que la précession est connue pour être une source possible d'effet dynamo, nous proposons aussi une étude MHD du problème avec des DNS pour déterminer laquelle des configurations est la plus "dynamogène".

7.4.1 Application à des écoulements de Von Kármán

Les écoulements de Von Kármán ont fait l'objet de nombreuses études expérimentales et numériques qui ont permis de mettre en avant certaines propriétés de l'écoulement pour des nombres de Reynolds modérés que nous proposons de retrouver avec la viscosité entropique dans le cadre de simulations sous résolues. Nous décrivons tout d'abord le procédé expérimental que nous reproduisons numériquement. Cette étude est d'abord réalisée avec des DNS sur des maillages fins. Ces résultats sont ensuite utilisés pour valider notre modèle de viscosité entropique (LES) en les comparant à des résultats LES obtenus sur des maillages plus grossiers.

Positionnement du problème

Nous proposons d'étudier une configuration expérimentale de type VKS avec des turbines TM87. Le problème consiste à entraîner un fluide dans un récipient cylindrique

avec deux turbines contra-rotatives. Ces turbines sont composées d'un disque muni de 8 pales de rayon de courbure égal à 72^o degrés. Le rayon du cylindre est égal à 100mm tandis que celui du disque est de 92.5mm. La distance entre les deux disques est fixée à 180mm. Une représentation 3D du dispositif et une coupe 2D qui récapitule les longueurs caractéristiques du dispositif sont représentées dans la figure 7.2.

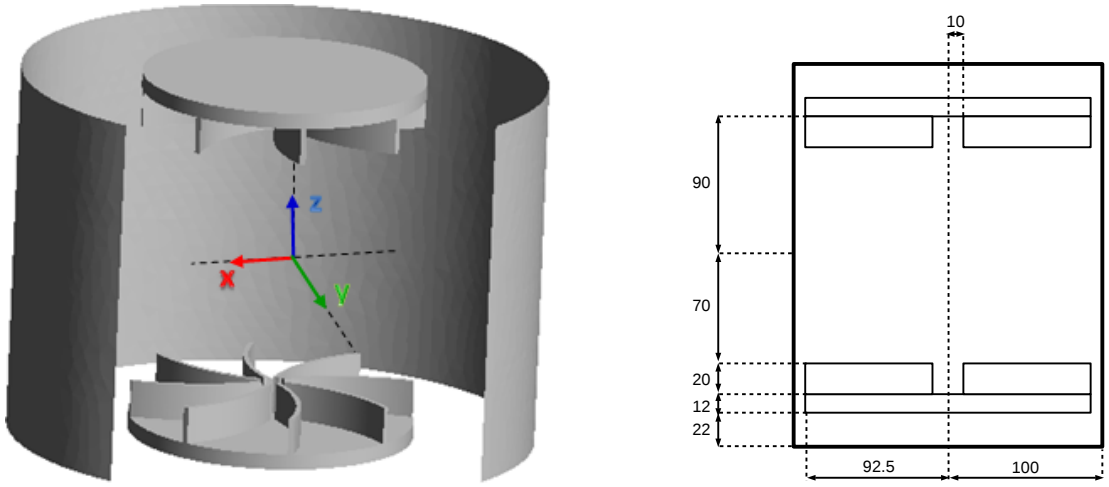

(a) Représentation 3D d'une configuration VKS (b) Coupe verticale 2D du dispositif.

Figure 7.2: Représentations 3D et 2D du dispositif expérimental (figure (a) de H. Zaidi et unité de la figure (b) en millimètres).

Les simulations numériques sont réalisées avec la technique de pseudo-pénalisation décrite précédemment et utilisent une fonction de pénalisation égale à 1 dans le fluide et 0 dans les turbines. De plus, on utilise des conditions de bord de Dirichlet homogènes car les parois sont immobiles dans le référentiel du laboratoire. Afin de pouvoir analyser nos simulations, nous calculons l'énergie cinétique, le couple, la vitesse U_{RMS} et les énergies poloidale (associée aux composantes radiale et verticale) et toroidale (associée à la composante azimutale) du champ de vitesse. Ces quantités sont aussi moyennées en temps, nous renvoyons à la section 4.1.2 pour plus de détails.

Régime hydrodynamique pour $R_e \leq 2500$ (DNS)

Nous validons notre méthode d'approximation en étudiant le régime hydrodynamique du problème pour $R_e \leq 208$. Cette étude nous permet de retrouver une loi du couple en R_e^{-1} pour de faibles nombres de Reynolds, voir figure 4.7. Nous en profitons pour rappeler que notre méthode présente une erreur en τR_e^{-1}. Pour obtenir cette loi de puissance, nous avons donc dû fixer la valeur de τR_e^{-1} et non celle du pas de temps. Nous retrouvons l'écoulement attendu à $R_e = 208$ qui est axisymétrique, stationnaire et composé de deux recirculations toriques poloidales (u_r, u_z) et d'une couche de mélange toroidale en u_θ (voir figure 4.9), ce qui valide notre méthode d'approximation.

Afin de valider notre modèle LES, nous proposons d'étudier l'écoulement pour $R_e = 500, 1000$ et 2500 avec des DNS pour, par la suite, comparer ces calculs à des résultats LES sur un maillage plus grossier. Nous notons que les calculs DNS et LES utilisent tous deux 64 modes de Fourier mais le maillage des DNS est deux fois plus fin près des turbines (pas de maillage 1/200) que celui des LES. Pour $R_e \geq 500$ l'écoulement devient instationnaire et brise son axisymétrie, de plus la valeur du couple décroît lorsque R_e augmente ce qui laisse intuiter une valeur asympotique déjà mise en évidence dans Ravelet et al. [95]. A

$R_e = 500$ le mode de Fourier $m = 2$ devient dominant (modulo les modes 0 et 8 dus à la présence des turbines contra-rotatives) comme dans [95]. Une seconde bifurcation dans la répartition de l'énergie cinétique sur les différents modes de Fourier intervient pour $R_e = 1000$ où le mode 3 devient dominant, voir la figure 7.3. Ce comportement

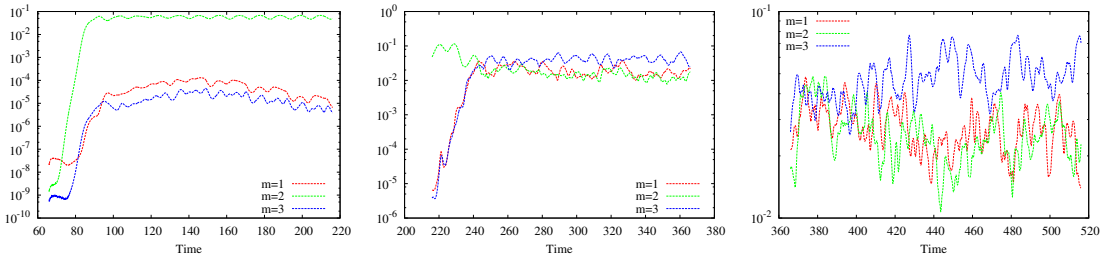

(a) $R_e = 500$. (b) $R_e = 1000$. (c) $R_e = 2500$.

Figure 7.3: Évolution temporelle de l'énergie cinétique des modes de Fourier $m = 1, 2$, and 3 pour $R_e \in \{500, 1000, 2500\}$.

avait déjà été observé avec des turbines TM73 par D. Castanon [18]. On peut noter que, pour $R_e = 2500$, le mode 3 reste dominant tandis que les modes 1 et 2 sont aussi non négligeables ce qui va entraîner une répartition plus homogène de l'énergie entre tous les modes de Fourier (voir la figure 4.14 pour une représentation des spectres de l'énergie). Des échanges de fluide entre les parties inférieure et supérieure du cylindre se mettent en place pour $R_e \geq 500$ et permettent de retrouver la présence d'un mode $m = 2$ pour $R_e = 500$ (voir figure 4.11). Finalement, nous retrouvons aussi la présence de structures tourbillonnaires entre les pales des turbines, déjà mises en évidence expérimentalement et numériquementr par Ravelet et al. [96] et numériquement par Kreuzahler et al. [60]. Notre méthode nous a donc permis de retrouver des résultats en accord avec de précédentes études expérimentales [94, 95] et numériques [18, 60] qui seront donc utilisés pour valider notre modèle de viscosité entropique.

Résultats LES avec la viscosité entropique pour $R_e \leq 5000$

La validation de notre modèle LES se fait par des comparaisons d'énergies, de spectres d'énergie, de visualisations des écoulements entres des simulations DNS-LES pour $R_e = 500, 1000$ et 2500. Tout d'abord, on peut noter que les quantités numériques calculées au cours des simulations LES et DNS diffèrent de $1 - 2\%$ comme le montrent les tableaux 4.1 et 4.3. La simulation LES à $R_e = 500$ retrouve aussi la bifurcation dans le spectre d'énergie (mode 2 dominant) et la même répartition de l'énergie sur les modes de Fourier que celui de la DNS, réalisée sur un maillage deux fois plus fin près des turbines. Après avoir vérifié que les simulations LES à $R_e = 1000$ et 2500 donnent des résultats similaires aux simulations DNS, ce qui valide notre modèle LES, nous avons décidé de mettre en valeur les bénéfices de la viscosité entropique par rapport à une simulation sans stabilisation réalisée sur le même maillage grossier. Pour ce faire, nous avons réalisé une simulation à $R_e = 1000$ avec le maillage LES mais sans stabilisation. Comme le montre la figure 7.4, le mode 2 reste dominant avec la simulations DNS sous résolue alors que la simulation LES montre bien un mode 3 qui devient dominant comme les simulations DNS à maillage fin.

Après avoir validé notre modèle LES, nous proposons une étude préliminaire du régime hydrodynamique pour $R_e = 5000$. Cette étude, qui sera prochainement poursuivie avec de plus grands nombres de Reynolds dans le but d'être comparée à des résultats expérimentaux de Dubrulle et al., a permis de confirmer que le couple semble tendre vers une valeur

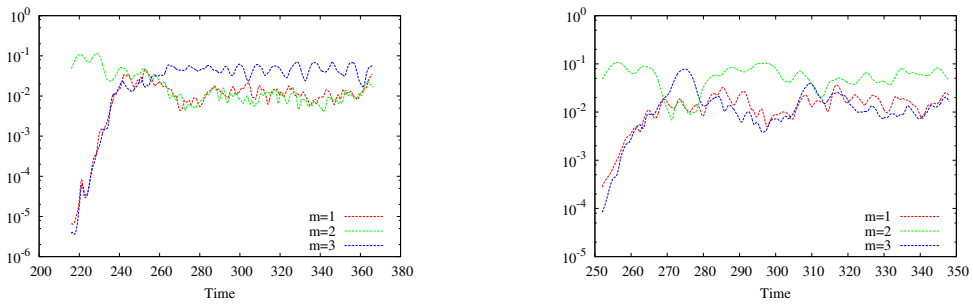

(a) LES. (b) DNS sous résolue.

Figure 7.4: Évolution temporelle de l'énergie cinétique des modes de Fourier 1, 2 et 3 avec $R_e = 1000$ pour des simulations LES et DNS réalisées sur le même maillage grossier.

asymptotique. Ce comportement est aussi notable avec d'autes quantités étudiées, telles que l'énergie cinétique ou la vitesse U_{RMS}, dont les valeurs moyennes varient de moins en moins lorsque R_e croît. Ce comportement est en accord avec une précédente étude numérique [60].

Conclusion

Une première étude à faibles nombres de Reynolds (inférieurs à 200) nous a permis de retrouver l'écoulement laminaire attendu et une loi du couple en R_e^{-1} ce qui valide l'adaptation de la technique de pseudo-pénalisation de Pasquetti et al. à des solides en mouvement et à des schémas de prédiction-correction. L'étude du régime hydrodynamique pour $R_e \geq 500$ nous permet de conclure que la viscosité entropique approche correctement les solutions d'un problème de VKS avec des maillages sous résolus pour des nombres de Reynolds cinétique modérés $R_e \leq 5000$. Ainsi, la viscosité entropique se trouve être un bon candidat pour réaliser des simulations à grands R_e. La suite logique de cette étude est la mise en place de calculs LES à plus grands R_e pour faire des comparaisons avec des résultats expérimentaux de l'équipe de B. Dubrulle du CEA Saclay. Une autre perspective est l'étude MHD de ce problème avec des turbines à forte perméabilité magnétique (configuration connue pour générer un champ magnétique principalement axisymétrique).

7.4.2 Application à des récipients cylindriques en précession

La section 4.2 présente, sous la forme d'un article en préparation, une étude hydrodynamique et magnétohydrodynamique de deux configurations de cylindre en précession dont nous proposons de relater les résultats majeurs. Dans un premier temps, nous décrivons les problèmes étudiés afin de proposer une étude du régime hydrodynamique des deux configurations. Ensuite, nous étudions le régime MHD des deux configurations et analysons l'influence de la présence de parois conductrices de l'électricité ou ferromagnétiques sur le seuil de la dynamo.

Positionnement du problème

Le problème consiste à suivre l'évolution d'un fluide conducteur de l'électricité dans un conteneur cylindrique entrainé par une rotation principale et une seconde rotation, dite de précession, d'axe différent et d'intensité inférieure (par exemple le mouvement d'une toupie). On peut noter que l'axe de la précession est fixe dans le référentiel du laboratoire et correspond à l'axe de la table tournante. Deux configurations sont étudiées, la première fait l'objet d'expériences en laboratoire à Dresden notamment [105] et utilise une rotation

principale autour de l'axe de symétrie du cylindre et une rotation de précession autour d'un axe qui lui est perpendiculaire. Cette configuration, que l'on dénommera "axial spin case", a déjà été le sujet d'études hydrodynamiques par Nore et al. [83] que nous proposons d'étendre à un plus grand intervalle de nombres de Reynolds cinétique grâce à la méthode de viscosité entropique. En complément, nous proposons aussi d'étudier une configuration de précession, dite "equatorial spin case", qui fait intervenir une rotation principale autour d'un axe radial du cylindre et une rotation de précession de la table tournante, voir figure 4.23. Cette étude complémentaire va nous permettre dans un premier de comparer les régimes hydrodynamiques de chaque configuration pour déterminer quelle est la plus à même de briser les symétries (comportement favorable à l'effet dynamo). Dans un second temps, une étude MHD des deux configurations nous permet de discerner laquelle est vraiment la plus favorable à l'effet dynamo. Finalement une analyse de l'influence des propriétés des couvercles et des parois latérales du cylindre (faites avec des matériaux conducteurs ou ferromagnétiques) sur le seuil de la dynamo pour le cas du "axial spin case" est proposée et pourrait trouver des applications dans les futures expériences de précession conduites à Dresden (Allemagne).

Régime hydrodynamique

L'étude hydrodynamique du "axial spin case" commence à $R_e = 4000$ par une comparaison entre des calculs DNS et des calculs LES réalisés sur un maillage plus grossier avec la viscosité entropique. Des comparaisons de l'évolution des énergies cinétiques et des spectres d'énergie au temps final sont proposées dans la figure 4.40. Le bon comportement de la viscosité entropique, qui retrouve des résultats très proches de ceux de la DNS ($1-2\%$ d'erreur relative), valide notre modèle LES ce qui nous a permis de réaliser des simulations hydrodynamiques jusqu'à $R_e = 15000$. Ces nouveaux résultats LES combinés à des précédents résultats de DNS pour $R_e \in [1200, 4000]$ suggèrent une loi de puissance de l'énergie cinétique dans le référentiel en précession en $R_e^{-0.48}$, voir figure 4.25. Cette loi suggère que le champ de vitesse moyenné en temps varie comme $R_e^{-1/4}$ et donc que le champ moyen devient nul à grands nombres de Reynolds. Une autre interprétation est que le champ de vitesse est d'amplitude 1 près des parois latérales du cylindre (qui sont en rotation) et que le fluide est entraîné par les parois dans une couche limite d'épaisseur $R_e^{-0.5}$. Des visualisations de l'écoulement pour différents nombres de Reynolds nous permettent de confirmer que l'écoulement dans le référence des murs tend vers une rotation solide opposée à la rotation principale (autour de l'axe de symétrie du cylindre). Ce comportement avait déjà été observé et discuté dans [82, 58].

La configuration "equatorial spin case" est étudiée avec des simulations DNS pour des nombres de Reynolds de 200 à 4000. Tout comme le "axial spin case", l'écoulement semble tendre vers une rotation solide dans le référentiel des murs opposée à la rotation principale (donc autour d'un axe radial). D'un autre côté, cette configuration brise plus facilement les symétries, en effet l'énergie antisymétrique sature pour $R_e \geq 2000$ autour de 6% contre 1% pour le "axial spin case", voir figure 4.32. Étant donné que les brisures de symétrie facilitent l'effet dynamo, ce résultat nous a conduit à étudier la partie MHD de ce problème pour les deux configurations pour déterminer laquelle est en effet la plus favorable à l'effet dynamo.

Effet dynamo (étude MHD)

Dans un premier temps, nous étudions le régime MHD du "equatorial spin case" pour $R_e = 1200$ comme Nore et al. l'avaient fait pour le "axial spin case" pour ce même nombre

de Reynolds cinétique. Nous montrons que le seuil d'apparition de l'effet dynamo pour le "equatorial spin case" est proche de $R_m^c = 2400$ ce qui est bien supérieur à celui du "axial spin case" égal à $R_m^c = 775$. Ainsi le "equatorial spin case" a beau briser plus facilement les symétries de l'écoulement, il reste moins favorable à l'effet dynamo. On peut noter que les champs magnétiques générés par ces deux configurations sont différents : dans le cas du "axial spin case", il est majoritairement dipolaire tandis que, pour le cas du "equatorial spin case", il est quadripolaire.

En complément, nous étudions aussi l'influence de la présence de parois conductrices de l'électricité ou ferromagnétiques sur le seuil de la dynamo pour le "axial spin case" qui est le sujet d'expériences à Dresden [105]. Tandis que la présence de parois ferromagnétiques réhausse le seuil de la dynamo, la présence de parois conductrices permet de baisser le nombre de Reynolds magnétique critique au delà duquel on constate de l'effet dynamo. Plus précisemment, c'est la présence de parois conductrices latérales qui favorise l'effet dynamo tandis que la présence de couvercles conducteurs augmente la valeur de R_m^c.

Conclusion

Nous avons donc validé la méthode de viscosité entropique comme modèle LES ce qui nous a permis de réaliser une étude hydrodynamique du problème jusqu'à $R_e = 15000$ et de mettre en évidence une loi en puissance de l'énergie cinétique dans le référentiel en précession en $R_e^{-0.48}$ pour le "axial spin case". L'étude du problème "equatorial spin case" nous a permis de montrer que briser les symétries n'est pas toujours synonyme d'être plus favorable à l'effet dynamo. Finalement nous avons montré qu'utiliser un conteneur avec des parois latérales conductrices de l'électricité permet d'abaisser le seuil d'apparition de l'effet dynamo ce qui pourrait trouver écho dans la réalisation d'expériences de précession à Dresden [105].

7.5 Approximation d'écoulements multiphasique avec la quantité de mouvement

Nous proposons un résumé du chapitre 5 qui présente, sous la forme d'un article en préparation, une nouvelle méthode d'approximation des équations de Navier-Stokes à densité variable. Dans un premier temps nous donnons quelques informations sur le nouveau modèle que nous avons développé, ensuite nous présentons quelques tests sur lesquels nous avons validé notre méthode.

7.5.1 Approximation numérique

Modélisation du problème hydrodynamique et stabilisation

L'approximation d'un écoulement multiphasique requiert d'approcher les solutions de l'équation de la masse (équation d'advection) et de la quantité de mouvement (équation de Navier-Stokes). Afin de reconstruire les propriétés physiques des fluides (densité et viscosité dynamique), nous avons décidé d'approcher l'équation de la masse en implémentant une méthode de level set. Notre méthode consiste à suivre l'évolution de l'interface entre les deux fluides en considérant une fonction ϕ à valeurs dans $[0, 1]$ telle que l'interface entre les deux fluides est représentée par $\phi^{-1}(1/2)$ et ϕ est solution de:

$$\partial_t \phi + \mathbf{u} \cdot \nabla \phi = 0. \tag{7.5.1}$$

La densité ρ et la viscosité dynamique η peuvent alors être reconstruites en utilisant ϕ, voir les équation 5.2.5- 5.2.6. Après avoir reconstruit ρ et η, nous approchons les équations de Navier-Stokes avec la quantité de mouvement $\mathbf{m} := \rho\mathbf{u}$, qui peuvent s'écrire:

$$\partial_t \mathbf{m} + \nabla\cdot(\mathbf{m}\otimes\mathbf{u}) - \frac{2}{R_e}\nabla\cdot(\eta\varepsilon(\mathbf{u})) + \nabla p = \frac{1}{W_e}\nabla\cdot\mathcal{S} - \frac{1}{F_r}\rho\mathbf{e}_z + \mathbf{f}, \tag{7.5.2a}$$

$$\nabla\cdot\mathbf{u} = 0, \tag{7.5.2b}$$

avec $\epsilon(u) = \nabla^s\mathbf{u}$ le gradient symétrisé de $\mathbf{u}$, $\mathcal{S}$ le tenseur lié à la tension superficielle défini dans l'équation 5.2.7 et R_e, F_r et W_e des nombres adimensionnés définis dans 5.2.2. L'utilisation de $\mathbf{m}$ comme variable d'approximation permet de travailler avec une matrice de masse indépendante du temps. Afin que la matrice de rigidité soit aussi indépendante du temps, nous réécrivons l'opérateur de diffusion sous la forme $\nabla\cdot(\overline{\nu}\varepsilon(\mathbf{m})) + \nabla\cdot(-\overline{\nu}\varepsilon(\mathbf{m}) + \eta\varepsilon(\mathbf{u}))$ avec $\overline{\nu} \geq \frac{\eta}{\rho}$. Le premier terme est alors traité de façon implicite tandis que le second est traité de façon explicite. Nous avons établi une preuve de stabilité, voir théorème 2, de notre méthode pour un cas simplifié. Nous renvoyons à [41] qui propose une analyse de stabilité complète de la méthode dont nous nous inspirons.

Afin de réduire les oscillations qui peuvent être générées en présence de grands rapports de densité ou viscosité, nous stabilisons les équations de la level set et de la quantité de mouvement avec la même viscosité entropique. Ainsi nous ajoutons le terme $\nabla\cdot(\nu_E\nabla\phi)$ dans le terme de droite de l'équation de la level set et le terme $\nabla\cdot(\nu_E\nabla\mathbf{m})$ dans le terme de droite des équations de Navier-Stokes. On note que la viscosité entropique ν_E est traitée de façon explicite et est construite avec le résidu des équations de Navier-Stokes. La définition rigoureuse de cette viscosité entropique est donnée dans la section 5.4.2.

Enfin l'ajout de la viscosité entropique dans l'équation d'advection qui régit l'évolution de la level set nous conduit à ajouter un terme de compression pour que la level set ne soit pas trop diffusée. Tandis que nous renvoyons à la section 5.4.3 pour plus d'informations techniques de cette méthode de compression, nous proposons dans la figure 7.5 de montrer son importance sur un problème de transport d'une fonction en escalier. Le lecteur

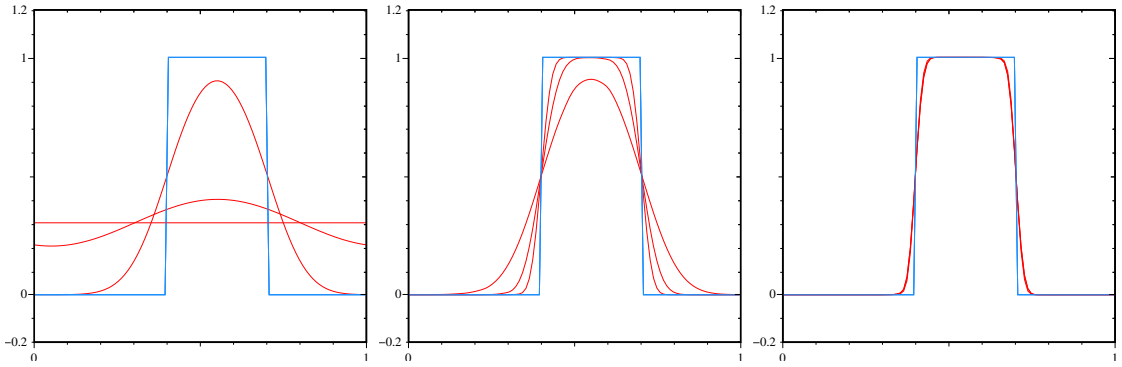

(a) Visc. 1er ordre (b) Entropy visc. (c) Entropy visc. + comp.

Figure 7.5: Transport linéaire de la fonction $\phi_0(x) = \mathbf{1}_{0.4\leq x\leq 0.7}$, solutions exacte en bleue et approchées en rouge au temps $T = 1,\ 10,\ 100$.

peut constaster que la stabilisation du problème avec une viscosité de premier ordre ou entropique entraîne trop de diffusion au cours du temps. La combinaison de la viscosité entropique et de notre méthode de compression (figure 7.5.c) permet de limiter l'effet diffusif de la viscosité entropique : la solution approchée reste constante au cours du temps et n'est pas aplatie.

Extension de l'algorithme à des problèmes MHD

Afin de pouvoir étudier des problèmes MHD, nous avons aussi modifié les équations de Maxwell pour que le code SFEMaNS puisse prendre en compte des fluides à conductivité électrique variable. Ce nouvel algorithme des équations Maxwell utilise le champ d'induction $\mathbf{B}$ comme variable d'approximation. Afin de travailler avec une algèbre constante, nous avons réécrit le terme diffusif comme dans les équations de Navier-Stokes, c'est-à-dire $\nabla\times(\frac{1}{\overline{\sigma}}\nabla\times\mathbf{b}) - \nabla\times((\frac{1}{\overline{\sigma}} - \frac{1}{\sigma})\nabla\times\mathbf{b})$ avec $\overline{\sigma} \leq \sigma_{\min}$. Le premier terme est alors traité de façon implicite tandis que le terme $\nabla\times((\frac{1}{\overline{\sigma}} - \frac{1}{\sigma})\nabla\times\mathbf{b})$ est traité de façon explicite ce qui nous permet de travailler avec une matrice de rigidité indépendante du temps et de réduire le temps de calcul associé à l'algorithme. Cette extension nous a permis de publier une étude des instabilités de Tayler dans les Batteries à Métaux Liquides dans [46]. L'algorithme a aussi été validé sur un problème de chute d'une bulle conductrice de l'électricité freinée par un champ magnétique vertical ambiant qui avait déjà été étudié par Tagawa [108].

7.5.2 Récapitulatif de quelques test numériques

Dans un premier temps, nous avons validé notre méthode avec des solutions manufacturées (le terme de forçage est pris égal au reste des termes de l'équation) et des problèmes d'ondes de gravité. Dans un second temps, nous avons poursuivi notre validation de la méthode avec des tests où le fluide est soit entraîné par des parois en rotation soit par des effets de tensions superficielles combinés à la gravité que nous proposons de décrire dans la suite.

Tests avec des parois en rotation

Nous avons testé notre algorithme avec un test de Newton Bucket qui consiste à remplir un récipient cylindrique d'un fluide lourd surmonté d'un fluide plus léger (rapport de densité 1000, de même pour la viscosité dynamique). Le cylindre est alors mis en rotation autour de son axe de symétrie. L'interface finale (à l'équilibre) est connue théoriquement et nous a permis de valider notre méthode. On note que la variation de la viscosité dynamique nécessite d'utiliser le gradient symétrique dans l'opérateur de diffusion car l'utilisation de l'opérateur $\nabla\cdot(\eta\nabla\mathbf{u})$ entraîne une erreur non négligeable sur la position finale de l'interface entre les deux fluides.

Afin de mettre en avant la nécessité d'écrire l'opérateur de diffusion sous la forme $\nabla\cdot(\eta\nabla^s\mathbf{u})$, nous proposons d'étudier une configuration proche de celle du Newton-Bucket. La seule différence est que seule la paroi inférieure du cylindre est en rotation (et non plus le cylindre entier). L'interface à l'équilibre n'est plus connue théoriquement, et pour valider nos calculs nous proposons de comparer nos résultats à des résultats expérimentaux et numériques de Kahouadji et Martin Witowski [53]. Comme le montre la figure 7.6, SFEMaNS permet bien de retrouver un profil d'élévation de la surface très proche de celui expérimental lorsque l'on utilise $\nabla^s\mathbf{u}$. L'utilisation du gradient non symétrique (trait noir pointillé) induit clairement un écart.

Tests avec tension surperficielle

Nous avons aussi réalisé plusieurs tests qui font intervenir des effets de tension superficielle. Dans un premier temps, nous avons utilisé une configuration de Newton-Bucket avec un nombre de Weber variant dans l'intervalle $[50, \infty[$ et comparé avec succès nos résultats numériques à ceux de Brady et Lopez [15]. Ensuite nous avons étudié la dynamique d'une bulle dans un milieu plus dense. Sous l'action conjointe de la gravité et de la tension superficielle, la bulle va alors monter mais aussi se déformer. Ce problème avait déjà été étudié par Hua et Lou dans [48], ce qui nous a permis de valider notre étude en comparant

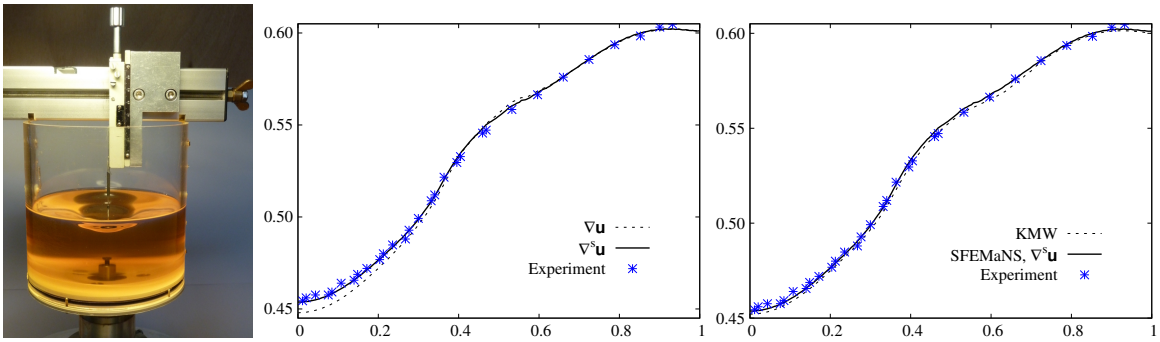

Figure 7.6: (a) Configuration expérimental avec une sonde qui mesure l'élévation de la surface (image de L. Martin Witkowski); (b) Profil de l'interface obtenu par SFEMaNS avec $\nabla \mathbf{u}$ (trait pointillé) et $\nabla^s \mathbf{u}$ (ligne solide) et par expériences (symbole $*$); (c) Solution numérique de SFEMaNS avec $\nabla^s \mathbf{u}$ (ligne solide), résultats de Kahouadji et Martin Witowski [53] numériques (ligne pointillée) et expérimentaux (symbole $*$)

la vitesse finale de la bulle et sa forme géométrique (voir tableau 5.6 et la figure 5.8) pour différents rapports de densité, viscosité dynamique et nombres de Weber.

On note que tous les problèmes étudiés jusqu'à présent étaient axisymétriques et donc ne dépendaient pas de la direction azimutale θ. Afin de vérifier le bon comportement de notre méthode pour des écoulements qui dépendent de θ, nous avons étudié un problème de bulle oscillante décrit dans [68]. Le problème consiste à suivre la dynamique d'une bulle dans un fluide de même densité et viscosité sous l'action unique de la tension superficielle. À l'instant initial la bulle est déformée avec une perturbation selon le mode de Fourier $m = 0$ ou $m = 1$. Gràce à Lamb [65], la période d'oscillation de la bulle est connue dans le cas d'un fluide parfait (R_e infini). Comme le montre la figure 5.9, nous retrouvons la période d'oscillation théorique lorsque R_e est supérieur à $100 - 500$.

En conclusion, nous avons présenté et validé une nouvelle méthode d'approximation d'écoulements multiphasiques. Cette méthode est inspirée de [41], où une analyse complète de la stabilité de l'algorithme est présentée. L'avantage principal de cette méthode est que la matrice de rigidité est indépendante du temps ce qui permet son implémentation dans des codes spectraux. Après avoir démontré la stabilité d'une version simplifiée de notre méthode, nous l'avons validée avec un large spectre de tests.

7.6 Conclusion

7.6.1 Résultats

Toutes les études menées durant cette thèse ont été motivées par l'amélioration du code SFEMaNS. Ce projet s'inscrit dans la continuité des thèses précédentes de R. Laguerre [63], A. Ribeiro [97] et F. Luddens [74] qui ont permis la naissance du code SFEMaNS et son développement en un code massivement parallèle qui peut approcher des problèmes MHD avec des effets thermiques ou des discontinuités de la perméabilité magnétique dans les directions radiale et verticale. Dans ce cadre, un des objectifs de cette thèse a été d'implémenter une méthode de stabilisation pour que des paramètres plus proches de ceux utilisés lors d'expériences puissent être envisagés. L'autre principal objectif a consisté à étendre l'action du code SFEMaNS à des problèmes d'écoulements multiphasiques.

Le premier objectif a été atteint en implémentant une méthode de stabilisation non

linéaire, dite de viscosité entropique, qui induit une diffusion proportionnelle au déséquilibre d'une équation d'énergie. Les bonnes performances de cette méthode LES ont été mises en valeur en étudiant des problèmes d'écoulements de von Kármán (VKS) ou de récipient cylindrique en précession qui sont tous deux le sujet d'expériences respectivement au CEA Saclay et à Dresden (Allemagne). Dans un premier temps, nous avons comparé des résultats DNS et LES pour des nombres de Reynolds modérés $R_e \leq 2500$ sur un problème de type VKS. Cela a permis de montrer le bon comportement de la viscosité entropique pour approcher des problèmes avec des maillages sous résolus. Cette méthode LES a retrouvé les résultats des DNS (réalisées avec un maillage plus fin) tandis que des simulations sur ce même maillage sous résolu sans stabilisation rataient des bifurcations dans le spectre d'énergie. L'étude numérique du problème pour $R_e \leq 2500$ nous a permis de retrouver une loi de puissance du couple K_p en R_e^{-1} pour des faibles nombres de Reynolds et des bifurcations dans le spectre d'énergie connues pour $R_e \in \{500, 1000\}$. Une étude préliminaire de l'écoulement pour $R_e = 5000$ a permis de retrouver des comportements similaires à ceux d'autres études expérimentales et numériques [95, 96, 60]. En conclusion, la méthode de viscosité entropique se trouve être un bon candidat pour approcher le régime hydrodynamique d'une configuration VKS avec des maillages sous résolus et pourrait être utilisée pour poursuivre cette étude avec des nombres de R_e cinétique plus élevés. Dans un second temps, nous avons utilisé la viscosité entropique pour étendre à un plus large intervalle de nombres de Reynolds cinétique une étude antérieure de Nore et al. [83] sur des cylindres en précesion de type "axial spin case". Après avoir validé le modèle LES avec des comparaisons DNS à $R_e = 4000$, des simulations LES jusqu'à $R_e \leq 15000$ combinées à des résultats DNS pour $R_e \leq 4000$ ont mis en évidence une loi de puissance de l'énergie cinétique dans le référentiel en précession en $R_e^{-0.48}$. Nous avons aussi montré que l'écoulement tend vers une rotation solide dans le référentiel des murs ce qui concorde avec des résultats expérimentaux obtenus à plus grands Reynolds dans [82]. En complément, un second type de précession, dit "equatorial spin case", a aussi été étudié et une étude MHD des deux configurations a été proposée pour déterminer la plus favorable à la génération d'un champ magnétique (effet dynamo). Bien que la configuration "equatorial spin case" permette de briser plus facilement les symétries de l'écoulement, elle s'est révelée être moins favorable à l'effet dynamo. Pour finir, nous avons constaté que le seuil de dynamo peut être abaissé en utilisant des parois latérales en cuivre ce qui pourrait trouver écho dans la préparation d'expériences de précession à Dresden [105].

L'extension du code SFEMaNS à des problèmes d'écoulements multiphasiques a nécessité le développement d'une nouvelle méthode d'approximation des équations de Navier-Stokes à densité variable. Après avoir implémenté une méthode de level set pour rendre compte de l'évolution de l'interface entre deux fluides, il nous restait à surmonter quelques difficultés pour approcher les solutions des équations de Navier-Stokes. Étant donné que la densité et la viscosité dépendent du temps et de l'espace, utiliser le champ de vitesse comme variable induirait une matrice de masse et un opérateur de diffusion qui dépendraient tous deux du temps et de l'espace. Pour travailler avec une algèbre indépendante du temps, où la matrice de rigidité est assemblée uniquement à l'initialisation, nous avons développé une méthode inspirée de [41] qui utilise la quantité de mouvement comme variable. La matrice de masse devient alors indépendante du temps et l'opérateur diffusif est réécrit de telle façon qu'il puisse être traité explicitement. La principale originalité de cette méthode est de stabiliser les équations de la masse (level set) et de la quantité de mouvement (Navier-Stokes) avec la même viscosité entropique, ce qui nous permet de simuler des rapports de densité

et viscosité élevés. On remarque que l'addition d'un terme de diffusion dans l'équation de la level set nous a conduit à ajouter un élément de compression pour que la level set ne se fasse pas aplatir au cours du temps. Au contraire de beaucoup de méthodes qui préfèrent ajouter une étape de compression à l'algorithme, comme dans [21], nous préférons ajouter un ingrédient de compression lors de la résolution de l'équation d'advection (level set). Cette méthode a été implémentée dans le code SFEMaNS et validée avec de nombreux tests analytiques et comparaisons expérimentales. Cette méthode a aussi été utilisée pour réaliser une étude préliminaire des instabilités des Batteries à Métaux Liquides (LMB). Cette étude, qui n'est pas rapportée dans ce manuscrit, a été publiée dans la revue Journal of Fluid Mechanics (W. Herreman, C. Nore, L. Cappanera and J.-L. Guermond, vol. 771, p79-114, 2015 [46]).

Pour conclure, on peut noter que l'étude de configurations VKS dans le chapitre 4 nécessitait la modélisation de turbines non axisymétriques en contra-rotation qui mettent le fluide en mouvement. Étant donné que le code SFEMaNS utilise une décomposition de Fourier dans la direction azimutale et approche les équations de Navier-Stokes avec des éléments finis 2D dans un plan méridien, une technique de pseudo-pénalisation [89] a été adaptée pour des schémas de type prédiction-correction des équations de Navier-Stokes. Son implémentation dans le code SFEMaNS, validée par des tests analytiques et l'étude de l'écoulement autour d'une sphère, nous permet maintenant de considérer des géométries non axisymétriques. Combinée à la précédente extension aux problèmes multiphasiques et à l'implémentation de la méthode de stabilisation de viscosité entropique, nous pouvons conclure que le code SFEMaNS est maintenant capable d'étudier la plupart des problèmes MHD avec des paramètres physiques plus proches de ceux utilisés en laboratoire.

7.6.2 Perspectives

Après une étude satisfaisante du régime hydrodynamique d'un problème de VKS avec des turbines TM87 pour des nombres de Reynolds modérés, la prochaine étape serait de prolonger notre étude avec la viscosité entropique pour de plus grands R_e. Étant donné que les DNS ne seront pas faisables pour de tels nombres de Reynolds, cette étude pourrait être comparée à des résultats expérimentaux en cours d'acquisition au CEA Saclay par l'équipe de B. Dubrulle. En parallèle des études menées dans ce manuscrit, le code a été adapté pour des problèmes avec des perméabilités magnétiques variables en temps et dans toutes les directions de l'espace par D. Castanon dans le cadre de sa thèse [18]. Cette extension permet maintenant l'étude MHD de problèmes de VKS qui sont connus pour générer un champ magnétique lorsque les turbines ont une perméabilité magnétique suffisamment grande.

En ce qui concerne l'extension de SFEMaNS à des problèmes multiphasiques, on peut noter que notre algorithme est d'ordre 1 en temps. Étant donné que l'utilisation de formule BDF2 pour la discrétisation temporelle de la dérivée en temps n'est pas stable pour de grands rapports de densité ou de viscosité, nous pensons combiner notre algorithme à une technique de Guermond et Minev (SIAM J. Sci. Comput., 2015 en impression). Cette technique nous permettrait d'obtenir un algorithme d'ordre 2 en temps par l'utilisation successive d'algorithmes d'ordre 1. De plus, l'étude des LMB, qui pourrait jouer un rôle futur dans le stockage d'énergie produite de façon intermittente et qui sera le sujet de futures expériences à Dresden [105], sera poursuivie. Pour être plus proche d'une configuration réaliste, les effets thermiques devront être considérés et nécessiteront des modifications du

code SFEMaNS.

Finalement, toutes les études précédentes ont permis à SFEMaNS de devenir un des codes MHD les plus complets. La prochaine étape est de rendre accessible ce code à d'autres équipes étudiant des problèmes MHD. Pour ce faire, la rédaction d'une documentation complète du code est en cours et devrait être finalisée en 2016.

Bibliography

[1] D. J. Acheson. *Elementary fluid dynamics*. Oxford University Press, 1990.

[2] A.S. Almgren, J.B. Bell, P. Colella, L.H. Howell, and M.L. Welcome. A conservative adaptive projection method for the variable density incompressible Navier-Stokes equations. *J. Comput. Phys.*, 142(1):1–46, 1998.

[3] D. M. Anderson, G. B. McFadden, and A. A. Wheeler. Diffuse-interface methods in fluid mechanics. In *Annual review of fluid mechanics, Vol. 30*, volume 30 of *Annu. Rev. Fluid Mech.*, pages 139–165. Annual Reviews, Palo Alto, CA, 1998.

[4] J. G. Andrews and K. W. Morton. A posteriori error estimation based on discrepancies in an entropy variable. *International Journal of Computational Fluid Dynamics*, 10(3):183–198, 1998.

[5] C. Bailly and G. Comte-Bellot. Turbulence (CNRS éditions). *Sciences et techniques de l'ingénieur*, 2003.

[6] S. Balay, S. Abhyankar, M. F. Adams, J. Brown, P. Brune, K. Buschelman, V. Eijkhout, W. D. Gropp, D. Kaushik, M. G. Knepley, L. Curfman McInnes, K. Rupp, B. F. Smith, and H. Zhang. PETSc users manual. Technical Report ANL-95/11 - Revision 3.5, Argonne National Laboratory, 2014.

[7] S. Balay, J. Brown, K. Buschelman, W. D. Gropp, D. Kaushik, M. G. Knepley, L. Curfman McInnes, B. F. Smith, and H. Zhang. PETSc Web page, 2011. http://www.mcs.anl.gov/petsc.

[8] S. Balay, W. D. Gropp, L. Curfman McInnes, and B. F. Smith. Efficient management of parallelism in object oriented numerical software libraries. In E. Arge, A. M. Bruaset, and H. P. Langtangen, editors, *Modern Software Tools in Scientific Computing*, pages 163–202. Birkhäuser Press, 1997.

[9] G. K. Batchelor. Note on a class of solutions of the navier-stokes equations representing steady rotationally-symmetric flow. *The Quarterly Journal of Mechanics and Applied Mathematics*, 4(1):29–41, 1951.

[10] Y. Bazilevs, V. M. Calo, J. A. Cottrell, T. J. R. Hughes, A. Reali, and G. Scovazzi. Variational multiscale residual-based turbulence modeling for large eddy simulation of incompressible flows. *Computer Methods in Applied Mechanics and Engineering*, 197(1):173–201, 2007.

[11] J. B. Bell and D. L. Marcus. A second-order projection method for variable- density flows. *J. Comput. Phys.*, 101:334–348, 1992.

[12] A. Bonito, J.-L. Guermond, and F. Luddens. Regularity of the Maxwell equations in heterogeneous media and Lipschitz domains. *Journal of Mathematical Analysis and applications*, 408(2):498–512, December 2013.

[13] A. Bonito, J.-L. Guermond, and B. Popov. Stability analysis of explicit entropy viscosity methods for non-linear scalar conservation equations. *Mathematics of Computation*, 83(287):1039–1062, 2014.

[14] M. Bourgoin, L. Marié, F. Pétrélis, C. Gasquet, A. Guigon, J. Luciani, M. Moulin, F. Namer, J. Burguete, A. Chiffaudel, et al. Magnetohydrodynamics measurements in the von Kármán sodium experiment. *Physics of Fluids (1994-present)*, 14(9):3046–3058, 2002.

[15] P. T. Brady, M. Herrmann, and J. M. Lopez. Two-fluid confined flow in a cylinder driven by a rotating end wall. *Phys. Rev. E*, 85:016308, Jan 2012.

[16] O. Cadot, S. Douady, and Y. Couder. Characterization of the low-pressure filaments in a three-dimensional turbulent shear flow. *Physics of Fluids (1994-present)*, 7(3):630–646, 1995.

[17] L. Caffarelli, R. Kohn, and L. Nirenberg. Partial regularity of suitable weak solutions of the Navier-Stokes equations. *Communications on pure and applied mathematics*, 35(6):771–831, 1982.

[18] D. Castanon-Quiroz. *Solution of the MHD equations in the presence of non-axisymmetric conductors using the Fourier-finite element method.* Phd thesis, Texas A&M University, College Station, 2015. In preparation.

[19] R. Clift, J. R. Grace, and M. E. Weber. *Bubbles, drops, and particles.* Courier Corporation, 2005.

[20] M. Costabel. A remark on the regularity of solutions of Maxwell's equations on Lipschitz domains. *Mathematical Methods in the Applied Sciences*, 12(4):365–368, 1990.

[21] T. Coupez. Convection Of Local Level Set Function For Moving Surfaces And Interfaces In Forming Flow. In J.M.A. César de Sá and A.D. Santos, editors, *AIP Conference Proceedings*, volume 908(1), 2007.

[22] T. Coupez, L. Silva, and L. Ville. Convected level set method for the numerical simulation of fluid buckling. *Internat. J. Numer. Methods Fluids*, (66):324–344, February 2010.

[23] T. G. Cowling. The magnetic field of sunspots. *Monthly Notices of the Royal Astronomical Society*, 94:39–48, 1933.

[24] S. Dong and J. Shen. A time-stepping scheme involving constant coefficient matrices for phase-field simulations of two-phase incompressible flows with large density ratios. *J. Comput. Phys.*, 231(17):5788–5804, 2012.

[25] M. Frigo and S. G. Johnson. The design and implementation of FFTW3. *Proc. of the IEEE*, 93(2):216–231, 2005.

[26] R. F. Gans. On hydromagnetic precession in a cylinder. *J. Fluid Mech.*, 45:111–130, 1970.

[27] A. Giesecke, C. Nore, F. Plunian, R. Laguerre, A. Ribeiro, F. Stefani, G. Gerbeth, J. Léorat, and J.-L. Guermond. Generation of axisymmetric modes in cylindrical kinematic mean-field dynamos of VKS type. *Geophys. Astrophys. Fluid Dyn.*, 104(2):249 – 271, 2010.

[28] A. Giesecke, C. Nore, F. Stefani, G. Gerbeth, J. Léorat, W. Herreman, F. Luddens, and J.-L. Guermond. Influence of high-permeability discs in an axisymmetric model of the Cadarache dynamo experiment. *New Journal of Physics*, 14(5):053005, 2012.

[29] A. Giesecke, C. Nore, F. Stefani, G. Gerbeth, J. Léorat, F. Luddens, and J.-L. Guermond. Electromagnetic induction in non-uniform domains. *Geophysical and Astrophysical Fluid Dynamics*, page 25, September 2010.

[30] S. Goto, A. Matsunaga, M. Fujiwara, M. Nishioka, S. Kida, M. Yamato, and S. Tsuda. Turbulence driven by precession in spherical and slightly elongated spheroidal cavities. *Physics of Fluids*, 26(5), 2014.

[31] J.-L. Guermond, R. Laguerre, J. Léorat, and C. Nore. An interior penalty galerkin method for the MHD equations in heterogeneous domains. *J. Comput. Phys.*, 221(1):349–369, January 2007.

[32] J.-L. Guermond, R. Laguerre, J. Léorat, and C. Nore. An interior penalty Galerkin method for the MHD equations in heterogeneous domains. *J. Comput. Phys.*, 221(1):349–369, 2007.

[33] J.-L. Guermond, R. Laguerre, J. Léorat, and C. Nore. Nonlinear magnetohydrodynamics in axisymmetric heterogeneous domains using a Fourier/finite element technique and an interior penalty method. *J. Comput. Phys.*, 228(8):2739–2757, May 2009.

[34] J.-L. Guermond, A. Larios, and T. Thompson. Validation of an entropy-viscosity model for large eddy simulation. In *Direct and Large-Eddy Simulation IX*, pages 43–48. Springer, 2015.

[35] J.-L. Guermond, J. Léorat, F. Luddens, C. Nore, and A. Ribeiro. Effects of discontinuous magnetic permeability on magnetodynamic problems. *J. Comput. Phys.*, 230(16):6299–6319, July 2011.

[36] J.-L. Guermond and R. Pasquetti. Entropy viscosity method for high-order approximations of conservation laws. In *Spectral and High Order Methods for Partial Differential Equations*, pages 411–418. Springer, 2011.

[37] J.-L. Guermond, R. Pasquetti, and B. Popov. Entropy viscosity method for nonlinear conservation laws. *J. Comput. Phys.*, 230(11):4248–4267, 2011.

[38] J.-L. Guermond, R. Pasquetti, and B. Popov. From suitable weak solutions to entropy viscosity. *J. Sci. Comput.*, 49(1):35–50, October 2011.

[39] J.-L. Guermond and L. Quartapelle. A projection FEM for variable density incompressible flows. *J. Comput. Phys.*, 165(1):167–188, 2000.

[40] J.-L. Guermond and A. Salgado. A splitting method for incompressible flows with variable density based on a pressure Poisson equation. *J. Comput. Phys.*, 228(8):2834 – 2846, 2009.

[41] J.-L. Guermond, A. J. Salgado, and J. Shen. Splitting for variable density flows. *SIAM Journal on Numerical Analysis*, 2015. In preparation.

[42] J.-L. Guermond and A.J. Salgado. Error analysis of a fractional time-stepping technique for incompressible flows with variable density. *SIAM Journal on Numerical Analysis*, 49(3):917–944, 2011.

[43] J.-L. Guermond and J. Shen. On the error estimates for the rotational pressure-correction projection methods. *Math. Comp.*, 73(248):1719–1737 (electronic), 2004.

[44] M. E. Gurtin, D. Polignone, and J. Viñals. Two-phase binary fluids and immiscible fluids described by an order parameter. *Math. Models Methods Appl. Sci.*, 6(6):815–831, 1996.

[45] A. Harten. The artificial compression method for computation of shocks and contact discontinuities. III. Self-adjusting hybrid schemes. *Math. Comp.*, 32:363–389, 1978.

[46] W. Herreman, C. Nore, L. Cappanera, and J.-L. Guermond. Tayler instability in liquid metal columns and liquid metal batteries. *J. Fluid Mech.*, 771:79–114, 2015.

[47] H. Homann and J. Bec. Finite-size effects in the dynamics of neutrally buoyant particles in turbulent flow. *Journal of Fluid Mechanics*, 651:81–91, 2010.

[48] J. Hua and J. Lou. Numerical simulation of bubble rising in viscous liquid. *J. Comput. Phys.*, 222(2):769–795, March 2007.

[49] T. J. R. Hughes, L. P. Franca, and G. M. Hulbert. A new finite element formulation for computational fluid dynamics: VIII. The Galerkin/least-squares method for advective-diffusive equations. *Computer Methods in Applied Mechanics and Engineering*, 73(2):173–189, 1989.

[50] T. J. R. Hughes, L. Mazzei, and K. E. Jansen. Large eddy simulation and the variational multiscale method. *Computing and Visualization in Science*, 3(1-2):47–59, 2000.

[51] A. Jackson, A. Sheyko, P. Marti, A. Tilgner, D. Cebron, S. Vantieghem, R. Simitev, F. Busse, X. Han, G. Schubert, S. Takehiro, Y. Sasaki, Y.-Y. Hayashi, A. Ribeiro, C. Nore, and J.-L. Guermond. A spherical shell numerical dynamo benchmark with pseudo-vacuum magnetic boundary conditions. *Geophys. J. Int.*, 196(2):712–713, 2014.

[52] C. Johnson, A. Szepessy, and P. Hansbo. On the convergence of shock-capturing streamline diffusion finite element methods for hyperbolic conservation laws. *Mathematics of computation*, 54(189):107–129, 1990.

[53] L. Kahouadji and L. Martin Witkowski. Free surface due to a flow driven by a rotating disk inside a vertical cylindrical tank: Axisymmetric configuration. *Physics of Fluids (1994-present)*, 26(7):072105, 2014.

[54] T. von Kármán. Über laminare und turbulente reibung. *ZAMM-Journal of Applied Mathematics and Mechanics/Zeitschrift für Angewandte Mathematik und Mechanik*, 1(4):233–252, 1921.

[55] G. Karypis and V. Kumar. A fast and high quality multilevel scheme for partitioning irregular graphs. *SIAM Journal on Scientific Computing*, 20(1):359–392, 1998.

[56] A. N. Kolmogorov. Dissipation of energy in locally isotropic turbulence. In *Dokl. Akad. Nauk SSSR*, volume 32, pages 16–18, 1941.

[57] A. N. Kolmogorov. The local structure of turbulence in incompressible viscous fluid for very large reynolds numbers. In *Dokl. Akad. Nauk SSSR*, volume 30, pages 299–303, 1941.

[58] D. Kong, Z. Cui, X. Liao, and K. Zhang. On the transition from the laminar to disordered flow in a precessing spherical-like cylinder. *Geophysical & Astrophysical Fluid Dynamics*, 109(1):62–83, 2015.

[59] D. Kong, X. Liao, and K. Zhang. The sidewall-localized mode in a resonant precessing cylinder. *Physics of Fluids*, 26(5):–, 2014.

[60] S. Kreuzahler, D. Schulz, H. Homann, Y. Ponty, and R. Grauer. Numerical study of impeller-driven von Kármán flows via a volume penalization method. *New Journal of Physics*, 16(10):103001, 2014.

[61] S. N. Kružkov. First order quasilinear equations with several independent variables. *Mat. Sb. (N.S.)*, 81 (123):228–255, 1970.

[62] R. Lagrange, P. Meunier, F. Nadal, and C. Eloy. Precessional instability of a fluid cylinder. *Journal of Fluid Mechanics*, 666:104–145, 1 2011.

[63] R. Laguerre. *Approximation des équations de la MHD par une méthode hybride spectrale-éléments finis nodaux: application à l'effet dynamo*. PhD thesis, Paris 7, 2006.

[64] R. Laguerre, C. Nore, J. Léorat, and J.-L. Guermond. Effects of conductivity jumps in the envelope of a kinematic dynamo flow. *CR Mécanique*, 334:593, 2006.

[65] S. H. Lamb. *Hydrodynamics*, volume isbn: 9780521458689. Cambridge Mathematical library, 6th edition edition, 1993.

[66] W. J. Layton and L. G. Rebholz. *Approximate deconvolution models of turbulence: analysis, phenomenology and numerical analysis*, volume 2042. Springer Science & Business Media, 2012.

[67] M. Le Bars, D. Cébron, and P. Le Gal. Flows driven by libration, precession, and tides. *Annual Review of Fluid Mechanics*, 47(1):163–193, 2015.

[68] H. Lemonnier, D. Jamet, and O. Lebaigue. *Validation of Advanced Computational Methods for Multiphase Flow*, volume ISBN: 1-56700-218-8. Begell house, inc., 1rst edition, 2005.

[69] A. Leonard. Energy cascade in large-eddy simulations of turbulent fluid flows. In *Turbulent Diffusion in Environmental Pollution*, volume 1, pages 237–248, 1974.

[70] J. Leray. Essai sur le mouvement d'un fluide visqueux emplissant l'espace. *Acta Math.*, 63:193–248, 1934.

[71] M. Lesieur, O. Metais, and P. Comte. Large-eddy simulations of turbulence. *J. Fluid Mech.*, 555:474, 2006.

[72] Y. Lin, J. Noir, and A. Jackson. Experimental study of fluid flows in a precessing cylindrical annulus. *Physics of Fluids*, 26(4):–, 2014.

[73] J. Lowengrub and L. Truskinovsky. Quasi-incompressible Cahn-Hilliard fluids and topological transitions. *R. Soc. Lond. Proc. Ser. A Math. Phys. Eng. Sci.*, 454(1978):2617–2654, 1998.

[74] F. Luddens. *Theoretical and numerical analysis of the magnetohydrodynamics equations : application to dynamo action.* Phd thesis, Université Paris Sud - Paris XI, December 2012.

[75] W. V. R. Malkus. Precession of the Earth as the cause of geomagnetism: Experiments lend support to the proposal that precessional torques drive the Earth's dynamo. *Science*, 160(3825):259–264, 1968.

[76] L. Marié, C. Normand, and F. Daviaud. Galerkin analysis of kinematic dynamos in the von Kármán geometry. *Physics of Fluids (1994-present)*, 18(1):017102, 2006.

[77] P. Marti, N. Schaeffer, R. Hollerbach, D. Cébron, C. Nore, F. Luddens, J.-L. Guermond, J. Aubert, S. Takehiro, Y. Sasaki, et al. Full sphere hydrodynamic and dynamo benchmarks. *Geophysical Journal International*, 197(1):119–134, 2014.

[78] S. Miralles, N. Bonnefoy, M. Bourgoin, Ph. Odier, J.-F. Pinton, N. Plihon, G. Verhille, J. Boisson, F. Daviaud, and B. Dubrulle. Dynamo threshold detection in the von Kármán sodium experiment. *Phys. Rev. E*, 88:013002, Jul 2013.

[79] H. K. Moffatt. *Magnetic Field Generation in Electrically Conducting Fluids.* Cambridge Monographs on Mechanics and Applied Mathematics. Cambridge University Press, Cambridge, UK, 1978.

[80] R. Monchaux, M. Berhanu, M. Bourgoin, M. Moulin, P. Odier, J.-F. Pinton, R. Volk, S. Fauve, N. Mordant, F. Pétrélis, et al. Generation of a magnetic field by dynamo action in a turbulent flow of liquid sodium. *Physical review letters*, 98(4):044502, 2007.

[81] R. Monchaux, M. Berhanu, M. Bourgoin, M. Moulin, Ph. Odier, J.-F. Pinton, R. Volk, S. Fauve, N. Mordant, F. Pétrélis, A. Chiffaudel, F. Daviaud, B. Dubrulle, C. Gasquet, L. Marié, and F. Ravelet. Generation of a magnetic field by dynamo action in a turbulent flow of liquid sodium. *Phys. Rev. Lett.*, 98:044502, Jan 2007.

[82] W. Mouhali, T. Lehner, J. Léorat, and R. Vitry. Evidence for a cyclonic regime in a precessing cylindrical container. *Experiments in Fluids*, 53(6):1693–1700, 2012.

[83] C. Nore, J. Léorat, J.-L. Guermond, and F. Luddens. Nonlinear dynamo action in a precessing cylindrical container. *Phys. Rev. E*, 84:016317, 2011.

[84] C. Nore, F. Moisy, and L. Quartier. Experimental observation of near-heteroclinic cycles in the von Kármán swirling flow. *Physics of Fluids (1994-present)*, 17(6):064103, 2005.

[85] C. Nore, D. Castanon Quiroz, J.-L. Guermond, J. Léorat, and F. Luddens. Numerical dynamo action in cylindrical containers. *The European Physical Journal Applied Physics*, 70(3):31101, 2015.

[86] C. Nore, M. Tartar, O. Daube, and L. S. Tuckerman. Survey of instability thresholds of flow between exactly counter-rotating disks. *Journal of Fluid Mechanics*, 511:45–65, 2004.

[87] C. Nore, L. S. Tuckerman, O. Daube, and S. Xin. The 1 [ratio] 2 mode interaction in exactly counter-rotating von Kármán swirling flow. *Journal of Fluid Mechanics*, 477:51–88, 2003.

[88] E. Olsson and G. Kreiss. A conservative level set method for two phase flow. *J. Comput. Phys.*, 210:225–246, 2005.

[89] R. Pasquetti, R. Bwemba, and L. Cousin. A pseudo-penalization method for high Reynolds number unsteady flows. *Appl. Numer. Math.*, 58(7):946–954, July 2008.

[90] R. Pasquetti and N. Peres. A penalty model of synthetic micro-jet actuator with application to the control of wake flows. *Computers & Fluids*, 114:203–217, 2015.

[91] S. B. Pope. *Turbulent flows*. Cambridge university press, 2000.

[92] G. Puppo. Numerical entropy production for central schemes. *SIAM Journal on Scientific Computing*, 25(4):1382–1415, 2004.

[93] J.-H. Pyo and J. Shen. Gauge-Uzawa methods for incompressible flows with variable density. *J. Comput. Phys.*, 221(1):181–197, 2007.

[94] F. Ravelet. *Bifurcations globales hydrodynamiques et magnétohydrodynamiques dans un écoulement de von Kármán turbulent*. PhD thesis, Ecole Polytechnique X, 2005.

[95] F. Ravelet, A. Chiffaudel, and F. Daviaud. Supercritical transition to turbulence in an inertially driven von Kármán closed flow. *Journal of Fluid Mechanics*, 601:339–364, 2008.

[96] F. Ravelet, B. Dubrulle, F. Daviaud, and P.-A. Ratie. Kinematic α tensors and dynamo mechanisms in a von Kármán swirling flow. *Physical review letters*, 109(2):024503, 2012.

[97] A. Ribeiro. *Approche spectrale/éléments finis pour des problèmes de magnétohydrodynamique non-linéaires*. PhD thesis, Université Paris Sud-Paris XI, 2010.

[98] P. H. Roberts. *An introduction to Magnetohydrodynamics*. first edition. Longmans, 1967.

[99] P. Sagaut. *Large Eddy Simulations for Incompressible Flows*, volume 3. Springer Berlin, 2000.

[100] B. Saint-Michel, E. Herbert, J. Salort, C. Baudet, M. Bon Mardion, P. Bonnay, M. Bourgoin, B. Castaing, L. Chevillard, F. Daviaud, et al. Probing quantum and classical turbulence analogy through global bifurcations in a von Kármán liquid helium experiment. *arXiv preprint arXiv:1401.7117*, 2014.

[101] V. Scheffer. Hausdorff measure and the Navier-Stokes equations. *Comm. Math. Phys.*, 55(2):97–112, 1977.

[102] J. A. Sethian. A fast marching level set method for monotonically advancing fronts. *Proc. Natl. Acad. Sci. USA*, 93:1591–1595, February 1996.

[103] J. Shen and X. Yang. A phase-field model and its numerical approximation for two-phase incompressible flows with different densities and viscosities. *SIAM J. Sci. Comput.*, 32(3):1159–1179, 2010.

[104] D. Shetty, J. Shen, A. J. Chandy, and S. H. Frankel. A pressure-correction scheme for rotational Navier-Stokes equations and its application to rotating turbulent flows. 2011.

[105] F. Stefani, S. Eckert, G. Gerbeth, A. Giesecke, Th. Gundrum, C. Steglich, T. Weier, and B. Wustmann. DRESDYN - a new facility for MHD experiments with liquid sodium. *Magnetohydrodynamics*, 48:103–113, 2012.

[106] F. Stefani, M. Xu, G. Gerbeth, F. Ravelet, A. Chiffaudel, F. Daviaud, and J. Léorat. Ambivalent effects of added layers on steady kinematic dynamos in cylindrical geometry : application to the VKS experiment. *Eur. J. Fluid Mech, B*, 25:894, 2006.

[107] A. Szepessy. Convergence of a shock-capturing streamline diffusion finite element method for a scalar conservation law in two space dimensions. *Mathematics of computation*, 53(188):527–545, 1989.

[108] T. Tagawa. Numerical simulation of two-phase flows in the presence of a magnetic field. *Mathematics and Computers in Simulation*, 72(2):212–219, 2006.

[109] A. Tilgner. Precession driven dynamos. *Phys. Fluids*, 17(3):034104, 2005.

[110] G. Verhille, N. Plihon, M. Bourgoin, Ph. Odier, and J.-F. Pinton. Induction in a von Kármán flow driven by ferromagnetic impellers. *New Journal of Physics*, 12(3):033006, 2010.

[111] C.-C. Wu and P. Roberts. On a dynamo driven by topographic precession. *Geophys. Astrophys. Fluid Dyn.*, 103(6):467–501, 2009.

[112] P. J. Zandbergen and D. Dijkstra. Von kármán swirling flows. *Annual review of fluid mechanics*, 19(1):465–491, 1987.

université PARIS-SACLAY

ÉCOLE DOCTORALE
Sciences mécaniques et énergétiques, matériaux et géosciences (SMEMAG)

Auteur (Author) : Loïc Cappanera
Titre : Stabilisation non linéaire des équations de la magnétohydrodynamique et applications aux écoulements multiphasiques
Title: Nonlinear stabilization of magnetohydrodynamics equations and applications to multiphase flows

Résumé : Les travaux présentés dans ce manuscrit se concentrent sur l'approximation numérique des équations de la magnétohydrodynamique (MHD) et sur leur stabilisation pour des problèmes caractérisés par des nombres de Reynolds cinétique élevés ou par des écoulements multiphasiques. Nous validons numériquement un nouveau modèle de Simulation des Grandes Échelles (ou Large Eddy Simulations, LES), dit de viscosité entropique, sur des écoulements de cylindre en précession ou créés par des turbines contra-rotatives (écoulement de Von Kármán). Ces études sont réalisées avec le code MHD SFEMaNS développé par J.-L. Guermond et C. Nore depuis 2002 pour des géométries axisymétriques. Ce code est basé sur une décomposition spectrale dans la direction azimutale et des éléments finis de Lagrange dans un plan méridien. Nous adaptons une méthode de pseudo-pénalisation pour prendre en compte des turbines en mouvement, ce qui étend le code SFEMaNS à des géométries quelconques. Nous présentons aussi une méthode originale d'approximation des équations de Navier-Stokes à densité variable qui utilise la quantité de mouvement comme variable et la viscosité entropique pour stabiliser les équations de la masse et du mouvement.
Mots clés : Écoulements multiphasiques, viscosité entropique, méthode de pseudo-pénalisation, méthode de level set, magnétohydrodynamique

Abstract: The investigations presented in this manuscript focus on the numerical approximation of the magnetohydrodynamics (MHD) equations and on their stabilization for problems involving either large kinetic Reynolds numbers or multiphase flows. We validate numerically a new Large Eddy Simulation (LES) model, called entropy viscosity, on flows driven by precessing cylindrical containers or counter-rotating impellers (Von Kármán flow). These studies are performed with SFEMaNS MHD-code developed by J.-L. Guermond and C. Nore since 2002 for axisymmetric geometries. This code is based on a spectral decomposition in the azimuthal direction and a Lagrange finite element approximation in a meridian plane. We adapt a pseudo-penalization method to report the action of rotating impellers that extends the range of SFEMaNS's applications to any geometry. We also present an original approximation method of the Navier-Stokes equations with variable density. This method uses the momentum as variable and stabilizes both mass and momentum equations with the same entropy viscosity.
Key words: Multiphase flows, entropy viscosity, pseudo-penalization method, level set method, magnetohydrodynamics